



UNIVERSITAT DE  
BARCELONA

## Solid Oxide Electrolysis Cells electrodes based on mesoporous materials

Elba María Hernández Rodríguez

**ADVERTIMENT.** La consulta d'aquesta tesi queda condicionada a l'acceptació de les següents condicions d'ús: La difusió d'aquesta tesi per mitjà del servei TDX ([www.tdx.cat](http://www.tdx.cat)) i a través del Dipòsit Digital de la UB ([diposit.ub.edu](http://diposit.ub.edu)) ha estat autoritzada pels titulars dels drets de propietat intel·lectual únicament per a usos privats emmarcats en activitats d'investigació i docència. No s'autoritza la seva reproducció amb finalitats de lucre ni la seva difusió i posada a disposició des d'un lloc aliè al servei TDX ni al Dipòsit Digital de la UB. No s'autoritza la presentació del seu contingut en una finestra o marc aliè a TDX o al Dipòsit Digital de la UB (framing). Aquesta reserva de drets afecta tant al resum de presentació de la tesi com als seus continguts. En la utilització o cita de parts de la tesi és obligat indicar el nom de la persona autora.

**ADVERTENCIA.** La consulta de esta tesis queda condicionada a la aceptación de las siguientes condiciones de uso: La difusión de esta tesis por medio del servicio TDR ([www.tdx.cat](http://www.tdx.cat)) y a través del Repositorio Digital de la UB ([diposit.ub.edu](http://diposit.ub.edu)) ha sido autorizada por los titulares de los derechos de propiedad intelectual únicamente para usos privados enmarcados en actividades de investigación y docencia. No se autoriza su reproducción con finalidades de lucro ni su difusión y puesta a disposición desde un sitio ajeno al servicio TDR o al Repositorio Digital de la UB. No se autoriza la presentación de su contenido en una ventana o marco ajeno a TDR o al Repositorio Digital de la UB (framing). Esta reserva de derechos afecta tanto al resumen de presentación de la tesis como a sus contenidos. En la utilización o cita de partes de la tesis es obligado indicar el nombre de la persona autora.

**WARNING.** On having consulted this thesis you're accepting the following use conditions: Spreading this thesis by the TDX ([www.tdx.cat](http://www.tdx.cat)) service and by the UB Digital Repository ([diposit.ub.edu](http://diposit.ub.edu)) has been authorized by the titular of the intellectual property rights only for private uses placed in investigation and teaching activities. Reproduction with lucrative aims is not authorized nor its spreading and availability from a site foreign to the TDX service or to the UB Digital Repository. Introducing its content in a window or frame foreign to the TDX service or to the UB Digital Repository is not authorized (framing). Those rights affect to the presentation summary of the thesis as well as to its contents. In the using or citation of parts of the thesis it's obliged to indicate the name of the author.

# **Solid Oxide Electrolysis Cells electrodes based on mesoporous materials**

Thesis by:

Elba María Hernández Rodríguez

Supervisors:

Albert Tarancón Rubio and Marc Torrell Faro

Tutor:

Joan Ramón Morante Leonart



**UNIVERSITAT<sub>DE</sub>  
BARCELONA**



# **Solid Oxide Electrolysis Cells electrodes based on mesoporous materials**

Memoria presentada para optar al grado de doctor por la  
Universidad de Barcelona

Programa de doctorado en Nanociencias

Autor/a:

Elba María Hernández Rodríguez

Director/a:

Albert Tarancón Rubio y Marc Torrell Faro

Tutor/a:

Joan Ramón Morante Leonart

Instituto de Investigación en Energía de Cataluña (IREC)



UNIVERSITAT DE  
BARCELONA



El Dr. Albert Tarancón Rubio y el Dr. Marc Torrell Faro, investigadores del Instituto de Investigación en Energía de Cataluña (IREC), CERTIFICAN:

Que la memoria titulada **Solid Oxide Electrolysis Cells based on mesoporous materials** presentada por Elba María Hernández Rodríguez para optar al grado de Doctor en el Programa de Nanociencias de la Universitat de Barcelona ha sido realizada bajo su dirección en el Instituto de Investigación en Energía de Cataluña (IREC).

Barcelona, a 26 de Julio de 2018

Dr. Albert Tarancón Rubio

Dr. Marc Torrell Faro







# Abstract

Solid Oxide Electrolysis Cells (SOECs) have been proposed in the last decades as a promising technology of energy storage. This technology transforms the excess of power generated by renewable energies into chemical energy through the production of synthetic fuels by catalytic reactions. Additionally, the development of technologies able to convert atmospheric CO<sub>2</sub> into valuable fuels has gained attention in a society increasingly concerned about the environmental issues related to the use of fossil fuels.

This thesis is focused on the implementation of mesoporous materials for the fabrication of SOEC electrodes. Mesoporous materials are characterized for presenting high surface area and stability at high temperatures. According to this, the objective is to enhance the performance and the long term stability of solid oxide electrolysis cells working on electrolysis and co-electrolysis modes.

The present work is organized in eight chapters. The first chapter introduces the current energy scenario, the basics of solid oxide electrolysis cells, and the state-of-the-art materials. The second chapter explains the experimental methods, procedures and techniques for synthesizing, fabricating and characterizing mesoporous materials and solid oxide electrolysis cells. The results achieved with this work are presented in the following five chapters. The third chapter is focused on the characterization of mesoporous materials. The following four chapters are devoted to the characterization of solid oxide electrolysis cells based on mesoporous materials fabricated on different configurations. Finally, the eighth chapter presents the conclusions achieved with this work.



# Acknowledgments

Ahora sí, el final de esta etapa se acerca.

En primer lugar, quiero agradecer a mis directores de tesis la oportunidad que me han dado, por haberme apoyado siempre a seguir adelante, y por la dirección de este trabajo. Albert, gracias por ser el primero en confiar en mí para este reto y por poner a mi alcance todas las herramientas posibles para que esta tesis sea hoy una realidad. Marc, gracias por tus infinitas inyecciones de energía, por estar siempre disponible para ayudarme, por estar pendiente de todos los detalles, y por todo lo que me has enseñado.

My gratitude also to Anke Hagen for allowing me to spend my mobility period in DTU facilities.

Quiero también recordar y agradecer a Juan Carlos por apostar por mí desde el principio, y por introducirme en el mundo de la investigación de las pilas de combustibles y de la impresión 3D.

Hace casi cuatro años que empecé esta aventura. Mucha gente ha pasado por el grupo de “Naniónica y Pilas de Combustible” desde que llegué en diciembre de 2014, y a los cuales agradezco muchas cosas. Al inicio de esta etapa, guardo muy buenos recuerdos compartidos con Pepín, Vero, y Marcus, gracias chicos por la calurosa bienvenida y por todo lo que me enseñaron nada más llegar. Guardo también recuerdos de muchas risas y buenos ratos con Miguel y Aneta, siempre disponibles para echarme una mano con lo que hiciera falta y dándome muy buenos consejos. Gerard, contigo sí que me he reído, gracias por tantas locuras compartidas, incluidos los choques de codos y las aventuras poco recomendables en ciudades francesas. Agradezco también a los veteranos Alex y Aitor por sus consejos y ayudas. A los chicos de las micro-pilas, Francesco, Iñigo y Nerea; a Mercè, Lucile, Cecilia, Federico, Simone, Isabel y Arianna por sus estar siempre ahí para darme ánimos, en especial en esta última época.

A Andrés y a Javi, que me acogieron como una más en su grupo nada más llegar. A Doris, por buscar siempre un hueco para ayudarme. A Marco, por explicarme y ayudarme con las medidas del BET.

Mis más sinceros agradecimientos a todos ustedes por compartir tantos buenos ratos, por el compañerismo y buen rollo que me ha rodeado siempre durante estos años, haciendo de ésta una etapa tan bonita que, sin duda, siempre guardaré en mi memoria con una sonrisa.

Agradezco el apoyo que he recibido siempre por mi gente de Tenerife. A mis amigos, con los que los reencuentros siempre valen más que cualquier despedida, y que han intentado entender (y creo que lo he conseguido) qué estaba haciendo en Barcelona. A *los nueve de cada viernes*, y a nuestros planes de años, que están ahí sin importar el tiempo que pase. A las de *una vez al mes* y nuestros *meetings*, con las que he compartido ya muchos años, y siempre están para apoyarme. A mis químicos, en especial a Pilar y a Provi, que siempre se organizan para buscar un hueco, y con las que sé que puedo contar para todo.

A mi familia, en especial a mis abuelos, por estar siempre esperándome con una sonrisa y por todos sus buenos deseos. A mi hermano y a Sinaí, por animarme a seguir y ayudarme en todo lo que pueden. Por supuesto, a mis padres, a los que quiero tanto, por su incondicional apoyo, y por estar siempre disponibles para ayudarme a conseguir lo que me proponga. A Josa, por su infinita paciencia, por todo lo que has hecho por mí, y por lo que esta tesis ha supuesto para nosotros.

Barcelona, a 24 de julio de 2018

# Index

<b>1. Introduction.....</b>	<b>1</b>
<b>1.1. Current energy scenario.....</b>	<b>5</b>
<b>1.2 Chemical Energy Storage: The use of Electrolysers.....</b>	<b>9</b>
<b>1.2.1 History of electrolysers.....</b>	<b>9</b>
<b>1.2.2. Principles and types of electrolysers.....</b>	<b>11</b>
<b>1.3. Solid Oxide Cells (SOCs) .....</b>	<b>14</b>
<b>1.3.1. SOEC basic operation principles.....</b>	<b>15</b>
<b>1.3.2. SOECs cells configuration and specific features.....</b>	<b>16</b>
<b>1.3.3. Thermodynamics of SOECs.....</b>	<b>18</b>
<b>1.4 Materials for SOC.....</b>	<b>23</b>
<b>1.4.1 Standard SOC materials.....</b>	<b>23</b>
<b>A. Electrolyte materials for SOC.....</b>	<b>25</b>
<b>B. Electrode materials for SOC.....</b>	<b>27</b>
<b>1.4.2 Mesoporous materials as SOEC electrodes.....</b>	<b>35</b>
<b>1.5 Scope of the thesis.....</b>	<b>37</b>
<b>1.6 References.....</b>	<b>40</b>
<b>2. Experimental methods.....</b>	<b>47</b>
<b>2.1. Chapter overview.....</b>	<b>51</b>
<b>2.2. Synthesis of mesoporous materials.....</b>	<b>52</b>
<b>2.2.1. Hard-template method.....</b>	<b>52</b>
<b>2.2.2. Synthesis of mesoporous KIT-6 template.....</b>	<b>53</b>
<b>2.2.3. Synthesis of mesoporous metal oxide replicas.....</b>	<b>56</b>

<b>2.3. Fabrication of mesoporous electrodes.....</b>	<b>58</b>
2.3.1. Impregnation for the fabrication of NiO-SDC fuel electrodes.....	58
2.3.2. Infiltration process for the fabrication of oxygen electrodes.....	59
<b>2.4. Cells fabrication techniques.....</b>	<b>61</b>
2.4.1. Tape casting.....	61
2.4.2. Pulsed Laser Deposition (PLD) .....	62
2.4.3. Air brushing technique.....	64
2.4.4. Infiltration technique.....	65
<b>2.5. Fabrication of Solid Oxide Electrolysis Cells (SOECs) .....</b>	<b>67</b>
2.5.1. Symmetrical cells of oxygen electrodes.....	67
2.5.2. Electrolyte supported SOECs.....	68
2.5.3. Fuel electrode supported SOECs.....	70
<b>2.6. Structural Characterization Techniques.....</b>	<b>71</b>
2.6.1. X-Ray Diffraction (XRD) .....	71
2.6.2. In-situ powder X-Ray Diffraction vs. Temperature.....	72
2.6.3. Low Angle X-ray Diffraction (LA-XRD) .....	73
2.6.4. Nitrogen physisorption measurements (BET) .....	73
2.6.5. Scanning Electron Microscopy (SEM) and Energy Dispersion X-ray (EDX) .....	76
2.6.6. Transmission Electron Microscopy (TEM) .....	78
<b>2.7. Electrochemical Characterization Techniques.....</b>	<b>79</b>
2.7.1. Electrochemical test stations for button and large area cells.....	79
2.7.2. Electrochemical Impedance Spectroscopy (EIS) .....	83
2.7.3. Galvanostatic and Potentiostatic modes for I-V curves.....	88
<b>2.8. References.....</b>	<b>90</b>

<b>3. Synthesis, characterization and optimization of mesoporous electrode materials</b>	<b>93</b>
.....	
<b>3.1. Chapter overview.....</b>	<b>97</b>
<b>3.2. Structural characterization of mesoporous materials.....</b>	<b>98</b>
<b>3.2.1. Structural characterization of mesoporous KIT-6.....</b>	<b>98</b>
<b>3.2.2. Structural characterization of mesoporous <math>\text{Sm}_{0.2}\text{Ce}_{0.8}\text{O}_{1.9}</math> (SDC).....</b>	<b>101</b>
<b>3.2.3. Structural characterization of mesoporous <math>\text{Ce}_{0.8}\text{Gd}_{0.2}\text{O}_{1.9}</math> (CGO) .....</b>	<b>105</b>
<b>3.2.4. Structural characterization of mesoporous NiO.....</b>	<b>108</b>
<b>3.3. Structural characterization of fabricated mesoporous electrodes.....</b>	<b>112</b>
<b>3.3.1. Structural characterization of <math>\text{Sm}_{0.2}\text{Ce}_{0.8}\text{O}_{1.9}</math> (SDC)-<math>\text{Sm}_{0.5}\text{Sr}_{0.5}\text{CoO}_{3-\delta}</math> (SSC) oxygen electrodes.....</b>	<b>113</b>
<b>3.3.2. Structural characterization of <math>\text{Ce}_{0.8}\text{Gd}_{0.2}\text{O}_{1.9}</math> (CGO)-<math>\text{La}_{0.6}\text{Sr}_{0.4}\text{Co}_{0.2}\text{Fe}_{0.8}\text{O}_3</math> (LSCF) oxygen electrodes.....</b>	<b>114</b>
<b>3.3.3. Structural characterization of NiO-<math>\text{Sm}_{0.2}\text{Ce}_{0.8}\text{O}_{1.9}</math> (SDC) fuel electrodes .....</b>	<b>116</b>
<b>3.4. Optimization of oxygen electrodes based on mesoporous materials on symmetric cells.....</b>	<b>117</b>
<b>3.5. Conclusion.....</b>	<b>123</b>
<b>3.6. References.....</b>	<b>125</b>
<b>4. Electrolyte- and fuel electrode-supported SOEC cells.....</b>	<b>127</b>
<b>4.1. Chapter overview.....</b>	<b>131</b>
<b>4.2. Characterization and performance of electrolyte-supported SDC-SSC SOECs.....</b>	<b>132</b>
<b>4.3. Characterization and performance of fuel electrode-supported SDC-SSC SOECs.....</b>	<b>137</b>
<b>4.4. Conclusions.....</b>	<b>146</b>

4.5. References.....	149
<b>5. Optimization of the oxygen electrode for enhancing the performance of SOEC cells.....</b>	<b>151</b>
5.1. Chapter overview.....	155
5.2. Characterization of the state-of-the-art SOEC cells.....	156
5.3. Optimization strategy of SOEC oxygen electrodes.....	157
5.4. Comparison of SOEC cells.....	160
5.4.1. Performance comparison of SOEC cells.....	160
5.4.2. Microstructural analysis of SOEC cells.....	169
5.5. Conclusions.....	174
5.6. References.....	175
<b>6. Performance and long-term stability of optimized SOEC cells in co-electrolysis mode.....</b>	<b>177</b>
6.1. Chapter overview.....	181
6.2. Electrochemical characterization and performance of the CGO-LSCF SOEC cells in co-electrolysis mode.....	183
6.3. Microstructural characterization of the CGO-LSCF SOEC cells.....	187
6.4. Results of the long-term operation tests of the CGO-LSCF SOEC cell in co-electrolysis mode.....	190
6.4.1. Long-term electrochemical characterization and performance.....	190
6.4.2. Post-test cell microstructural characterization.....	194
6.5. Conclusions.....	199
6.6. References.....	201

<b>7. Scale up of developed fuel electrode supported SOEC: Large Area Cells.....</b>	<b>203</b>
<b>7.1. Chapter overview.....</b>	<b>207</b>
<b>7.2. Microstructural characterization of the oxygen electrode functional layers applied in large area cells.....</b>	<b>208</b>
<b>7.3. Electrochemical characterization of large area SOECs.....</b>	<b>212</b>
<b>7.3.1. Electrochemical characterization of large cells under electrolysis mode .....</b>	<b>212</b>
<b>7.3.2. Electrochemical characterization under co-electrolysis mode.....</b>	<b>219</b>
<b>7.4. Results of the long-term operation test on large area SOECs.....</b>	<b>224</b>
<b>7.4.1. Electrochemical characterization and performance.....</b>	<b>224</b>
<b>7.4.2. Post-test microstructural characterization.....</b>	<b>227</b>
<b>7.5. Comparison of the performance of fuel electrode-supported cells (button- and large area cells) .....</b>	<b>231</b>
<b>7.6. Conclusions.....</b>	<b>232</b>
<b>7.7. References.....</b>	<b>235</b>
<b>8. Conclusions.....</b>	<b>237</b>
<b>APPENDIX.....</b>	<b>243</b>
<b>A. Resumen de la Tesis.....</b>	<b>245</b>
<b>SCIENTIFIC CONTRIBUTIONS.....</b>	<b>253</b>

# ***Chapter 1***

*Introduction*



<b>1. Introduction .....</b>	<b>5</b>
<b>1.1. Current energy scenario.....</b>	<b>5</b>
<b>1.2 Chemical Energy Storage: The use of Electrolysers.....</b>	<b>9</b>
<b>1.2.1 History of electrolysers .....</b>	<b>9</b>
<b>1.2.2. Principles and types of electrolysers.....</b>	<b>11</b>
<b>1.3. Solid Oxide Cells (SOCs).....</b>	<b>14</b>
<b>1.3.1. SOEC basic operation principles.....</b>	<b>15</b>
<b>1.3.2. SOECs cells configuration and specific features.....</b>	<b>16</b>
<b>1.3.3. Thermodynamics of SOECs .....</b>	<b>18</b>
<b>1.4 Materials for SOC .....</b>	<b>23</b>
<b>1.4.1 Standard SOC materials.....</b>	<b>23</b>
<b>A. Electrolyte materials for SOC .....</b>	<b>25</b>
<b>B. Electrode materials for SOC .....</b>	<b>27</b>
<b>1.4.2 Mesoporous materials as SOEC electrodes .....</b>	<b>35</b>
<b>1.5 Scope of the thesis.....</b>	<b>37</b>
<b>1.6 References.....</b>	<b>40</b>



## **1. Introduction**

### **1.1. Current energy scenario**

During the last decades, global warming and climate change effects have already become evident gaining importance in the social debate [1]. Among these environmental issues, air pollution has become a public health problem in industrialized and developed countries as a consequence of the emission of greenhouse gasses mainly from transportation and industrial sectors [2,3].

In the last decades, the global energetic model has been based on the centralized production of electricity and its distribution. Fossil fuels, such as petroleum and natural gas, have been the main energy sources employed to cover the world's demand. This has been possible up to now due to the existence of big enough fuel reserves [2]. However, the location of those reserves on politically unstable regions and its progressive decrease, have resulted on the continuous increase of the crude oil quotation [4]. The main disadvantage of these energy sources lies on the direct relation of its consumption (by combustion in engines) with the massive emission of carbon dioxide (CO<sub>2</sub>) [4].

According to this, finding alternative clean and sustainable energy sources able to cover the world's population demand have become a need. The establishment of an alternative energy system based on carbon-neutral and Renewable Energy Sources (RES) is one of the possible strategies to reduce the carbon dioxide emissions from current fossil fuels consumption [5]. Among other institutions, European Union (EU) has promoted environmental and energy policies as well as a route map to minimize the carbon dioxide emissions [6].

Technologies based on employing RES like solar, wind and hydro have been recently developed for the production of green electricity. These energy sources are characterized for being site-specific and intermittent due to its nature. As a consequence, the production of power from RES does not typically match the energy demand of the consumers [7]. In this direction, the development of Energy Storage Systems (ESS) may play an important role enabling the storage of the electricity generated by variable renewable energy sources [8]. Besides, ESS can mitigate power variations and enhances the electrical system flexibility, keeping the balance between

production and demand [9]. Therefore, the combination of RES and ESS may result on a feasible alternative scenario competitive against conventional fossil fuel sources.

### Electricity Storage Systems

Different technologies for the storage of renewable electricity are under current development [9]. According to the type of energy accumulated, they can be classified as chemical, electrochemical, mechanical, electrical or thermal [8,10].

Among other options, the electrical energy can be stored through chemical compounds. The chemical energy carrier must be readily available, technically feasible, economically competitive, and environmentally friendly [4]. Alternatively to chemical storage, electrochemical energy storage consists on the accumulation of energy from chemicals that react in electrochemical devices. Among the electrochemical ones, the focus has been traditionally on the development of batteries [7,11,12]. In mechanical storage, electrical energy can be stored in flywheels, based on the accumulation of kinetic energy, by pumping water in Pumped-Storage Hydroelectricity (PSH) or as compressed air in Compressed Air Energy Storage (CAES) [8,10]. Direct electrical storage can be achieved by accumulating electrostatic charges in Super Capacitors Energy Storage (SES), or as a magnetic field in Superconducting Magnetic Energy Storage (SMES) systems [8,10]. Lastly, Thermal Energy Storage (TES) collects heat for its later use in systems like hot water (H<sub>2</sub>O) tanks, phase-change materials or storage heaters [8,10].

The energy capacity and power supply (discharge time) are major features for determining the technology that better fits each application (**Figure 1.1**) [10]. PSH, CAES or flow batteries are preferred for managing energy while high power technologies like batteries, SES, SMES or flywheels are usually the choice for ensuring power quality.

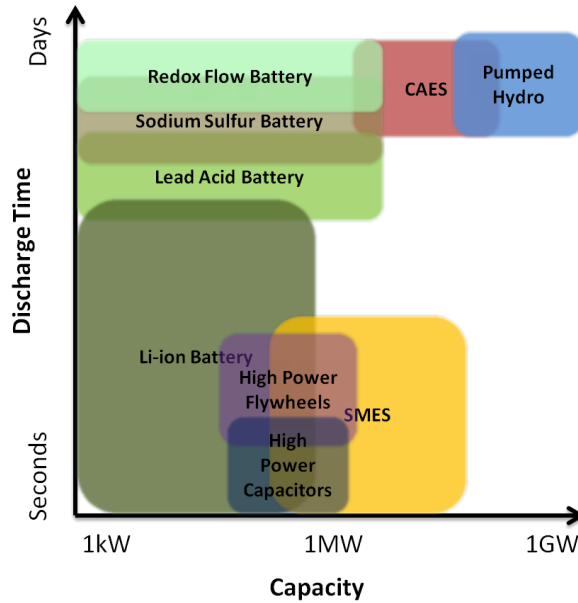


**Figure 1.1:** Discharge time and energy capacity for different storage technologies [10].

### Hydrogen (H<sub>2</sub>) as fuel

According to chemical energy carrier requirements, hydrogen, which is the most abundant element in the universe, has been presented as a promising fuel [1]. The interest of applying hydrogen in the transportation sector has increased with the possibility of using it as a fuel in combustion engines [2] or in fuel cells [5], generating water as the main exhaust product [4]. It has been presented as an alternative for the replacement of fossil fuels due to its high energy density, which can be up to 2.75 times greater than hydrocarbons fuels [13]. However, hydrogen still requires the development of advanced storage technologies for allowing high enough energy densities.

Nowadays, most of the hydrogen is produced from non-sustainable nor clean processes [4]. It is usually obtained by steam reforming of natural gas. In this process, natural gas is combined with high temperature steam generating hydrogen, carbon monoxide (CO) and carbon dioxide [14]. CO and CO<sub>2</sub> are removed from the mixture in order to obtain pure hydrogen.

Alternatively, hydrogen can be produced from renewable energies [5]. Specifically, it can be produced by thermochemical water splitting, photocatalytic water splitting and water electrolysis [7]. Due to the current low efficiency of both thermochemical and photocatalytic technologies, water electrolysis is probably the preferred one when

coupled to renewable electricity sources, anticipating the feasibility of a more sustainable energy system [2,15,16]. In particular, wind energy systems combined with water electrolysis is considered one of the most promising storage solutions for suppressing generation fluctuations: (i) when the energy demand is lower than the electricity production from wind mills/farms, the excess electricity is sent to the electrolyser to store it by producing hydrogen; (ii) when the energy demand exceeds the available energy capacity, the stored hydrogen can be used to generate electricity via highly efficient fuel cell technology [8].

Although the direct injection of electrolysed hydrogen into the gas grid is a valuable option, efforts and investments would be needed for the adaptation of the current distribution infrastructure to the highly volatile hydrogen gas [17], or the deployment of a specific one, which would take decades due to the intrinsic difficulties in changing from one energy infrastructure to another [11]. On the other hand, the production of methane will allow the possibility of using the existing infrastructure of natural gas for its store and transportation [11].

#### Carbon dioxide as a feedstock reactant for generating new fuels

In spite of the environmental awareness and the different international agreements signed by multiple governments, the current use of fossil fuels as the main energy source results on continuously increasing carbon dioxide concentration in the atmosphere. Since CO<sub>2</sub> is considered the main cause of global warming, developing processes able to capture, transform and recycling CO<sub>2</sub> constitute one of the main challenges for achieving environmental and energy sustainability.

After capture, the CO<sub>2</sub> can be combined with hydrogen to generate synthetic methane by means of catalytic processes such as the Sabatier reaction. If the used hydrogen comes from water electrolysis, the process is called Power-to-Gas.

Recycling CO<sub>2</sub> and its conversion on methane, through Power-to-Gas, would allow the storage of renewable energies into chemical species and its later consumption, closing the carbon cycle. The resulting synthetic methane can be injected into the existing gas grid for its storage and distribution without any potential limitation.

Alternatively, it is also possible the direct dissociation of  $\text{CO}_2$  and  $\text{H}_2\text{O}$  by co-electrolysis processes resulting in the production of  $\text{H}_2$  and  $\text{CO}$  (syngas gas) [18]. Syngas is considered an intermediate building block employed for the synthesis of different hydrocarbons via de Fischer-Tropsch or Sabatier process [17,19]. Among other, methane, methanol, and dimethyl ether are the simplest and cheapest to produce [11].

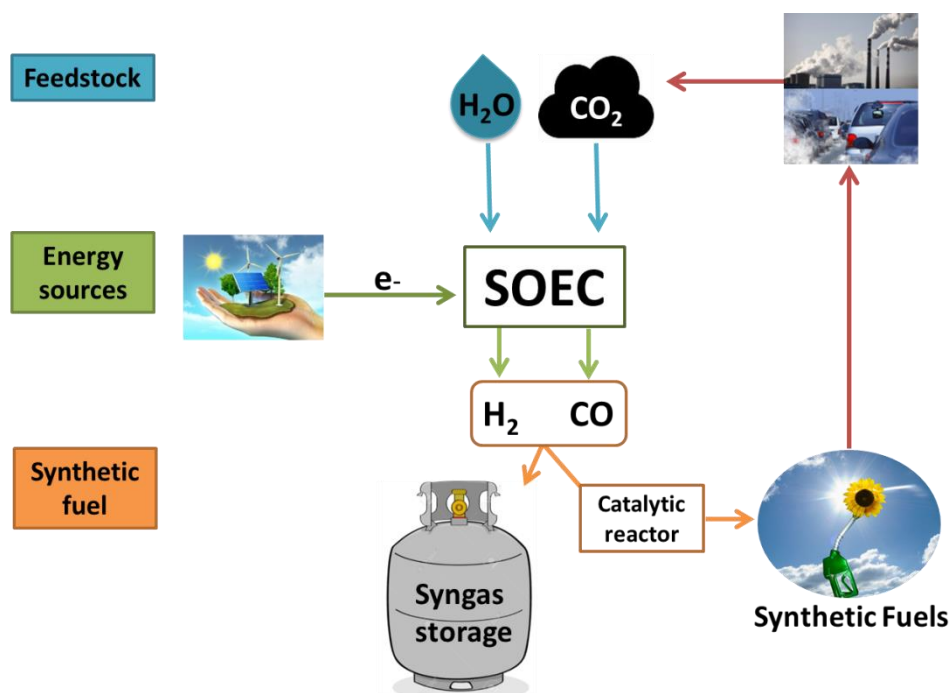


**Figure 1.2:** CO<sub>2</sub> neutral energy cycle for the production of chemical fuels from renewable energies based on the SOEC technology.

This electrolysis technology considers as a limiting factor the efficiency of the transformation of the electricity into gas. However, advanced Solid Oxide Electrolysis Cells (SOECs) can reach efficiencies higher than 85% [20], which justifies the interest for its development and optimization. SOECs are presented in this thesis as an efficient and flexible alternative for achieving efficient chemical storage of electrical energy from renewable sources.

## 1.2 Chemical Energy Storage: The use of Electrolysers

### 1.2.1 History of electrolysers

As recently reviewed by Laguna [15], the history of the electrochemical process of water electrolysis for converting water and Direct Current (DC) electricity into gaseous hydrogen and oxygen was firstly demonstrated by Nicholson and Carlisle in 1800. In

the 1820s, Faraday clarified the principles and in 1934 the word “electrolysis” was introduced [15]. It started to be commercially used for the production of hydrogen in 1902 by the Oerlikon Engineering Company. Along the same period, Nernst developed the high temperature electrolyte  $\text{ZrO}_2$  with 15%  $\text{Y}_2\text{O}_3$ , establishing the basis of solid oxide electrolysis and Solid Oxide Fuel Cells (SOFC) [15]. In 1951, the first commercially available high pressure electrolyser (30 bar) was presented by Lurgi and, in the 1980s Donitz and Erdle reported the first SOEC results using electrolyte-supported tubular SOEC [21].

Regarding the history of electrolysis of  $\text{CO}_2$  and  $\text{CO}_2/\text{H}_2\text{O}$  mixtures, this technology was initially investigated in the 1960s as a way of producing  $\text{O}_2$  for life support and propulsion in submarines and spacecrafts [20]. Westinghouse Research Laboratories in the USA made pioneer contributions to high temperature co-electrolysis for aerospace applications [22]. Chandler *et al.* succeeded in building and operating a number of small scale systems with oxygen production rates of  $150 \text{ cc}\cdot\text{min}^{-1}$  [23]. The concept of using solid electrolyte electrolysis batteries for the generation of  $\text{O}_2$  from decomposition of  $\text{CO}_2$  and/or  $\text{H}_2\text{O}$  instead of carrying a heavily oxygen storage was firstly proposed by Elikan *et al.* [24] at Westinghouse Research Laboratories under the support of the National Aeronautics and Space Administration (NASA). Ash *et al.* firstly proposed the use of solid oxide electrolysis of  $\text{CO}_2$  as an In Situ Resource Utilization (ISRU) technology to generate  $\text{O}_2$  from the predominately  $\text{CO}_2$  atmosphere of Mars [25]. Richter performed experiments using yttria-stabilized zirconia (YSZ) as the solid electrolyte [26]. In the 1990s, Sridhar *et al.* proposed using produced CO and  $\text{O}_2$  by electrolysis as a fuel under fuel cell mode for the generation of electricity [27,28].

The concept of production of synthetic fuels such as methane and methanol from atmospheric  $\text{CO}_2$  combined with Low Temperature Electrolysis (LTE) was proposed in the 1960s and 1970s [11]. The economy of methanol production was presented and patented by Shell in the 1970s [29,30]. Extracting  $\text{CO}_2$  from the exhaust of industrial plants was also presented. The interest of producing synthetic fuels from the combination of atmospheric  $\text{CO}_2$  and hydrogen via low or High Temperature Electrolysis (HTE) started at the 1990s.

The development of SOEC was slowed down around 1990 due to low fossil fuel prices [31]. Research activity in HTE as a green energy technology has increased significantly from the beginning of the 21<sup>st</sup> century up today focusing on the adaptation of state-of-the-art (SoA) SOFC technology, the improvement of durability and performance of stacks, and the reduction of the cost of the syngas production. Research groups from Europe and China, reference American national labs such as NASA and Idaho National Laboratory (INL), reputed universities such as University of Northwestern, California or Florida, and companies like Ceramtec or Sunfire have focused some of their activities on high temperature electrolysis and co-electrolysis with the aim of enabling scalable energy storage and production of sustainable synthetic fuels [22].

### **1.2.2. Principles and types of electrolyzers**

Electrolyzers convert electrical energy into chemical energy by reducing certain species. More specifically, an electrolysis cell can dissociate H<sub>2</sub>O, CO<sub>2</sub> or the mixture of H<sub>2</sub>O and CO<sub>2</sub> by using electricity. Electrolysis cells are devices able to force these non-spontaneous chemical reactions by the injection of a current. Basically, an electrolysis cell is composed by the oxygen electrode, the fuel electrode and the ionic-conductor electrolyte. The electrons circulate through an external circuit and are employed for the reduction of species at the fuel electrode and the oxidation at the oxygen electrode while the generated ions pass through the electrolyte. This technology is attractive for its simplicity since performs the dissociation in a single step and the products are eventually released separately in the two compartments of the cell.

The electrolysis of water taking place in a typical cell consists on the reduction of water to hydrogen at the fuel electrode, and the production of O<sub>2</sub> by oxidation at the oxygen electrode. A scheme of H<sub>2</sub>O electrolysis is presented in **Figure 1.3**.

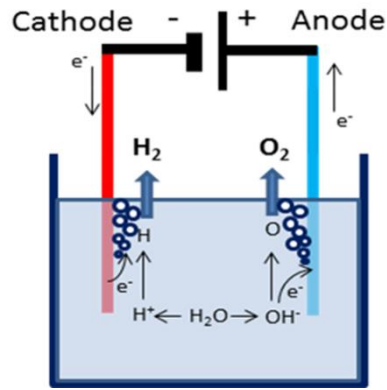


**Figure 1.3:** Scheme of the electrolysis of water by injecting electrical current.

There are three types of electrolyzers that can be classified depending on the nature of their electrolyte, which determines their operation temperature: Alkaline Electrolysis Cells (AECs) (**Figure 1.4a**) and Proton Exchange Membrane Electrolysis Cells (PEMECs) (**Figure 1.5a**) working at low temperatures ( $T < 200\text{ }^{\circ}\text{C}$ ), and SOECs (**Figure 1.6a**) operating at high temperatures ( $T > 600\text{ }^{\circ}\text{C}$ ). AECs and PEMECs are the most mature technologies for water electrolysis and are already available in the market (**Figure 1.4b and 1.5b**), achieving energy efficiencies up to 70% [32]. However, both of them present lower efficiencies than SOECs (up to 85%) mainly due to their higher electrical energy demand and higher internal resistances [32].

Among the different types of electrolyzers, alkaline electrolyzers are the most common. The alkaline electrolyzers are formed by a liquid electrolyte, in which two metal electrodes are immersed (**Figure 1.4**) [10]. The electrolyte usually is a solution of KOH. This configuration consists on the movement of hydroxide ions from the fuel electrode to the oxygen electrode. A diaphragm is introduced for separating the formed gas species. Since they operate at relatively low current densities, these cells are usually operated at high cell voltages (1.8-2.4 V) to achieve an acceptable hydrogen production rate. However, alkaline cells can only electrolyse steam to form hydrogen, and because of that, the synthesis gas and methane can be only produced a posteriori by catalytic reaction of the hydrogen with  $\text{CO}_2$  [11].

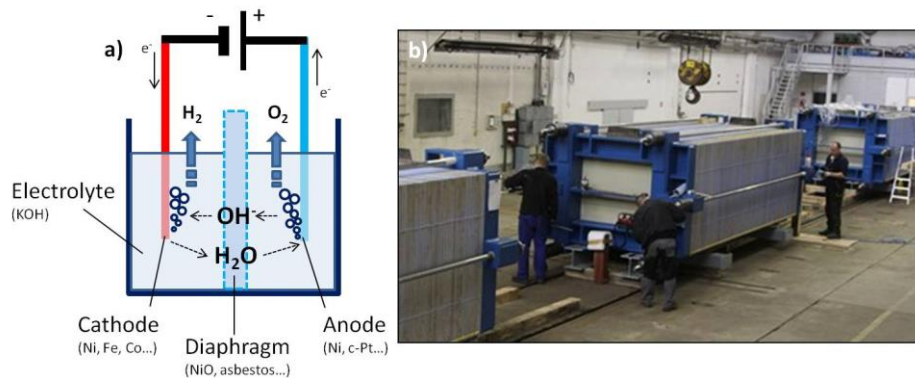


**Figure 1.4:** a) Scheme of an AEC and b) example of a commercial stack [10].

Alternatively, PEMECs (**Figure 1.5**) include a proton conducting solid polymeric membrane as electrolyte, and a fuel and oxygen electrodes [10]. This type of electrolyzers is based on the flow of protons, generated in the oxygen electrode, to the fuel electrode, where hydrogen is produced. The main advantage compared to AECs is that PEMECs usually operate at the same or higher temperature than AECs, what results on higher production rates of hydrogen.

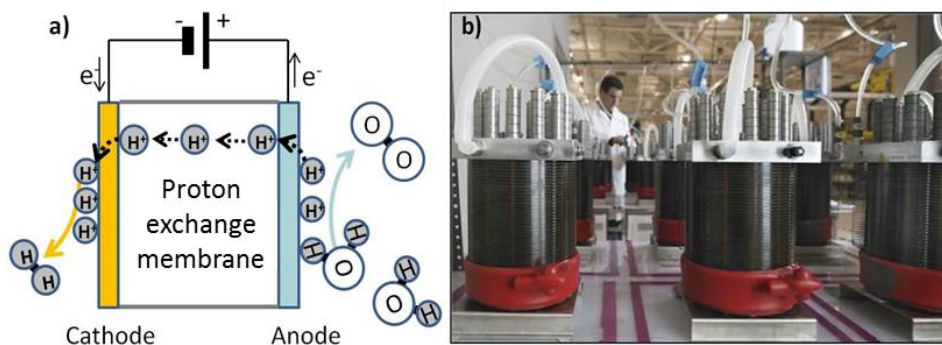


**Figure 1.5:** a) Scheme of a PEMEC and b) image of a commercial device [10]

There are two types of high temperature electrolyzers: the ones with solid oxide electrolytes (**Figure 1.6a**) and those with a molten mixture of carbonate salts as electrolytes. SOECs (750-850 °C) have attracted attention in the last times as a promising energy storage device. Although this technology is the less mature, stacks and systems are currently commercialized by some industrial actors (**Figure 1.6b**). The main advantages of SOEC respects other electrolysis technologies are: (i) that presents superior energy conversion efficiency, less electricity consumption and low internal resistance; and (ii) that it allows H<sub>2</sub>O and CO<sub>2</sub> electrolysis or co-electrolysis without big phenomena or durability issues [33].

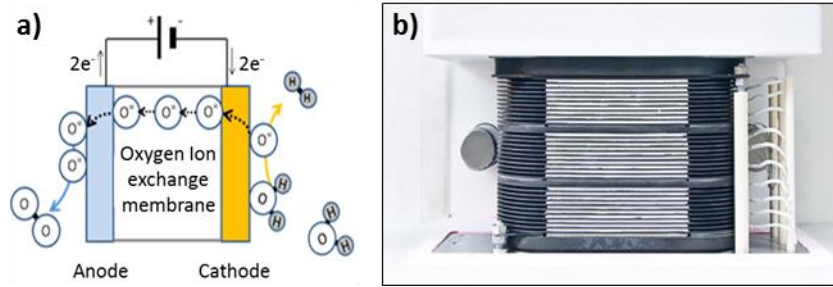


**Figure 1.6:** a) Scheme of a SOEC and b) Commercial electrolyser stack fabricated by Sunfire [10]

The Molten Carbonate Electrolysis Cells (MCECs) operate between 600-700 °C, generating a highly conductive molten salt with carbonate  $\text{CO}_3^{2-}$  ions responsible of the Ionic Conductivity (IC) [11,17]. The  $\text{CO}_3^{2-}$  ions transported through the electrolyte reduce  $\text{H}_2\text{O}$  and generate  $\text{CO}_2$ , but the  $\text{CO}_2$  produced is mixed with released  $\text{O}_2$  at the oxygen electrode. The main disadvantage of this type of electrolyzers is that  $\text{CO}_2$  needs to be separated before extracting the exhaust gas.

In order to compare technologies, typical I-V curves for different types of cells are presented in **Figure 1.7**. It is observed that SOECs are able to achieve higher current densities at lower voltages than AEC and PEMEC. This is, both the efficiency (consumed electrical energy/chemical energy of the electrolysis products) and the production rate (products mass/time) are remarkably higher.

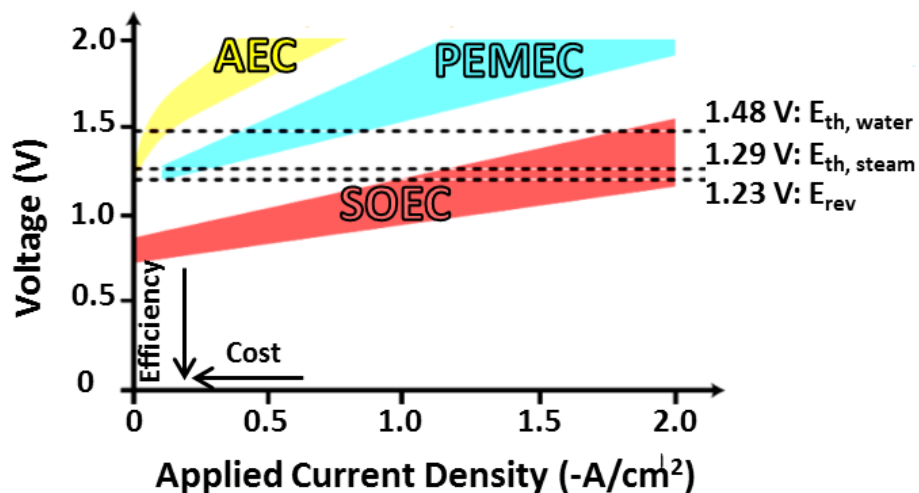


**Figure 1.7:** Typical ranges of I-V polarization curves for AEC, PEMEC and SOEC water electrolysis cells. Adapted from reference[17].

### 1.3. Solid Oxide Cells (SOCs)

In general, Solid Oxide Cells (SOCs) are known as electrochemical devices based on ceramic materials (oxides) which can operate in fuel cell and electrolysis modes. Fuel

cells generate power from a fuel (typically H<sub>2</sub>), while its operation on electrolysis mode allows injection of current to reduce a certain compound/fuel.

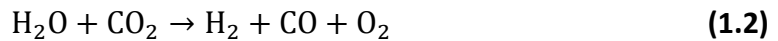
### 1.3.1. SOEC basic operation principles

In a SOEC, electrical energy and H<sub>2</sub>O are supplied to the fuel electrode that acts as cathode. Generated oxygen ions are transported through the electrolyte, which is ionic conductor, to the oxygen electrode acting as anode. H<sub>2</sub> product is obtained from the fuel electrode reduction reactions **(1.3, 1.4)** when it works in electrolysis, while O<sub>2</sub> is the obtained by product from the oxidation reaction **(1.5)** taking place in the oxygen electrode **(Figure 1.8a)**.

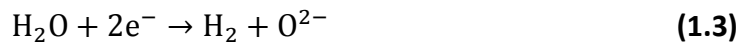
The overall reaction of the water electrolysis is:



When using CO<sub>2</sub>, or H<sub>2</sub>O and CO<sub>2</sub> as fuels, i.e. in co-electrolysis mode, the overall reaction of H<sub>2</sub>O and CO<sub>2</sub> co-electrolysis is:



The reactions in the fuel electrode under electrolysis and co-electrolysis gas compositions are, respectively:



The reaction in the oxygen electrode is (in any case):



The electrochemical reactions taking place on these devices being used as electrolyzers are the inverse reactions to those that take place when are used as fuel cells **(Figure 1.8b)**, what results in opposite cell polarization and the exchange of anode and cathode roles [15]. This reversibility suggests the possibility of using the same unit as SOFC/SOEC.

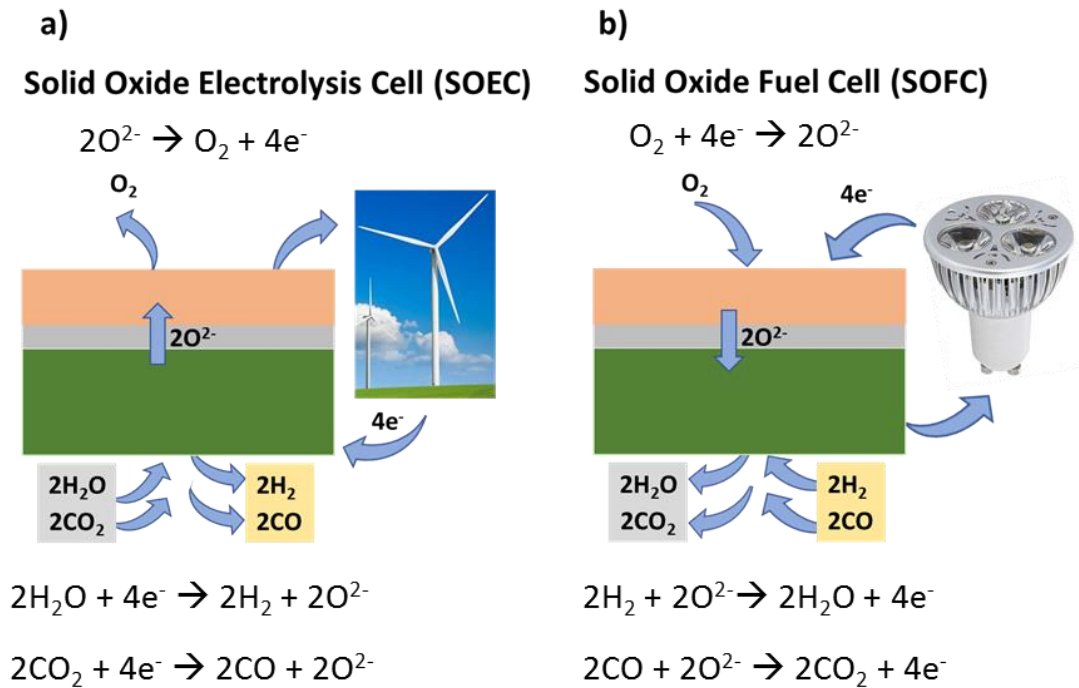


**Figure 1.8:** Scheme of the operation principle of a) SOECs and b) SOFCs [31].

Therefore, the so-called Reversible Solid Oxide Cells (RSOCs) can work for power generation converting fuel chemical energy to electric energy as SOFCs, and for hydrogen production converting excess clean electrical power generated by renewable energies to chemical energy as SOECs. Thus, RSOCs are presented as a promising solution to alternate power generation and electricity energy storage in highly efficient closed loops (~50% round trip efficiency has been proved so far) [34]. It is important to notice here that the material demands change when the operation mode of the cell is changed. Compared to fuel cells, the electrolysis cells are operated at highly demanding conditions like higher water or steam content at the fuel electrode inlet and higher current densities [35].

### 1.3.2. SOECs cells configuration and specific features

A high temperature electrolysis cell (SOEC) is a device consisting of fuel and oxygen porous electrodes and, a dense ceramic electrolyte able to conduct oxygen ions at high operation temperatures (650-850 °C) [17]. The most common architectures developed up to now are tubular and planar. Although promising results on both tubular and microtubular cells designs have been reported, planar SOECs are still the SoA architecture. From the mechanical support point of view, there are three possibilities

depending on the support component: the fuel electrode, the electrolyte and the oxygen electrode-supported cells (labelled as FESC, ESC and OESC, respectively) have been employed so-far (**Figure 1.9**) [11,36]. The most common choice is the fuel electrode configuration in order to reduce the resistance associated to the electrolyte, therefore, lowering the operating temperature.

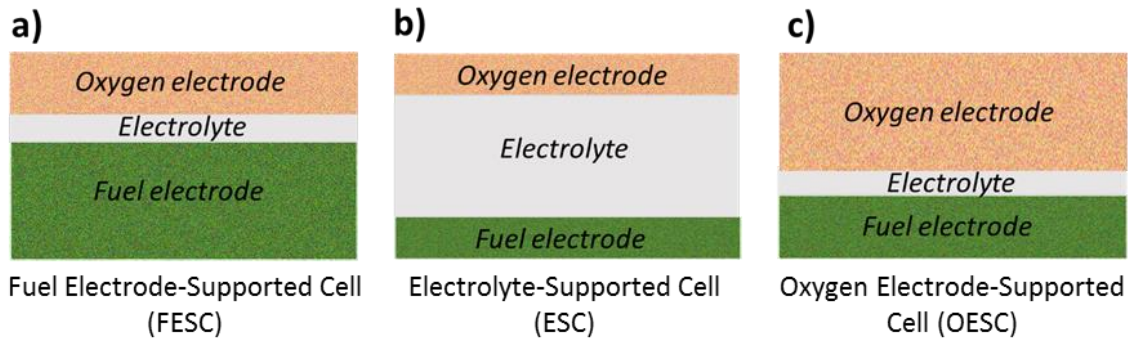


**Figure 1.9:** Scheme of the (a) fuel electrode-supported, (b) electrolyte-supported, and (c) oxygen electrode-support architectures for SOECs.

Performing electrolysis at high temperatures has thermodynamic and kinetics advantages in terms of reduction of the electricity demand by heat energy and increase of reaction rates by internal resistance reduction, respectively. A higher rate of hydrogen and syngas are produced per injected current density at SOEC operation temperatures, compared with other electrolysis cell technologies, since the reactions are thermally activated. That results on higher efficiencies than other technologies since heat energy allows reducing the electricity needed for the dissociation. A reduction of the resistance associated to the electrolyte is also occurring since the ionic conduction follows an Arrhenius type behaviour (see next **section 1.5.1** for a detailed explanation). Furthermore, at high temperature the kinetics of the electrolysis reactions increase, resulting in a decrease in electrical losses in the cell because of the lower polarization losses from the electrode reactions [35]. As a consequence, the need of expensive catalyst materials is also reduced and these devices are presented as a cost-efficient solution [11,15,17,22]

A comparison of the typical performance (I-V curve) of H<sub>2</sub>O, CO<sub>2</sub> and co-electrolysis is presented in **Figure 1.10**. It shows that the performance of CO<sub>2</sub> electrolysis using SOEC at 850 °C is lower than H<sub>2</sub>O/CO<sub>2</sub> co-electrolysis, and that the lowest Area Specific Resistance (ASR) (slope of the curve) is presented by H<sub>2</sub>O electrolysis [22]. The results presented in **Figure 1.10** evidences the possibility of using SOEC for co-electrolysis of

both H<sub>2</sub>O and CO<sub>2</sub>. However, the Reverse Water Gas Shift (RWGS) reaction (CO<sub>2</sub> + H<sub>2</sub> → H<sub>2</sub>O + CO) may also have influence on the overall co-electrolysis performance. In the literature, the contributions of the RWGS reaction to the overall process has been extensively discussed [37]. The amount of CO<sub>2</sub> electrolysed or coming from the WGS reaction is difficult to determine because of the fact that the reaction strongly depends on variables such as temperature, pressure, gas flow rates and compositions [22].

Even though the H<sub>2</sub>O electrolysis presents lower ASR, the conversion of CO<sub>2</sub> is considered extremely useful to produce high added value sustainable fuels or chemicals that cannot be achieved by individual H<sub>2</sub>O electrolysis and simple catalytic reactions. In addition to this, the co-electrolysis presents two important advantages: (i) it is more energy efficient than the two separate electrolysis processes of H<sub>2</sub>O and CO<sub>2</sub> since the energy consumption is slightly lower than for CO<sub>2</sub> electrolysis; (ii) only one reactor is needed to produce syngas [37].

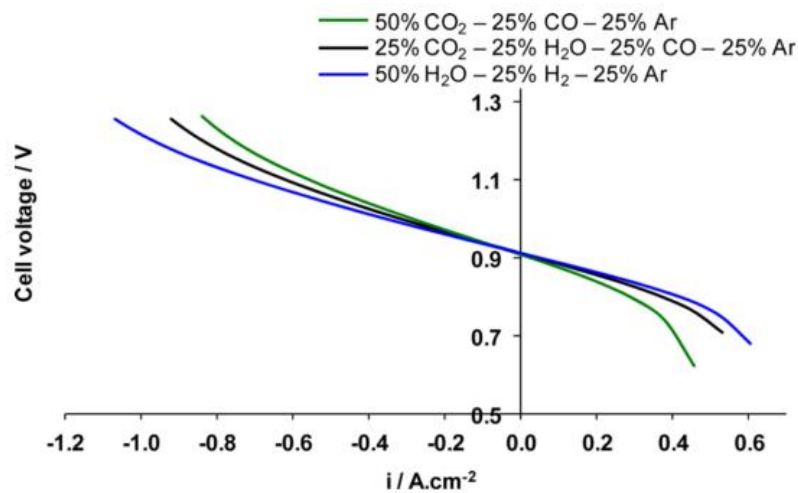


**Figure 1.10:** Polarization characterization of a planar Ni-YSZ/YSZ/LSM-YSZ SOEC under electrolysis (50% H<sub>2</sub>O-25% H<sub>2</sub>-25% Ar), H<sub>2</sub>O/CO<sub>2</sub> co-electrolysis (25% H<sub>2</sub>O-25% CO<sub>2</sub>-25% CO-25% Ar) and CO<sub>2</sub> electrolysis (50% CO<sub>2</sub>-25% CO-25% Ar) [22].

### 1.3.3. Thermodynamics of SOECs

The Gibbs free energy ( $\Delta G$ ) determines the minimum electric energy needed for the electrolysis process. It is function of the enthalpy change ( $\Delta H$ ) as the total energy demand, the temperature ( $T$ ) and the change of entropy ( $\Delta S$ ) as heat demand term ( $T\Delta S$ ). The three thermodynamic parameters ( $\Delta G$ ,  $\Delta H$  and  $\Delta S$ ) are function of the operation temperature. The Gibbs free energy  $\Delta G$  mathematical expression is given by:

$$\Delta G = \Delta H - T\Delta S \quad (1.6)$$

The minimum energy required for the dissociation of H<sub>2</sub>O to H<sub>2</sub> (1.7) and CO<sub>2</sub> to CO (1.8) is given by the enthalpy of the reactions [17]:



High temperature electrolysis reactions of both H<sub>2</sub>O and CO<sub>2</sub> are endothermic, as it shows its enthalpy of formation ( $\Delta H_f$ ). In consequence, heat energy ( $T \Delta S$ ) needs to be supplied in order to avoid the decrease of temperature.

The thermodynamics values of  $\Delta G$ ,  $\Delta H$  and  $T\Delta S$  change in function of the H<sub>2</sub>O and CO<sub>2</sub> electrolysis operation temperatures, as it is presented in **Figure 1.11**. Since both reactions are endothermic, the increase of the operation temperature indicates an increase of the total energy demand ( $\Delta H$ ), which is supplied by the also increasing heat demand ( $T\Delta S$ ). Contrary, a decrease of the electric energy demand ( $\Delta G$ ) is observed when the operation temperature is increased. The pass of electrical current through the cell during operation generates heat by Joule effect. This generated heat is directly proportional to the operation temperature and is provided to the total energy demand for H<sub>2</sub>O and CO<sub>2</sub> dissociations. Besides, this heat demand can be supplied by an external heat source, as the generated by renewable energies and waste heat, increasing the efficiency of the process. As consequence of that, performing electrolysis at high operation temperatures allows substituting the electric demand by heat demand which is more economic and more efficient. Because of that, electrolysis performed by SOEC is a highly efficient and promising technology for generating H<sub>2</sub> and CO [11,15,22].

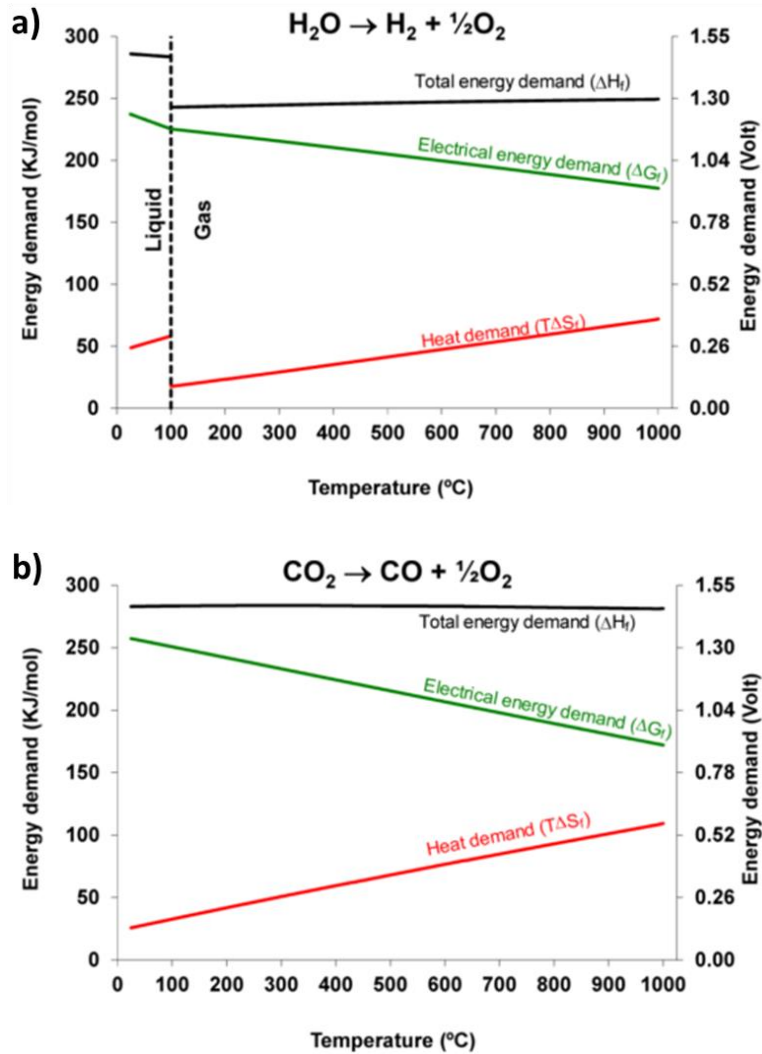


**Figure 1.11:** Variation of the thermodynamic parameters for (a)  $\text{H}_2\text{O}$  and (b)  $\text{CO}_2$  electrolysis at atmospheric pressure and from 0 to 1000°C SOEC operation temperatures [11].

Production of synthetic gas by co-electrolysis of  $\text{H}_2\text{O}$  and  $\text{CO}_2$  in SOECs is a combination of reactions (1.3) and (1.4) to produce both  $\text{H}_2$  and  $\text{CO}$ . The variation of the thermodynamics values of  $\Delta H$ ,  $\Delta G$  and  $T\Delta S$  of  $\text{H}_2\text{O}$  and  $\text{CO}_2$  co-electrolysis with the operation temperature are presented in **Figure 1.12**. It is possible to observe that  $\Delta H$  is maintained almost constant from 200 to 1000 °C, while the decrease of the electrical energy demand is similar to the increase of the heat demand in the studied range of temperatures[22]. Therefore, the conclusions from the individual electrolysis of  $\text{CO}_2$  and water can be extrapolated to the co-electrolysis process.

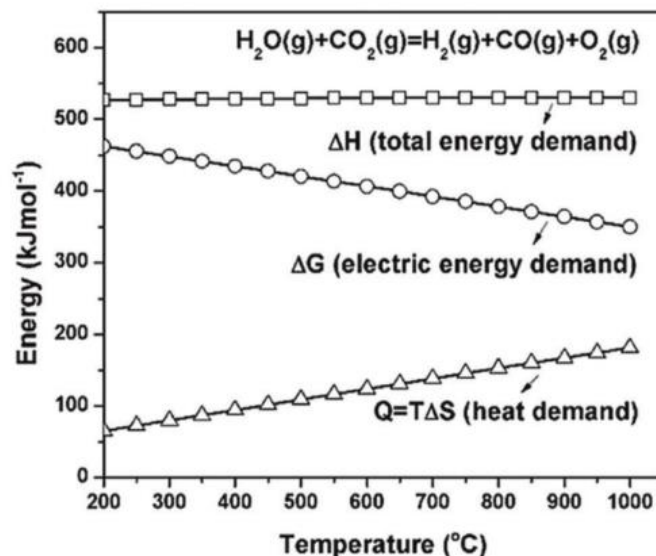


**Figure 1.12:** Changes of  $\Delta H$ ,  $\Delta G$  and  $T\Delta S$  thermodynamics parameters with the operation temperature (200-1000 °C) for  $H_2O$  and  $CO_2$  co-electrolysis reaction [22].

As it has been presented in **Figure 1.10**,  $CO_2$  electrolysis is more complicated than  $H_2O$  and  $CO_2$  co-electrolysis, and because of that, co-electrolysis is the best route for reducing  $CO_2$ . However, the Water Gas Shift (WGS) reaction (1.9) and the RWGS reaction (1.10) compete with the co-electrolysis reaction. WGS reaction implies  $H_2O$  reduction, while  $CO_2$  is reduced in the reverse electrochemical process, the RWGS reaction [22]. The reactions are presented as follows:



The relation between the total energy demand ( $\Delta H$ ) and the electric energy demand ( $\Delta G$ ) with temperature for the WGS reaction is presented in **Figure 1.13**. It is observed that both electrochemical parameters sharply decrease at 100 °C due to the phase change from water to steam. It is also appreciable that the  $\Delta G$  value of the WGS reaction is in equilibrium ( $\Delta G=0$ ) at 816 °C, indicating the maximum temperature favouring the WGS reaction. In contrast, RWGS reaction becomes spontaneous ( $\Delta G>0$ ) at temperatures higher than 816 °C, as it is also shown in **Figure 1.13**. [17,22].

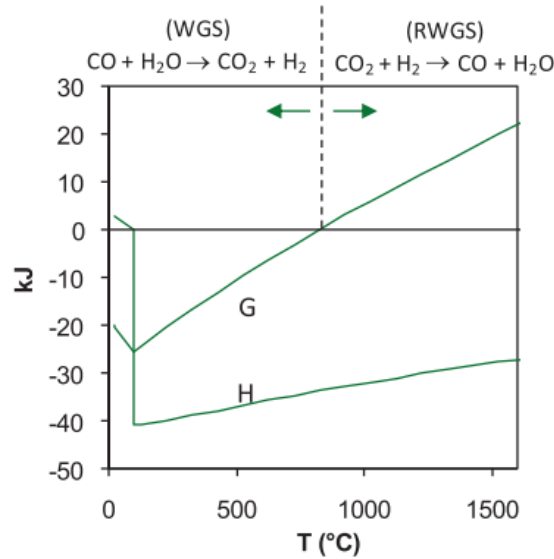


**Figure 1.13:** Relationship between  $\Delta G$  and  $\Delta H$  of the water gas shift reaction [17].

The reversible potential ( $E_{rev}$ ) or Open Circuit Voltage (OCV) is defined as the minimum voltage to be applied over the two electrodes for splitting  $H_2O$  or  $CO_2$ . It is determined by the Gibbs free energy of formation ( $\Delta G_f^\theta$ ) and is function of both pressure and temperature [11]. Its expression at 25 °C and 1 atm is given by **(1.11)**, and its value is 1.23 V for  $H_2O$  (**Figure 1.7**).

$$E_{rev}^\theta = \frac{\Delta G_f^\theta}{nF} \quad (1.11)$$

Taking into account the direct relation between the  $E_{rev}$  and  $\Delta G$ , and the decreasing tendency of the electrical energy demand ( $\Delta G$ ) when the operation temperature is increased for both  $H_2O$  and  $CO_2$  electrolysis (**Figure 1.11**), it is concluded that working at high temperatures reduces the reversible potential. As consequence, it is again demonstrated that operating in the typical SOEC range of temperatures is thermodynamically advantageous.

The total energy demand of an electrolyser perfectly isolated would be supplied by the Joule heat produced from the pass of current through the cell, without receiving any external heat. The termoneutral potential ( $E_{tn}$ ) is defined as the minimum voltage required for the cell operation achieving 100 % of electrical conversion efficiency [15]. Its expression is presented in **(1.12)**, where  $\Delta H_f$  is the total energy demand for the electrolysis reaction, of either  $H_2O$  or  $CO_2$ ,  $n$  is the number of electrons involved in the reaction and  $F$  is the Faraday constant [11,15].

$$E_{tn} = \frac{\Delta H_f}{nF} \quad (1.12)$$

$E_{tn}$  value is function of the temperature and pressure of the operation. For example,  $E_{tn}$  decreases from 1.48 to 1.29 V when the electrolyser operation temperature is changed from 25 to 850 °C (**Figure 1.3**). In the same direction,  $E_{tn}$  decreases from 1.47 to 1.46 V then the CO<sub>2</sub> electrolysis is changed from 25 to 850 °C [11].

Besides, an increase of the voltage needs to be considered for changing the phase of water from liquid into steam. It is denominated vaporization voltage ( $E_{vap}$ ) and is determined by the water enthalpy ( $\Delta H_{vap}$ ). In a thermally insulated electrolyser, the potential needed for the electrolysis of H<sub>2</sub>O or CO<sub>2</sub> is determined by the sum of the values given applying the expressions **(1.12)** and **(1.13)** [15].

$$E_{vap} = \frac{\Delta H_{vap}}{nF} \quad (1.13)$$

According to the typical I-V curves of different types of electrolysers presented in **Figure 1.7**, and the analysis of the SOEC thermodynamics presented in this section, it is clear, that operating SOEC at high temperatures is very advantageous [11,17].

## 1.4 Materials for SOCs

### 1.4.1 Standard SOC materials

SOFC and SOEC technologies are based in the same electrochemical reactions working on reverse mode. Operation, materials and degradation mechanisms have been extensively studied for SOFC during years. The connection between both technologies, as well as the possibility of alternatively using the same device in fuel (SOFC) and electrolysis (SOEC) modes, have allowed implementing the knowledge acquired for SOFC on the development of SOECs. Specifically, the best performing SOFC materials have been employed as the basis for studying SOECs [38]. **Figure 1.14** presents a list of various materials used for electrolytes, anodes, cathodes, diffusion barrier layers, interconnectors and seals in SOFCs. According to the similarities between the two technologies, the state-of-the-art SOEC materials can be found among the listed compounds.

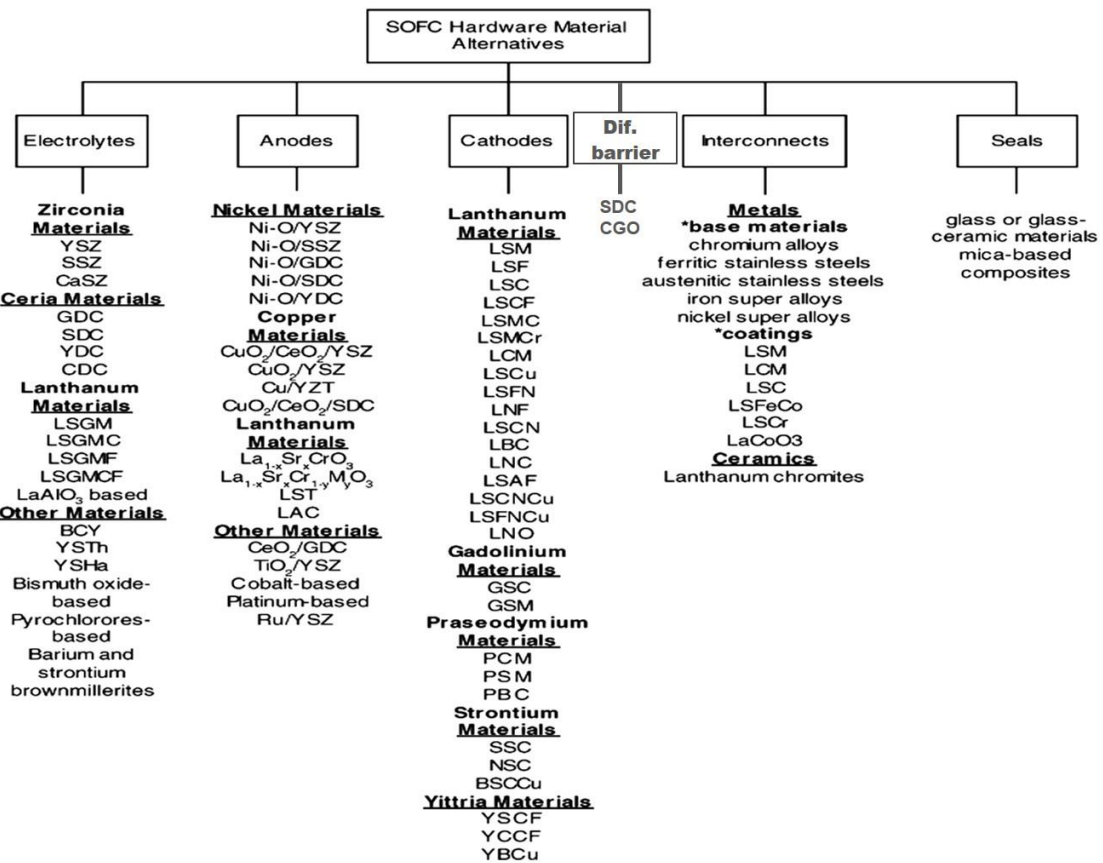


**Figure 1.14:** Materials used for SOFC components (electrolytes, electrodes, diffusion barriers, interconnects and seals) [39].

State-of-the-art SOEC components are yttria-stabilized zirconia ( $ZrO_2-8 \text{ mol}\%Y_2O_3$ , 8YSZ) for the electrolyte and Ni-YSZ cermet for the fuel electrode. The oxygen electrode is typically made of Mixed Ionic Electronic Conductors (MIECs) such as Lanthanum Strontium Cobalt Oxide ( $La_{0.6}Sr_{0.4}Co_{0.2}O_3$ -LSC) and lanthanum strontium cobalt ferrite ( $La_{0.6}Sr_{0.4}Co_{0.2}Fe_{0.8}O_3$ -LSCF). A thin barrier layer of gadolinia-doped cerium Oxide ( $Ce_{0.8}Gd_{0.2}O_{1.9}$ -CGO) is usually added between the LSCF or LSC and the YSZ to avoid material reactivity at high temperature fabrication steps. Besides, LSCF-CGO composite has been proposed to replace the LSCF or LSC single-phase electrodes in order to improve the mechanical compatibility with the electrolyte [38].

SOECs operate at high temperature and, because of that, there are important limitations on the selection of electrodes and electrolytes materials regarding: (i) high conductivities; (ii), compatibility of Thermal Expansion Coefficients (TECs) to prevent material failures, and (iii) dimensional/mechanical/chemical/thermal stabilities [7,11,40].

### A. Electrolyte materials for SOCs

The importance of the electrolyte to the performance of SOCs lies on its contribution to the ohmic internal resistance. A good electrolyte is characterized for presenting poor Electronic Conductivity (EC) to prevent short circuit, excellent O<sup>2-</sup> ionic conductivity and chemical stability under both reducing and oxidizing atmospheres. Besides, the electrolyte and the electrode material in contact need to present good thermal and chemical stability, as well as similar TECs. The electrolyte materials should also have low cost and be environmentally friendly, in concordance with the aim of developing sustainable SOCs technology. The electrolyte should also be as thin as possible to minimize its contribution to the ohmic resistance and present a dense structure to separate the products generated from both electrodes, and ensure gas-tightness.

The ionic conductivity of ceramic electrolytes **(1.14)** is thermally activated, following an Arrhenius dependence:

$$\sigma = \frac{\sigma_0}{T} e^{\frac{-E_a}{kT}} \quad \text{(1.14)}$$

where  $\sigma$  is the ionic conductivity,  $\sigma_0$  is the constant exponential prefactor,  $T$  is the temperature,  $E_a$  is the activation energy and  $K$  is the Boltzmann constant.

According to this, the logarithm of the conductivity is usually represented vs. the inverse temperature as presented in **Figure 1.15** for different SOCs electrolytes [36]. Among other factors, the IC of the electrolyte and its thickness have influence in the overall performance of the cell, determining the optimum supporting configuration of the cell at a certain temperature. In fact, the development of fuel electrode-supported cells allowed reducing the electrolyte thickness, what resulted in a reduction of SOCs operation temperature and improved performances.

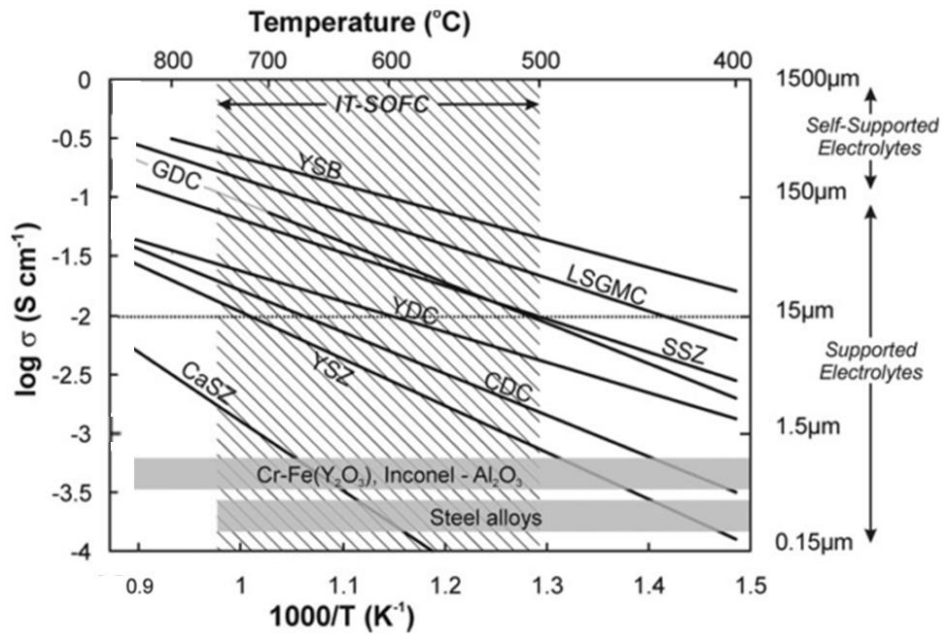


**Figure 1.15:** Arrhenius plot of specific ionic conductivity of SOCs electrolytes and operational range of interconnect materials as a function of the temperature. Conductivity data are from Wincewicz and Cooper [41]. The presented electrolytes are: YSB  $[(\text{Bi}_2\text{O}_3)_{0.75}(\text{Y}_2\text{O}_3)_{0.25}]$ ; LSGMC  $(\text{La}_x\text{Sr}_{1-x}\text{Ga}_y\text{Mg}_{1-y-z}\text{Co}_z\text{O}_3; x \approx 0.8, y \approx 0.8, z \approx 0.085)$ ; CGO  $(\text{Ce}_{0.9}\text{Gd}_{0.1}\text{O}_{1.95})$ ; SSZ  $[(\text{ZrO}_2)_{0.8}(\text{Sc}_2\text{O}_3)_{0.2}]$ ; YDC  $(\text{Ce}_{0.8}\text{Y}_{0.2}\text{O}_{1.96})$ ; CDC  $(\text{Ce}_{0.9}\text{Ca}_{0.1}\text{O}_{1.8})$ ; YSZ  $[(\text{ZrO}_2)_{0.92}(\text{Y}_2\text{O}_3)_{0.08}]$ ; CaSZ  $(\text{Zr}_{0.85}\text{Ca}_{0.15}\text{O}_{1.85})$  [36].

Zirconia ( $\text{ZrO}_2$ ) based materials have been extensively studied as electrolytes for SOCs [15,42]. Doping zirconia with lower oxidation state cations (aliovalent) such as  $\text{Y}^{3+}$  stabilizes the cubic/tetragonal structure and increase its oxygen ion conductivity by introducing oxygen vacancies [36]. The resulting YSZ is the typical electrolyte material used in SOCs and presents good IC and stability at high temperatures (600-1000 °C) and a broad range of  $p\text{O}_2$  without showing EC. The highest oxide ion conductivity is achieved for compositions with 8% of yttria content (8YSZ) [43].

However, the YSZ conductivity drastically decreases at lower temperatures. Other materials with higher ionic conductivities at low temperatures have been proposed to overcome this issue. Among them, doping with  $\text{Sc}^{3+}$  results on scandia-stabilized zirconia ( $\text{Sc}_2\text{O}_3\text{-ZrO}_2$ , ScSZ). This material has been suggested as electrolyte since it presents the highest IC among all the zirconia based. However, ScSZ presents stability problems related to the amount of Sc used for doping: the electrolyte shows large degradation if Sc content is too low, while the ScSZ phase changes from cubic to rhombohedral when Sc content is increased. It has been found as possible solution that substituting  $\text{Sc}_2\text{O}_3$  by  $\text{Yb}_2\text{O}_3$ , what results in ytterbium scandia-stabilized zirconia

$(\text{Yb}_2\text{O}_3)_{0.06}(\text{Sc}_2\text{O}_3)_{0.04}(\text{ZrO}_2)_{0.9}$  (6Yb4ScSZ) electrolyte. This material maintains its phase stable and high conductivity [44]

Another family of materials comes from the studies of doped ceria as a promising electrolyte for Intermediate Temperature (IT) operation. Ceria ( $\text{CeO}_2$ ) has a fluorite structure and oxygen vacancies are introduced by substituting  $\text{Ce}^{4+}$  with divalent alkaline earth or trivalent rare earth ions (**Figure 1.16**).  $\text{Gd}^{3+}$  and  $\text{Sm}^{3+}$  trivalent ions are used to dope ceria in order to increase the electrolyte conductivity at lower temperatures, resulting in samarium-doped cerium Oxide ( $\text{Ce}_{0.8}\text{Sm}_{0.2}\text{O}_{1.9}$ -SDC) and CGO compounds [45]. However, some investigations have shown partial reduction of  $\text{Ce}^{4+}$  to  $\text{Ce}^{3+}$  when operating in electrolysis mode [15].

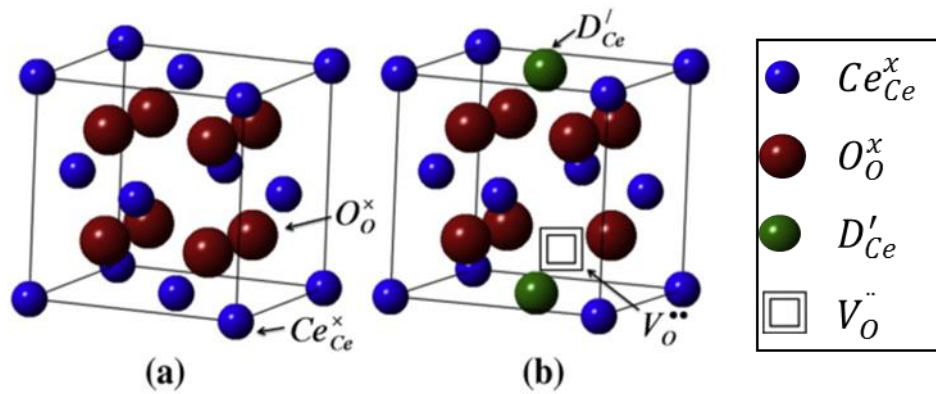


**Figure 1.16:** (a) Cubic fluorite structure of ceria, (b) oxygen vacancy in acceptor doped ceria system. [39]. The defects are expressed using the Kröger-Vink notation [46].

It is generally found, and it is the case for ceria and zirconia based electrolytes, that the highest oxygen ion conductivity is observed when the aliovalent doping cation is closest to the ionic radius of the host cation. In the case of  $\text{Zr}^{4+}$  it is  $\text{Sc}^{3+}$  and in the case of  $\text{Ce}^{4+}$  it is  $\text{Sm}^{3+}$  or  $\text{Gd}^{3+}$  [36][36].

Zirconia-based electrolytes have lower IC than other materials, however, low enough resistances can be achieved by fabricating the electrolyte with a thickness lower than  $10\ \mu\text{m}$  in the SOEC operating temperatures. [36]. **In this thesis**, 6Yb4ScSZ and 8YSZ are the electrolytes that have been used.

## B. Electrode materials for SOCs

In general, a SOEC electrode material should present electronic conductivity, ionic conductivity and, for the purposes of this thesis, high Catalytic Activity (CA) to  $\text{H}_2\text{O}$  and

CO<sub>2</sub> reduction reactions, on one side, and to O<sub>2</sub> oxidation, on the other side (**Figure 1.17a**). The interface between the IC, the EC and the gas phase is the active area where the electrode reaction takes place and it is called the Triple Phase Boundary (TPB). According to this, the enlargement of the active area of the electrodes results in the improvement of the electrochemical performance.

The microstructure and porosity of electrodes should also allow a proper gas transportation to provide the TPB active points with the corresponding gases for both the oxygen evolution and reduction of H<sub>2</sub>O and CO<sub>2</sub>.

**In this thesis**, a composite material was employed as a fuel electrode. It was fabricated by mixing an EC (NiO, that will become metallic nickel after reduction) and an IC (YSZ) materials (**Figure 1.14b**). On the other hand, IC (SDC and CGO) and MIEC (samarium strontium cobaltite, Sm<sub>0.5</sub>Sr<sub>0.5</sub>CoO<sub>3</sub>-SSC and LSCF) materials have formed composites (SDC-SSC and CGO-LSCF) employed as oxygen electrodes (**Figure 1.17c**). MIEC are single materials that provide gathered the IC and EC functionalities. For this material, the electrochemical active area corresponds to the interface between the solid and the gas phase (Two Phase Boundary – 2PB), and it is extended to the entire electrode. [22,47].

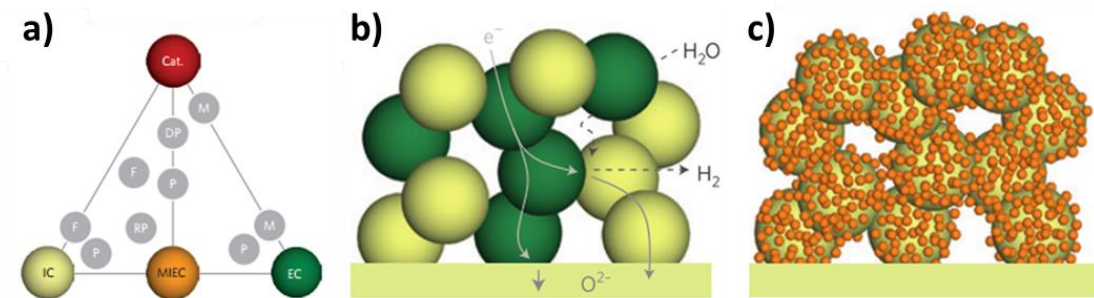


**Figure 1.17:** SOFC and SOEC electrode materials and microstructures. **a)** Diagram of the three key functionalities of the electrodes (vertices) and classes of materials (grey circles). Functionality includes: Ion Conduction (IC), Electron Conduction (EC), or Mixed Ion and Electron Conduction (MIEC), and Catalytic Activity (Cat., CA). Classes of materials includes: Metals (M), Fluorite (F), Perovskite (P), Double Perovskite (DP), and Ruddlesden-Popper (RP) phases. Schematic illustration of electrodes showing the key types of microstructures and classes of functional materials following the same coding as presented in **a)**: **b)** IC-EC composite structure, illustrating the TPB fuel electrode in SOEC mode; **c)** IC coated with a percolating layer of MIEC employed as an oxygen electrode [47].

### Oxygen electrode in SOCs

The Oxygen Reduction Reaction (ORR) and the Oxygen Evolution Reaction (OER) occur on the oxygen electrode of SOFC and SOEC, respectively. The kinetics of those

reactions has important influence on the overall SOC performance. Mixed ionic and electronic conductor single-phase materials such as perovskites, double-perovskite oxides and Ruddlesden-Popper (RP) crystal phases, are currently used for oxygen electrodes [22,47]. Those materials present high ionic and electronic conductivity, which extends the TPB zone for the electrochemical reaction to the entire electrode, decreases the electrode polarization resistance, and decreases the partial pressure at the interface [47-50]. Besides, MIEC materials present large surface exchange rate constant.

Although the mainly electronic conductor Lanthanum Strontium Manganite ( $\text{LaSrMnO}_3$ -LSM) has been commonly used as SOFC cathode material [51,52], and later for SOEC oxygen electrodes, [48] in order to improve the TPB, LSM-YSZ composite has also been used mixing the good IC of the YSZ and the thermal and chemical compatibility of LSM and YSZ. [53]. The performance of LSM rapidly decreases under SOEC operation conditions [54] and, as a consequence alternative materials have been proposed for IT solid oxide cells.

Cobalt-containing perovskites oxides such as SSC, LSC and LSCF [22,47,48,52-56] have been presented as a valuable option for substituting conventional LSM at lower temperature. Those materials are MIEC with high CA [52], which results in better performance and lower polarization resistances than LSM [57]. However, the operation of those materials on fuel and electrolysis mode has shown different degradation mechanisms. One problem is related to the reactivity of lanthanum strontium cobaltite oxygen electrode materials with YSZ. The chemical reaction between both phases, directly associated with the phases decomposition [56], leads to the formation of lanthanum zirconate ( $\text{La}_2\text{Zr}_2\text{O}_7$ ) and strontium zirconate ( $\text{SrZrO}_3$ ) insulating phases. Those phases difficult the oxygen ion diffusion through the electrolyte-oxygen electrode interface resulting on a reduction of the durability and performance of the cell [48,51,53,58,59]. In this case, a diffusion barrier layer is needed between the electrolyte and the oxygen electrode in order to hinder the formation of those secondary phases [48,56,60]. Many studies have demonstrated that the interlayer quality is of key importance for achieving high SOEC performance.

Specifically, it has been found that a dense CGO barrier layer is useful for obtaining high performances [38].

Another critical issue associated with SOEC operation under high current densities is the delamination of the oxygen electrode [50]. Virkar [61] has developed a model for explaining this delamination taking place in the electrolyte-oxygen electrode interfaces. This model holds that the increase of the oxygen partial pressure within the electrolyte causes voids in the interface and the disconnection of the electrolyte from the oxygen electrode, leading to the delamination of the interface.

More electrode mechanical degradation issues are related to the TECs mismatch between the electrolyte and the oxygen electrode materials. SSC and LSCF have larger TECs ( $\sim 24 \cdot 10^{-6} \text{ K}^{-1}$  for SSC and  $17.5 \cdot 10^{-6} \text{ K}^{-1}$  for LSCF) than the ones measured for YSZ electrolyte ( $10.5 \cdot 10^{-6} \text{ K}^{-1}$  for 8% YSZ) [48,51]. This results on the delamination of electrolyte-oxygen electrode interfaces, and the formation of cracks in the oxygen electrode under long-term operation or thermal cycles [48,51,59,60,62]. In order to mitigate the large TEC difference between both phases, composites of a MIEC material and ionic conductors, like SDC-SSC and LSCF-CGO, have been proposed as oxygen electrodes [63]. Besides, the use of oxygen electrodes based of this type of composites present some advantages. On one hand, the microstructural stability of the oxygen electrodes is enhanced by improving the mechanical properties [64]. On the other hand, those composites present a higher density of TPBs [48], which decreases the polarization resistance compared to pure MIEC electrodes under electrolysis operation [55,59], and improves the electrochemical performance.

Oxygen electrodes based on composites fabricated by infiltration of porous backbones have also been proposed. A typical backbone for infiltration is required to be mechanically strong and have a very high porosity, facilitating the penetration of the infiltration solution and allowing transport of gas species [47,64]. The infiltration consists in the introduction of a liquid solution composed of dissolved metal nitrates into a porous backbone, its drying, and the formation of the desired oxide phase through a low-temperature thermal treatment for reaching crystallization (**Figure 1.18**) [32,47,63-65]. The application of the infiltration technique for the fabrication of composites to be functionalized as electrodes allows optimizing the transports of

electrons, gases and ions along the electrode [64,66]. Furthermore, the possible chemical reactions between the infiltrated and backbone phases are minimized because of the low calcination temperature on the thermal treatment required for the infiltrated phase formation [64]. In the case of SDC, it has much better chemical compatibility with SSC than does YSZ since not chemical reaction occurs until temperatures higher than 1100 °C [58], which avoids the formation of the previously mentioned insulating phases.

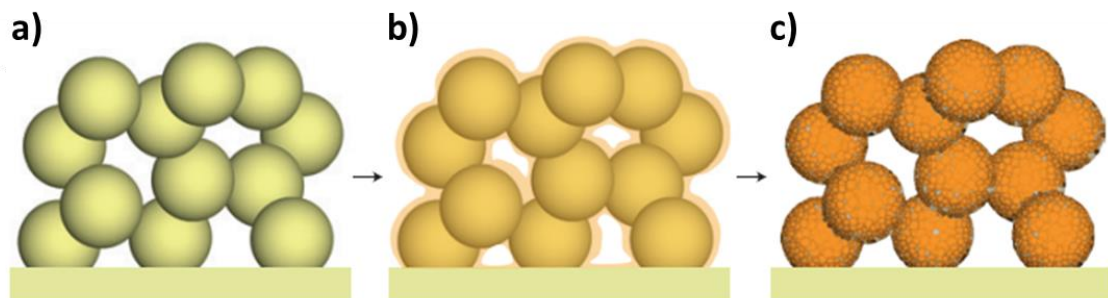


**Figure 1.18:** An ionic conductor (i.e. SDC/CGO) backbone (a) is coated with a MIEC perovskite (i.e. SSC/LSCF) by infiltration (b) to form a nanostructure with a rich TPB area (c) [47].

The reaction pathways on the bulk and surface of the oxygen electrode in SOEC can be described (in the case of MIECs or IC-MIECs) by the following steps (**Figure 1.19**) [48]. The first path, corresponding to the bulk, is composed of the oxygen ionic transfer at the CGO/MIEC interface (1), followed by the oxygen release step in the MIEC (2). The second corresponds to the surface pathway. This path involves the direct electrochemical oxidation of the oxide ions at the TPBs (4). It takes place in parallel to the oxygen exchange at the MIEC/gas interface (bulk pathway). Both reaction paths lead to form adsorbed oxygen atoms on the surface of the electrode, which are finally released by the desorption step to produce gaseous molecules (3).

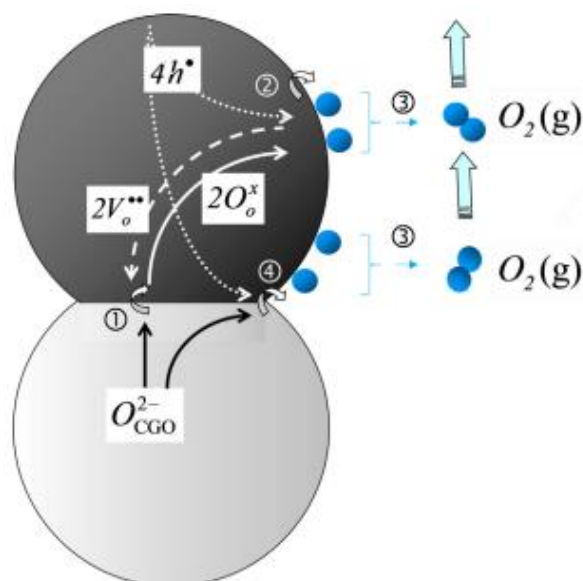


**Figure 1.19:** Schematic representation of the reaction pathways implemented in a model for oxygen oxidation in SOEC [48]

**In this thesis**, nanostructured composites fabricated by the infiltration of LSCF or SSC cobaltite solutions on SDC or CGO mesoporous ionic conductor scaffolds are employed as oxygen electrodes. Additionally, a CGO diffusion barrier layer is introduced between the electrolyte and the fabricated oxygen electrode. This approach may result on an optimized microstructure for ensuring the mechanical stability of the electrolyte-oxygen electrode interface. Furthermore, increasing TPB active points improves the electrode performance and enhances the oxygen electrode reaction kinetics.

### Fuel electrode in SOCs

The electrochemical reaction for steam oxidation occurs in the SOFC anodes. Contrary, steam and  $\text{CO}_2$  reduction reactions take place in fuel electrodes when SOCs operate on electrolysis mode (SOECs). The Ni-YSZ cermet (**Figure 1.17b**) is the most used material on both fuel and electrolysis configurations. This material is functionalized as porous fuel electrode in SOEC due to its reasonable electrocatalytic activity for splitting  $\text{H}_2\text{O}/\text{CO}_2$  at high operation temperatures, low cost, excellent thermal stability, and appropriate thermal expansion coefficient of both Ni and YSZ phases [22,67]. Ionic conductor materials, like YSZ and SDC, are incorporated to the fuel electrode with the aim of increasing its IC, for adjusting the electrolyte and fuel

electrode thermal expansion coefficients, and extend TPBs to the entire fuel electrode thickness [68]. The EC of the composite is provided by the Ni phase.

In addition to the phases intrinsic performance of the Ni-YSZ material, its microstructure is directly affecting to the electrode polarization resistance [22,69]. Different microstructural factors are important for achieving an effective transport of gases, ions and electrons; and for determining the electrochemical activity of SOECs. The existence of high density of TPB active points (composed by Ni, YSZ, and pores diffusion) [70], and the mean particle diameter of both phases are among them. Experimental results of Ni-based cermet cathodes under electrolysis [71] and co-electrolysis gas compositions have showed good electrochemical performance with high electrolysis current density and low polarization resistance [68].

The electrochemical efficiency of SOEC has been widely improved using Ni-YSZ fuel electrode-supported cells, which limit ionic losses [70]. The Ni-YSZ fuel electrode presents two different microstructures, which are directly associated to the electrolysis performance of the electrolysis cells. The support is composed by a porous and thick current collector layer. This layer is related to gas transport and can cause high resistances at high current densities. On top of the support, a thin layer is functionalized as catalyst. This functional layer is optimized to decrease overpotentials, accelerate the electrochemical processes, and improve the IC of the YSZ in the composite.

The microstructure of long-term tested Ni-YSZ fuel electrodes has been analysed [72]. Post-mortem microscopy studies reveal damages on its microstructure. Decrease of the Ni-YSZ contact area, loss of Ni percolation, migration of Ni from the electrolyte-fuel electrode interface and formation of cracks along the electrode are among the most typical microstructural observed damages. It has been reported that these phenomena are caused by impurity inclusion in and around Ni particles, formation of  $ZrO_2$  nanoparticles, morphology changes, and Ni oxidation generating volumetric expansions.

Those analyses show that the microstructure and applied operation conditions have important influence on the agglomeration and oxidation of Ni, as well as in the degradation of the Ni-YSZ electrode. Besides, it has been shown that this degradation

becomes irreversible when the cell is operated at high current densities and high steam partial pressure. A 3D reconstruction of the Ni-YSZ functional layer before and after cell operation under  $-0.5 \text{ A/cm}^2$  of injected current density is presented in **Figure 1.20**, as an example. That reconstruction presents the evolution of the microstructure showing Ni coarsening while keeping the YSZ backbone microstructure unchanged [72].

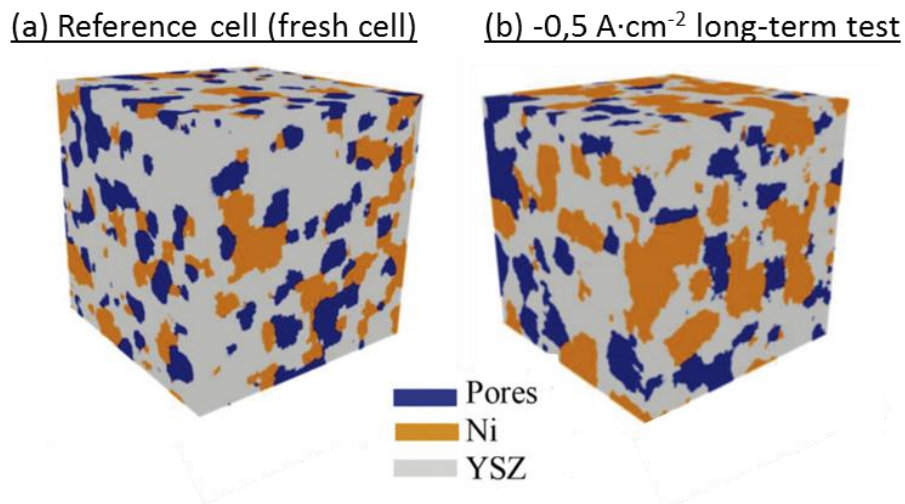


**Figure 1.20:** 3D reconstructions of the Ni-YSZ functional layer of a) reference and b)-0.5 A/cm<sup>2</sup> long-term tested sample. Nickel phase is orange, the porosity is blue and YSZ is grey [72].

The post-mortem characterization of the Ni-YSZ fuel electrode has revealed that some fabrication and operation conditions need to be respected in order to maintain an optimal microstructure. Some of those key points are: (i) decreasing the particle size and ensuring the interconnection between Ni and YSZ phases in order to keep high TPB density and avoid Ni migration, (ii) selecting appropriated test conditions, and (iii) reduce overpotentials for a given current density [73-75]. Nowadays, different fabrication and operation methods like infiltrating CGO into Ni-YSZ and alternate SOFC and SOEC operation, are studied for recovering failure and degradation mechanisms of the fuel electrode with the aim of extending the lifetime of the systems [67,76].

Furthermore, some authors have reported especial degradation of Ni-YSZ fuel electrode under electrolysis applications. Although the fuel electrode generates hydrogen from the electrochemical reduction of steam, a small flow of the same hydrogen gas is required for avoiding the re-oxidation of Ni to NiO, what could suppose a 5-10% increase of volume, under electrolysis operation [15]. As a consequence of that, researchers have focused on proposing alternative materials

[40]. Perovskite oxides have been proposed to be used as fuel electrodes since they present excellent properties such as mixed conductivities and catalytic activity. However, perovskite oxides present issues for catalyze  $\text{CO}_2$ , and of stability for keeping the micro and nano structure of the fuel electrode at high temperatures and highly reducing conditions [22]. Nickel/doped ceria cermets have also been studied for electrolysis [15]. Mixing doped-ceria with Ni provides adequate electronic and ionic conductivities, as well as electrocatalytic activity, which is an ideal combination for the fuel electrode in SOEC [77].

**In this thesis**, two fuel electrode configurations have been employed: Ni-YSZ fuel electrode-supported cells, and Ni-SDC fuel electrodes on 6Yb4ScSZ electrolyte-supported cells. Ni-SDC was synthesised by impregnating NiO mesoporous material with SDC precursors in order to form a mesoporous nanocomposite.

#### **1.4.2 Mesoporous materials as SOEC electrodes**

The IUPAC classifies materials according to their pores widths in macropores, mesopores and micropores. Mesopores present pores sizes between 2 and 50 nm [78], and they have become highly applicable due to its nanometric structure and high surface area (**Figure 1.21**). The development of procedures able to control the structure and pore architecture of mesoporous materials has been extensively used in different fields like chemistry and materials science [79]. In particular, the hard-template method consists on employing a material as mould to replicate its nanostructure and was developed with the aim of synthesising ordered mesoporous materials. Specifically, this method allows controlling and modifying the pore size and wall thickness of mesoporous metal oxides. The hydrothermal conditions applied during the synthesis are altered with this propose by changing the crystallization temperatures [80].

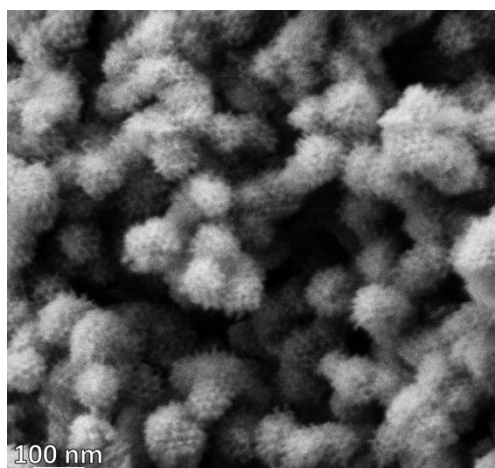


**Figure 1.21:** SEM micrograph of NiO synthesised mesoporous powder synthesised by using the hard-template method.

An ordered mesoporous template is needed for the application of the hard-template method. In this thesis, KIT-6 is employed as mesoporous silica template, which presents a three-dimensional (3D) cubic structure and  $Ia3d$  symmetry. This material has highly ordered mesoporous structure, narrow pore size distribution and high surface area. In order to fulfil different applications requirements, the mesoporous structures and particles morphologies obtained from applying the hard-template method can be tuned in terms of pore size, wall thickness and particle size [81-83].

It has been published that replicated mesoporous structures are very stable at high temperatures [84]. This has become an important issue to be solved in nanomaterials [85], which usually collapse at high temperatures. The stability of synthesised mesoporous materials up to 1100 °C has been demonstrated due to the partial crystallization of the metal oxide before the template removal, which allows entering in a self-limited grain growth regime [86], that slows down the grain size growth with the time. Among the multiple applications of these mesoporous materials, its stability at high temperature allows applying them for the fabrication of nanostructured SOEC electrodes with the aim of improving the overall cell performance and durability [87]. Specifically, the utilization of this type of materials ensures a homogeneous distribution of the phases constituting the nanocomposite. That results in an increase of active TPB points where the electrochemical reaction can take place, a reduction of

the current density in each point, a significant decrease of the polarization resistance [88], and an improvement of the ionic conduction pathway.

In particular, a well-defined ceramic scaffold can be used to avoid the agglomeration of the metallic part of a fuel electrode cermet at the typical SOEC operation temperatures. Besides, good connectivity along the metallic pathway avoids the generation of isolated and electrochemically inactive areas [89]. Moreover, mesoporous metal oxides can be infiltrated with nitrate salts for its functionalization as SOEC oxygen electrodes. The nanostructure of the composite favours the gas penetration for the subsequent electrochemical reaction. Experimental results have demonstrated that mesoporous nanocomposite electrodes exhibit good performance, thermal stability and excellent durability under SOFC and SOEC operation modes [84,85,87-90].

**In this thesis**, mesoporous materials have been synthesised for being applied at oxygen and fuel electrodes. The mesoporous KIT-6 has been always used as template.

## **1.5 Scope of the thesis**

This thesis is focused on the use of high surface area and thermally stable mesoporous metal oxide materials as oxygen electrodes for enhancing the performance of solid oxide electrolysis cells electrodes working under electrolysis and co-electrolysis modes. Firstly, the work aims to successfully synthesize reproducible mesoporous metal oxides by applying the hard-template method. Secondly, the work is devoted to apply these materials for the fabrication of highly performing and long-term stable SOECs for a final scale up of the process. This work encompasses the work developed on the European ECo project<sup>1</sup>.

The procedures for synthesising mesoporous materials with different microstructures, the fabrication of electrolysis cells, and the optimization of experimental set-ups for the cells characterization on (co-)electrolysis mode have been

---

<sup>1</sup> ECo Project, "Efficient Co-Electrolyser for Efficient Renewable Energy Storage", FCJ HU (H2020) no. 699892 (ECo).

optimized in this work<sup>2</sup>. It is expected that this work is used as basis for future developments on (co-)electrolysis of the “Nanoionics and Fuel Cells group” in the Department of Advanced Materials for Energy at IREC.

The thesis is organized as described in the following:

**Chapter 1** briefly analyses the current energy scenario presenting electrolysers as a promising technology for the storage of chemical energy. According to this and within the scope of this thesis, basic principles, main features and thermodynamics of SOECs are also detailed. Lastly, the state-of-the-art materials of SOECs are reviewed.

**Chapter 2** describes all the experimental methods and techniques employed in this thesis. A detailed explanation of the procedures applied for the synthesis of materials and for fabrication of electrodes and cells is presented. The techniques applied for the characterization of synthesised materials and of fabricated cells are also explained.

**Chapter 3** presents the results obtained from the structural characterization of the mesoporous materials and fabricated electrodes. The optimization of the attachment of the mesoporous scaffold for the fabrication of oxygen electrodes is also detailed.

**Chapter 4** compares electrolyte- and fuel electrode-supported cell configurations based on the same oxygen electrode. The electrochemical performance and the microstructural characterization of these cells are considered for that purpose. The applicability of these materials as SOEC electrodes is for the first time demonstrated and the results are presented in this section.

**Chapter 5** presents a study focused on analysing the influence of the oxygen electrode interface on the SOEC performance. The electrochemical and microstructural characterization of barrier layers and oxygen electrodes fabricated applying different methods are discussed in this chapter.

**Chapter 6** shows the performance of SOEC cells on co-electrolysis mode containing the optimized oxygen electrode, fabricated by infiltration of mesoporous scaffolds. The long-term stability of infiltrated mesoporous composites is also demonstrated for the

---

<sup>2</sup> This thesis is a natural extension of a previous work developed by Dr. Laura Almar during her PhD work entitled “Ordered mesoporous metal oxides for solid oxide fuel cells and gas sensors” (2014).

first time in this chapter. Microstructural characterization of the cells and its correlation with the electrochemical results are presented in this chapter.

**Chapter 7** shows results of the scale-up of the mesoporous-based electrodes for the fabrication of large area cells. Their electrochemical performance and long-term stability will be also discussed in this chapter.

The conclusions of this thesis will be finally presented in **Chapter 8**.

## 1.6 References

- [1] M. Balat and M. Balat, "Political, economic and environmental impacts of biomass-based hydrogen," *Int. J. Hydrogen Energy*, vol. 34, no. 9, pp. 3589–3603, 2009.
- [2] S. Singh, S. Jain, V. Ps, A. K. Tiwari, M. R. Nouni, J. K. Pandey, and S. Goel, "Hydrogen: A sustainable fuel for future of the transport sector," *Renew. Sustain. Energy Rev.*, vol. 51, pp. 623–633, 2015.
- [3] G. Marbán and T. Valdés-Solís, "Towards the hydrogen economy?," *Int. J. Hydrogen Energy*, vol. 32, pp. 1625–1637, 2007.
- [4] M. Balat, "Potential importance of hydrogen as a future solution to environmental and transportation problems," *Int. J. Hydrogen Energy*, vol. 33, pp. 4013–4029, Aug. 2008.
- [5] S. Ehsan and M. A. Wahid, "Hydrogen production from renewable and sustainable energy resources: Promising green energy carrier for clean development," *Renew. Sustain. Energy Rev.*, vol. 57, pp. 850–866, 2016.
- [6] E. Commission, "Implementing the Energy Efficiency Directive," Brussels, 2013.
- [7] M. Ni, M. K. H. Leung, and D. Y. C. Leung, "Technological development of hydrogen production by solid oxide electrolyzer cell (SOEC)," *Int. J. Hydrogen Energy*, vol. 33, pp. 2337–2354, 2008.
- [8] S. Ould Amrouche, D. Rekioua, T. Rekioua, and S. Bacha, "Overview of energy storage in renewable energy systems," *Int. J. Hydrogen Energy*, vol. 41, pp. 20914–20927, 2016.
- [9] B. Dunn, H. Kamath, and J. M. Tarascon, "Electrical energy storage for the grid: A battery of choices," *Science (80-. )*, vol. 334, pp. 928–935, 2011.
- [10] A. Tarancón, C. Fábrega, A. Morata, M. Torrell, and T. Andreu, "Power-to-fuel and artificial photosynthesis for chemical energy storage," in *Materials for Sustainable Energy Application*, Pan Stanford Publishing Pte Ltd, 2016, pp. 1–68.
- [11] S. D. Ebbesen, S. H. Jensen, A. Hauch, and M. B. Mogensen, "High temperature electrolysis in alkaline cells, solid proton conducting cells, and solid oxide cells," *Chem. Rev.*, vol. 114, pp. 10697–10734, 2014.
- [12] S. H. Jensen, X. Sun, S. D. Ebbesen, R. Knibbe, and M. Mogensen, "Hydrogen and synthetic fuel production using pressurized solid oxide electrolysis cells," *Int. J. Hydrogen Energy*, vol. 35, pp. 9544–9549, Sep. 2010.
- [13] I. K. Kapdan and F. Kargi, "Bio-hydrogen production from waste materials," *Enzyme Microb. Technol.*, vol. 38, pp. 569–582, 2006.
- [14] T. Rostrup-Nielsen, "Manufacture of hydrogen," *Catal. Today*, vol. 106, pp. 293–296, 2005.
- [15] M. A. Laguna-Bercero, "Recent advances in high temperature electrolysis using

- solid oxide fuel cells: A review," *J. Power Sources*, vol. 203, pp. 4–16, 2012.
- [16] M. Ni, M. K. H. Leung, D. Y. C. Leung, and K. Sumathy, "A review and recent developments in photocatalytic water-splitting using TiO<sub>2</sub> for hydrogen production," *Renew. Sustain. Energy Rev.*, vol. 11, pp. 401–425, 2007.
- [17] C. Graves, S. D. Ebbesen, M. Mogensen, and K. S. Lackner, "Sustainable hydrocarbon fuels by recycling CO<sub>2</sub> and H<sub>2</sub>O with renewable or nuclear energy," *Renew. Sustain. Energy Rev.*, vol. 15, no. 1, pp. 1–23, 2011.
- [18] M. Samavati, M. Santarelli, A. Martin, and V. Nemanova, "Thermodynamic and economy analysis of solid oxide electrolyser system for syngas production," *Energy*, vol. 122, pp. 37–49, 2017.
- [19] W.L. Becker, R.J. Braun, M. Penev, and M. Melaina, "Production of Fischer-Tropsch liquid fuels from high temperature solid oxide co-electrolysis units," *Energy*, vol. 47, pp. 99–115, 2012.
- [20] C. Graves, S. D. Ebbesen, and M. Mogensen, "Co-electrolysis of CO<sub>2</sub> and H<sub>2</sub>O in solid oxide cells: Performance and durability," *Solid State Ionics*, vol. 192, pp. 398–403, 2011.
- [21] E. Dönitz, W. ; Erdle, "High-temperature electrolysis of water vapor—status of development and perspectives for application," *Int. J. Hydrogen Energy*, vol. Vol.10(5), pp. 291–295, 1985.
- [22] Y. Zheng, J. Wang, B. Yu, W. Zhang, J. Chen, J. Qiao, and J. Zhang, "A review of high temperature co-electrolysis of H<sub>2</sub>O and CO<sub>2</sub> to produce sustainable fuels using solid oxide electrolysis cells (SOECs): advanced materials and technology," *Chem. Soc. Rev.*, vol. 46, pp. 1427–1463, Mar. 2017.
- [23] H. W. Chandler and F. Z. Pollara, *Oxygen regeneration in a solid electrolyte system*, 62nd ed. American Institute of Chemical Engineers, 1966.
- [24] L. Elian, *Oxygen regeneration in solid electrolyte batteries: Fundamental considerations*, 62nd ed. American Institute of Chemical Engineers, 1966.
- [25] R. L. Ash, W. L. Dowler, and G. Varsi, "Feasibility of rocket propellant production on Mars," *Acta Astronaut.*, vol. 5, pp. 705–724, 1978.
- [26] R. RICHTER, "Basic investigation into the production of oxygen in a solid electrolyte process," in *16th Thermophysics Conference*, 1981, pp. 1–14.
- [27] K. R. Sridhar, "Oxygen production on Mars using solid oxide electrolysis," *Solid State Ionics*, vol. 93, pp. 321–328, 1997.
- [28] K. R. Sridhar, C. S. Iacomini, and J. E. Finn, "Combined H<sub>2</sub>O/CO<sub>2</sub> Solid Oxide Electrolysis for Mars In Situ Resource Utilization," *J. Propuls. Power*, vol. 20, pp. 892–901, Sep. 2004.
- [29] M. Steinberg, "Electrolytic synthesis of methanol from CO<sub>2</sub>," 13-Mar-1976.
- [30] J. G. Lewis and A. J. Martin, "Method For Obtaining Carbon Dioxide From The Atmosphere and For Production Of Fuels," 02-Sep-1979.

- [31] S. D. Ebbesen and M. Mogensen, "Electrolysis of carbon dioxide in Solid Oxide Electrolysis Cells," *J. Power Sources*, vol. 193, pp. 349–358, 2009.
- [32] M. Götz, J. Lefebvre, F. Mörs, A. McDaniel Koch, F. Graf, S. Bajohr, R. Reimert, and T. Kolb, "Renewable Power-to-Gas: A technological and economic review," *Renew. Energy*, vol. 85, pp. 1371–1390, 2016.
- [33] C. D. Ridjan I, Mathiesen B, "Synthetic fuel production costs by means of solid oxide electrolysis cells," *Energy*, vol. 76, pp. 104–113, 2014.
- [34] Y. Tan, A. Wang, L. Jia, D. Yan, B. Chi, J. Pu, and J. Li, "High-performance oxygen electrode for reversible solid oxide cells with power generation and hydrogen production at intermediate temperature," *Int. J. Hydrogen Energy*, vol. 42, pp. 4456–4464, 2017.
- [35] A. Hauch, S. D. Ebbesen, S. H. Jensen, and M. Mogensen, "Highly efficient high temperature electrolysis," *J. Mater. Chem.*, vol. 18, pp. 2331–2340, 2008.
- [36] D. J. L. Brett, A. Atkinson, N. P. Brandon, and S. J. Skinner, "Intermediate temperature solid oxide fuel cells," *Chem. Soc. Rev.*, vol. 37, pp. 1568–1578, 2008.
- [37] S. D. Ebbesen, C. Graves, and M. Mogensen, "Production of synthetic fuels by co-electrolysis of steam and carbon dioxide," *Int. J. Green Energy*, vol. 6, pp. 646–660, Dec. 2009.
- [38] J. Laurencin, M. Hubert, D. F. Sanchez, S. Pylypko, M. Morales, A. Morata, B. Morel, D. Montinaro, F. Lefebvre-Joud, and E. Siebert, "Degradation mechanism of  $\text{La}_{0.6}\text{Sr}_{0.4}\text{Co}_{0.2}\text{Fe}_{0.8}\text{O}_{3-\delta}$  /  $\text{Gd}_{0.1}\text{Ce}_{0.9}\text{O}_{2-\delta}$  composite electrode operated under solid oxide electrolysis and fuel cell conditions," *Electrochim. Acta*, vol. 241, pp. 459–476, 2017.
- [39] N. Mahato, A. Banerjee, A. Gupta, S. Omar, and K. Balani, "Progress in Material Selection for Solid Oxide Fuel Cell Technology: A Review," *Prog. Mater. Sci.*, vol. 72, pp. 141–337, Feb. 2015.
- [40] X. Yue and J. T. S. Irvine, "Alternative Cathode Material for CO<sub>2</sub> Reduction by High Temperature Solid Oxide Electrolysis Cells," *J. Electrochem. Soc.*, vol. 159, pp. F442–F448, 2012.
- [41] K. C. Wincewicz and J. S. Cooper, "Taxonomies of SOFC material and manufacturing alternatives," *J. Power Sources*, vol. 140, pp. 280–296, 2005.
- [42] O. Yamamoto, Y. Arati, Y. Takeda, N. Imanishi, Y. Mizutani, M. Kawai, and Y. Nakamura, "Electrical conductivity of stabilized zirconia with ytterbia and scandia," *Solid State Ionics*, vol. 79, pp. 137–142, 1995.
- [43] A. Lakki, R. Herzog, C. R. M. Weller H. Schubert, and M. K. G. B. O. GoÈrke, "Mechanical loss, creep, diffusion and ionic conductivity of  $\text{ZrO}_{2-8}$  mol% $\text{Y}_2\text{O}_3$  polycrystals," *J. Eur. Ceram. Soc.*, vol. 20, pp. 285–296, 2000.
- [44] F. Yuan, J. Wang, H. Miao, C. Guo, and W. G. Wang, "Investigation of the crystal structure and ionic conductivity in the ternary system  $(\text{Yb}_2\text{O}_3)_x(\text{Sc}_2\text{O}_3)_{1-x}$ ,"

- x)-(ZrO<sub>2</sub>) 0.89 (x = 0-0.11)," *J. Alloys Compd.*, vol. 549, pp. 200–205, 2013.
- [45] B. Zhao, Y. Tong, Y. Zhao, T. Yang, F. Yang, Q. Hu, and C. Zhao, "Preparation of ultra-fine Sm<sub>0.2</sub>Ce<sub>0.8</sub>O<sub>1.9</sub> powder by a novel solid state reaction and fabrication of dense Sm<sub>0.2</sub>Ce<sub>0.8</sub>O<sub>1.9</sub> electrolyte film," *Ceram. Int.*, vol. 41, pp. 9686–9691, 2015.
- [46] F. A. Kröger and H. J. Vink, "Relations between the Concentrations of Imperfections in Crystalline Solids," *Solid State Phys.*, vol. 3, pp. 307–435, Jan. 1956.
- [47] J. T. S. Irvine, D. Neagu, M. C. Verbraeken, C. Chatzichristodoulou, C. Graves, and M. B. Mogensen, "Evolution of the electrochemical interface in high-temperature fuel cells and electrolyzers," *Nat. Energy*, vol. 1, pp. 1–13, 2016.
- [48] J. Laurencin, M. Hubert, K. Couturier, T. Le Bihan, P. Cloetens, F. Lefebvre-Joud, and E. Siebert, "Reactive Mechanisms of LSCF Single-Phase and LSCF-CGO Composite Electrodes Operated in Anodic and Cathodic Polarizations," *Electrochim. Acta*, vol. 174, pp. 1299–1316, 2015.
- [49] H. Fan, Y. Zhang, and M. Han, "Infiltration of La<sub>0.6</sub>Sr<sub>0.4</sub>FeO<sub>3-δ</sub> nanoparticles into YSZ scaffold for solid oxide fuel cell and solid oxide electrolysis cell," *J. Alloys Compd.*, vol. 723, pp. 620–626, 2017.
- [50] Z. Pan, Q. Liu, M. Ni, R. Lyu, P. Li, and S. H. Chan, "Activation and failure mechanism of La<sub>0.6</sub>Sr<sub>0.4</sub>Co<sub>0.2</sub>Fe<sub>0.8</sub>O<sub>3-δ</sub> air electrode in solid oxide electrolyzer cells under high-current electrolysis," *Int. J. Hydrogen Energy*, vol. 43, pp. 5437–5450, 2018.
- [51] H. Zhang, F. Zhao, F. Chen, and C. Xia, "Nano-structured Sm<sub>0.5</sub>Sr<sub>0.5</sub>CoO<sub>3-δ</sub> electrodes for intermediate-temperature SOFCs with zirconia electrolytes," in *Solid State Ionics*, 2011, vol. 192, pp. 591–594.
- [52] J.-C. Chang, M.-C. Lee, R.-J. Yang, Y.-C. Chang, T.-N. Lin, C.-H. Wang, W.-X. Kao, and L.-S. Lee, "Fabrication and characterization of Sm<sub>0.2</sub>Ce<sub>0.8</sub>O<sub>2-ι</sub>-Sm<sub>0.5</sub>Sr<sub>0.5</sub>CoO<sub>3-ι</sub> composite cathode for anode supported solid oxide fuel cell," *J. Power Sources*, vol. 196, pp. 3129–3133, 2010.
- [53] L. dos Santos.Gómez, J. M. Porrás-Vázquez, E. . Losilla, F. Martín, J. R. Ramos-Barrado, and D. Marrero-López, "Stability and performance of La<sub>0.6</sub>Sr<sub>0.4</sub>Co<sub>0.2</sub>Fe<sub>0.8</sub>O<sub>3-d</sub> nanostructured cathodes with Ce<sub>0.8</sub>Gd<sub>0.2</sub>O<sub>1.9</sub> surface coating," *J. Power Sources*, vol. 347, pp. 178–185, 2017.
- [54] H. Fan, M. Keane, N. Li, D. Tang, P. Singh, and M. Han, "Electrochemical stability of La<sub>0.6</sub>Sr<sub>0.4</sub>Co<sub>0.2</sub>Fe<sub>0.8</sub>O<sub>3-δ</sub>-infiltrated YSZ oxygen electrode for reversible solid oxide fuel cells," *Int. J. Hydrogen Energy*, vol. 39, pp. 14071–14078, 2014.
- [55] Y. Wang, Z. Yang, M. Han, and J. Chang, "Optimization of Sm<sub>0.5</sub>Sr<sub>0.5</sub>CoO<sub>3-δ</sub>-infiltrated YSZ electrodes for solid oxide fuel cell/electrolysis cell," *RSC Adv.*, vol. 6, pp. 112253–112259, 2016.
- [56] M. Torrell, A. Morata, P. Kayser, M. Kendall, K. Kendall, and A. Tarancón, "Performance and long term degradation of 7 W micro-tubular solid oxide fuel

- cells for portable applications," *J. Power Sources*, vol. 285, pp. 439–448, 2015.
- [57] P. Hjalmarrsson, X. Sun, Y. L. Liu, and M. Chen, "Influence of the oxygen electrode and inter-diffusion barrier on the degradation of solid oxide electrolysis cells," *J. Power Sources*, vol. 223, pp. 349–357, 2013.
- [58] F. Wang, D. Chen, and Z. Shao, "Sm<sub>0.5</sub>Sr<sub>0.5</sub>CoO<sub>3-δ</sub>-infiltrated cathodes for solid oxide fuel cells with improved oxygen reduction activity and stability," *J. Power Sources*, vol. 216, pp. 208–215, 2012.
- [59] H. Fan and M. Han, "Electrochemical stability of Sm<sub>0.5</sub>Sr<sub>0.5</sub>CoO<sub>3-δ</sub> infiltrated YSZ for solid oxide fuel cells or electrolysis cells," *Faraday Discuss.*, vol. 182, pp. 477–491, 2015.
- [60] H. Jung and J. Young, "A promising high-performance lanthanum ferrite-based composite cathode for intermediate temperature solid oxide fuel cells," *Solid State Ionics*, vol. 244, pp. 30–34, 2013.
- [61] A. V. Virkar, "Mechanism of oxygen electrode delamination in solid oxide electrolyzer cells," *Int J Hydrog. Energ.*, vol. 35, pp. 9527–9543, 2010.
- [62] F. Wang, D. Chen, and Z. Shao, "Sm<sub>0.5</sub>Sr<sub>0.5</sub>CoO<sub>3-δ</sub>-infiltrated cathodes for solid oxide fuel cells with improved oxygen reduction activity and stability," *J. Power Sources*, vol. 216, pp. 208–215, 2012.
- [63] K. J. Yoon, M. Biswas, H. Kim, M. Park, J. Hong, H. Kim, J. Son, J. Lee, B. Kim, and H. Lee, "Nano-tailoring of infiltrated catalysts for high-temperature solid oxide regenerative fuel cells," *Nano Energy*, vol. 36, pp. 9–20, 2017.
- [64] W. H. Kan, A. J. Samson, and V. Thangadurai, "Trends in electrode development for next generation solid oxide fuel cells," *J. Mater. Chem. A*, vol. 4, pp. 17913–17932, 2016.
- [65] T. Z. Sholklapper, C. P. Jacobson, S. J. Visco, and L. C. Dejonghe, "Synthesis of dispersed and contiguous nanoparticles in solid oxide fuel cell electrodes," *Fuel Cells*, no. 5, pp. 303–312, 2008.
- [66] D. Ding, X. Li, S. Y. Lai, K. Gerdes, and M. Liu, "Enhancing SOFC cathode performance by surface modification through infiltration," *Energy Environ. Sci.*, vol. 7, pp. 552–575, 2014.
- [67] A. Hauch, M. Marchese, A. Lanzini, and C. Graves, "Re-activation of degraded nickel cermet anodes - Nano-particle formation via reverse current pulses," *J. Power Sources*, vol. 377, pp. 110–120, 2018.
- [68] Y. Wang, T. Liu, L. Lei, and F. Chen, "High temperature solid oxide H<sub>2</sub>O/CO<sub>2</sub> co-electrolysis for syngas production," *Fuel Process. Technol.*, vol. 161, pp. 248–258, 2017.
- [69] W. H. Kan and V. Thangadurai, "Challenges and prospects of anodes for solid oxide fuel cells (SOFCs)," *Ionics (Kiel)*, vol. 21, pp. 301–318, 2015.
- [70] F. Usseglio-Viretta, J. Laurencin, G. Delette, J. Villanova, P. Cloetens, and D. Leguillon, "Quantitative microstructure characterization of a NieYSZ bi-layer

- coupled with simulated electrode polarisation," *J. Power Sources*, vol. 256, pp. 394–403, 2014.
- [71] Z. Zhan and L. Zhao, "Electrochemical reduction of CO<sub>2</sub> in solid oxide electrolysis cells," *J. Power Sources*, vol. 195, pp. 7250–7254, 2010.
- [72] E. Lay-Grindler, J. Laurencin, J. Villanova, P. Cloetens, P. Bleuet, A. Mansuy, J. Mougin, and G. Delette, "Degradation study by 3D reconstruction of a nickel-yttria stabilized zirconia cathode after high temperature steam electrolysis operation," *J. Power Sources*, vol. 269, pp. 927–936, 2014.
- [73] M. B. Mogensen, A. Hauch, X. Sun, M. Chen, Y. Tao, S. D. Ebbesen, K. V. Hansen, and P. V. Hendriksen, "Relation Between Ni Particle Shape Change and Ni Migration in Ni-YSZ Electrodes – a Hypothesis," *Fuel Cells*, vol. 17, pp. 434–441, 2017.
- [74] A. Hauch, K. Brodersen, M. Chen, and M. B. Mogensen, "Ni / YSZ electrodes structures optimized for increased electrolysis performance and durability," *Solid State Ionics*, vol. 293, pp. 27–36, 2016.
- [75] M. Pihlatie, A. Kaiser, P. H. Larsen, and M. Mogensen, "Dimensional Behavior of Ni-YSZ Composites during Redox Cycling," *J. Electrochem. Soc.*, vol. 156, no. 3, pp. B322–B329, 2009.
- [76] T. L. Skafte, J. Hjelm, P. Blennow, and C. Graves, "Reactivating the Ni-YSZ electrode in solid oxide cells and stacks by infiltration," *J. Power Sources*, vol. 378, pp. 685–690, 2018.
- [77] V. Papaefthimiou, D. K. Niakolas, F. Paloukis, D. Teschner, A. Knop-Gericke, M. Haevecker, and S. Zafeiratos, "Operando observation of nickel/ceria electrode surfaces during intermediate temperature steam electrolysis," *J. Catal.*, vol. 352, pp. 305–313, 2017.
- [78] IUPAC, "Reporting physisorption data for gas / solid systems with special reference to the determination of surface area and porosity area International Union of Pure and Applied Chemistry," *Pure Appl. Chem.*, vol. 57, pp. 603–619, 1985.
- [79] W. Li and D. Zhao, "An overview of the synthesis of ordered mesoporous materials," *Chem. Commun.*, vol. 49, pp. 943–946, 2013.
- [80] Y. Ren, Z. Ma, and P. G. Bruce, "Ordered mesoporous metal oxides: synthesis and applications," *Chem. Soc. Rev.*, vol. 41, pp. 4909–4027, 2012.
- [81] W. Wang, R. Qi, W. Shan, X. Wang, Q. Jia, J. Zhao, C. Zhang, and H. Ru, "Synthesis of KIT-6 type mesoporous silicas with tunable pore sizes, wall thickness and particle sizes via the partitioned cooperative self-assembly process," *Microporous Mesoporous Mater.*, vol. 194, pp. 167–173, 2014.
- [82] H. Yang and D. Zhao, "Synthesis of replica mesostructures by the nanocasting strategy," *J. Mater. Chem.*, vol. 15, pp. 1217–1231, 2005.
- [83] F. Kleitz, S. Hei Choi, and R. Ryoo, "Cubic Ia3d large mesoporous silica: synthesis

and replication to platinum nanowires, carbon nanorods and carbon nanotubes," *Chem. Commun.*, pp. 2136–2137, 2003.

- [84] L. Almar, T. Andreu, A. Morata, M. Torrell, L. Yedra, S. Estradé, F. Peiró, and A. Tarancón, "High-surface-area ordered mesoporous oxides for continuous operation in high temperature energy applications," *J. Mater. Chem. A*, vol. 2, pp. 3134–3141, 2014.
- [85] L. Almar, A. Morata, M. Torrell, M. Gong, T. Andreu, M. Liu, and A. Tarancón, "A Durable Electrode for Solid Oxide Cells: Mesoporous Ce<sub>0.8</sub>Sm<sub>0.2</sub>O<sub>1.9</sub> Scaffolds Infiltrated with a Sm<sub>0.5</sub>Sr<sub>0.5</sub>CoO<sub>3-δ</sub> Catalyst," *Electrochim. Acta*, vol. 235, pp. 646–653, 2017.
- [86] J. L. M. Rupp, A. Infortuna, and L. J. Gauckler, "Microstrain and self-limited grain growth in nanocrystalline ceria ceramics," *Acta Mater.*, vol. 54, pp. 1721–1730, 2006.
- [87] M. Torrell, L. Almar, A. Morata, and A. Tarancón, "Synthesis of mesoporous nanocomposites for their application in solid oxide electrolyser cells: microstructural and electrochemical characterization," *Faraday Discuss.*, vol. 182, pp. 423–435, 2015.
- [88] L. Almar, A. Morata, M. Torrell, M. Gong, M. Liu, T. Andreu, and A. Tarancón, "Synthesis and characterization of robust, mesoporous electrodes for solid oxide fuel cells," *J. Mater. Chem. A*, vol. 4, pp. 7650–7657, 2016.
- [89] L. Almar, B. Colldeforns, L. Yedra, S. Estradé, F. Peiró, A. Morata, T. Andreu, and A. Tarancón, "High-temperature long-term stable ordered mesoporous Ni–CGO as an anode for solid oxide fuel cells," *J. Mater. Chem. A*, vol. 1, pp. 4531–4538, 2013.
- [90] Y. Chen, K. Gerdes, and X. Song, "Nanoionics and Nanocatalysts : Conformal Mesoporous Surface Scaffold for Cathode of Solid Oxide Fuel Cells," *Sci. Rep.*, vol. 6, pp. 1–8, 2016.

# ***Chapter 2***

*Experimental methods*



<b>2. Experimental methods.....</b>	<b>51</b>
<b>2.1. Chapter overview .....</b>	<b>51</b>
<b>2.2. Synthesis of mesoporous materials .....</b>	<b>52</b>
<b>2.2.1. Hard-template method .....</b>	<b>52</b>
<b>2.2.2. Synthesis of mesoporous KIT-6 template .....</b>	<b>53</b>
<b>2.2.3. Synthesis of mesoporous metal oxide replicas .....</b>	<b>56</b>
<b>2.3. Fabrication of mesoporous electrodes .....</b>	<b>58</b>
<b>2.3.1. Impregnation for the fabrication of NiO-SDC fuel electrodes .....</b>	<b>58</b>
<b>2.3.2. Infiltration process for the fabrication of oxygen electrodes.....</b>	<b>59</b>
<b>2.4. Cells fabrication techniques .....</b>	<b>61</b>
<b>2.4.1. Tape casting .....</b>	<b>61</b>
<b>2.4.2. Pulsed Laser Deposition (PLD).....</b>	<b>62</b>
<b>2.4.3. Air brushing technique.....</b>	<b>64</b>
<b>2.4.4. Infiltration technique.....</b>	<b>65</b>
<b>2.5. Fabrication of Solid Oxide Electrolysis Cells (SOECs) .....</b>	<b>67</b>
<b>2.5.1. Symmetrical cells of oxygen electrodes .....</b>	<b>67</b>
<b>2.5.2. Electrolyte supported SOECs.....</b>	<b>68</b>
<b>2.5.3. Fuel electrode supported SOECs .....</b>	<b>70</b>
<b>2.6. Structural Characterization Techniques .....</b>	<b>71</b>
<b>2.6.1. X-Ray Diffraction (XRD).....</b>	<b>71</b>
<b>2.6.2. In-situ powder X-Ray Diffraction vs. Temperature .....</b>	<b>72</b>
<b>2.6.3. Low Angle X-ray Diffraction (LA-XRD).....</b>	<b>73</b>
<b>2.6.4. Nitrogen physisorption measurements (BET) .....</b>	<b>73</b>
<b>2.6.5. Scanning Electron Microscopy (SEM) and Energy Dispersion X-ray (EDX) .....</b>	<b>76</b>
<b>2.6.6. Transmission Electron Microscopy (TEM) .....</b>	<b>78</b>

<b>2.7.</b>	<b>Electrochemical Characterization Techniques .....</b>	<b>79</b>
<b>2.7.1.</b>	<b>Electrochemical test stations for button and large area cells .....</b>	<b>79</b>
<b>2.7.2.</b>	<b>Electrochemical Impedance Spectroscopy (EIS) .....</b>	<b>83</b>
<b>2.7.3.</b>	<b>Galvanostatic and Potentiostatic modes for I-V curves .....</b>	<b>88</b>
<b>2.8.</b>	<b>References.....</b>	<b>90</b>

## 2. Experimental methods

### 2.1. Chapter overview

The present chapter presents the experimental methods and instruments employed during the research performed in this thesis, which can be divided in three main parts: (i) synthesis of mesoporous materials (**sections 2.2 and 2.3**), (ii) fabrication of electrochemical cells (**section 2.4 and 2.5**), and (iii) structural and electrochemical characterization techniques (**sections 2.6 and 2.7**).

The description of the synthesis method and procedures for the fabrication of ceramic mesoporous materials is included in (**section 2.2**). This section presents the hard-temple method, explaining its principles and main steps for its successful implementation, and taking into account that the replica final structure is controlled choosing suitable synthesis parameters. The KIT-6 synthesis procedure is also detailed in this section. This silica-based template was selected for this thesis since it has a defined interconnected pore network. Moreover, its structure is highly reproducible from the template to the replica. Lastly, the procedure for applying the hard-template method using KIT-6 as template and obtaining different mesoporous metal oxides as replicas is also explained. Specifically, samarium-doped-ceria ( $\text{Sm}_{0.2}\text{Ce}_{0.8}\text{O}_{1.9}$ -SDC), gadolinium-doped-ceria ( $\text{Ce}_{0.8}\text{Gd}_{0.2}\text{O}_{1.9}$ -CGO) and nickel (NiO) mesoporous oxides replicas were synthesised in this thesis.

Mesoporous metal oxides were synthesised for being used in the fabrication of Solid Oxide Electrolysis Cell (SOEC) electrodes (**section 2.3**) through its impregnation (**section 2.3.1**) and infiltration (**section 2.3.2**). The used techniques for the fabrication of the different parts of a SOEC in this thesis are briefly explained in **section 2.4**. Those techniques are tape casting, Pulsed Laser deposition (PLD), air brushing and infiltration. Different types of electrochemical cells were fabricated (**section 2.5**). The oxygen electrode has a very important influence on the overall cell performance. A set of oxygen electrode symmetrical cells was prepared and studied for optimizing the oxygen electrode fabrication procedure (**section 2.5.1**). Two different configurations, electrolyte-supported (**section 2.5.2**) and fuel electrode-supported (**section 2.5.3**) cells (ESC and FESC), were fabricated for being tested in electrolysis and co-electrolysis modes.

Characterization techniques were essentially used to study the structure and electrochemical techniques to measure the performance of the materials. Structural techniques (**section 2.6**) were applied for characterizing the synthesised mesoporous materials as well as the fabricated and tested electrochemical cells. On the other hand, electrochemical characterization techniques (**section 2.7**) were used for measuring the performance and understanding the different electrochemical processes involved when the fabricated cells were tested in electrolysis and co-electrolysis mode.

## **2.2. Synthesis of mesoporous materials**

There are two methods for the synthesis of mesoporous metal oxides: soft and hard-template. The soft-templating method is cheap, and the synthesis process does not require specific conditions. Although it allows obtaining a variety of mesoporous structures, the obtained replica present poor thermal stability at high temperatures. As a consequence, synthesised materials cannot be used for high temperature applications like solid oxide electrolysis cells. Contrary, the hard template method, and specifically the route followed during this work, allows using the obtained replicas for high temperature applications. In this thesis, this method has been employed for the synthesis of mesoporous materials [1]. As it is presented in next sections, this type of materials is used for the fabrication of mesoporous electrodes with the aim of increasing the Triple Phase Boundary (TPB) density, which results in the enhancement of the electrodes and the overall electrolysis cells performance.

### **2.2.1. Hard-template method**

The nanocasting or hard-template method allows the synthesis of novel mesostructured materials stable at high temperatures, broadening the range of applications in which mesoporous materials can be employed. The hard-template method also offers the possibility to control the replica structure by choosing the template. Different silica (MCM-41, MCM-48, SBA-15, SBA-16, KIT-6 and FDU-12) and carbon (CMK-1 and CMK-3) mesoporous materials are being used as hard templates in function of the desired pore architecture. Among them, mesoporous silicates with high ordered structures, narrow pore size distribution and high surface area have attracted

much attention from the materials community due to their potential applications [2]. Furthermore, the obtained replicas are crystalline and stable at high temperatures [1].

The synthesis of mesoporous materials applying the hard template method can be summarized in three main steps: i) precursors infiltration ii) phase formation and iii) cleaning. A scheme of the hard template is showed in **Figure 2.1**. Firstly, the mesoporous silica template is infiltrated with a solution of the replica precursors. Silica based KIT-6 was used as hard template in this thesis. The method employed in this thesis involves mixing in ethanol the mesoporous silica template with metal nitrates precursors of the desired phase. A high degree of infiltration and wetting of the precursors solution within the hard template is achieved using ethanol as solvent due to its lower surface tension compared with water [3]. Nitrate precursors are expected to migrate into the pores by capillary condensation during the controlled evaporation of ethanol.

Secondly, the desired crystalline solid phase is formed within the silica template through the decomposition of the precursors inside the pores with a calcination treatment. Then the mesoporous silica template is removed from the replica without affecting its structure. Several washing steps are performed with a 2 M NaOH to the obtained powder. As a result, it is obtained a material perfectly replicating the mesoporous structure. Hence, the choice of the template and precursors, the impregnation technique, and the appropriate heat treatment are of high relevance for nanocasting [1,4,5,6].

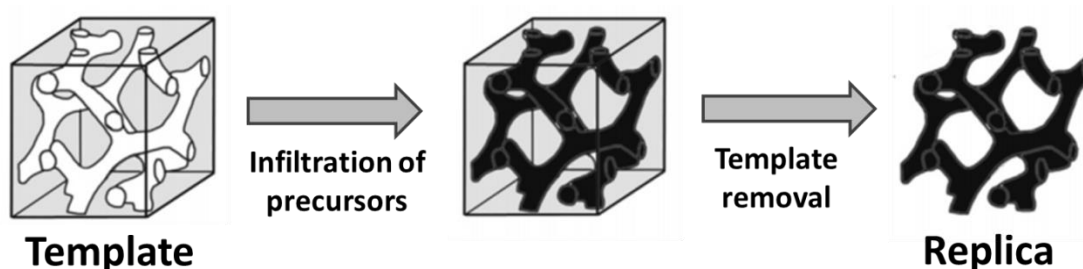


**Figure 2.1:** Scheme of the hard-template method employing a template with cubic structure and  $1a3d$  symmetry such as KIT-6 [7].

### 2.2.2. Synthesis of the mesoporous KIT-6 template

During this work, KIT-6 ordered mesoporous silica was employed as a hard-template for the synthesis of different metal oxide mesoporous replicas. It presents a three-

dimensional (3D) cubic structure with the space group  $Ia3d$ , which pore shape and connectivity can be represented by a pair of two interpenetrated network of channels (**Figure 2.1**) [8]. KIT-6 was one of the first templates allowing a perfect replication of its cubic structure. Nowadays, it is considered the best choice for synthesising materials with that structure [4].

Highly reproducible mesoporous  $Ia3d$  KIT-6 are obtained following the method based on the one published by Kleitz *et al.* in 2003 [8]. For the synthesis of KIT-6 powder, 1:1 (wt%) mixture of Pluronic P123 triblock copolymer ( $EO_{20}PO_{70}EO_{20}$ , EO:ethylene oxide and PO:propylene oxide) surfactant, 0.5 M HCl and Mili-Q water were mixed for 5 hours keeping the temperature at 36 °C or 90 °C depending on the desired final microstructure. These two templates are, from now on, denoted in this work as KIT-6-36 and KIT-6-90, respectively. After the addition of 1-Butanol (BuOH) and lately of tetraethyl orthosilicate (TEOS) as the silicon source, the resulting mixture was stirring during 24 h at the same temperature than the synthesis process (36 or 90 °C) for performing the hydrothermal treatment. The mole ratio of the components was kept as  $TEOS:P123:HCl:H_2O:BuOH = 1:0.017:1.83:195:1.31$ . After filtering and cleaning with Mili-Q water, a calcination step up to 550 °C for 5 h was carried out for the complete elimination of the surfactant.

The KIT-6 synthesis mechanism [8,9] is here detailed and a scheme is presented in **Figure 2.2**. Added butanol is responsible of volume swelling of block-copolymer micelles hydrophobic parts, forming lamellar mesophase aggregates. The TEOS silica source compound is introduced into the P-PO chain of the P123 surfactant according to its hydrophobicity, migrates into P-EO area, and hydrolyses into silica (**Figure 2.2a**). This hydrolysis reaction is catalysed by HCl. Silicates condensation increase during the hydrothermal treatment (36 or 90 °C), what results on the obtention of its ordered cubic  $Ia3d$  mesophase (**Figure 2.2b**). Finally, the surfactant is removed by calcination (**Figure 2.2c**).

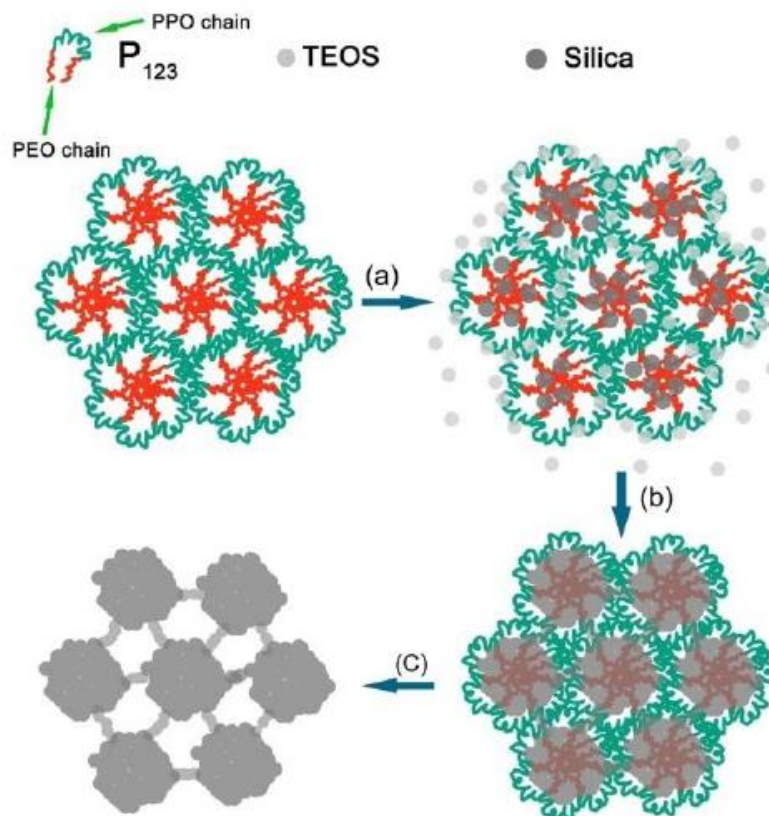


**Figure 2.2:** Scheme of the silica KIT-6 formation mechanism consisting on the addition and diffusion of TEOS (silicon source) into the P123 surfactant structure (a), formation of the ordered silicon structure (b), and calcination of the surfactant (c) [10].

KIT-6 contains two sets of mesopores. The hydrothermal temperature applied to the silica template during the synthesis process determines its pore size. Besides, it influences the formation of micropores channels connecting both mesoporous sets. On one hand, low hydrothermal temperature results in a minor interconnectivity between the two sets of KIT-6. The replica obtained from applying the hard template method grows within only one set of the two KIT-6 mesopores, resulting in a replica with similar wall thickness than for the high synthesis temperature, but a distribution of two pore diameters: a small one of the same size than at high temperature synthesis of the template, and another larger pore diameter equivalent to the dimensions of two walls plus a pore of KIT-6. Furthermore, the proportion of the larger pores decreases with increasing template synthesis temperature. Therefore, the pores size, the pores volume and the wall thickness of the metal oxide replicas change as a function of the employed template; and it is also possible to control the appearance and proportion of large pores in the replica by varying the KIT-6 synthesis temperature (**Figure 2.3a**). In the other hand, both sets of interpenetrating mesopores are connected by micropores

at high hydrothermal synthesis temperatures, what ensures complete filling of both sets of mesopores at the same time when infiltrating with the nitrates precursors solution. The resulting mesoporous replica has the wall thickness equivalent to the size of the KIT-6 mesopores and a only pore diameter ( $\approx 3$  nm) equivalent to the KIT-6 wall thickness (**Figure 2.3b**) [1,3,5].

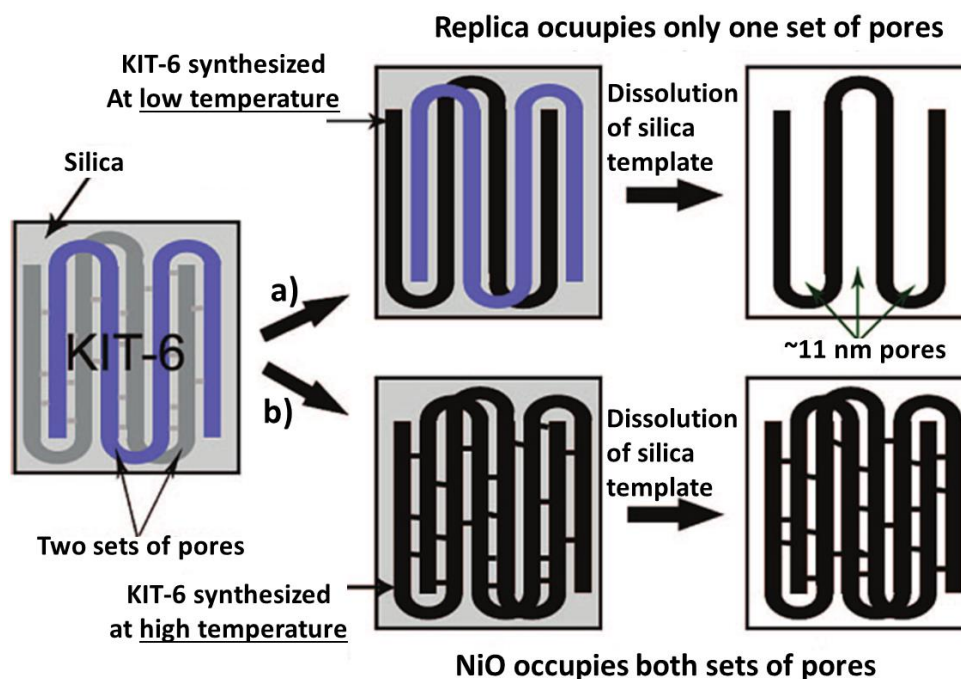


**Figure 2.3:** Mechanism by which two pore sizes in mesoporous metal oxides can be obtained impregnating the two pores sets of KIT-6 as hard template [3].

### 2.2.3. Synthesis of mesoporous metal oxide replicas for this thesis

The hard-template method was applied in this thesis for obtaining ordered mesoporous oxides with crystalline walls as replicas of KIT-6 mesoporous silica templates, which presents a periodic ordered pore microstructure [3]. Replicated mesoporous materials were employed in this thesis for the fabrication of SOEC electrodes with the aim of enhancing the device performance through the increase of the TPB density next to the electrolyte interface. A wide range of mesoporous materials has been reported to be synthesised applying this method [3,5,11]. In this thesis,  $\text{Sm}_{0.2}\text{Ce}_{0.8}\text{O}_{1.9}$ ,  $\text{Ce}_{0.8}\text{Gd}_{0.2}\text{O}_{1.9}$  and NiO mesoporous metal oxides were synthesised applying the hard template method. KIT-6 templates with different pore size distribution were employed.

Stoichiometric amount of the nitrates precursors of the desired active electrode material were mixed on ethanol (10 mL of ethanol per 1 g of KIT-6) and the mixture

was stirred until its complete dissolution. Then the silica template KIT-6 was added keeping the ratio 1.5 mmol of metal cations ( $M^{n+}$ ) per 0.15 g of KIT-6. Resulting mixture was kept in continuous stirring during 2 or 3 hours in order to promote the nitrates precursors impregnation within the KIT-6 template pores. Ethanol was used as solvent since it favours the impregnation of the complete surface of the template. As function of the KIT-6 morphology, which depends of the hydrothermal temperature during the synthesis, one or two KIT-6 mesoporous sets of channels are filled during the impregnation process (**Figure 2.3**). This changes the final pore size of the obtained replica. According to the low hydrothermal temperature applied for the synthesis of the three employed KIT-6, only one of the two interpenetrated set of mesopores were filled during the SDC, CGO and NiO precursors impregnation, each of them with different pore size distribution.

The obtained mixture was left 24 hours at 60 °C for drying the impregnated template by controlled removal of the ethanol solvent. Dried sample was then fired at 600 °C during 5 hours for obtaining the desired phase. Nitrates were used as precursors to facilitate the elimination of decomposition products via the gas phase during the calcination step. Specifically, those precursors react with the atmospheric oxygen, and are decomposed and eliminated as exhausted gas. In this thermal treatment, cations are grouped inside the template pores forming the metal oxide phase following the stoichiometry of the added nitrate precursors.

Repetitive cleaning baths with a solution of 2 M NaOH solution and deionized water were performed to remove the silica template. The alkaline solution dissolve the silica template without affecting the mesoporous synthesised oxides. Specifically, a ratio of 0.4 g of mesoporous powder was dispersed in 50 mL of alkaline washing solution and stirred for 1 hour at 70°C for promoting the dissolution of the silica. After that, the solid and the liquid phases were separated by centrifugation (10 min at 10000 rpm). This process was repeated 3 times. The cleaning procedure was repeated using deionized water until reaching pH=7 in order to eliminate the alkaline solution. At the end of this process, the desired phase (SDC, CGO or NiO mesoporous) was obtained. These powders were used to fabricate the different electrodes as it is detailed in the following sections of the present work. In order to compile the different followed

routes, **Table 2.1** summarizes the precursors and templates used for the synthesis of each mesoporous metal oxide.

Synthesised mesoporous material	Acronym	KIT-6	Precursors	Dedicated section
Samarium-doped-ceria ( $\text{Sm}_{0.2}\text{Ce}_{0.8}\text{O}_{1.9}$ )	SDC	KIT-6-36	$\text{Sm}(\text{NO}_3)_3 \cdot 6\text{H}_2\text{O}$ $\text{Ce}(\text{NO}_3)_3 \cdot 6\text{H}_2\text{O}$	Chapter 3 section 3.2.2
Gadolinium-doped-ceria ( $\text{Ce}_{0.8}\text{Gd}_{0.2}\text{O}_{1.9}$ )	CGO	KIT-6- commercial	$\text{Gd}(\text{NO}_3)_3 \cdot 6\text{H}_2\text{O}$ $\text{Ce}(\text{NO}_3)_3 \cdot 6\text{H}_2\text{O}$	Chapter 3 section 3.2.3
Nickel oxide (NiO)	NiO	KIT-6-90	$\text{Ni}(\text{NO}_3)_2 \cdot 6\text{H}_2\text{O}$	Chapter 3 section 3.2.4

**Table 2.1:** Information for the synthesis of metal oxide mesoporous materials and dedicated section in the present document.

### 2.3. Fabrication of mesoporous electrodes

This thesis presents the fabrication of SOEC electrodes based on mesoporous materials. The Ni-SDC material for fabricated fuel electrodes was synthesised by impregnation. The functional layer of oxygen electrodes was fabricated by infiltration of sintered mesoporous materials. Both techniques are presented in this section.

#### 2.3.1. Impregnation for the fabrication of NiO-SDC fuel electrodes

As it has been already explained, KIT-6 is composed of two sets of mesopores. The applied hydrothermal temperature during the synthesis allows changing the pore size values and its proportion. Both sets of pores are filled during the same infiltration procedure only when the KIT-6 template has been synthesised at high temperature. In this case, micropores growth connecting both sets of pores.

The impregnation approach consists on using the synthesised mesoporous oxide (i.e. NiO) as template to generate a replica of a second material (i.e. SDC or CGO) on the remaining empty set of mesopores. As consequence, a mesoporous cermet is generated. In this thesis, NiO mesoporous metal oxide was impregnated with SDC in order to form a NiO-SDC mesoporous cermet (**Figure 2.4**) to be used as fuel electrode in SOEC devices. Synthesised mesoporous NiO was used as template for applying the hard-template method impregnating it with  $\text{Sm}(\text{NO}_3)_3 \cdot 6\text{H}_2\text{O}$  and  $\text{Ce}(\text{NO}_3)_3 \cdot 6\text{H}_2\text{O}$  as precursors of the SDC phase. Changing the ratio between NiO powder and SDC

precursors between 50:50 (wt%) and 65:35 (wt%), different NiO:SDC cermet were synthesised and will be referred in the text as NiO-SDC(50) and NiO-SDC(65) respectively. This process starts with the dissolution of the nitrates precursors in ethanol and its mixture with mesoporous NiO stoichiometrically added. After 2 hours of stirring, the resulting mixture was dried for 5 hours at 60 °C. Lately, a thermal treatment up to 900 °C for 5 hours was performed to crystallize the ceramic SDC inside the NiO template, and it is obtained a mesoporous NiO-SDC cermet.

The two obtained cermet powders were synthesised for fabricating a bilayer fuel electrode composed by a functional layer close to the electrolyte using NiO-SDC(50), and a thicker layer next to the current collector employing NiO-SDC(65). This double layer was fabricated for improving the ionic and electronic conductivity, and hence the TPB density, along the fuel electrode; as well as for decreasing the fuel electrode polarization resistance. Specifically, NiO-SDC(50) is expected to result in an improvement of oxygen ions collection and distribution along the fuel electrode, and NiO-SDC(65) to favour electrons circulation. This fuel electrode was fabricated on electrolyte-supported cells, what is presented on **section 2.5.2** of this chapter. The structural and electrochemical characterization of these materials are presented in **chapter 3**.

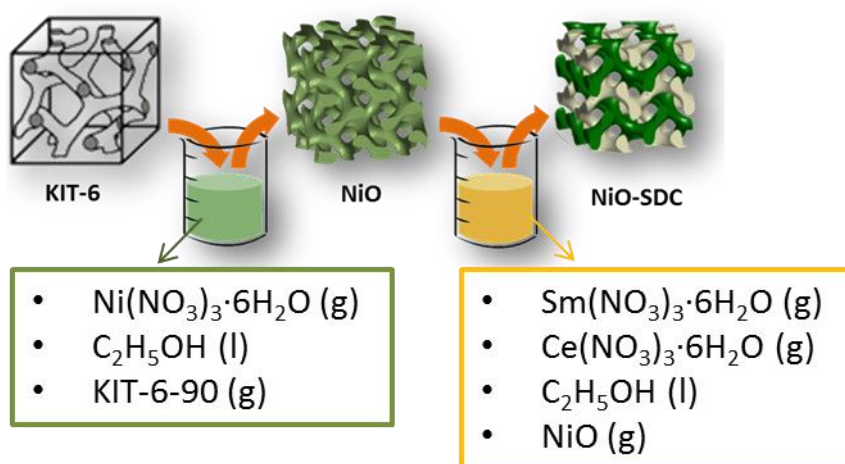


**Figure 2.4:** Scheme of the synthesis of NiO-SDC mesoporous composite material by impregnation.

### 2.3.2. Infiltration process for the fabrication of oxygen electrodes

Once SDC and CGO mesoporous materials were deposited on the cell, the functionalization of the material as oxygen electrode was achieved through its

infiltration with  $(\text{Sm}_{0.5}\text{Sr}_{0.5}\text{CoO}_3)$  SSC and  $(\text{La}_{0.6}\text{Sr}_{0.4}\text{Co}_{0.2}\text{Fe}_{0.8}\text{O}_3)$  LSCF catalytic active solutions.

The infiltration process mainly consists in the introduction of a liquid solution composed by dissolved metal precursors (nitrates, sulfates, hydroxides) into a porous backbone, drying the solvent of the solution, and a final calcination step with the aim of forming the desired oxide phase [12,13]. Specifically, that solution is composed by stoichiometric amounts of metal nitrates precursors, which are mixed with surfactants and complex agents with the aim of favouring cations group and the phase formation. Capillary forces dominate the displacement of the infiltration solution inside the porous backbone, and because of this reason, the solvent employed in the solution should ensure a proper wettability of the backbone. The last step consists in performing a thermal treatment that results in the formation of particles or a continuous thin film on top of the backbone, as it is showed in **Figure 2.5**.

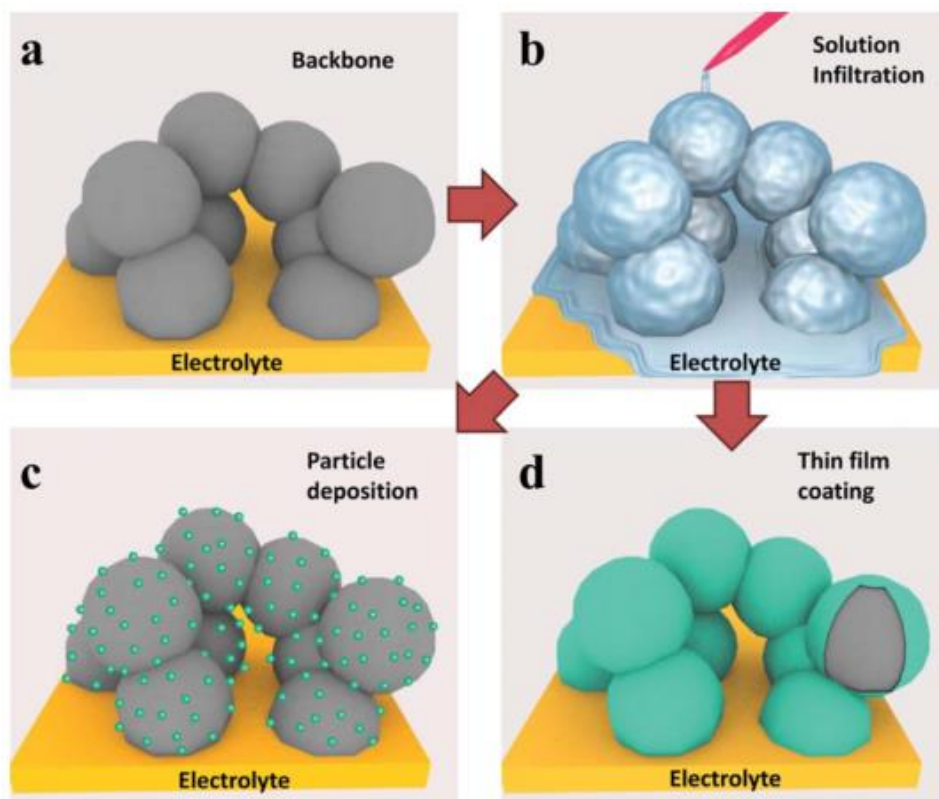


**Figure 2.5:** Scheme of a typical infiltration process : a) a deposited and sintered electrode backbone; b) an infiltration solution covering the backbone; two typical morphologies of infiltrated electrode can result from the thermal treatment : c) particle deposition and d) thin film coating [12].

Further details about the performed fabrication procedure for the fabrication of mesoporous materials are described in the next **section 2.4.4**.

## Cobalt as sintering aid for mesoporous materials

One of the main problems related to the fabrication of electrodes based on mesoporous materials is related to sintering those materials to the substrate. In order to overcome this issue, cobalt (Co) was introduced for making easier the sintering of the mesoporous scaffold. Specifically, the impregnation of Co on the mesoporous scaffold minimizes the sintering temperature required for achieving a good attachment of the scaffold, what is especially interesting for the fabrication of SOEC oxygen electrodes based on mesoporous materials. Applying the hard-template method described in **section 2.2.3**, synthesised mesoporous SDC was impregnated with cobalt nitrate ( $\text{Co}(\text{NO}_3)_3 \cdot 6\text{H}_2\text{O}$ ). 2% molar of  $\text{Co}(\text{NO}_3)_3 \cdot 6\text{H}_2\text{O}$  nitrate was solved in ethanol to favour the impregnation of the mesoporous SDC, and after a thermal treatment at 600 °C for 5 h, it was obtained the impregnated compound from now denoted as SDC-Co. Lately, this SDC-Co scaffold was infiltrated with SSC Mixed Ionic and Electronic Conductor (MIEC) in order to functionalize it as SOEC oxygen electrode. A series of electrolyte-supported symmetrical cells were prepared for testing and optimizing the ceramic scaffold and its sintering temperature to the cell support, and they are presented in next **section 3.4**.

### **2.4. Cells fabrication techniques**

This section explains the techniques and details the specific conditions that were applied for the fabrication of the cells tested during this thesis.

#### **2.4.1. Tape casting**

The tape casting technique allows obtaining extensive, flat and thin ceramic tapes. The tapes are formed by using the so-called “doctor blade” deposition technique of a slurry prepared by mixing different proportions of the ceramic materials, water or organic solvents, a dispersant, a binder and a plasticizer. The adjustment of the blade-substrate gap, which is the distance between the blade and the substrate, determines the thickness of the extended tape when the “doctor blade” advances along the substrate. This tape casted layer is dried to evaporate the solvents. Finally, the green tape, which is typically flexible, is cut to the desired shape and sintered to produce a ceramic layer.

In this thesis, this technique is applied for the fabrication of both 6Yb4ScSZ electrolyte supports for electrolyte-supported cells, and the Ni-YSZ fuel electrode/YSZ electrolyte bi-layer for fuel electrode-supported cells. The fabrication was carried out by the companies FAE S.A.U. (Spain) [14] (**Figure 2.6**) and HTceramix (Switzerland) [15], respectively.

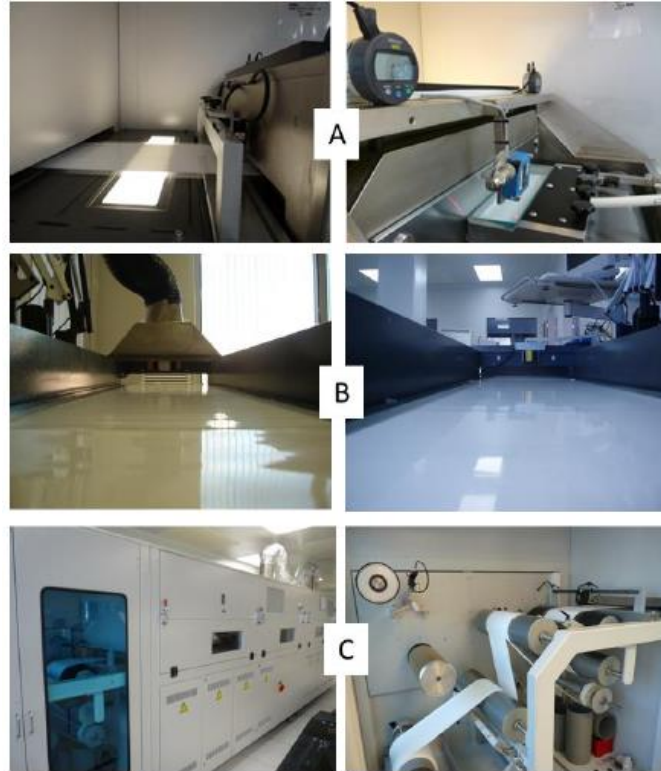


**Figure 2.6:** Tape casting equipment located at FAE S.A.U. (Spain). (a) Deposition of the slurry on a substrate employing a doctor blade, (b) drying of the tape, (c) rolling of the tape for its storage [14].

#### 2.4.2. Pulsed Laser Deposition (PLD)

The pulsed laser deposition is a physical vapor technique used for the deposition of high quality thin films of solid materials with a crystalline structure obtained at much lower temperatures than the typical crystallization process under equilibrium. It uses a high-energy pulsed laser as an external power source to melt, evaporate and ionize material from the target (see insert **Figure 2.7**). A system of lens and mirrors are aligned for directing the laser beam to the target material, which is inside a high vacuum chamber. This substrate can be heated to enhance the crystallization process. The ablation produces a plasma plume and the material is deposited as a thin film on the substrate. A picture of the PLD equipment located at IREC and used along this thesis is presented in **Figure 2.7**.

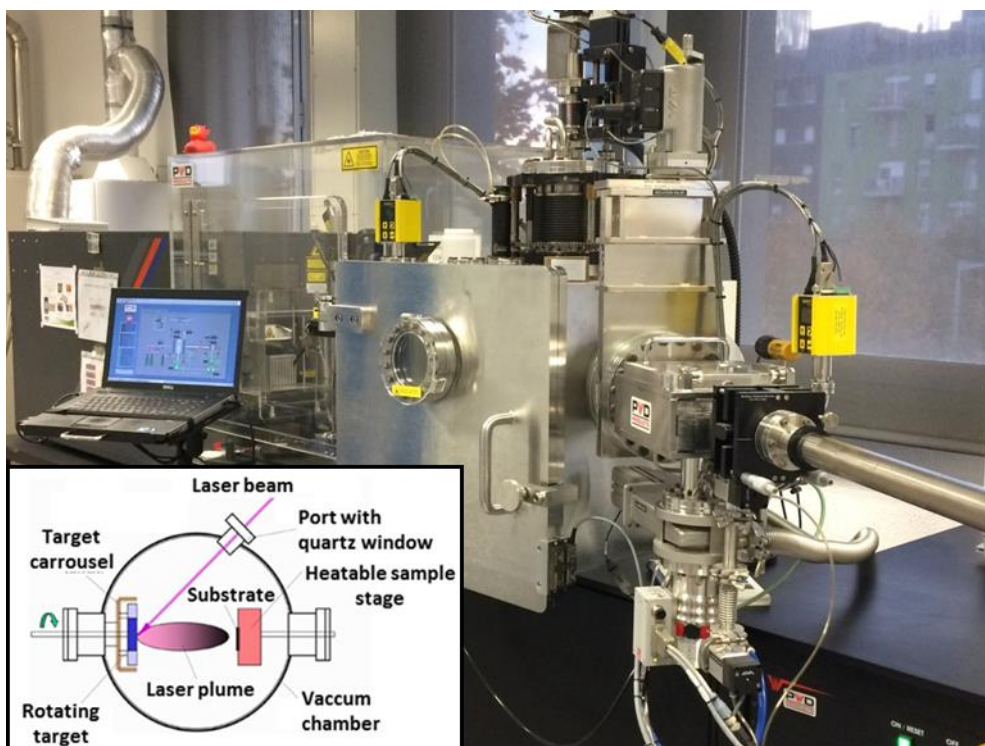


**Figure 2.7:** PLD equipment located at IREC and used for the deposit of CGO barrier layers. The inset is a scheme of the PLD set-up.

In this thesis, PLD was used for the deposition of dense and thin CGO barrier layers films in the interface between the electrolyte and the oxygen electrode. As explained in the introduction of this thesis, CGO interlayers are deposited for avoiding the reactivity between both compounds, what leads to the formation of insulating phases. Since this problem comes from the reaction between Sr of oxygen electrode materials and Zr of electrolytes, mainly forming the insulating  $\text{SrZrO}_3$  [16-18], this barrier layer was growth in both sides of electrolyte-supported symmetrical oxygen electrode cells and on the oxygen electrode side of the electrolyte and fuel electrode-supported SOEC, as it is presented in next sections of this chapter.

The equipment used is a PLD5000 from PVD Products (**Figure 2.7**). In the PLD chamber, the CGO target was irradiated with a KrF excimer laser with a characteristic 248 nm-wavelength and a typical laser density of  $0.075 \text{ J/cm}^2$ . The laser beam pulses with a frequency of 10 Hz at 20 mT in  $10 \text{ cm}^3$  of  $\text{O}_2$  atmosphere. The substrate was located at a distance of 9 cm from the target. A CGO barrier layer of ca.  $2 \mu\text{m}$  in thickness was deposited at  $100 \text{ }^\circ\text{C}$  for electrolyte-supported symmetrical cells and electrolyte-supported SOEC. After optimizing parameters for the PLD deposition of this layer, the  $2 \mu\text{m}$ -thick CGO barrier layer was deposited at  $100 \text{ }^\circ\text{C}$  and later at  $600 \text{ }^\circ\text{C}$  for

fuel electrode-supported cells, and a post-deposition thermal treatment was performed up to 1350 °C for 5 h for the densification of the deposited CGO barrier layer.

### 2.4.3. Air brushing technique

The air brushing technique is a method of deposition commonly used for the fabrication of porous electrodes in Solid Oxide Cells (SOCs) in planar surfaces or tubes [19-21]. In this thesis, the air brushing technique was employed for the deposition of powder material on both sides of the electrolyte with the aim of fabricating different layers.

Commercial materials or synthesised mesoporous ones were used for the preparation of different inks based on ethanol. Polyvinyl Pyrrolidone (PVP) was added (1% wt.) as powder dispersant in each prepared ink. The resulting mixture was stirred until it is completely mixed. Different parameters were controlled during the air brushing to get reproducible deposition of materials and hence, reproducible electrodes. The air pressure was fixed at 2 bar, 20 cm was the distance kept between the aerograph and the substrate to be deposited, the temperature of the sample holder was fixed at 70 °C in order to ensure the ethanol evaporation before arriving to the substrate, and the amount of material was maintained constant for each deposited layer.

Deposited thicknesses for different materials were controlled and monitored by studying the difference on the weight of the substrate before and after the deposition of different number of layers. Following this approach, different layers of the final devices were deposited: the roughness layer of CGO (<1 µm), the SDC or CGO scaffold of the functional layer (10-12 µm), and the SSC and LSCF electrodes layers; both composing the oxygen electrodes.

Both manual and automated sprayers have been used in this thesis. The automated spray-coater consists of 3 axis (x, y and z) automatically controlled within a 3D printing frame (Print3D Solutions) [22], which ensures the reproducibility of the layers (**Figure 2.8b**). The temperature of the substrate-holder where the sample is located during the deposition can be controlled, typically being fixed at 50 °C. The pressure supplied to

the air brush is fixed at 2.5 bar, for a nozzle hole diameter of 0.6 mm. Finally, the airbrusher distance to the substrate is maintained at 8.5 cm.

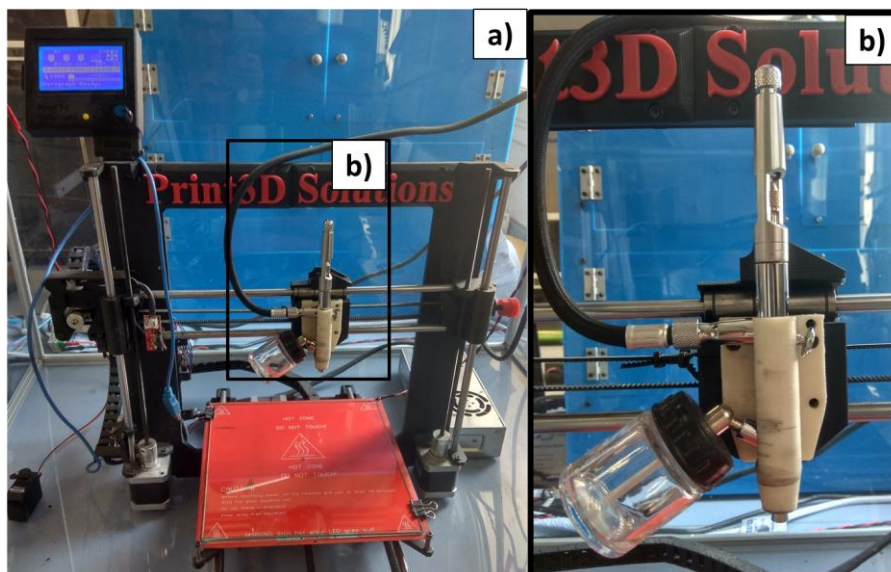


**Figure 2.7:** a) 3 axis automatic air brushing equipment employed for the deposition of electrode layers. b) Zoom showing the air brusher.

#### 2.4.4. Infiltration technique

As indicated in the previous section, the infiltration technique was applied in this thesis for the fabrication of oxygen-electrode mesoporous materials. The application of infiltration for the fabrication of SOCs electrodes results on an enhancement of the electrode activity and stability and an improvement of the cell performance [23,24]. This is due to the modifications introduced on the surface of the materials where the infiltration is done and allows controlling the backbone/infiltrate resulting morphology.

The main advantages of surface modification of electrodes through infiltration have been extensively described in the literature and summarized in the following lines [12,13,25]. First, it is an effective approach for enhancing electro-catalytic activity and improving the stability of the electrodes. Second, it allows using a wide variety of active materials that cannot be used applying a conventional electrode fabrication process due to its high reactivity with other cell components. In this sense, both the backbone and the infiltrate materials compatibility should prevent the formation of undesirable secondary phases. Since infiltration requires much less material compared

to the standard electrode fabrication process, the infiltrated material can be fired at lower temperatures to form the desired phase.

In this thesis, two infiltration solutions to form the SSC and LSCF pure phases have been prepared for the infiltration of SDC and CGO synthesised mesoporous backbones. Stoichiometric amount of the nitrate precursors is mixed in a mixture of water and ethanol to form a 0.1 M solution. To control the exact amount of infiltration solution a micropipette (LLG micropipette/10-100  $\mu\text{L}$ ) was used. **Table 2.2** indicates the precursors employed for the preparation of each infiltration solution, as well as the sections with the characterization of the resulting composites. Besides, a stoichiometric amount of glycine as complexing agent and 1 % of PVP over the total weight is added as surfactant.

Infiltration solution	Acronym	Precursors	Dedicated section
$\text{Sm}_{0.5}\text{Sr}_{0.5}\text{CoO}_3$	SSC	$\text{Sm}(\text{NO}_3)_3 \cdot 6\text{H}_2\text{O}$ $\text{Sr}(\text{NO}_3)_2 \cdot 6\text{H}_2\text{O}$ $\text{Co}(\text{NO}_3)_2 \cdot 6\text{H}_2\text{O}$	Chapter 3 section 3.3.1
$\text{La}_{0.6}\text{Sr}_{0.4}\text{Co}_{0.2}\text{Fe}_{0.8}\text{O}_3$	LSCF	$\text{La}(\text{NO}_3)_3 \cdot 6\text{H}_2\text{O}$ $\text{Sr}(\text{NO}_3)_2$ $\text{Co}(\text{NO}_3)_2 \cdot 6\text{H}_2\text{O}$ $\text{Fe}(\text{NO}_3)_2$	Chapter 3 section 3.3.2

**Table 2.2:** Information of the solutions prepared for the infiltration of mesoporous materials and dedicated section for the nanocomposite characterization in this thesis.

After each step of infiltration, a calcination step is performed. In the first and the second step the thermal treatment raises up to 500  $^{\circ}\text{C}$  for 30 minutes each. In the third step, this thermal treatment is repeated, and another ramp is added for raising the temperature up to 800  $^{\circ}\text{C}$  for 3 h. The thermal treatment up to 500  $^{\circ}\text{C}$  is performed to eliminate the nitrates from the precursors and facilitate cations diffusion inside the pores of the mesoporous backbone. In the last step, the maximum temperature of the thermal treatment temperature is increased to 800  $^{\circ}\text{C}$  in order to achieve the formation of the desired crystalline SSC or LSCF phase. The characterization of infiltrated mesoporous materials is presented in **chapter 3** of this thesis.

## 2.5. Fabrication of Solid Oxide Electrolysis Cells (SOECs)

This section presents the procedures followed for the fabrication of the different tested cells all along this thesis.

### 2.5.1. Symmetrical cells of oxygen electrodes

Symmetrical cells were prepared and electrochemically tested for optimizing the oxygen electrode fabrication procedure. Specifically, cells based on different mesoporous scaffolds and sintering temperatures were fabricated.

6Yb4ScSZ electrolyte-supported cells of 200  $\mu\text{m}$  in thickness (fabricated by FAE S.A.U. [14]) and 2 cm of diameter were employed for the fabrication and test of oxygen electrode symmetrical cells.

CGO barrier layers of around 2  $\mu\text{m}$  were deposited at 100  $^{\circ}\text{C}$  on both sides of the cell for avoiding the formation of  $\text{SrZrO}_3$  insulating phases, as it has been previously explained. Lately, a thin layer of bulk CGO was airbrushed on top of the barrier layer for creating roughness on the surface, and in consequence, facilitate the attachment of the mesoporous scaffold. This roughness layer was sintered in a thermal treatment at 1350  $^{\circ}\text{C}$  for 2 h.

Afterwards, two different mesoporous scaffolds were deposited and infiltrated for constituting the oxygen electrode functional layer. Specifically, mesoporous samarium-doped-ceria and SDC impregnated with 2% molar of cobalt (SDC-Co) scaffolds, were alternative deposited as ionic conductive paths on the oxygen electrode side of different cells, and sintered at 800, 900 and 1000  $^{\circ}\text{C}$ . The cobalt was added as sintering aid to decrease the sintering temperature of the mesoporous powder to the barrier layer while keeping its structure. The scaffolds were infiltrated and sintered at 800  $^{\circ}\text{C}$  to form SSC nanoparticles on the surface of the backbone. Finally, SSC

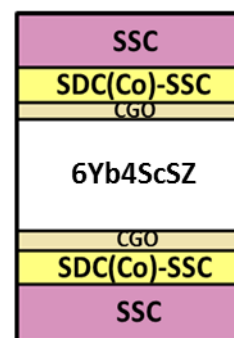


**Figure 2.9:** Scheme of the configuration of an electrolyte-supported symmetrical SOEC based on SDC and SDC-Co mesoporous materials.

layers were airbrushed on top of the infiltrated scaffold for sintering at 900  $^{\circ}\text{C}$  for 5h, resulting on SDC-SSC and SDC-Co-SSC oxygen electrodes. **Figure 2.9** presents a scheme of the resulting symmetrical cells configuration. The electrochemical characterization

of this series of electrolyte-supported symmetrical cells is presented in **section 3.4** of this thesis.

### **2.5.2. Electrolyte-supported SOECs**

Once oxygen electrodes were optimized, which are critical for SOEC operation, the first generation of electrolysis cells based on mesoporous materials were fabricated for being tested under real operation conditions. The procedure performed for the fabrication of those cells is presented as follows.

The same 6Yb4ScSZ electrolyte supports of 2 cm of diameter used for the preparation and test of symmetrical cells were tested as electrolyzers at high temperature. Following the same procedure as it has been described in the previous section, a CGO barrier layer (2  $\mu\text{m}$ ) was deposited on the interface between the electrolyte and the oxygen electrode. The fuel electrode based on mesoporous NiO impregnated with SDC mesoporous material was composed of two layers. A first functional layer of NiO-SDC(50) and a second current collector layer of NiO-SDC(65). The functional layer presents higher proportion of the SDC ionic conductor to avoid thermal expansion mismatches at the operation and fabrication temperatures, enhance oxide-ion collection from the electrolyte interfaces, and improve the ionic phase distribution at the interface, increasing active TPB points. The NiO-SDC(65), with higher proportion of nickel, was deposited on top of the functional layer increasing the electronic conductivity and favouring the electrochemical reactions and the current collection. Both fuel electrode layers were consecutively deposited and sintered to the electrolyte applying a single thermal treatment up to 1200 °C for 2h. This NiO-SDC fuel electrode based on mesoporous material ensures a good connectivity between the ionic and electronic conductive phases in the interface with the electrolyte. The presence of SDC along the entire fuel electrode enlarges the active TPB active points and avoids the nickel agglomeration during operation. This material engineering solution for ensuring the percolation of both pathways also results on a homogeneous distribution of the current along the electrode, what decreases the fuel electrode polarization resistance and thus improve the fuel electrode performance; and ensures the stability of the nanostructure on long operation times.

A CGO roughness layer was also deposited on top of the CGO barrier layer, as it has been described for symmetrical cells in the previous section. According to the obtained results from the optimization of oxygen electrodes based on mesoporous materials, synthesised SDC mesoporous backbones were sintered at 900 °C for 5h. After three infiltration steps with thermal treatments up to 800 °C, the MIEC SSC phase was formed, resulting in a SDC-SSC oxygen electrode functional layer. The SSC electrode layer was also deposited and sintered at 900 °C according with the conditions described in the previous section. **Figure 2.10** shows a scheme of the main steps for the fabrication of the oxygen electrode, which is made of a SDC-SSC functional layer and a SSC electrode layer. The electrochemical characterization of these fabricated cells is presented in **section 3.5** of this thesis.

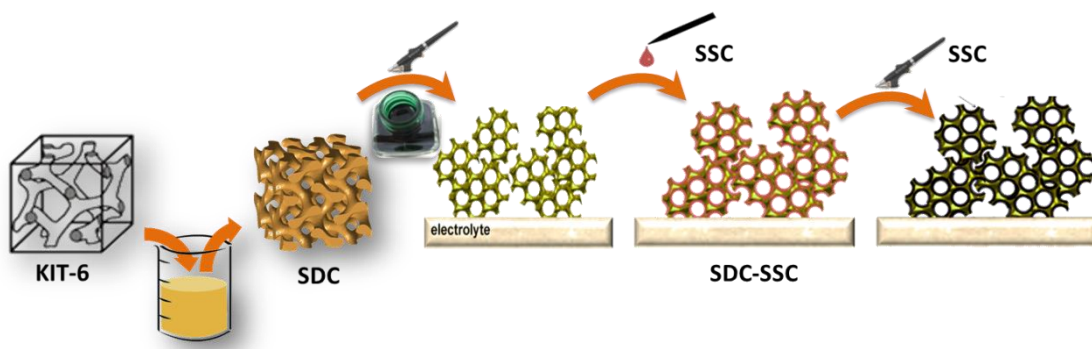


**Figure 2.10** : Scheme of the fabrication process of the oxygen electrode.

A scheme of the final configuration of the fabricated electrolyte-supported SOECs is represented in **Figure 2.11** once both electrodes were deposited.

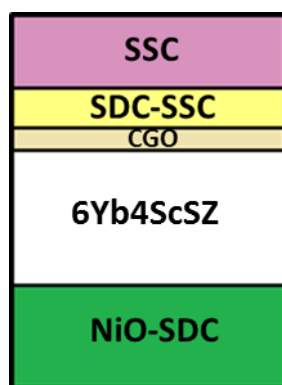


**Figure 2.11**: Scheme of the configuration of an electrolyte-supported SOEC with electrodes based on mesoporous materials.

### 2.5.3. Fuel electrode-supported SOECs

Besides the ESC, the main part of the presented work has been performed using fuel electrode-supported cells. The fabrication of these cells is described in the following. Fuel electrode supports of NiO-YSZ (300  $\mu\text{m}$  in thickness) and YSZ electrolyte of 7  $\mu\text{m}$  were provided by HTceramix (Switzerland) [15] in the frame of the H2020 European ECo project (grant agreement no. 699892). In the frame of the project and this thesis, two different sized cells have been tested with this configuration (**Figure 2.12**): button cells of 2 cm of diameter (1.54  $\text{cm}^2$  of active area) and square cells of 5x5  $\text{cm}^2$  (16  $\text{cm}^2$  of active area).

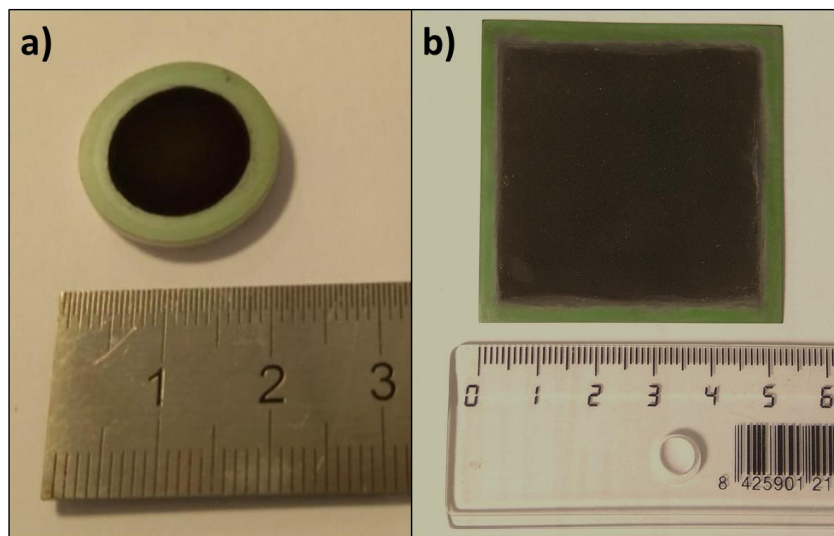


**Figure 2.12:** Fuel electrode-supported cells a) circular button cell of 1.54  $\text{cm}^2$  and b) square cell of 16  $\text{cm}^2$ .

For button fuel electrode-supported half cells, the first required step was the deposition of the CGO barrier layer. This layer was deposited at 600  $^{\circ}\text{C}$  by PLD, and a post-thermal treatment up to 1150  $^{\circ}\text{C}$  was performed for its densification. The roughness of the CGO layers and the oxygen electrode were deposited following the procedure described in **section 2.4.3**. Two different composites, SDC-SSC and CGO-LSCF, were tested as oxygen electrodes for this fuel electrode-supported cell configuration. Synthesised mesoporous SDC and CGO were deposited forming layers of 10-12  $\mu\text{m}$ , which were sintered at 900  $^{\circ}\text{C}$  for 5h. Its infiltration, for the formation of SSC and LSCF phases, respectively, was achieved with a thermal treatment up to 800  $^{\circ}\text{C}$ . Additionally, SSC and LSCF electrodes layers were air brushed using respective bulk material inks based in ethanol. As for the SSC electrode layer deposited for

symmetrical cells, this layer was sintered at 900 °C for 5 h. The electrochemical characterization and its discussion is presented in the **chapter 4** of this thesis.

The CGO barrier layer of the 5x5 cm<sup>2</sup> square cells was deposited by screen printing at HTceramix (Switzerland) [15]. The deposition of different powder materials by the air brushing technique was performed employing the already described 3-axis automatic spray-coater. For these cells, the oxygen electrode functional layer was fabricated through the infiltration of the CGO mesoporous backbone with LSCF, resulting in Ni-YSZ/YSZ/CGO<sub>bl</sub>/CGO-LSCF/LSCF electrolyser cell. The results and discussion regarding these measurements are presented in **chapter 6** of this work.

## 2.6. Structural Characterization Techniques

Different techniques employed for the structural characterization of the used materials and the tested samples are briefly explained and described in this section.

### 2.6.1. X-Ray Diffraction (XRD)

X-Ray diffraction (XRD) is a non-destructive characterization technique commonly used in crystallography for compositional analysis and phase identification of crystalline materials, including powders, pellets and thin films. When the wavelength radiation is comparable to the interatomic distances of a crystal, the Bragg diffraction results in constructive interferences (**Figure 2.13**). The constructive or destructive interference is intensified by the scattering of the crystallographic plane of the material under study, resulting in a characteristic pattern of the crystal. The Bragg's law equation (**2.1**) is:

$$n \lambda = 2d \sin \vartheta \quad (2.1)$$

where  $n$  is an integer,  $\lambda$  is the wavelength of the incident radiation,  $d$  is the distance between atomic layers and  $\vartheta$  represents the angle of incidence of the wavelength. The analysis of the generated pattern allows identifying the characteristic crystalline phase and determining the lattice parameter of the crystal.

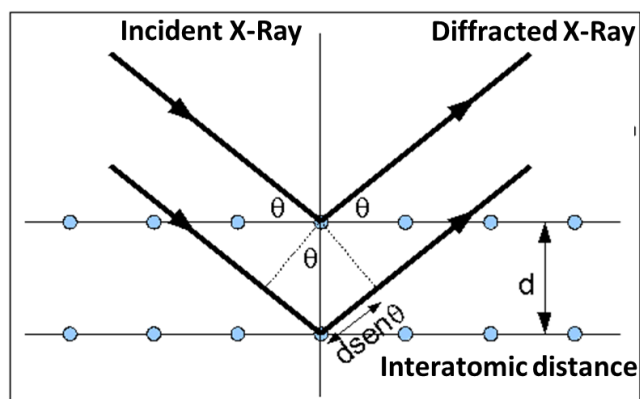


**Figure 2.13:** Scheme of the Bragg's law.

This technique was used in this work to identify and corroborate the phase of all the synthesised and prepared materials. The equipment used is located at IREC (**Figure 2.14**). It is a Bruker-D8 Advance using copper  $K_{\alpha}$  radiation with a nickel filter and Lynxeye 1D detector. The measurements were performed at room temperature in flat plate geometry in the range from 20 to 90° of  $2\theta$ .

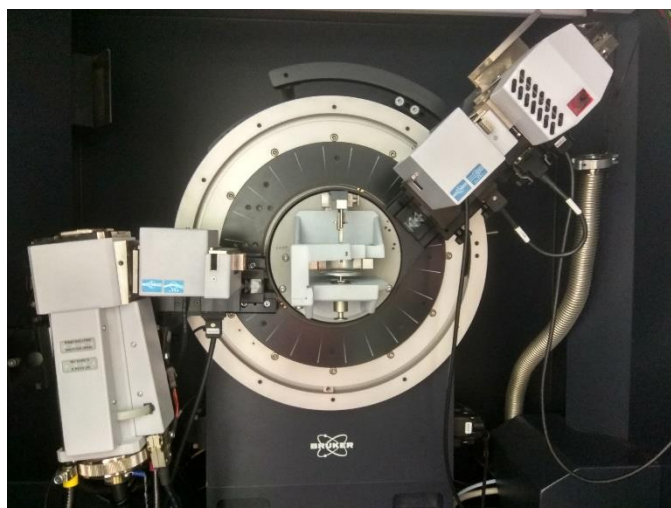


**Figure 2.14:** X-ray diffraction equipment located at IREC.

#### **2.6.1.1. In-situ powder X-Ray Diffraction vs. Temperature**

In-situ XRD is a technique that acquires XRD pattern of the same sample at different temperatures, allowing the observation of the structural evolution of a material with time, specifically, the study of changes or crystallization of the phases. This technique allows obtaining the different XRD pattern of a sample in one experiment, saving time respect the analysis of series of samples annealed individually, and avoids quenching steps for freeze the high temperature phases.

The same XRD equipment (Bruker-D8 Advance) coupled to a furnace-type heater, Anton Paar XRK 900, has been used from room temperature to 850 °C. The powder has been heated up to 850 °C in atmospheric pressure. A diffractogram has been recorded at room temperature at the beginning of the experiment, at 500 °C, from it each 50 °C up to 850 °C, and reversibility when cooling down to room temperature. The experiment consisting in the observation of the evolution of both SDC and SSC phases from synthesised mesoporous SDC powder infiltrated by SSC. It has been concluded from this experiments that both phases are stables and any secondary phase is formed at the fabrication and operation temperatures.

#### **2.6.1.2. Low Angle X-ray Diffraction (LA-XRD)**

Low angle X-ray diffraction (LA-XRD) is a non-destructive technique, usually performed at angles between 0° and 10°. It follows the same principles of X-ray diffraction, in this case for investigating nanostructures from < 1 nm up to 200 nm in size. Therefore, the structure and space group symmetry of the ordered mesoporous materials are detected.

LA-XRD has been employed in this thesis for studying the periodicity of the mesoporous structure of SDC, CGO and NiO synthesised materials. Besides, lattice parameters of mesoporous materials have been calculated applying Bragg's law (**section 2.6.1**). The equipment used was Expert-Pro Diffractometer (Cu-K $\alpha$ 1 and Cu-K $\alpha$ 2 radiation). The measurements were performed in a  $2\theta$  range between 0.2° and 5°, where the periodicity of the mesoporous structure can be detected due to lattice parameters in the range of the tens of nm.

#### **2.6.2. Nitrogen physisorption measurements and BET method**

Gas adsorption measurements are used for determining the surface area and pore size distribution of solid materials [26]. The Brunauer-Emmett-Teller (BET) gas adsorption method is the standard procedure most used for the determination of the surface area and/or porosity of porous materials. Nitrogen (N<sub>2</sub>) is the preferred gas as adsorptive for the surface area determination. Langmuir work was based on monolayer adsorption. That model was adapted to highly porous adsorbents and it constitutes the base of the BET method [27]. The pore size distribution is the

dispersion of pore volume with respect to pore size. The most popular method for deriving the pore size distribution from an appropriate nitrogen isotherm is the Barrett, Joyner and Halenda (BJH) method. In this thesis, the desorption isotherm is used for applying the BJH model.

According to the definitions, *adsorption* is defined as the enrichment of one or more components in an interfacial layer. Specifically, *physisorption* refers to an adsorbate gas brought into contact with the surface of a solid (the adsorbent). Pores determined by physisorption can be classified according to their sizes in macropores, mesopores and micropores. Mesopores present pores width between 2 and 50 nm, while pores of macropores materials are higher than 50 nm, and in micropores materials they are smaller than 2 nm. However, it is called *absorption* when the molecules of the adsorptive penetrate the surface layer and enter the structure of the solid.

The relation, at constant temperature, between the total gas adsorbed and the equilibrium pressure of the gas is plot as an *adsorption isotherm*. Each of the points constituting the isotherm curve represents the consecutive admission of gas by the adsorbent. When both the adsorption and desorption curves do not coincide, the area created in the middle of both isotherms is named *adsorption hysteresis*. As it has been previously indicated, applying the BET method to the recorded adsorption isotherm allows determining the surface area.

Physisorption in mesopores basically takes place in two steps: monolayer-multilayer adsorption and capillary condensation (**Figure 2.15**). Firstly, monolayer adsorption takes place at lower  $P/P_0$  relative pressure, where all the adsorbed molecules are in contact with the surface layer of the adsorbent. When the adsorption continues, not all the adsorbed molecules are in contact with the surface layer of the adsorbent and successive layers are formed (multilayer adsorption). The residual pore space which remains after multilayer adsorption is filled with condensate separated from the gas phase, taking place the capillary condensation.

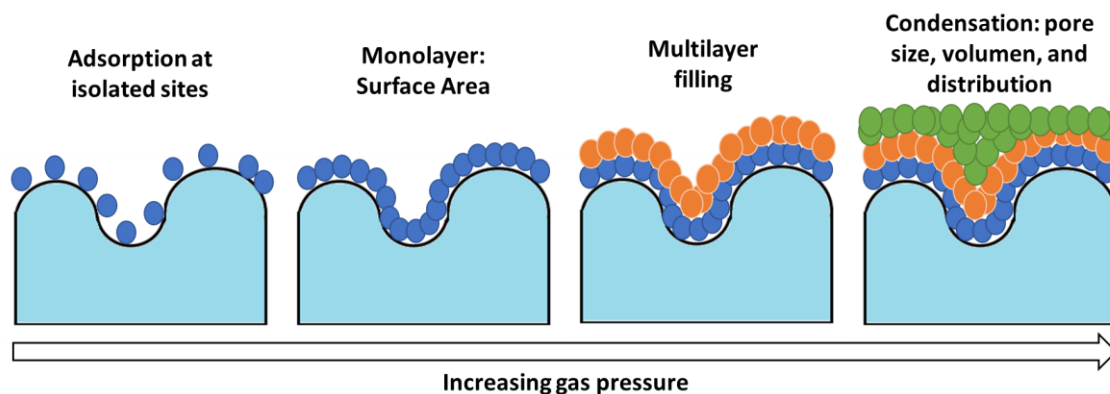


**Figure 2.15:** Scheme of the physisorption mechanism of a gas on a porous solid.

Physisorption isotherms may be classified into six types representative of different pores sizes in function of the resulting shape of the isotherm. Among them, the isotherm classified as Type IV is typically related to mesoporous materials since it presents a characteristic hysteresis loop, which is associated to the capillary condensation taking place in materials having pores width in this range (**Figure 2.16a**).

These hysteresis loops can present different shapes in function of different pores structures. In Type H1 both branches are almost vertical and parallel in a specific range of gas adsorption (**Figure 2.16b**). H1 is associated with porous materials consisting on agglomerates of uniform and ordered spheres with narrow distribution of pore size, and this is the hysteresis loop of the mesoporous materials characterized in this thesis.

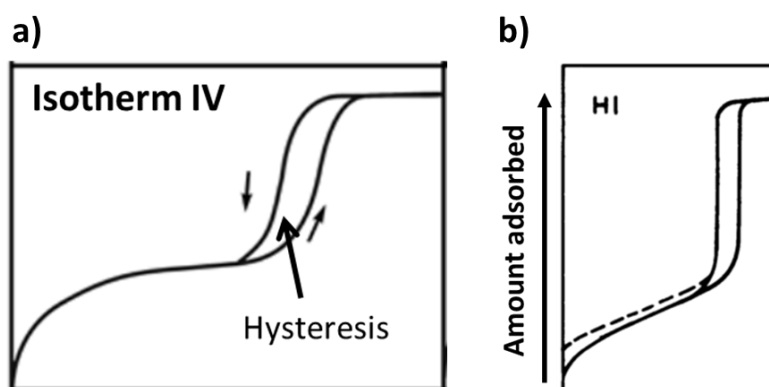


**Figure 2.16:** Scheme of (a) isotherm IV and (b) H1 hysteresis Type characteristic of mesoporous materials.

In this thesis,  $N_2$ -physisorption measurements were applied to mesoporous materials, which present pores width between 2 and 50 nm. The used equipment is a Micromeritics TriStar II 3020 surface analyser (**Figure 2.17**) at the temperature of liquid nitrogen (77 K) to study the surface area and the distribution of pores of the

synthesised and commercial mesoporous materials. The adsorption-desorption isotherms are plotted in this thesis for mesoporous materials.

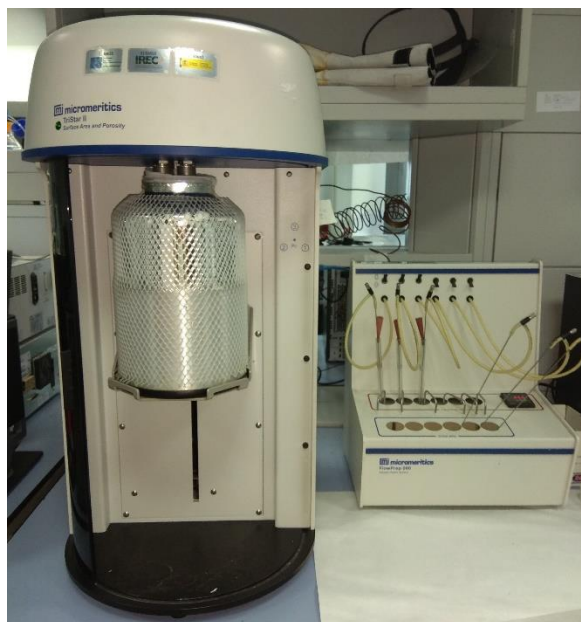


**Figure 2.17:** Equipment for performing N<sub>2</sub>-physisorption measurements located at IREC.

### **2.6.3. Scanning Electron Microscopy (SEM) and Energy Dispersion X-ray (EDX)**

Scanning Electron Microscopy (SEM) is one of the main electronic microscopy techniques used for the characterization of microstructures getting high resolution micrographs of surfaces and the cross-section of the fabricated samples.

The micrographs are generated by scanning a sample with a focused beam of high-energy electrons. The interaction of these electrons with the surface of the sample generates a variety of signals that are detected on their corresponding detectors, generating the micrographs. The beam of electrons which typically have energy from ~eV to keV is focused by a series of electromagnetic lenses to a spot size up to 1 nm. A scheme of a SEM set-up is shown in **Figure 2.18**.

Accelerated electrons impact with the sample and cause electrons to be scattered from the sample due to elastic or inelastic events. Low energy electrons resulting from inelastic scattering are secondary electrons and are detected by a Secondary Electron Detector (SE2) and it is the most common imaging mode. They are produced when the electron beam enters into it with different angles of incidence. Due to the low energy (< 50 eV) of these electrons, they are generated few nanometers from the surface of the sample and contain information about its morphology and topography. The InLens

detector of the SEM efficiently collects secondary electrons. This detector symmetrically rotates around the optical axis due to the existence of a magnetic field. It provides information about the morphology and surface topography. Specifically, this detector allows acquiring micrographs with high contrast at low voltages and small working distances. According to this, the InLens detector highlights and allows observing the electronic percolation path when metallic phases are part of the electrode, as in the case of Ni-SDC or Ni-YSZ fuel electrodes composites materials employed in this thesis. Backscattered electrons (BSE) are higher energy electrons produced by elastic scattering interactions with atoms. In particular, backscattered electrons are useful for identification of areas with different chemical composition since elements with different atomic number backscatter different. Finally, X-rays are produced by the interaction of the electrons with the sample, specifically, when the electron beam removes an inner shell electron of the sample, causing a higher energy electron to fill the shell and releasing energy. These characteristic X-rays are used to identify the composition and abundance of the elements of the sample. This specific detection is called Energy Dispersive X-Ray spectroscopy (EDX).

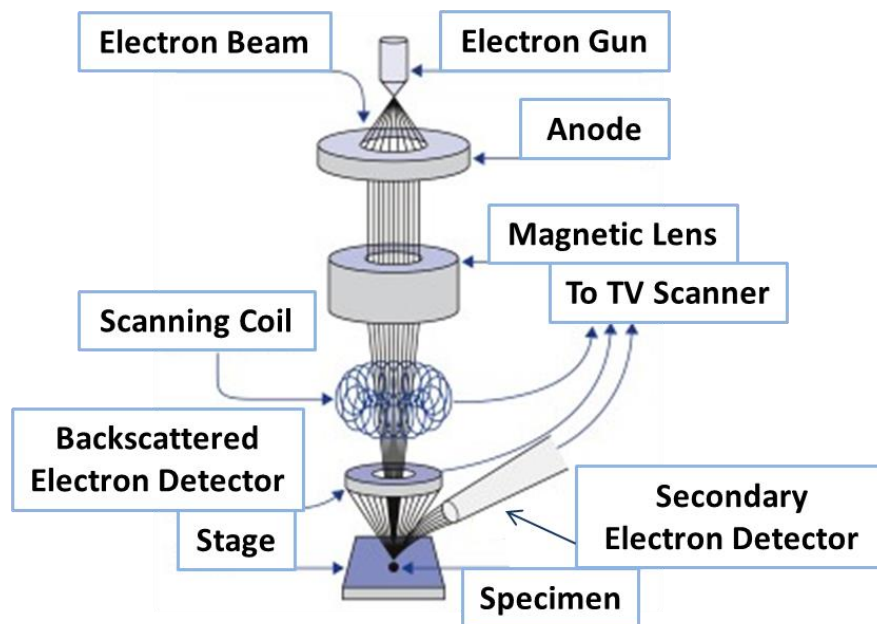


**Figure 2.18:** Scheme of the SEM set-up specifying the location of secondary and backscattered detectors in relation to the sample.

SEM has been routinely used in this thesis to investigate the morphology of the synthesised powders as well as the cross-section of electrolyser cells before and after the electrochemical characterization. The equipment located at IREC is a Carl ZEISS

Auriga scanning electron microscope with an EDX spectroscope (**Figure 2.19**). Furthermore, SEM coupled to EDX has been applied for obtaining mappings of the main elements involved in the oxygen electrode cross-section in order to validate the infiltration technique.



**Figure 2.19:** Scanning electron microscope coupled to EDX located at IREC.

#### **2.6.4. Transmission Electron Microscopy (TEM)**

Transmission Electron Microscopy (TEM) utilizes a beam of high-energy electrons. The micrograph is generated from the beam of electrons that are transmitted through a sample, magnified and usually focused onto a fluorescent screen or detected by CCD camera detector. A scheme of a TEM set-up is shown in **Figure 2.20**.

Two different types of imaging are possible depending on which electrons are collected. On one side, bright field micrographs are obtained when looking only at unscattered electrons. On the other side, the observation of those scattered electrons results on a dark field micrograph. The two types of imaging are complementary and are used depending on the information required. Much higher resolution and crystallographic information are obtained using TEM than using SEM.

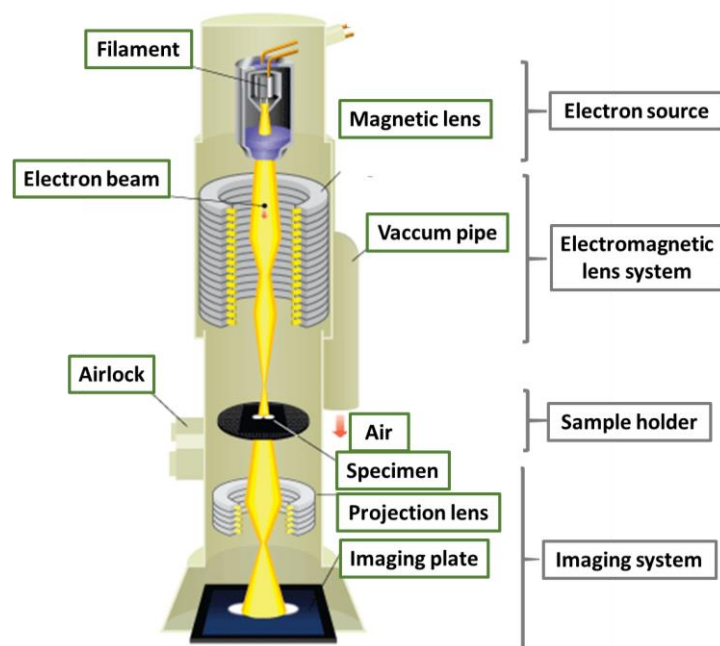


**Figure 2.20:** Scheme of the TEM set-up.

TEM has been used in this thesis for the structural characterization of the synthesised mesoporous material. Besides, this technique allows the determination of the pore size validating the results obtained by the pore size distribution from N<sub>2</sub>-physisorption measurements.

## 2.7. Electrochemical Characterization Techniques

The experimental set-ups employed for the electrochemical characterization of the prepared cells are described for button cells (1.54 cm<sup>2</sup>) and for square cells (25 cm<sup>2</sup>). Besides, I-V polarization curves and Electrochemical Impedance Spectroscopy (EIS) measurements, as well as, galvanostatic and polarization measurements were employed to measure the performance and determine the electrochemical processes involved under operation in our SOCs cells. A brief explanation of the set-ups and fundamentals of these techniques are presented in this section.

### 2.7.1. Electrochemical test stations for button and large area cells

As it has been already explained in **section 2.5.3**, two different cell configurations have been measured in this thesis: circular button cells of 2 cm of diameter and 1.54 cm<sup>2</sup> of active area, and square cells of 25 cm<sup>2</sup> (16 cm<sup>2</sup> of active area). Hence, two different set-ups have been used for their electrochemical characterization.

### **Button cells test station**

The set-up for the electrochemical characterization of circular SOEC cells is located at IREC and it is composed by (Figure 2.21):

- Button cell holder for electrochemical tests (Probostat)
- Tubular furnace
- Mass flow controllers and meters
- Steam generator and heated lines
- Potentiostat and Galvanostat for electrochemical measurements

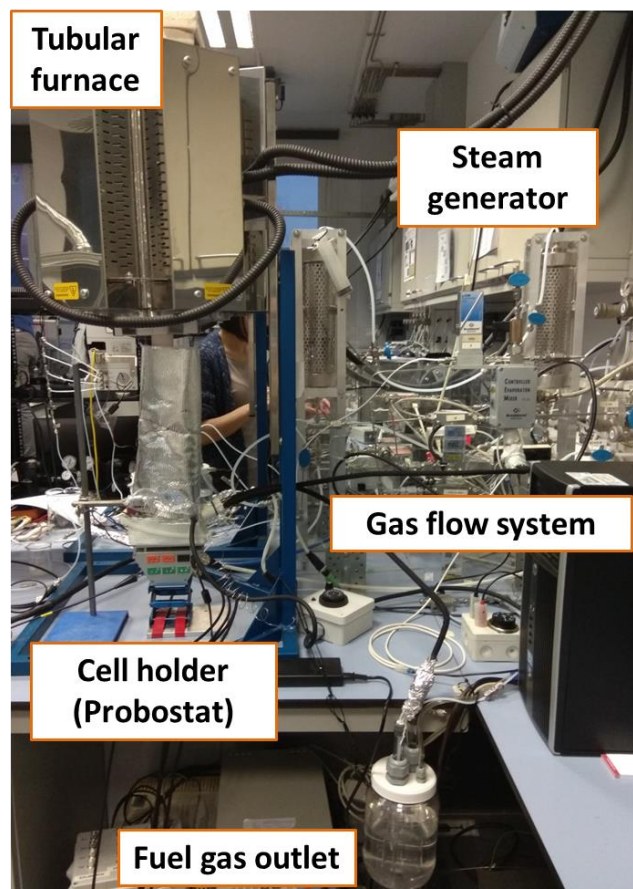


**Figure 2.21:** Experimental set-up for SOEC electrochemical characterization located at IREC.

A gas mixer system composed by different pipes and gas flow meters supplies gas with controlled composition to the test station. Specifically, steam is produced in a steam generator working at 120-140 °C using the water provided by a tank. Generated steam is conducted to the test station through heated lines for avoiding steam condensation. The ceramic sample holder used here is a ProboStat™ from NorECs (Figure 2.22) [28]. Platinum and gold wires and meshes have been used for contacting

the fuel and oxygen electrode, respectively. Gas tightness is mandatory since pure hydrogen is always included in the fuel electrode gas compositions. Ceramabond™ from Aremco has been used for sealing both electrodes atmospheres. During the electrochemical measurements, it is located in a tubular furnace working at the SOEC operation temperature range for the electrochemical characterization. The electrochemical measurements (both I-V curves and impedance measurements) are acquired using a potentiostat/galvanostat Parstat 2273 from PAR. A sealed tank with liquid water condensates gasses coming from the fuel electrode while the gasses from the oxygen electrode are directed to the general extraction of the laboratory. The electrochemical measurements have been controlled using different programs developed in Matlab at IREC.

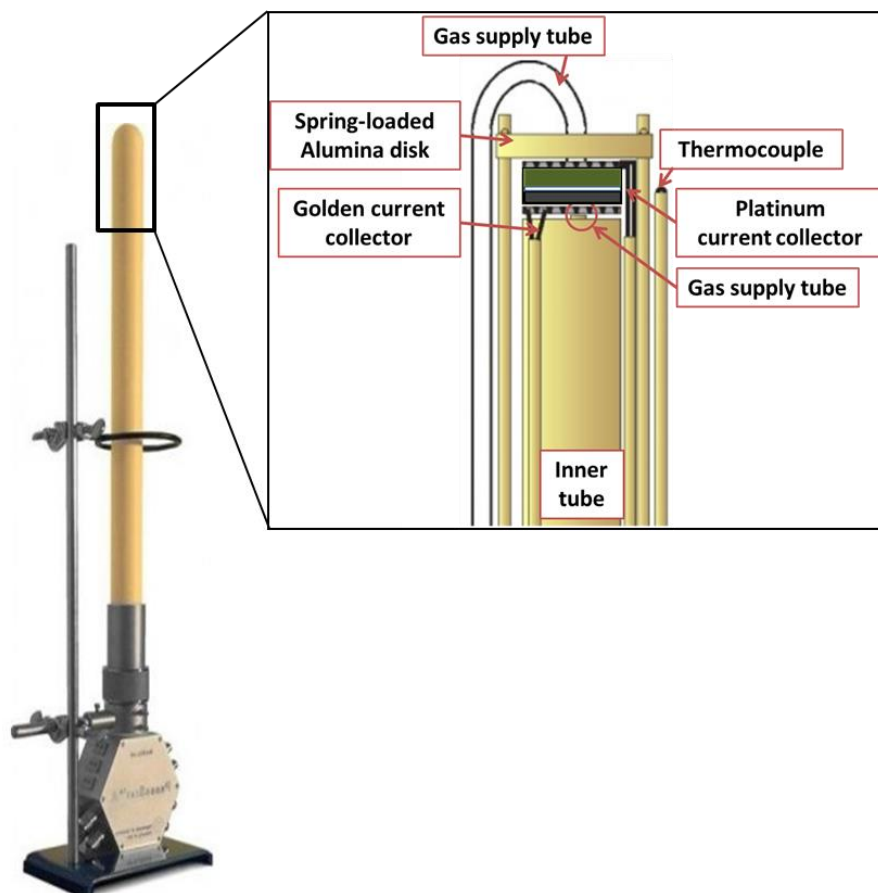


**Figure 2.22:** Sample holder ProboStat™ from NorECs and, scheme of the inner set-up including a fuel electrode-supported SOEC [28].

### **Large area cells**

Large area (5x5 cm<sup>2</sup>) fuel electrode-supported cells have been electrochemically characterized at Denmark Technical University (DTU) facilities. The experimental set-

up is located enclosed in a fume hood with uninterrupted ventilation, and it is composed by the following elements (**Figure 2.23**):

- Ceramic sample holder (**Figure 2.24**)
- Electrically heated furnace
- Steam generator and steam pipes
- Gas flow inlet system
- Electrical components for control and measurement, including mass flow controllers, power supply and Keithley multimeter for data acquisition
- Exhaust gas system
- Ventilation system

The software employed to automate and control the measurements have been specifically developed at DTU.

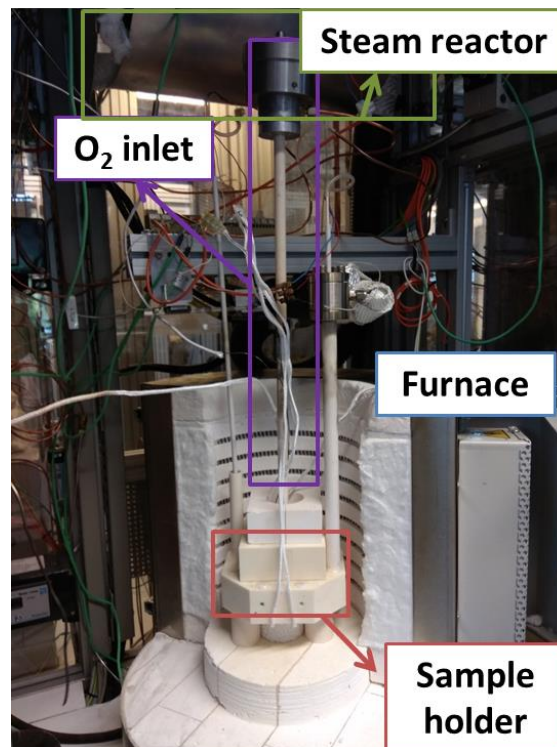


**Figure 2.23:** Set-up for electrochemical measurements of 5x5 cm<sup>2</sup> SOEC cells at DTU.

The assembly step is considered the most important step for the successful measurement of a sample. The sample holder is also home-made at DTU (**Figure 2.24a**). It is composed by a ceramic holder connected to two tubes: one for the fuel

electrode gas inlet and another for the fuel electrode gas outlet. The ceramic holder has a cavity of 0.7 mm depth where different materials are stacked. On the bottom there is platinum foil contacting two wires for the fuel electrode measurement and the fuel electrode of the cell. On top there are planar and corrugated nickel meshes as current collectors, both stacked. On the surface of that cavity, a gold ring is located as a sealant (Figure 2.24b), and on top, the fuel electrode of the cell is directly in contact with the corrugated nickel mesh. The use of that gold ring frame ensures the insulation of both chambers even at SOEC operation temperatures. A ceramic block has been located on top for keeping the tight set-up (Figure 2.24c), and a golden mesh has been placed later as current collector.

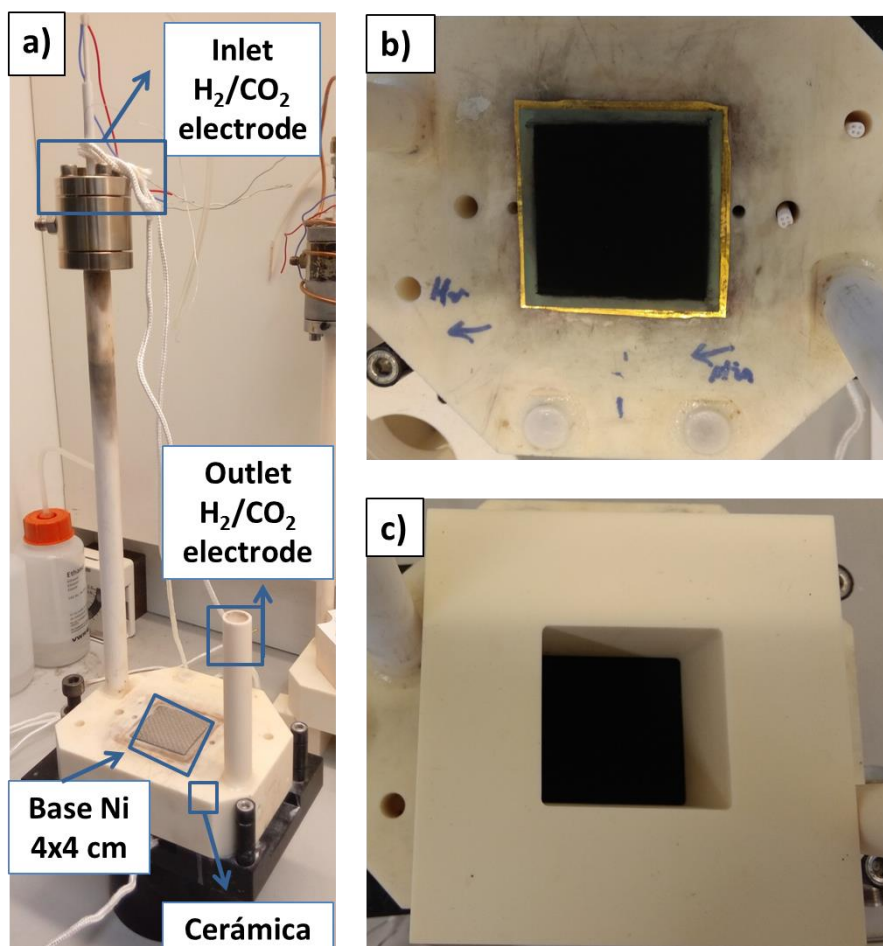


**Figure 2.24:** a) Sample holder employed at DTU for electrochemical measurement of SOEC samples, b) Golden ring placed as sealant and sample on top, and c) ceramic block placed on top.

### 2.7.2. Electrochemical Impedance Spectroscopy (EIS)

Electrochemical impedance spectroscopy measurements are an important tool for the in-situ study of SOEC systems [29]. In general, it is possible to define impedance as

a resistance generated by the flow of both direct and alternative currents (DC and AC) through a circuit basically composed of resistors, capacitors and inductors. More specifically, this powerful tool allows characterizing the performance and mechanism of SOEC electrodes materials, studying the SOEC degradation mechanisms of different configurations (symmetrical cells, single cell and stacks) during high temperature electrolysis, and can be employed as a complementary technique to post-mortem characterization techniques. Besides, this technique can be used for systematic analysis of in operando cells, developing tests varying the temperature, current density or gasses flows.

EIS are measured in a wide frequency range, typically from MHz to mHz. The voltage can be expressed by equation (2.2), where  $E_0$  is the amplitude and  $w$  the angular frequency. In the same way, the injected current can be expressed as (2.3), being  $\theta$  a phase shift of  $I(t)$  with respect to  $E(t)$ . The impedance defined by the equation (2.4) can be expressed as a complex number in terms of real ( $Z'$ ) and imaginary part ( $Z''$ ).

$$E(t) = E_0 \cdot e^{i\omega t} \quad (2.2)$$

$$I(t) = I_0 \cdot e^{i(\omega t + \theta)} \quad (2.3)$$

$$Z(\omega) = \frac{E(t)}{I(t)} = |Z|e^{-i\theta} = |Z| \cos \theta - i |Z| \sin \theta = Z' - iZ'' \quad (2.4)$$

The applicability of this expression requires a linear dependence of the current with respect to the voltage. Thus, a small voltage (when the measurements are performed on potentiostatic mode) or current (measurements on galvanostatic mode) has to be applied in order to keep a linear regime (Figure 2.25).

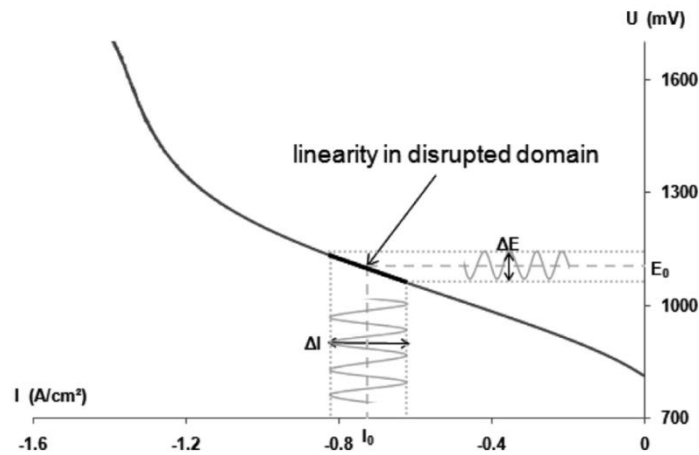


**Figure 2.25:** Scheme of a polarization curve in SOEC with linear response to applied current or voltage [30].

Those measurements are usually represented in Nyquist or Bode plots. Varying experimental parameters like the current applied, temperature and reactant composition, frequency shifts are observed in the impedance spectra. The comparison of the corresponding Nyquist and Bode plots recorded varying experimental parameters allows concluding information about the electrochemical processes dominating the system under different experimental conditions.

The simplest Nyquist plot found for a system with an only conduction mechanism is a semicircle of diameter  $R$  (material's resistance) appearing with the centre at the position  $(R/2, 0)$  on the  $Z'$  axis (**Figure 2.26**).

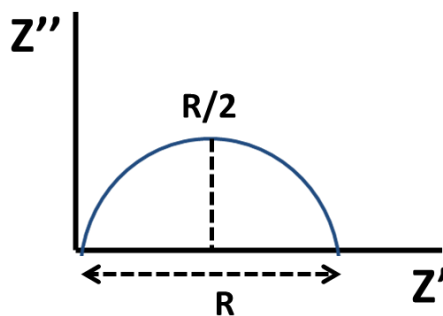


**Figure 2.26:** Scheme of the Nyquist plot corresponding to a RC element.

Electrical Equivalent Circuits (EECs) are commonly used as tool for interpreting EIS measurements. This tool consists in fitting a measured impedance with an EEC resulting from the series or parallel combination of ideal electrical elements like resistances, capacitors and inductors; and non-ideal ones, such as Constant Phase Elements (CPEs).

Studying complex systems, as an electrolyte sandwiched by two electrodes, several different mechanisms take place, such as ionic conductivity through the electrolyte, and charge transfer or mass transport on the electrode/electrolyte interface. Those different processes are represented by different semicircles or arcs in the corresponding Nyquist plot. Each electrochemical process is represented by an element of the EEC, and presents a characteristic time, what allows its identification. **Figure 2.27** shows a Nyquist plot that would correspond to a simple cell, with the associated equivalent circuit also depicted. The electrolyte and electrode process are reflected as multiple semicircles in the graph. Each arc is ascribed to a resistance and capacitance parallel circuit, presented as RC on the equivalent circuit, and are characterized by the specific time constant of a process ( $\tau = 1/RC$ ). As a result, a linear combination of RC circuits is used to fit this system.

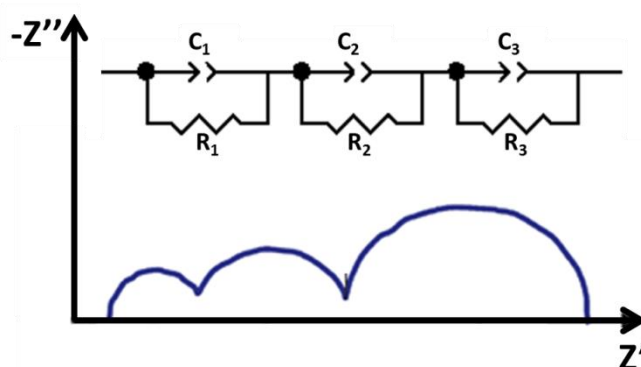


**Figure 2.27:** Scheme of a Nyquist plot from an EIS measurement and of the proposed electrical equivalent circuit.

However, a better analysis is necessary for a proper understanding of the impedance spectrum if overlapping occurs, as it is observed in the experimental Nyquist plots presented in this thesis. RC circuits do not fit well the experimental impedance spectra since most of the times different semicircles appear overlapped or depressed in the complex plane. EIS technique presents the ability of separating into individual processes the contribution of each cell component to the total resistance (**Figure 2.28**). Ideal capacitances (C) have been substituted for constant phase elements for fitting experimental data since they describe non-ideal capacitances. CPE considers a distribution of relaxation times and a  $n$  value related to the depression angle introduced. Values of  $n$  are obtained from the fitting and can variate in the range  $0 \leq n \leq 1$ .

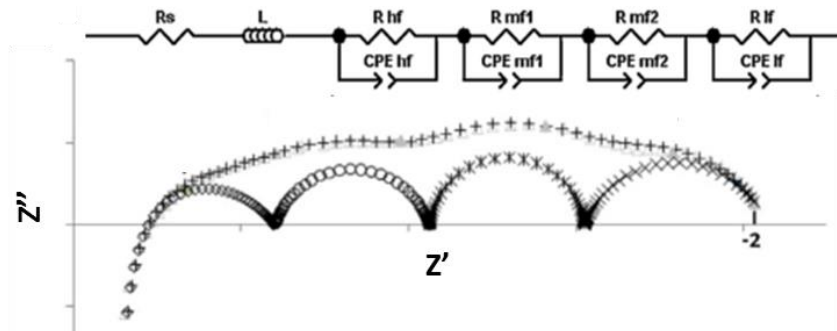


**Figure 2.28:** Example of a fitting done on an experimental impedance spectra using the specified electrical equivalent circuit [31].

Impedance spectroscopy data are also studied in the form of Bode plots, where  $-Z''$  imaginary ( $Z''$ ) component of the Nyquist is plotted vs the log of the frequency. These types of plots are used to study the development of the impedance when different conditions (such as gas compositions, injected current density or operation temperature) have been used in any of the electrodes chambers. The study is based on a change in the impedance response at a given frequency where a stronger  $-Z''$  imaginary contribution is interpreted as an increase in resistance for this specific electrode reaction. Bode plot highlights the characteristic frequency where the compared spectra deviate, allowing the identification of the SOEC electrochemical processes and the electrode where it takes place. In this thesis, the method is employed for analysing the dependencies of the electrode reactions with the partial pressures of gas compositions (**Figure 2.29**) [32,33].

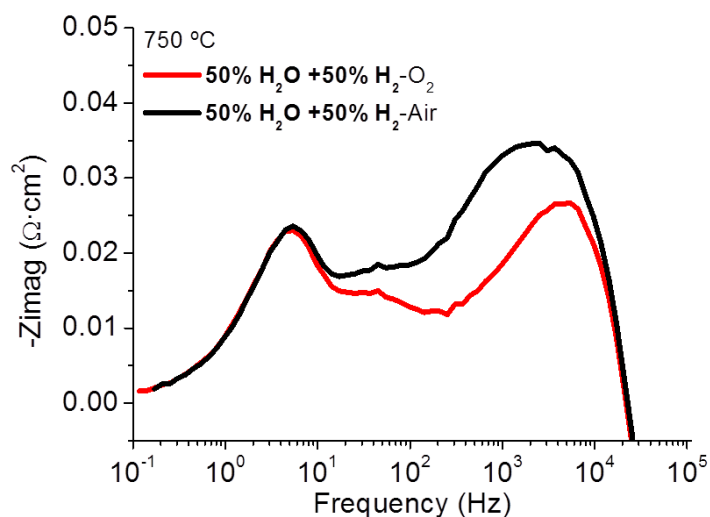


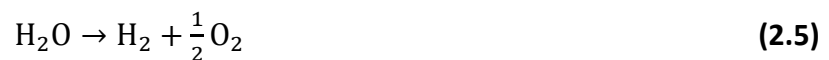
**Figure 2.29:** Bode plot comparing the contribution of two different fuel electrode gas compositions to the resistance.

EIS measurements have been widely used in this thesis for characterization of the different electrodes prepared for SOECs. The EIS measurements of the electrochemical cells have been carried out using a potentiostat/galvanostat Parstat 2273 from PAR. Impedance Spectroscopy measurements were carried out in a frequency range from 2 MHz to 100 mHz by applying an AC signal of 50 mV of voltage amplitude over Open Circuit Voltage (OCV) operation voltage. All the generated impedance spectra were fitted employing an EEC on Zview software.

### 2.7.3. Galvanostatic and Potentiostatic modes for I-V curves

The electrolysis cells overall performance was characterized measuring polarization or I-V curves. These plots represent the variation of the potential (V) versus the injected current density ( $j/\text{cm}^2$ ). A scheme of a typically obtained I-V curve on electrolysis mode is presented in **Figure 2.30**. This type of measurements can be carried out in galvanostatic or potentiostatic modes. The potentiostatic measurement uses a potentiostat for controlling the voltage difference between the two electrodes of the cell, measuring the resultant current flow between them. When measuring in galvanostatic mode, the instrument controls the cell current flowing between the two electrodes and measures the voltage.

The OCV of a cell is measured on galvanostatic mode applying a negligible current flow between the electrodes and measuring the voltage generated between them. Its value is determined by the Nernst equation. Its expression for steam electrolysis **(2.5)** is here presented as **(2.6)**. The OCV value is dependent on the difference on  $p\text{O}_2$  between both electrodes. In consequence, the comparison of the OCV theoretical value and the measured one allows controlling the goodness of the sealing between the two electrodes.



$$E = E^\circ + \frac{RT}{2F} \ln \frac{P_{\text{H}_2\text{O}}}{P_{\text{H}_2} \cdot P_{\text{O}_2}^{1/2}} \quad (2.6)$$

On electrolysis operation mode, the measured voltage increases with the injected current density, as it can be observed in **Figure 2.30**. This variation is caused by the contribution of different overpotentials at different regions of the I-V curve, which

dominate the resistance of the cell. At low current densities, the main contribution comes from activation overpotentials ( $\eta_{act}$ ) mainly caused by the activation of electrodes for the electrochemical reactions. In the middle of the I-V curve, the ohmic overpotential ( $\eta_{ohm}$ ) presents the highest contribution. This overpotential reflects the resistance of ions and electrons for passing through the electrolyte and the electrodes respectively, and any other ohmic processes. At higher injected currents, the difficulties of transportation of  $H_2O$  and  $CO_2$  molecules to the active reaction sites generates the diffusion overpotential ( $\eta_{diff}$ ).

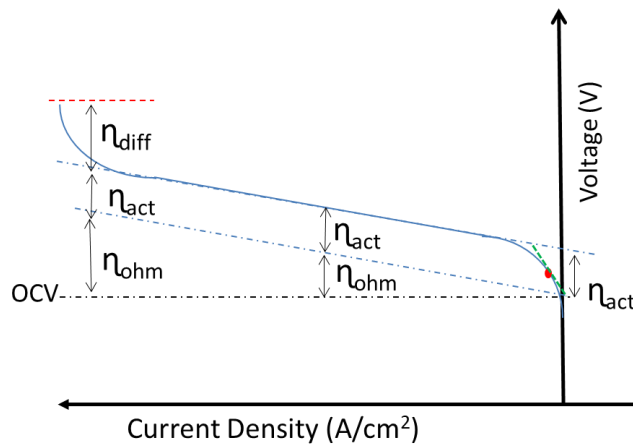


**Figure 2.30:** Scheme of a measured I-V curve for SOEC specifying predominant overpotentials in each region.

In this work, the potential or injected current of the electrochemical cells were monitored using a potentiostat/galvanostat Parstat 2277 from PAR. This equipment allowed obtaining current density-voltages (I-V) curves for characterizing SOECs under different operation conditions (temperature, steam injection, gas compositions...).

## 2.8. References

- [1] Y. Ren, Z. Ma, and P. G. Bruce, "Ordered mesoporous metal oxides: synthesis and applications," *Chem. Soc. Rev.*, vol. 41, pp. 4909–4027, 2012.
- [2] H. Yang and D. Zhao, "Synthesis of replica mesostructures by the nanocasting strategy," *J. Mater. Chem.*, vol. 15, pp. 1217–1231, 2005.
- [3] F. Jiao, A. H. Hill, A. Harrison, A. Berko, A. V Chadwick, and P. G. Bruce, "Synthesis of Ordered Mesoporous NiO with Crystalline Walls and a Bimodal Pore Size Distribution," *J. AM. CHEM. SOC. 2008*, vol. 130, pp. 5262–5266, 2008.
- [4] W. Li and D. Zhao, "An overview of the synthesis of ordered mesoporous materials," *Chem. Commun.*, vol. 49, pp. 943–946, 2013.
- [5] A. Ruplecker, F. Kleitz, E.-L. Salabas, and F. Schüth, "Hard Templating Pathways for the Synthesis of Nanostructured Porous Co<sub>3</sub>O<sub>4</sub>," *Chem. Mater*, vol. 19, pp. 485–496, 2007.
- [6] A. H. Lu and F. Schüth, "Nanocasting: A versatile strategy for creating nanostructured porous materials," *Adv. Mater.*, vol. 18, pp. 1793–1805, 2006.
- [7] Y. Ye, C. Jo, I. Jeong, and J. Lee, "Functional mesoporous materials for energy applications: solar cells, fuel cells, and batteries," *Nanoscale*, vol. 5, pp. 4584–4605, 2013.
- [8] F. Kleitz, S. Hei Choi, and R. Ryoo, "Cubic Ia3d large mesoporous silica: synthesis and replication to platinum nanowires, carbon nanorods and carbon nanotubes," *Chem. Commun.*, pp. 2136–2137, 2003.
- [9] F. Yuan, J. Wang, H. Miao, C. Guo, and W. G. Wang, "Investigation of the crystal structure and ionic conductivity in the ternary system (Yb<sub>2</sub>O<sub>3</sub>)<sub>x</sub>-(Sc<sub>2</sub>O<sub>3</sub>)<sub>(0.11-x)</sub>-(ZrO<sub>2</sub>)<sub>0.89</sub> (x = 0-0.11)," *J. Alloys Compd.*, vol. 549, pp. 200–205, 2013.
- [10] L. Guo, Y. Fan, and N. Teramae, "Vapor phase synthesis of mesoporous silica rods within the pores of alumina membranes," *New J. Chem.*, vol. 36, pp. 1301–1303, 2012.
- [11] P. Yang, S. Zhou, and J. Lei, "Preparation of ordered mesoporous nanocrystalline ceria and ceria-zirconia for soot oxidation," *J. Wuhan Univ. Technol. Mater. Sci. Ed.*, vol. 31, pp. 113–117, 2016.
- [12] D. Ding, X. Li, S. Y. Lai, K. Gerdes, and M. Liu, "Enhancing SOFC cathode performance by surface modification through infiltration," *Energy Environ. Sci.*, vol. 7, pp. 552–575, 2014.
- [13] W. H. Kan, A. J. Samson, and V. Thangadurai, "Trends in electrode development for next generation solid oxide fuel cells," *J. Mater. Chem. A*, vol. 4, pp. 17913–17932, 2016.
- [14] "FAE S.A.U." [Online]. Available: <http://www.fae.es/es/>.
- [15] "HTceramix S.A." [Online]. Available: <http://www.solidpower.com/en/about-us/locations/>.
- [16] J. Laurencin *et al.*, "Reactive Mechanisms of LSCF Single-Phase and LSCF-CGO

- Composite Electrodes Operated in Anodic and Cathodic Polarisation,” *Electrochim. Acta*, vol. 174, pp. 1299–1316, 2015.
- [17] J. Laurencin *et al.*, “Degradation mechanism of  $\text{La}_{0.6}\text{Sr}_{0.4}\text{Co}_{0.2}\text{Fe}_{0.8}\text{O}_{3-\delta}/\text{Gd}_{0.1}\text{Ce}_{0.9}\text{O}_{2-\delta}$  composite electrode operated under solid oxide electrolysis and fuel cell conditions,” *Electrochim. Acta*, vol. 241, pp. 459–476, 2017.
- [18] M. Morales *et al.*, “Multi-scale analysis of the diffusion barrier layer of gadolinia-doped ceria in a solid oxide fuel cell operated in a stack for 3000 h,” *J. Power Sources*, vol. 344, pp. 141–151, 2017.
- [19] G. Taillades, P. Pers, V. Mao, and M. Taillades, “High performance anode-supported proton ceramic fuel cell elaborated by wet powder spraying,” *Int. J. Hydrogen Energy*, vol. 41, pp. 12330–12336, 2016.
- [20] A. M. Hernández, L. Mogni, and A. Caneiro, “ $\text{La}_2\text{NiO}_{4+\delta}$  as cathode for SOFC: Reactivity study with YSZ and CGO electrolytes,” *Int. J. Hydrogen Energy*, vol. 35, pp. 6031–6036, 2010.
- [21] T. Jiang, Z. Wang, B. Ren, J. Qiao, W. Sun, and K. Sun, “Compositionally continuously graded cathode layers of  $(\text{Ba}_{0.5}\text{Sr}_{0.5})(\text{Fe}_{0.91}\text{Al}_{0.09})\text{O}_{3-\delta}\text{Gd}_{0.1}\text{Ce}_{0.9}\text{O}_2$  by wet powder spraying technique for solid oxide fuel cells,” *J. Power Sources*, vol. 247, pp. 858–864, 2014.
- [22] “Print3D Solutions.” [Online]. Available: <http://print3dsolutions.net/la-empresa/equipos/>.
- [23] Y. Wang, Z. Yang, M. Han, and J. Chang, “Optimization of  $\text{Sm}_{0.5}\text{Sr}_{0.5}\text{CoO}_{3-\delta}$  -infiltrated YSZ for solid oxide fuel cells/electrolysis cells,” *RSC Adv*, vol. 182, pp. 112253–112259, 2016.
- [24] H. Fan, Y. Zhang, and M. Han, “Infiltration of  $\text{La}_{0.6}\text{Sr}_{0.4}\text{FeO}_{3-\delta}$  nanoparticles into YSZ scaffold for solid oxide fuel cell and solid oxide electrolysis cell,” *J. Alloys Compd.*, vol. 723, pp. 620–626, 2017.
- [25] K. J. Yoon *et al.*, “Nano-tailoring of infiltrated catalysts for high-temperature solid oxide regenerative fuel cells,” *Nano Energy*, vol. 36, pp. 9–20, 2017.
- [26] IUPAC, “Reporting physisorption data for gas / solid systems with special reference to the determination of surface area and porosity area International Union of Pure and Applied Chemistry,” *Pure Appl. Chem.*, vol. 57, pp. 603–619, 1985.
- [27] K. Sing, “The use of nitrogen adsorption for the characterisation of porous materials,” in *Colloids and Surfaces A: Physicochemical and Engineering Aspects*, 2001, vol. 187–188, pp. 3–9.
- [28] “NorECs.” [Online]. Available: <http://www.norecs.com/index.php?page=ProboStat>.
- [29] A. Nechache, M. Cassir, and A. Ringuedé, “Solid oxide electrolysis cell analysis by means of electrochemical impedance spectroscopy: A review,” *J. Power Sources*, vol. 258, pp. 164–181, 2014.
- [30] A. Nechache, M. Cassir, and A. Ringuedé, “Solid oxide electrolysis cell analysis by means of electrochemical impedance spectroscopy: A review,” *Journal of Power*

Sources, vol. 258. pp. 164–181, 2014.

- [31] A. Nechache *et al.*, “Diagnosis of a cathode-supported solid oxide electrolysis cell by electrochemical impedance spectroscopy,” *Electrochim. Acta*, vol. 210, pp. 596–605, 2016.
- [32] R. Barfod, M. Mogensen, T. Klemensø, A. Hagen, Y.-L. Liu, and P. Vang Hendriksen, “Detailed Characterization of Anode-Supported SOFCs by Impedance Spectroscopy,” *J. Electrochem. Soc.*, vol. 154, no. 4, pp. B371–B378, 2007.
- [33] M. J. Jørgensen and M. Mogensen, “Impedance of Solid Oxide Fuel Cell LSM/YSZ Composite Cathodes,” *J. Electrochem. Soc.*, vol. 148, no. 5, pp. A433–A442, 2001.

# ***Chapter 3***

*Synthesis, characterization  
and optimization of  
mesoporous electrode  
materials*



<b>3. Synthesis, characterization and optimization of mesoporous electrode materials</b>	<b>97</b>
3.1. Chapter overview .....	97
3.2. Structural characterization of mesoporous materials .....	98
3.2.1. Structural characterization of mesoporous KIT-6 .....	98
3.2.2. Structural characterization of mesoporous $\text{Sm}_{0.2}\text{Ce}_{0.8}\text{O}_{1.9}$ (SDC).....	101
3.2.3. Structural characterization of mesoporous $\text{Ce}_{0.8}\text{Gd}_{0.2}\text{O}_{1.9}$ (CGO) .....	105
3.2.4. Structural characterization of mesoporous NiO .....	108
3.3. Structural characterization of fabricated mesoporous electrodes.....	112
3.3.1. Structural characterization of $\text{Sm}_{0.2}\text{Ce}_{0.8}\text{O}_{1.9}$ (SDC)- $\text{Sm}_{0.5}\text{Sr}_{0.5}\text{CoO}_{3-\delta}$ (SSC) oxygen electrodes .....	113
3.3.2. Structural characterization of $\text{Ce}_{0.8}\text{Gd}_{0.2}\text{O}_{1.9}$ (CGO)- $\text{La}_{0.6}\text{Sr}_{0.4}\text{Co}_{0.2}\text{Fe}_{0.8}\text{O}_3$ (LSCF) oxygen electrodes .....	114
3.3.3. Structural characterization of NiO- $\text{Sm}_{0.2}\text{Ce}_{0.8}\text{O}_{1.9}$ (SDC) fuel electrodes	116
3.4. Optimization of oxygen electrodes based on mesoporous materials on symmetric cells .....	117
3.5. Conclusion .....	123
3.6. References .....	125



### 3. Synthesis, characterization and optimization of mesoporous electrode materials

#### 3.1. Chapter overview

The Chapter 3 of this thesis presents the synthesis, characterization, functionalization and application of mesoporous materials as Solid Oxide Cell (SOC) electrodes. The synthesis process for obtaining stable ordered mesoporous samarium-doped ceria ( $\text{Sm}_{0.2}\text{Ce}_{0.8}\text{O}_{1.9}$ -SDC), gadolinium-doped ceria ( $\text{Ce}_{0.8}\text{Gd}_{0.2}\text{O}_{1.9}$ -CGO) and nickel (NiO) oxides, based on promoting its crystallization inside a mesoporous silica KIT-6 template was presented in **section 2.2**. The mesoporosity of KIT-6, SDC, CGO and NiO materials has been characterized by nitrogen ( $\text{N}_2$ ) physisorption measurements-BET and Low-Angle X-Ray Diffraction (LA-XRD). Besides, synthesised replica powders have been characterized by scanning and transmission microscopies (SEM and TEM) and X-Ray Diffraction (XRD and LA-XRD) techniques, confirming the success of the applied synthesis method for obtaining the desired ordered mesoporous materials. Those results are presented in **section 3.2**.

The functionalization of both SDC and CGO ceramic Ionic Conductor (IC) materials was achieved by their infiltration with catalytic active and Mixed Ionic Electronic Conductor (MIEC) materials such as the samarium strontium cobaltite ( $\text{Sm}_{0.5}\text{Sr}_{0.5}\text{CoO}_{3-\delta}$ -SSC) and lanthanum strontium cobalt ferrite ( $\text{La}_{0.6}\text{Sr}_{0.4}\text{Co}_{0.2}\text{Fe}_{0.8}\text{O}_3$ -LSCF) perovskites, respectively. As a result, SDC-SSC and CGO-LSCF nanocomposite materials have been obtained. The characterization of the obtained nanocomposites is presented in **section 3.3** to discuss the applicability of this new materials architecture as oxygen electrodes for high temperature Solid Oxide Electrolysis Cells (SOECs) (**section 3.3.1** and **section 3.3.2**). In the case of the nickel oxide (NiO) (**section 3.3.3**), its functionalization as fuel electrode has been achieved by the impregnation of its pore network with the SDC ionic conductor material, forming the NiO-SDC nanocomposite cermet.

Finally, once the synthesis of the electrodes has been successfully achieved, electrolyte-supported symmetrical cells with different electrodes based on mesoporous scaffolds were fabricated using different sintering temperatures. These cells have been characterized by means of electrochemical tests in order to optimise the attachment with the electrolyte and minimise the contact resistance contributions (**section 3.4**).

### 3.2. Structural characterization of mesoporous materials

As it is explained in **section 2.2**, the hard-template or nanocasting method was applied in this thesis for the fabrication of mesoporous materials [1]. Different silica mesoporous templates, commercially known as KIT-6 and synthesised at different hydrothermal temperatures, were used as templates for the nanocasting process. Mesoporous  $\text{Sm}_{0.2}\text{Ce}_{0.8}\text{O}_{1.9}$ -SDC,  $\text{Ce}_{0.8}\text{Gd}_{0.2}\text{O}_{1.9}$ -CGO and NiO materials were synthesised as replicas of the defined KIT-6 template. A detailed structural characterization of the mesoporous materials used for the fabrication of SOEC electrodes is presented in the following sections.

#### 3.2.1. Structural characterization of mesoporous KIT-6

Three different KIT-6 morphologies were used as silica templates for the fabrication of the electrodes. The difference of the used KIT-6 powders is related to their structure and the diameter and number of open channels present. These parameters can be modified during the synthesis of the KIT-6 by varying the temperature of the hydrothermal step. Hydrothermal temperatures of 36 and 90 °C were applied for the synthesis of the different templates, to which will refer as KIT-6-36 and KIT-6-90 respectively during this discussion. A third template, based on the commercial available KIT-6 (ACS Material [2]), and called in the document KIT-6-commercial, was also used as template. The three mesoporous templates were structurally characterized by  $\text{N}_2$ -physisorption and LA-XRD techniques.

The application of the Brunauer-Emmett-Teller (BET) model to the  $\text{N}_2$ -physisorption measurements [3] allowed calculating the mesoporous surface area of the three different used templates, obtaining values higher than 600  $\text{m}^2/\text{g}$  for the three templates (**Figure 3.1**). Specifically, BET areas of 696, 666 and 867  $\text{m}^2/\text{g}$  were obtained for KIT-6-36, KIT-6-commercial and KIT-6-90 respectively. The detailed analysis of the three obtained adsorption-desorption isotherms (**Figure 3.1**) confirms the mesoporous nature of the material employed as template and differences in their main pore size.

More specifically, among the six possible types of isotherms (**section 2.6.2**), the presented ones (**Figure 3.1a**) follow the Type IV model. This type of isotherm shows a characteristic hysteresis loop appearing due to the capillary condensation, which takes

place in the mesopores once the monolayer-multilayer adsorption has occurred. The hysteresis loop, which shape changes in function of the pores structures, is classified as H1 Type, and it points the presence of narrow distribution of pore sizes. Main pore sizes were calculated applying the Barrett-Joyner-Halenda (BJH) method to the desorption isotherm, as it is presented in **Figure 3.1b**. This analysis reveals differences on the pore sizes of the different templates as it was expected after the analysis of the isotherms.

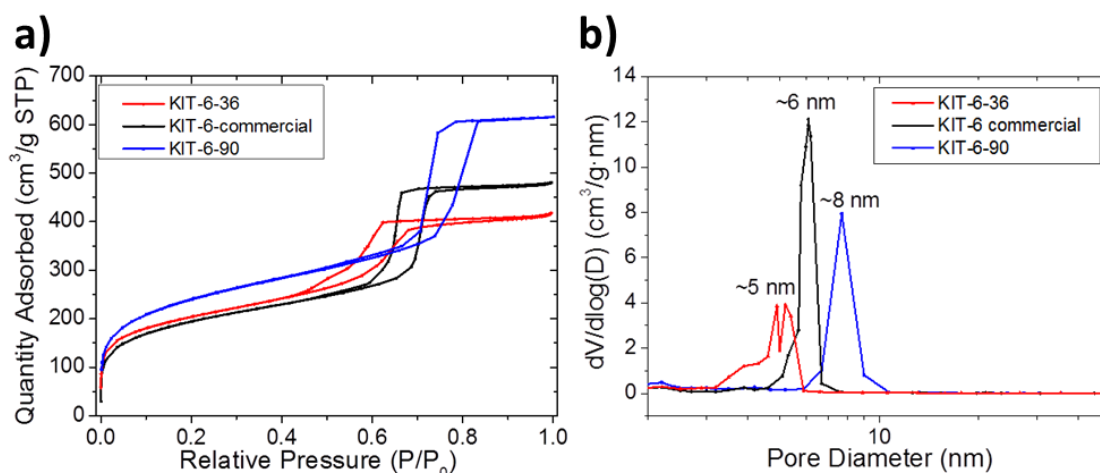


**Figure 3.1:** N<sub>2</sub>-physorption characterization of KIT-6-36, KIT commercial and KIT-6-90 a) N<sub>2</sub> adsorption-desorption isotherms and b) pore size distribution applying the BJH method.

The characteristic hysteresis observed during the adsorption-desorption cycle for this type of mesoporous materials is shifted to higher relative pressures when the pore size is larger, since more pore volume needs to be filled by N<sub>2</sub> (**Figure 3.1a** and **3.1b**). The structural values resulting from N<sub>2</sub>-physorption measurements and modelling are presented in **Table 3.1**, where periodicity-lattice parameter values were calculated by applying the Bragg's law to the characteristic (211) diffraction peaks presented in **Figure 3.2**. KIT-6 presents larger periodicity-lattice parameters and pore sizes when the hydrothermal temperature is performed at higher temperatures since capillary condensation takes place. According to this, KIT-6-90, which was treated at 90 °C, presents the highest periodicity-lattice parameter (24 nm) and pore size (8 nm) if compared with KIT-6-36 and KIT-6-commercial. Periodicity-lattice parameter values of 21.4 and 22.2 nm, and pore sized of 5 and 6 nm were characterized for KIT-6-36 and KIT-6-commercial, respectively.

	BET (m <sup>2</sup> /g)	Periodicity-lattice parameter (nm)	Pore size (nm)
KIT-6-36	735 ± 2	21.4	5
KIT-6 commercial	703 ± 2	22.2	6
KIT-6-90	867 ± 3	23.8	8

**Table 3.1:** Structural parameters of KIT-6 templates obtained by N<sub>2</sub>-physisorption measurements and LA-XRD.

LA-XRD analyses were also performed on the three KIT-6 templates in order to study the symmetry and periodicity of the KIT-6 structure. **Figure 3.2** presents the three obtained diffractogram for KIT-6-36, KIT-6-commercial and KIT-6-90. The three used KIT-6 present similar patterns. The pattern shows a main sharp peak at  $2\theta=1.08$ , 0.97 and 0.91 indexed as (211), and weaker ones at  $2\theta=1.24$ , 1.12 and 1.05 indexed as (220) for KIT-6-36, KIT-6-commercial and KIT-6-90, respectively. Another weak reflection indexed as (332) is found at  $2\theta=1.90$  and 1.73 for KIT-6-commercial and KIT-6-90. These analyses reveal that the synthesised materials presents *la3d* symmetry, similar to the one reported by Kleitz *et al* [4] and confirms the suitability of the synthesis process presented in **section 2.2.1** for obtaining the KIT-6 template. The shifts of the characteristic (211) diffraction peaks observed in **Figure 3.2** explain the differences on the periodicity-lattice parameter values calculated for the three templates (**Table 3.1**).

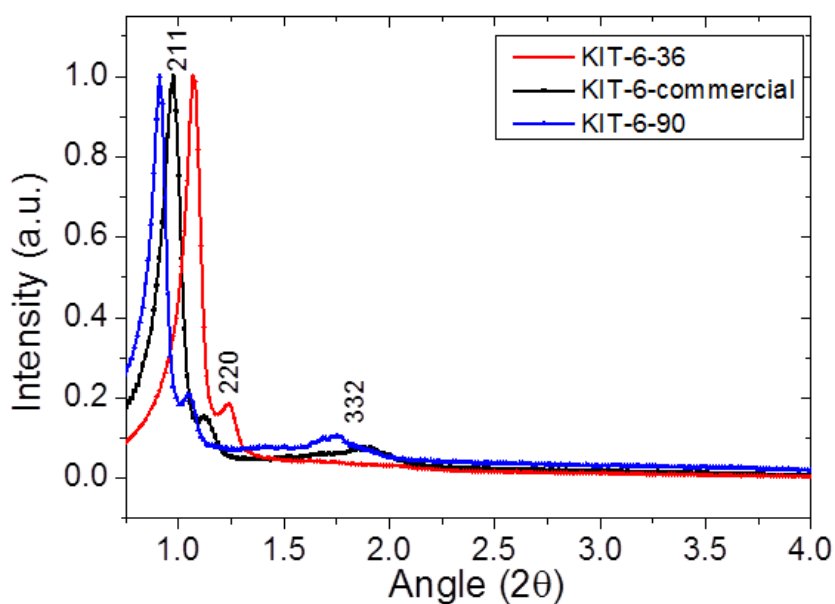


**Figure 3.2:** Low-angle X-ray diffractogram of KIT-6-36, KIT-6-commercial and KIT-6-90 templates.

Once the key parameters of the different templates were characterised, the template was chosen depending on the desired mesoporous structure of the replica.

### 3.2.2. Structural characterization of mesoporous $\text{Sm}_{0.2}\text{Ce}_{0.8}\text{O}_{1.9}$ (SDC)

SDC was synthesised by the hard template method using samarium ( $\text{Sm}(\text{NO}_3)_3 \cdot 6\text{H}_2\text{O}$ ) and cerium ( $\text{Ce}(\text{NO}_3)_3 \cdot 6\text{H}_2\text{O}$ ) nitrates for impregnating the KIT-6-36 template (**section 2.2.3**). In this thesis, the obtained SDC mesoporous replica is used as scaffold for the fabrication of oxygen electrodes materials. Therefore, the synthesis of the mesoporous SDC should be followed by infiltration, enhancing the Triple Phase Boundary (TPB) length compared with the standard composite electrodes while allowing the gas phase circulation along the electrode. The as-obtained mesoporous SDC powders were characterized by  $\text{N}_2$ -physisorption, LA-XRD, XRD and Scanning Electron Microscopy (SEM) in order to confirm and study the obtained phase and the desired microstructure.

The surface area and the pore size of solid materials are determined through the nitrogen adsorption-desorption measurements at the obtained mesoporous material surfaces and the application of two different methods of analysis. In this case, the BET method is applied to evaluate the specific surface area of SDC mesoporous materials, while the mesopore size distribution is calculated by using the BJH method to analyse the obtained desorption branch of the  $\text{N}_2$  isotherm [5]. **Figure 3.3a** shows the  $\text{N}_2$  adsorption-desorption isotherms obtained for the fabricated SDC mesoporous powder. The adsorption isotherm represents the amount of  $\text{N}_2$  absorbed to the mesoporous under measurement at constant temperature and equilibrium gas pressure [3]. BET area of  $110 \pm 15 \text{ m}^2/\text{g}$  was obtained.

As it is explained in **section 2.6.2**, in this isotherm it is possible to distinguish the effect of a preliminary cover of the material by the gas (monolayer adsorption), followed by the accumulation of successive gas layers (multilayer adsorption), and the capillary condensation taking place for recovering the remaining free pore space. The obtained physisorption isotherms can be typically classified into six different types as a function of the pore type and size present on the studied sample (named as Type I to Type VI) [3]. The different rate for the adsorption and desorption of the gas in the

surface of the mesoporous generates the observed hysteresis loop between both isotherms. Different pore structures can be distinguished by their characteristic hysteresis loop of physisorption isotherms, which present different shapes (named as H1 to H4). The isotherm obtained when analysing the obtained mesoporous SDC powder belongs to Type IV, which is typically characterized by the hysteresis loop appearing due to the capillary condensation in mesopores. The one shown in **Figure 3.3a**, corresponds to H1 Type, which is typical of mesoporous materials of ordered and uniform spheres and indicating the presence of narrow pore size distributions, as it is expected for a pore distribution generated by a mesoporous periodic template.[3]. These results are in good agreement with the hysteresis loops obtained for KIT-6 in this thesis (**section 3.2.1**) and in the literature [6-10].

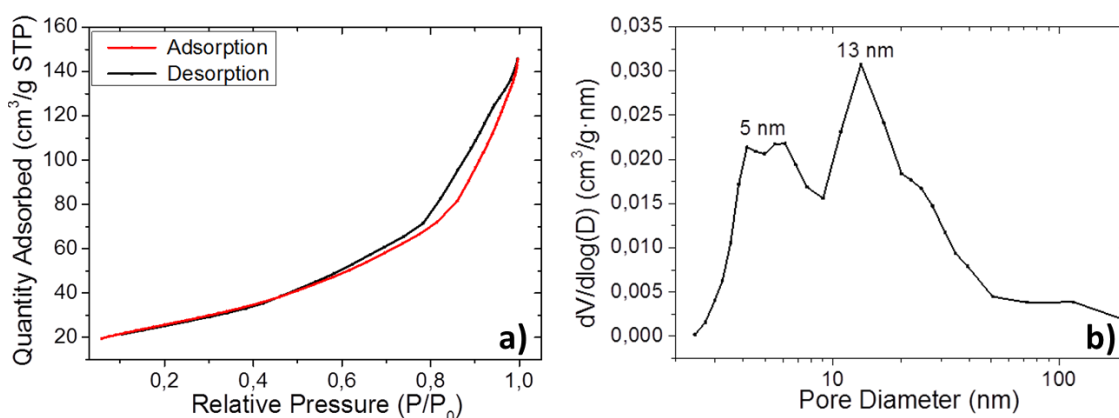


**Figure 3.3:** N<sub>2</sub>-physorption characterization of mesoporous synthesised SDC material a) experimentally obtained IV Type isotherm with characteristic H1 hysteresis loop b) pore size distribution obtained by application of the BJH method.

The analysis of the desorption isotherm data based on the BJH method revealed that the pore distribution is centred in 5 and 13 nm, as shown in **Figure 3.3b**. In concordance with what has been reported in **Chapter 2** for the replication of metal oxides, a bimodal pore size distribution with higher contribution of the large pore (13 nm) was obtained due to the disconnection of the two channels of the silica template, which is a consequence of the tuned microstructure obtained for the KIT-6-36 following the low hydrothermal temperature during the former synthesis process [3,7]. Moreover, the two pore sizes of the mesoporous material increase the active surface area to be infiltrated, which may result on an enhancement of the TPB distribution and a final improvement of the electrode performance.

LA-XRD characterizes the periodicity of the mesoporous structure obtained by the SDC replicated material, which microstructure is reproduced from the silica template. LA-XRD diffractograms were obtained for both the used KIT-6-36 and the synthesised replica SDC after its thermal and cleaning treatments (**Figure 3.4**). The obtained diffractogram presents an ordered mesoporous structure with cubic  $Ia3b$  symmetry in good agreement with literature data [6]. As it can be seen in **Figure 3.2** and **Figure 3.4**, two diffraction peaks are characteristics of KIT-6-36: the main one labelled as (211) and centred at  $2\theta=1.08^\circ$ , and the other (220) centred at  $2\theta=1.24^\circ$ . The SDC powder presents its main peak (211) in the same  $2\theta=1.08^\circ$  position as the template. That confirms the periodic structure of the original silica template has been transferred to the SDC replica maintaining the KIT-6-36 symmetry ( $Ia3b$  symmetry group) and morphology. As it has been previously indicated, the periodicity-lattice parameters of the KIT-6 mesoporous template and the obtained replica were calculated applying the Bragg's law to the (211) diffraction peak, in this case defined as the wall to wall distance of the mesoporous structure, resulting in 22 nm in both cases.

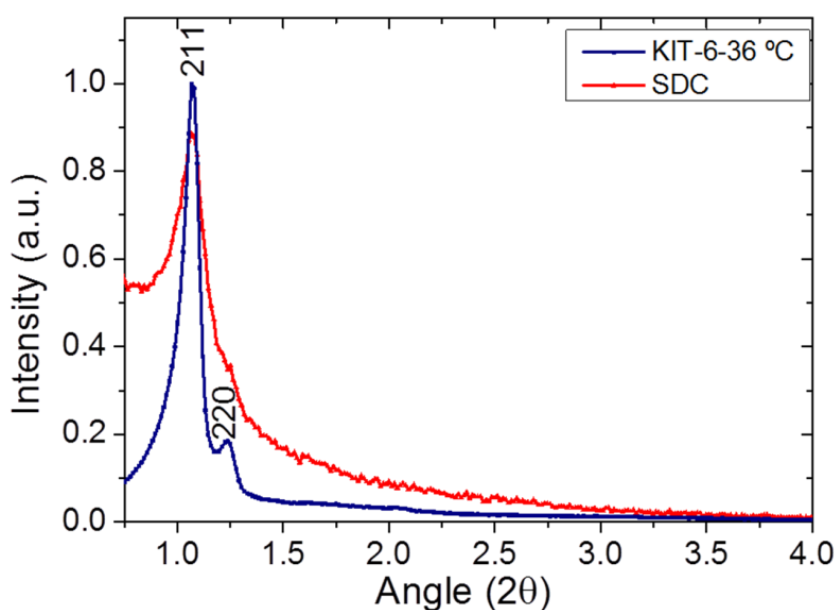


**Figure 3.4:** LA-XRD of KIT-6 mesoporous pattern and the obtained replica SDC.

The mesoporous SDC has been also microstructurally characterised. A SEM image of the synthesised SDC mesoporous particles is shown in **Figure 3.5a**. **Figure 3.5b** presents a Transmission Electron Microscopy (TEM) micrograph of the same powder. The pore size measured in **Figure 3.5b** shows a distribution from 6 to 9 nm, what fits with the pore size distribution of SDC obtained from the analysis of the  $N_2$  desorption isotherm.

Besides, the SDC wall thickness measured in the TEM image presented in **Figure 3.5b** fits with the pore size of KIT-6-36 measured by N<sub>2</sub>-physisorption measurements (**section 3.2.1**), as it is expected since KIT-6-36 walls act as mold of the SDC pores. Both images confirm the reproducibility of the mesoporosity of the replica by the synthesised powder, which was previously characterized by N<sub>2</sub>-physisorption and low-angle XRD techniques.

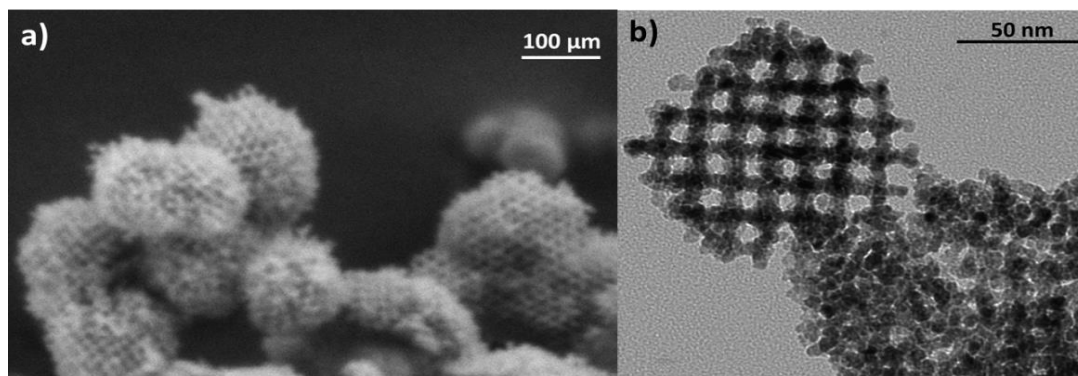


**Figure 3.5:** Microscopy images of SDC synthesised powder a) SEM and b) TEM.

X-Ray Diffraction (XRD) was also performed in order to confirm the crystalline desired phase of the SDC scaffold. The X-Ray diffractogram obtained for synthesised SDC mesoporous powder is presented in **Figure 3.6**. According to the pattern, the obtained signal was indexed as a single cubic phase with space group *Fm-3m* and lattice parameter  $a=5.43$  Å. This SDC phase was formed after a thermal treatment up to 600 °C of the silica template infiltrated by the SDC precursors. This result validates the applied synthesis method for obtaining SDC single phase powder.

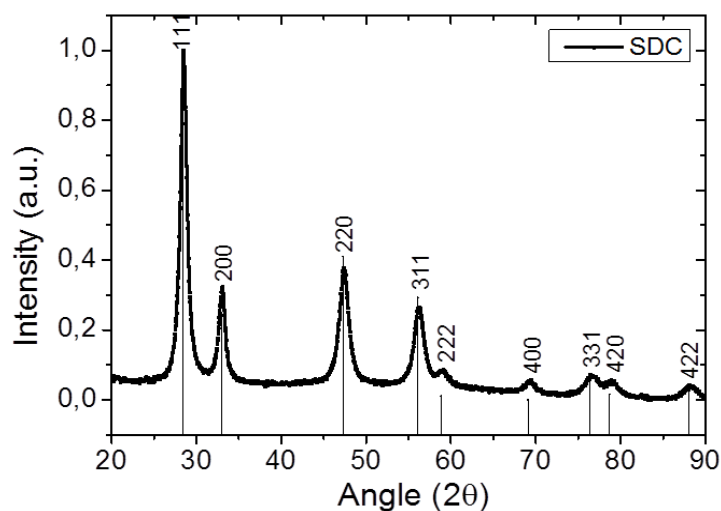


**Figure 3.6:** XRD of synthesised SDC mesoporous powder at 600 °C. The reflexions are indexed according to the *Fm-3m* cubic space group.

The confirmation of the SDC phase and of the periodic distribution of the pore network support the selected approach, which is based on the homogeneous infiltration of the SDC ceramic scaffold with catalytic active electrode material to be applied as a SOEC oxygen electrode.

### 3.2.3. Structural characterization of mesoporous $\text{Ce}_{0.8}\text{Gd}_{0.2}\text{O}_{1.9}$ (CGO)

In this case, CGO mesoporous material is characterized. Gadolinium ( $\text{Gd}(\text{NO}_3)_3 \cdot 6\text{H}_2\text{O}$ ) and cerium ( $\text{Ce}(\text{NO}_3)_3 \cdot 6\text{H}_2\text{O}$ ) nitrates were used as precursors for the impregnation of commercial mesoporous silica KIT-6 (KIT-6-commercial), following the hard template method previously described in the **section 2.2.3**.

Mesoporous CGO will be also functionalized as SOEC oxygen electrode through its infiltration with the same previously described goal: increasing the active points (TPB) for the electrochemical reactions.

The mesoporosity and periodicity of synthesised CGO powders were structurally characterized applying different techniques. On one hand, the mesoporosity of synthesised CGO powders, specifically its surface area and pore size distribution, were determined using  $\text{N}_2$ -physisorption measurements. On the other hand, the periodicity of the material was studied applying LA-XRD [11]. **Figure 3.7a** shows the  $\text{N}_2$  adsorption-desorption isotherm of synthesised CGO powder. As it has been previously explained for SDC (**section 3.2.2**), it is possible to distinguish between six different types of isotherms according to the pore size. The isotherm shown in **Figure 3.7a** is classified as Type IV, as it was for the SDC. Its first zone corresponds to the preliminary monolayer and multilayer adsorption. The remaining pore space is filled by capillary condensation typical of mesoporous materials, which generates a hysteresis loop. In this case, the observed hysteresis loop corresponds to Type H1, typical for materials with uniform and ordered spheres with confined pore sizes distributed. Besides, the obtained isotherm and hysteresis loops are characteristics of KIT-6 [6]. This fact verifies the applied hard-template method for transferring the mesoporous structure from the template to the replica. BET specific surface area of  $97 \pm 2 \text{ m}^2/\text{g}$  was obtained by applying the Brunauer-Emmett-Teller method. The BJH method was applied to the obtained desorption isotherm curve for studying the pore size distribution of

synthesised CGO mesoporous material, mainly centred in 3 nm, as shown in **Figure 3.7b**. It is also observed a contribution around 20 nm probably forming a pore size distribution due to the commercial KIT-6 synthesis temperature.

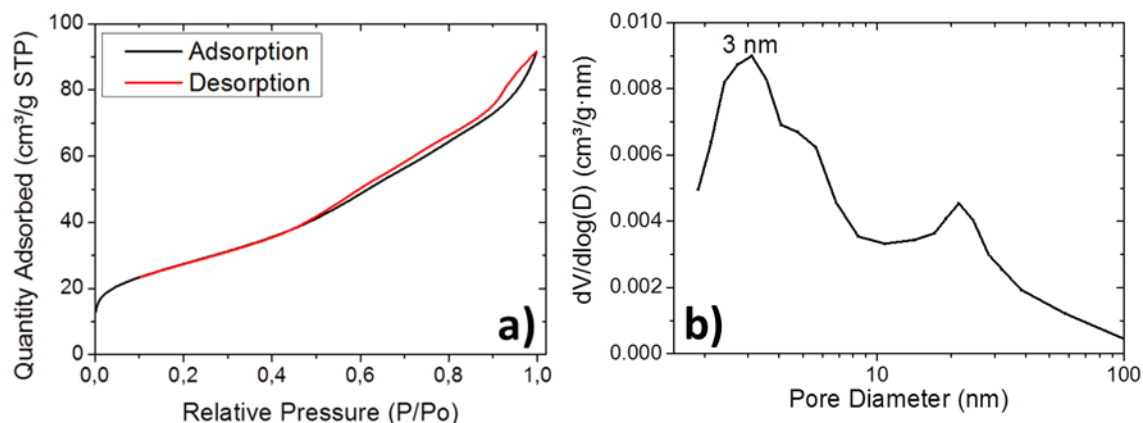


**Figure 3.7:** BET characterization of mesoporous synthesised CGO material a) experimentally obtained Type IV isotherm with characteristic hysteresis loop b) pore size distribution.

As it has been previously introduced, LA-XRD (**Figure 3.8**) was performed in order to study the periodicity of the mesoporosity of the CGO synthesised powder [11]. The KIT-6-commercial pattern shows a main sharp peak at  $2\theta=0.97^\circ$  indexed as (211) and a weak one at  $2\theta=1.12^\circ$  indexed as (220) [6]. The CGO replica presents the same main peak (211) slightly shifted. That shift could be assigned to a difference of the periodicity-lattice parameter of the two compared structures. However, since in this case CGO was synthesised as replica of KIT-6-commercial template, the same periodicity-lattice parameter should have been obtained for both template and replica or a slight shrinkage of the CGO structure occurred during the synthesis process. The analysis of the LA-XRD reveals that the ordered mesoporous structure is successfully transferred from KIT-6-commercial template (*la3d* symmetry) to the CGO replica, which shows the same group of symmetry [6,11]. In this case, the lattice is the sum of the pore size and the wall thickness. According to the position of the characteristic (211) diffraction peak and applying the Bragg's law, the periodicity-lattice parameter of the mesoporous periodicity is 21 nm.

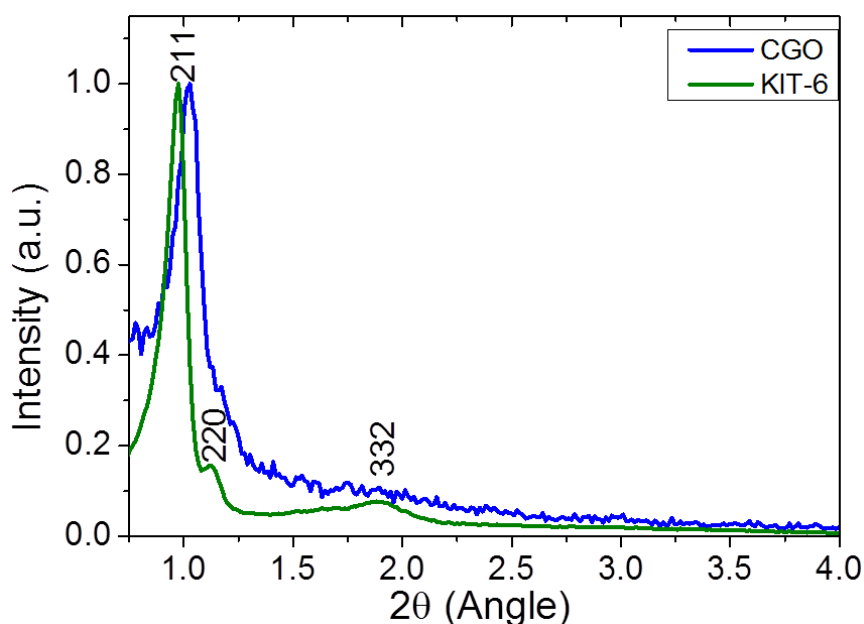


**Figure 3.8:** LA-XRD diffractograms of the typical KIT-6 template and the CGO obtained replica after removal of the silica.

Scanning and transmission electron microscopies (SEM and TEM) techniques were employed for the microstructural characterization of the obtained CGO mesoporous powder after its synthesis and cleaning process. Micrographs obtained from this characterization are presented in **Figure 3.9**. The SEM image (**Figure 3.9a**) shows a set of mesoporous particles where it is possible to see the ordered structure mainly in all particles, what confirms the success of the applied synthesis method and their periodic structure, previously characterized by applying LA-XRD. To analyse the morphology and confirm the pore size value obtained from the  $N_2$ -physisorption measurement, the samples were also observed by TEM, which also allows the analysis of the periodic nanoporosity characteristic of mesoporous materials. TEM confirms the replication of the silica template since the CGO pore size and wall thickness measured in the image presented in **Figure 3.9b** are similar to the ones obtained for the SDC and commercial KIT-6 pore sizes measured applying  $N_2$ -physisorption technique. Note that the presented image clearly shows the pore network of a single mesoporous particle. As consequence of that structure, it is proved that synthesised CGO backbone can be infiltrated to be functionalized as a SOEC oxygen electrode.

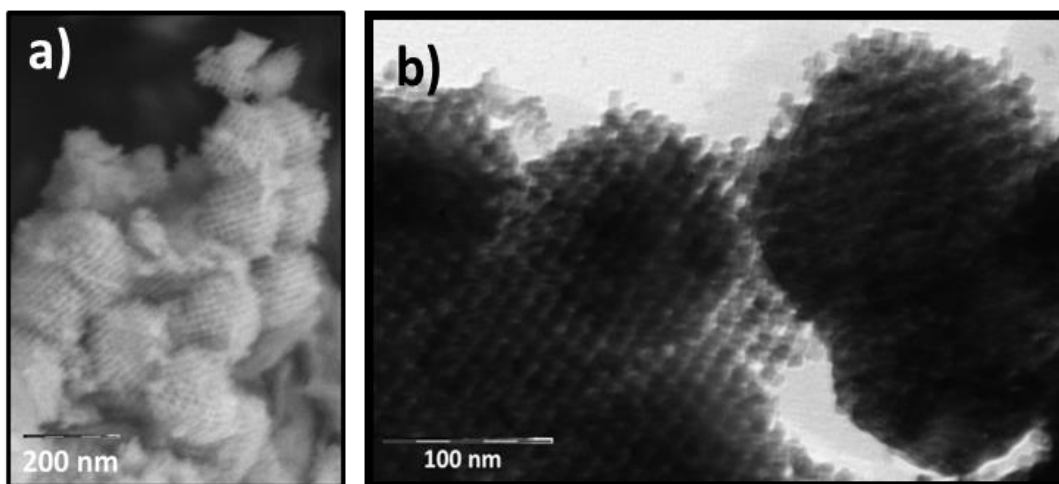


**Figure 3.9:** SEM and TEM images of synthesised CGO mesoporous powder.

X-ray diffraction was performed to characterise the obtained phase. The X-Ray diffractogram, presented in **Figure 3.10**, shows a main peak pattern indexed as simple cubic phase with space group  $Fm-3m$  and lattice parameter  $a=5.43 \text{ \AA}$ , which is characteristic of the CGO and confirms the obtained phase after the thermal treatment at  $600 \text{ }^\circ\text{C}$  for 5 h of the synthesised powder without any secondary or parasitic phase.

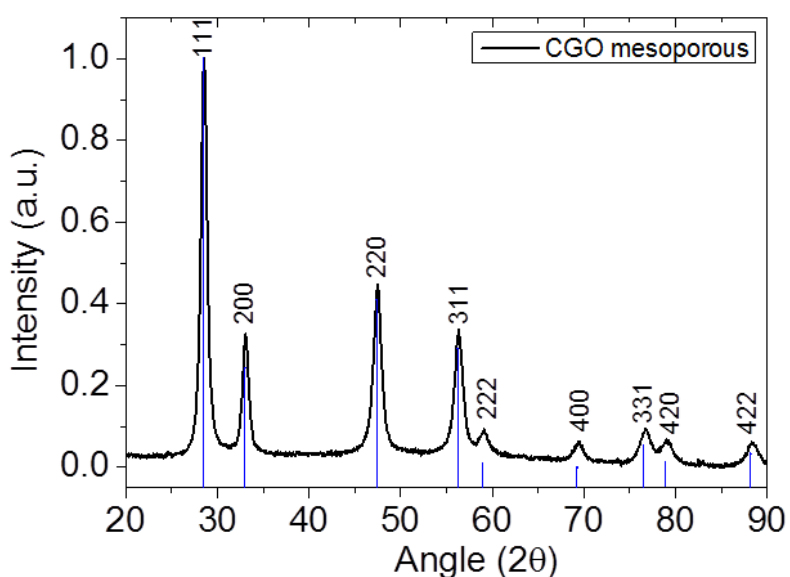


**Figure 3.10:** XRD of synthesised CGO mesoporous powder at  $600 \text{ }^\circ\text{C}$ . The reflections are indexed according to the  $Fm-3m$  space group.

#### 3.2.4. Structural characterization of mesoporous NiO

The present section includes the studies of the structural characterization of NiO mesoporous powders, which were synthesised by applying the hard-template method. In this case, KIT-6-90 powder was impregnated by  $\text{Ni}(\text{NO}_3)_2 \cdot 6\text{H}_2\text{O}$  as Ni precursor. Further details about the synthesis of mesoporous replicas are explained in **section**

**2.2.3.** Until now, the presented materials were employed for the fabrication of the oxygen electrodes of SOEC. In this case, the obtained mesoporous NiO was employed for the synthesis of a NiO-SDC cermet to be applied as fuel electrode. This material structure was equally characterized by N<sub>2</sub>-physisorption measurements, LA-XRD, XRD and SEM.

According to the already characterized SDC and CGO mesoporous materials, N<sub>2</sub>-physisorption measurements of the synthesised and cleaned mesoporous NiO mesoporous surface were performed to determine its specific surface area and pore size distribution. The application of the BET method defined surface areas of  $72 \pm 9$  m<sup>2</sup>/g from the N<sub>2</sub> adsorption-desorption isotherm. The shape of the isotherm brings information for determining the pore size distribution of the studied material. As it is explained in **section 2.6.2** and for previously studied SDC and CGO synthesised materials, the isotherm presented in **Figure 3.11a** for NiO mesoporous material is Type IV. Its hysteresis is classified as H1, characteristic of mesoporous structures. The isotherm and its characteristic hysteresis loop presented in **Figure 3.11a** allow confirming the mesoporosity of the NiO material.

The application of the BJH method to the N<sub>2</sub>-physisorption isotherm determined the pore size distribution presented in **Figure 3.11b**, which is mainly centred in 3.5 nm. Besides, a huge pore sizes distribution is observed from 13 nm to more than 100 nm [3,7,10].

As it has been previously explained in **section 2.2.2**, it is possible to control the proportion of larger and smaller pores sizes varying the KIT-6 synthesis temperature, which tunes its microstructure. The literature shows that temperatures higher than 90 °C are usually applied with the aim of ensuring the formation of micropores connecting both KIT-6 sets of mesopores [10]. According to this, the important proportion of pores of 13 nm (**Figure 3.11**) shows that the temperature of 90 °C was not high enough for ensuring the formation of micropores connecting both mesoporous channels, and as a consequence of that, both sets of mesopores were disconnected in some particles of the KIT-6-90, leading to the existence of a differentiated second pore size contribution in the NiO mesoporous material. Based on that, the distribution of larger pores sizes observed in **Figure 3.11** probably represents

the interparticle porosity. This result is consistent with the pore size distribution of synthesised mesoporous SDC, in which a higher proportion of the 13 nm pore was obtained because of the lower (36 °C) KIT-6 synthesis temperature.

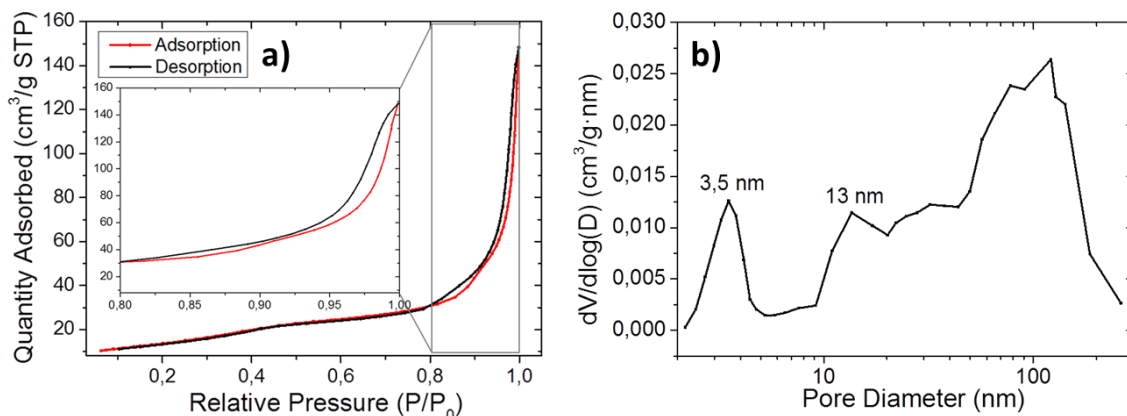


**Figure 3.11:** a) N<sub>2</sub> adsorption-desorption isotherm material and b) pore size distribution of mesoporous synthesised NiO.

In order to study the transference of the periodicity of the structure from the KIT-6-90 mesoporous template to the NiO mesoporous replica, LA-XRD was performed from  $2\theta=0$  to  $4^\circ$  on both the template and replica materials. **Figure 3.12** shows that the synthesised NiO replica maintained the cubic *1a3d* symmetry characteristic from the used template [6,7,8,10], keeping the main diffraction peak indexed as (211) at  $2\theta=0.91^\circ$ , another diffraction indexed as (220) at  $2\theta=1.07^\circ$ , and a width peak indexed as (332) at  $2\theta=1.78^\circ$  [12]. As it can be clearly seen, the diffractogram of NiO is very similar to the characteristic one of KIT-6-90. According to the position of the characteristic (211) diffraction and applying the Bragg's law, it was possible to calculate the periodicity-lattice parameter of the cubic cell of the KIT-6-90 and NiO that resulted on 24 nm, in both cases, also confirming the transference of the mesoporous periodic structure from the template to the metal oxide replica.

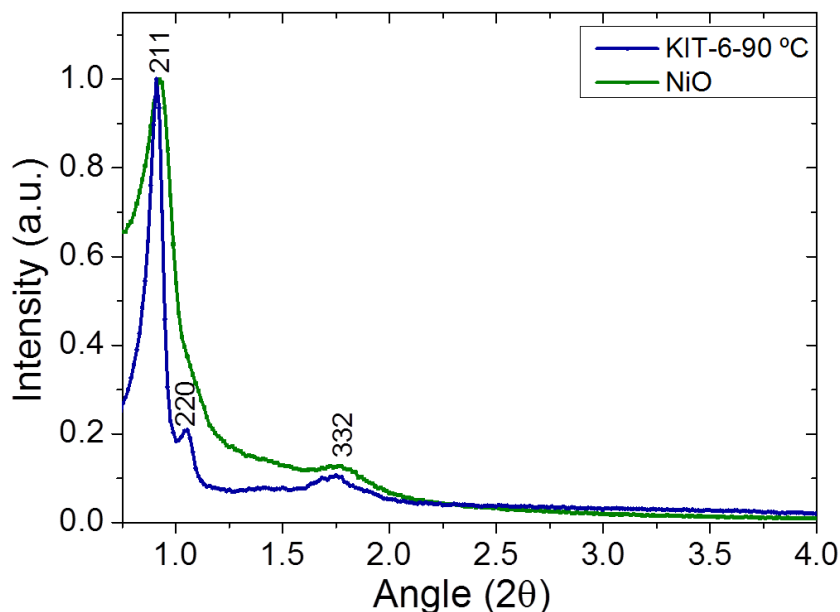


**Figure 3.12:** LA-XRD of KIT-6 mesoporous pattern and the obtained NiO mesoporous replica.

Scanning and transmission electron microscopies images of NiO synthesised at 600 °C, and after being cleaned from silica are presented in **Figure 3.13**. The SEM micrograph (**Figure 3.13a**) allows a general observation of the periodic mesoporous structure replicated from the template to most of the particles of the synthesised NiO, confirming the success of the applied approach. The inset micrograph of the **Figure 3.13a** shows a higher magnification to observe clearer the ordered and repeated pore network. **Figure 3.13b** shows the replicated pore network of a NiO particle by transmission microscopy (TEM) and allows confirming the pore size determined from the N<sub>2</sub>-physisorption measurements. The NiO wall thickness measured in this TEM image fits with the KIT-6-90 pore size determined by N<sub>2</sub>-physisorption measurements (**section 3.2.1**), validating the hard-template method for the NiO synthesised material, as previously confirmed by other characterization techniques as LA-XRD and N<sub>2</sub>-physisorption measurements. This NiO synthesised mesoporous material was later impregnated and functionalized as a fuel electrode.

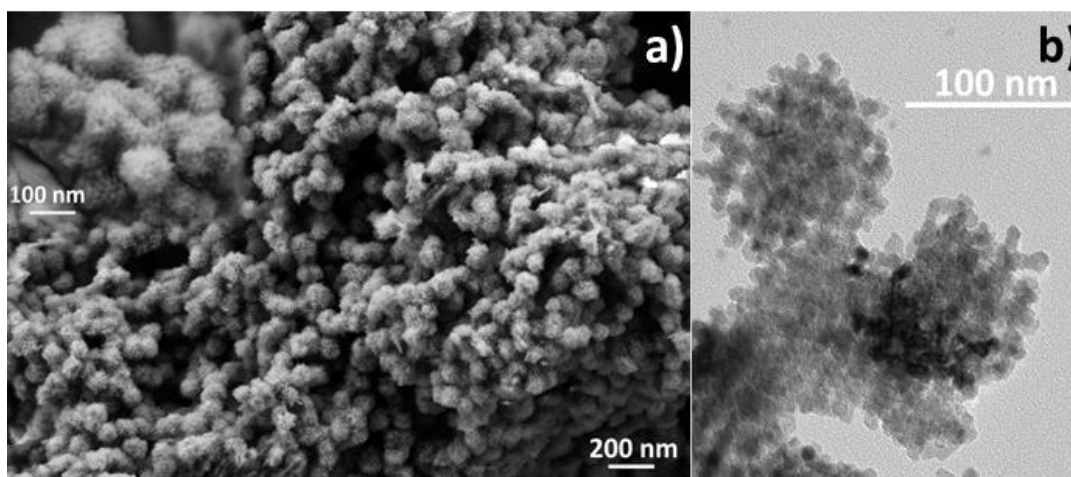


**Figure 3.13:** NiO periodic mesoporous structure observed by a) SEM and b) TEM.

The X-Ray diffractogram of **Figure 3.14** presents the NiO mesoporous powder phase. According to the NiO reference, the synthesised mesoporous material is indexed as a cubic phase with  $Fm-3m$  space group and the lattice parameter is  $a=4.18$  Å. No secondary phases or deviations from the desired phase are observed validating the synthesis procedure for obtaining it.

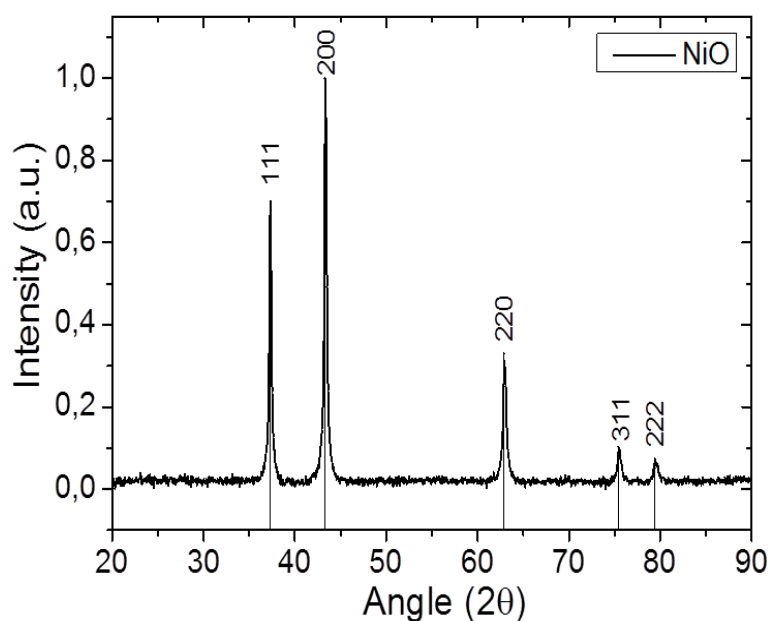


**Figure 3.14:** XRD of synthesised NiO mesoporous powder at 600 °C. The reflections are indexed in the  $Fm-3m$  space group.

### 3.3. Structural characterization of fabricated mesoporous electrodes

In order to improve the state of the art electrodes, this work presents the approach of infiltrating mesoporous ceramic materials to fabricate nanocomposites.

### 3.3.1. Structural characterization of Sm<sub>0.2</sub>Ce<sub>0.8</sub>O<sub>1.9</sub> (SDC)-Sm<sub>0.5</sub>Sr<sub>0.5</sub>CoO<sub>3-δ</sub> (SSC) oxygen electrodes

Sm<sub>0.2</sub>Ce<sub>0.8</sub>O<sub>1.9</sub> mesoporous powder was successfully synthesised and its mesoporosity, periodicity and crystallinity were confirmed through the application of different characterization techniques. The infiltration of this ceramic material with a catalytic active material was needed in order to functionalize it as Mixed Ionic and Electronic Conductor (MIEC) oxygen electrode [13-15]. The thermal evolution of the Sm<sub>0.5</sub>Sr<sub>0.5</sub>CoO<sub>3-δ</sub> phase after the infiltration of the SDC scaffold, and the optimal attachment temperature of the ceramic SDC to the electrolyte were studied under different temperatures.

The SDC ionic conductor mesoporous scaffold material was infiltrated with the catalytic active SSC material (**section 2.4.4**) in order to generate the SDC-SSC nanocomposite [16]. In order to check the phase compatibility of the composite compound, high temperature-XRD was carried out up to 850 °C. The evolution of both phases was followed measuring X-Ray diffractograms within an “in-situ” XRD temperature chamber, where the measurements were performed at room temperature (25 °C), heating up to 50 °C and from 500 °C to 850 °C every 50 °C, and at cooling down following the same temperature steps. The X-Ray diffractograms recorded for the SDC infiltrated by SSC at different temperatures, as well as the reference pattern for both SDC and SSC are showed in **Figure 3.15** [11]. The SDC presents a cubic phase as previously explained in **Figure 3.6**. The SSC, formed by interdiffusion of the cations provided by the nitrates precursors after the thermal treatment at 800 °C, presents the expected orthorhombic phase with *Pnma* space group and lattice parameter of  $a=5.40$ ,  $b=7.58$  and  $c=5.36$  Å in agreement with what has reported the literature [16]. The diffraction peaks widths along the diffractogram decreased after the thermal treatment due to the increase of the grain size. Besides, a shifting to lower angles can be observed in the diffraction reflections as expected when increasing the temperature, i. e. corresponding to a thermal expansion. Both SDC and SSC keep the reflection angle and the relative intensity of the pattern. An unknown secondary phase ( $2\theta\approx 31.5^\circ$ ) starts to form at 850 °C. Since the maximum temperature to reach by these SOEC cells is 750 °C, during operation, and 800 °C,

during the fabrication, we can consider this composite stable under our conditions. However, it will be important to pay attention to this secondary phase formation, especially in long-term tests and when hot spots formation is expected.

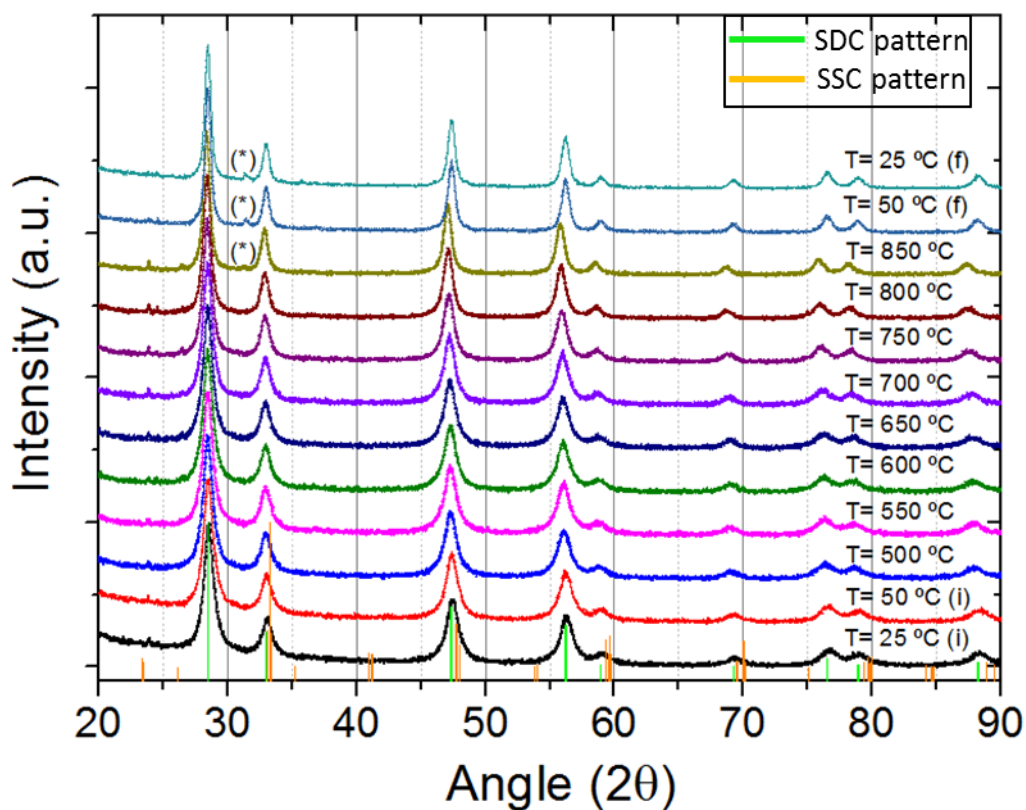


**Figure 3.15:** X-Ray diffractograms of SSC infiltrating SDC mesoporous powder recorded for at 25 °C, heating up at 50 °C and from 500 to 850 °C, and at 50°C and 25°C during the cooling down.

### 3.3.2. Structural characterization of $\text{Ce}_{0.8}\text{Gd}_{0.2}\text{O}_{1.9}$ (CGO)- $\text{La}_{0.6}\text{Sr}_{0.4}\text{Co}_{0.2}\text{Fe}_{0.8}\text{O}_3$ (LSCF) oxygen electrodes

The previously discussed structural characterization of synthesised mesoporous CGO (**section 3.2.3**) has confirmed the hard-template method for obtaining the CGO phase with a mesoporous periodic structure. According to this, the here proposed electrode consists on an intimately connected nanocomposite composed by the CGO ionic conductor and  $\text{La}_{0.6}\text{Sr}_{0.4}\text{Co}_{0.2}\text{Fe}_{0.8}\text{O}_3$  catalytically active and MIEC to obtain an optimised nanocomposite electrode. Similar to the previously reported SDC-SSC, the CGO-LSCF is studied in this section. Special attention is paid to the study of the percolation of the LSCF as electron conductive phase as a critical parameter for the optimal performance of a composite oxygen electrode in SOEC.

The mesoporous network of synthesised CGO powder was infiltrated to form the LSCF as the catalytic active material in order to attain a functionalized IC-MIEC oxygen electrode nanocomposite. The followed infiltration process was detailed in the **section 2.4.4**. A systematic and precise control of the infiltration volume, which was adjusted to the volume of the mesoporous backbone, was studied and is discussed in this section with the aim of optimising the infiltration procedure [17-19]. Note that an excess of the infiltration solution or too quick evaporation of the solvent could block the mesopores. As a consequence, the active phase precursors appear accumulated on top of the mesoporous layers, which results in a thin layer of material associated with high resistance that decreases the electrode performance. After different tests and their microstructural characterisation, the total infiltration volume/scaffold thickness ratio of required solution for the infiltration is around  $8\pm 1 \mu\text{L}/\mu\text{m}$ , as it is demonstrated in **Chapter 4**.

As described in **section 2.4.4**, the infiltration process has to be performed by three separate infiltration steps (10  $\mu\text{L}$  are dispersed in each one according to the optimized volume). Each of them are followed by a thermal treatment up to 500 °C in order to eliminate the organic phase and reorganise the cations, and a final step at 800 °C to achieve the desired LSCF phase [20].

To confirm that the desired phase was obtained, XRD was performed to the CGO-LSCF nanocomposite. The result and its corresponding patterns are presented in **Figure 3.16**. According with what has been already discussed in **Figure 3.10**, it is confirmed that the presented CGO phase belongs to the cubic *Fm-3m* space group. The LSCF phase is indexed as cubic with space group *Pm-3m* and a lattice parameter of  $a=3.84 \text{ \AA}$ , in concordance with the presented pattern [21]. Presented X-Ray diffractogram fits with the pattern corresponding to each of both phases, confirming that the CGO-LSCF composite has been obtained. This result confirms the successful synthesis of the CGO and of the correct LSCF phase through the adopted procedure of infiltration, and validates the presented method for the fabrication of CGO-LSCF composites to be functionalized as oxygen electrode.

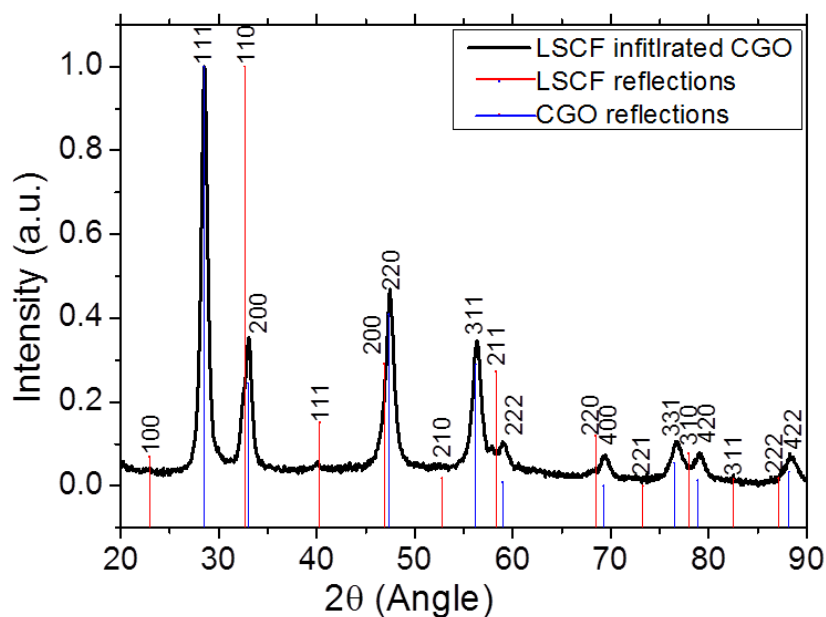


**Figure 3.16:** XRD of synthesised CGO sintered at 900 °C, infiltrated and thermally treated up to 800°C to get the LSCF phase. CGO and LSCF diffraction peaks were indexed according to *Fm-3m* and *Pm-3m* space groups, respectively.

### 3.3.3. Structural characterization of NiO-Sm<sub>0.2</sub>Ce<sub>0.8</sub>O<sub>1.9</sub> (SDC) fuel electrodes

Mesoporous NiO was structurally characterized in **section 3.2.4** where the obtained results demonstrated the success of the hard-template method using KIT-6-90 as mesoporous template. For its functionalization as fuel electrode material, mesoporous NiO was impregnated with SDC, synthesising the NiO-SDC cermet based on mesoporous materials. This section presents the characterization of the synthesised NiO-SDC mesoporous nanocomposite. Note that in this case, the approach is different since the former material is the active phase and the synthesis is not designed to generate an infiltration that produces a thin active layer film, but the generation of a composite through the intimate mixture of both phases.

Firstly, the X-Ray diffractogram of SDC impregnating NiO was recorded at room temperature obtaining the expected NiO-SDC composite diffraction peaks, shown in **Figure 3.17** as well as both SDC and NiO patterns [16]. SDC and NiO present the same cubic structure and space group (*Fm-3m*) that has been previously reported in **Figure 3.6** and **Figure 3.14**, respectively.

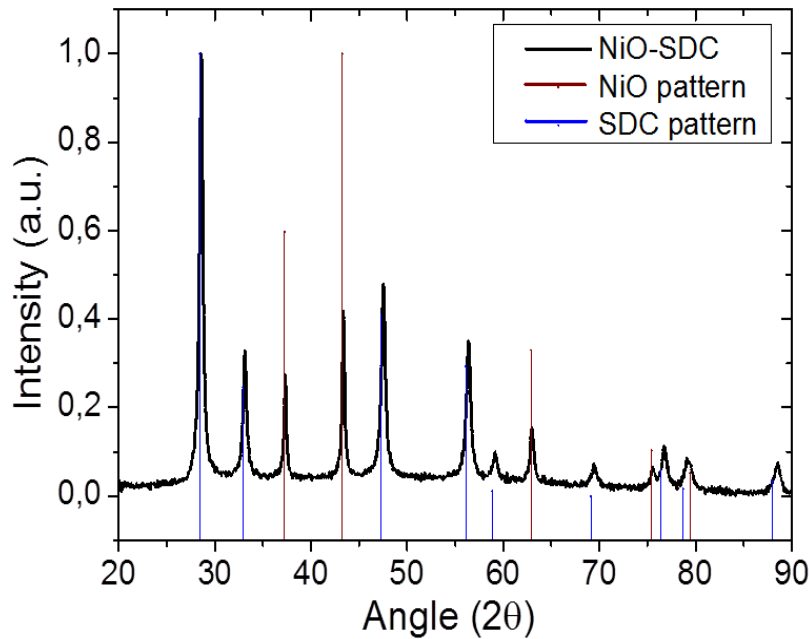


**Figure 3.17:** XRD diffractogram of mesoporous SDC impregnating NiO, resulting in SDC-NiO powder after a thermal treatment up to 600 °C.

The obtained results approve the successful synthesis of this NiO-SDC composite. As a consequence, this composite based on mesoporous ceramics is presented as an alternative fuel electrode material to be deposited on Electrolyte-Supported Cells (ESCs).

### **3.4. Optimization of oxygen electrodes based on mesoporous materials on symmetric cells**

Once the proper synthesis of the composites to be used as oxygen electrodes has been validated, the fabrication of symmetric cells is needed to optimize the attachment of the oxygen electrodes to the electrolyte. The resistance derived from a poor optimization of the attachment of the electrodes is considered one of the major sources of voltage drop in the final device. This is especially important in the case of mesoporous materials becoming one of the main challenges in the fabrication of solid oxide cells based on these materials.

All the ESCs used for the fabrication of oxygen electrode symmetrical cells have a circular shape of  $\approx 1.90$  cm in diameter. They were fabricated by tape casting and supplied by FAE S.A.U (Spain) [22]. These cells were based on 6Yb4ScSZ sintered tapes of 200  $\mu\text{m}$  in thickness.

A study using different IC ceramic scaffolds and applying different thermal treatments was carried out in order to overcome the issues of the adhesion between the mesoporous scaffold and the electrolyte while keeping nanostructured electrodes. It is important to consider that, in spite of the durability problems associated to nanostructures when they are used in energy applications, the stability of mesoporous materials such as CGO and SDC has been demonstrated at temperatures up to 1000 °C, confirming the possibility of employing these high surface area mesoporous metal oxide materials for high-temperature applications [11]. Moreover, following what had been reported by Kleinlogel *et al.* [23], where the use of cobalt (Co) for doping CGO is presented with the aim of increasing the material density at lower temperatures, the use of Co has been also explored. The role of cobalt as a sintering aid was analysed in order to minimize the sintering temperature while optimizing the attachment keeping the mesostructure of the powder.

Pure SDC powder was impregnated with cobalt nitrate ( $\text{Co}(\text{NO}_3)_3 \cdot 6\text{H}_2\text{O}$ ) as a precursor to synthesise mesoporous samarium doped ceria with 2% molar of cobalt (SDC-Co) [24] A detailed description of the applied impregnation procedure for the synthesis of this material is explained in **section 2.3.2**.

In order to explore different possible ways for fabricating the optimal mesoporous scaffold for the oxygen electrode, six different options were prepared on electrolyte-supported symmetrical cells. The mesoporous scaffold was changed from SDC and SDC-Co for studying the different attachment temperatures at 800, 900 and 1000 °C to the electrolyte. **Table 3.2** lists all the fabricated samples with the oxygen electrode composition and attachment temperature.

Sample name	Oxygen electrode material	Attachment temperature (°C)
SDC 800	$\text{Sm}_{0.2}\text{Ce}_{0.8}\text{O}_2 - \text{Sm}_{0.5}\text{Sr}_{0.5}\text{CoO}_3$	800
SDC 900	$\text{Sm}_{0.2}\text{Ce}_{0.8}\text{O}_2 - \text{Sm}_{0.5}\text{Sr}_{0.5}\text{CoO}_3$	900
SDC 1000	$\text{Sm}_{0.2}\text{Ce}_{0.8}\text{O}_2 - \text{Sm}_{0.5}\text{Sr}_{0.5}\text{CoO}_3$	1000
SDC-Co 800	$\text{Sm}_{0.2}\text{Ce}_{0.8}\text{O}_2 - 2\%\text{Co} - \text{Sm}_{0.5}\text{Sr}_{0.5}\text{CoO}_3$	800
SDC-Co 900	$\text{Sm}_{0.2}\text{Ce}_{0.8}\text{O}_2 - 2\%\text{Co} - \text{Sm}_{0.5}\text{Sr}_{0.5}\text{CoO}_3$	900
SDC-Co 1000	$\text{Sm}_{0.2}\text{Ce}_{0.8}\text{O}_2 - 2\%\text{Co} - \text{Sm}_{0.5}\text{Sr}_{0.5}\text{CoO}_3$	1000

**Table 3.2:** Composition and characteristic attachment temperatures of prepared oxygen electrode based symmetrical cells.

As explained in **section 2.5.1**, the fabrication of the oxygen electrode consisted on the deposition of SDC on top of the CGO barrier layer by air brushing, followed by a thermal treatment up to the studied attachment temperature (**Table 3.2**). Therefore, all the cells were infiltrated as described in previous sections. A micrograph of the electrolyte-oxygen electrode interface of a symmetrical cell where the SDC mesoporous scaffold was attached at 900 °C is presented in **Figure 3.18**. This cross-section shows the fabrication of a homogeneous SDC-SSC layer, which is well attached to the CGO barrier layer.

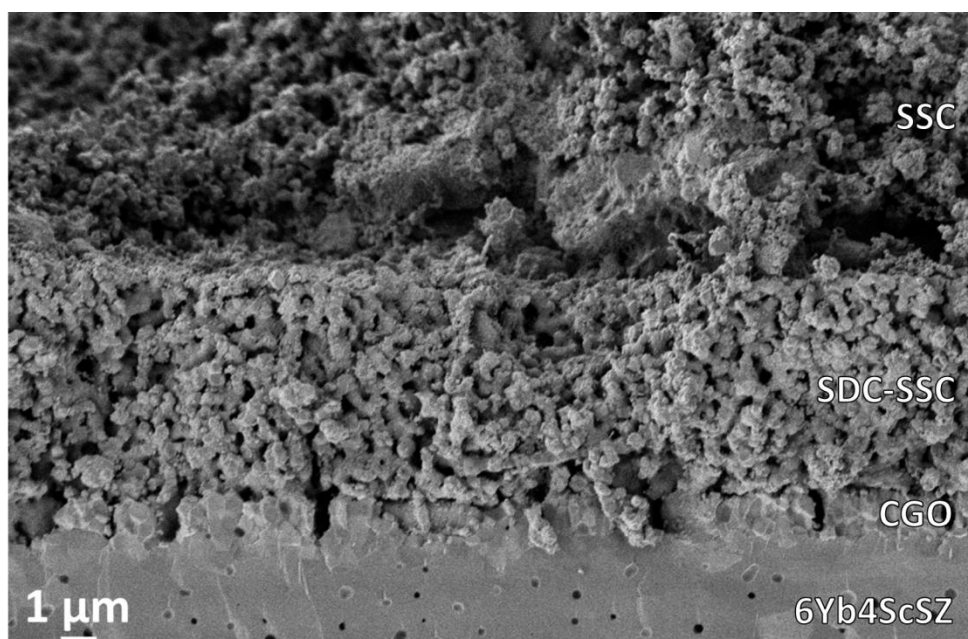


**Figure 3.18:** SEM cross-section micrograph of the electrolyte-oxygen electrode interface of a symmetrical cell in which the SDC mesoporous scaffold was attached to the electrolyte at 900 °C.

Electrochemical Impedance Spectroscopy (EIS) measurements of prepared symmetrical cells based on ceramic SDC or SDC-Co scaffolds were measured at 750 °C under equilibrium voltage and the same atmosphere composition for both electrodes. Obtained Nyquist plots are presented in **Figure 3.19**, where the serial and polarization resistance measured for each symmetrical cell can be followed.

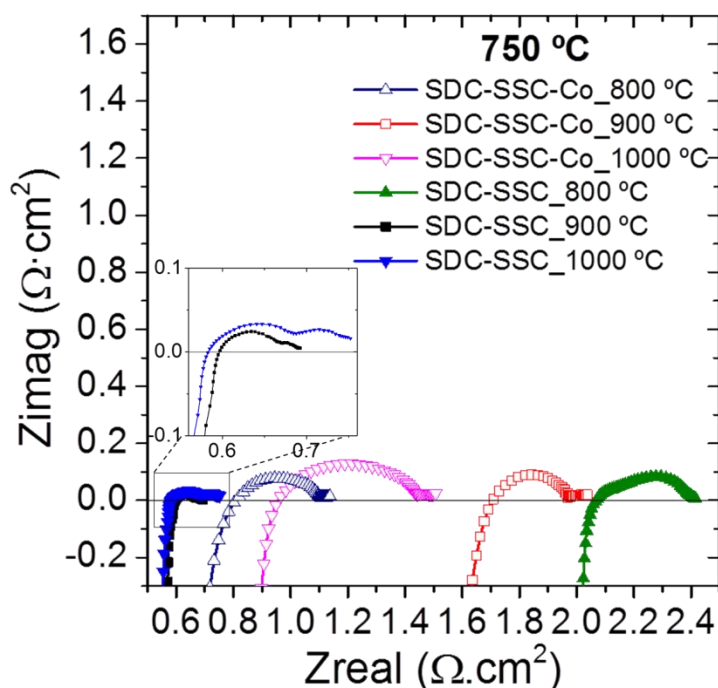


**Figure 3.19:** Nyquist plot of the six prepared SDC and SDC-Co symmetrical cells attached at 800, 900 and 1000 °C from EIS measurements at 750 °C.

The serial and polarization resistances obtained from the fitting of the EIS measurements to an equivalent circuit (see below) were evaluated in order to optimize the attachment temperature of the ceramic scaffold to the electrolyte. Presented values were obtained by fitting measured Nyquist arcs with the equivalent circuit  $LR_s(R_1Q_1)(R_2Q_2)$  composed of an inductance  $L$ , a serial resistance  $R_s$ , and two contributions of the polarization resistance,  $R_1Q_1$  and  $R_2Q_2$ . The  $L$  element presents the contribution of the experimental set-up, and it is usually observed in the Nyquist plot of SOEC measured in standard stations. The serial resistance is associated with the electrolyte resistance and other in series ohmic contributions, including the current collection losses and the contact resistance in the interfaces, which can be reduced optimising the attachment of the mesoporous scaffold to the electrolyte. The  $RQ$  elements of the equivalent circuits indicate a circuit of resistance ( $R$ ) in parallel with a Constant Phase Element (CPE) substituting a pure capacitance ( $C$ ). This CPE ( $Q$ ) is a constant phase element associated to a distribution of relaxation frequencies, and a depression angle represented by  $n$  ( $0 \leq n \leq 1$ ). The capacitance values allow identifying different electrochemical processes occurring in the electrodes. Arrhenius plots of the serial and polarization resistances of SDC-SSC and SDC-Co-SSC oxygen electrode symmetrical cells are presented in **Figure 3.20** and **Figure 3.21**, respectively. As it can

be seen in both figures, the obtained values of the serial and polarization resistances show important differences as a function of the use of cobalt in the mesoporous SDC, and of the applied attachment temperature.

Regarding the serial resistance (**Figure 3.20**), the obtained values are close the literature reported for ScSZ electrolytes in the range from 650 °C to 850 °C (for the same area and thickness) [25,26]. These values are normalized to the thickness of the electrolyte, which is  $200\pm 20$   $\mu\text{m}$ . The best attachments, resulting in the lowest associated resistances, are achieved by SDC-SSC and SDC-Co-SSC symmetrical cells attached at 1000 °C. It is also observed that SDC-SSC thermally treated up to 900 °C presents very similar serial resistance value than SDC-Co-SSC treated at 1000 °C.

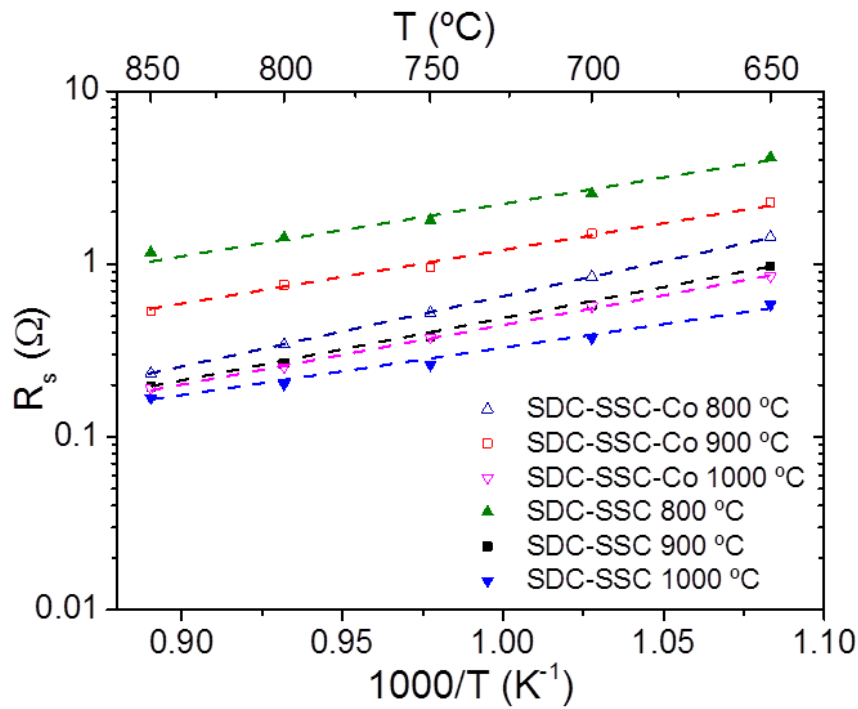


**Figure 3.20:** Arrhenius plot of the serial resistance ( $R_s$ ) for different symmetrical cells attached at 800, 900 and 1000 °C measured in the temperature range between 650 and 850 °C.

Regarding the total polarization resistances (**Figure 3.21**), the best values,  $R_p = 0.037 \Omega \cdot \text{cm}^2$ , were measured at 850 °C for the infiltrated SDC based oxygen electrode attached at 900 °C. These values of polarization resistance are below the target value of  $0.25 \Omega \cdot \text{cm}^2$ , which defines a reasonable performance of the cells, at temperatures as low of 750 °C for attachments carried out at  $T > 900$  °C.

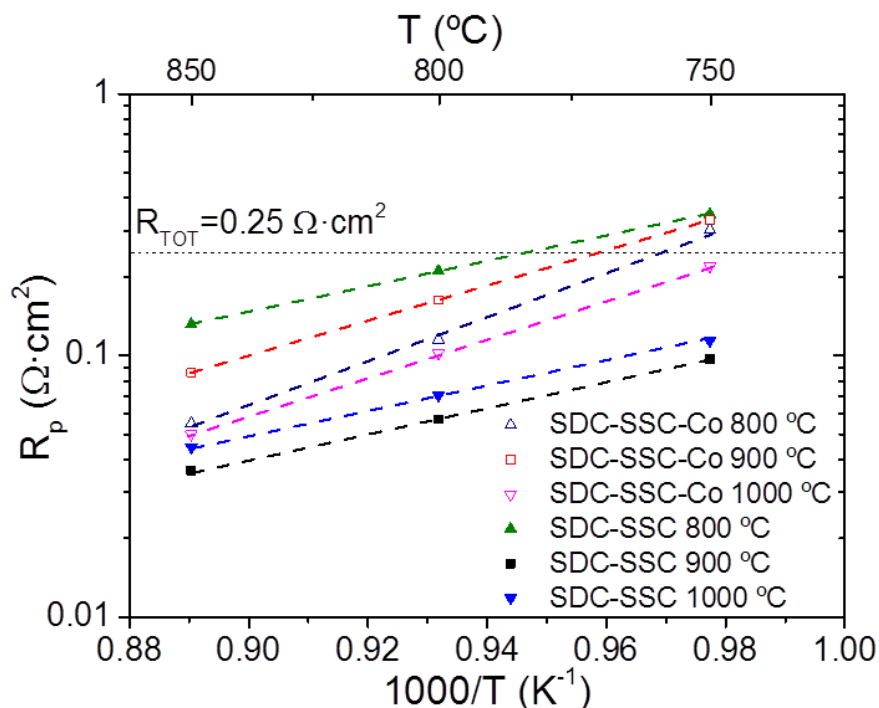


**Figure 3.21:** Arrhenius plot of the total polarization resistances ( $R_p$ ) of the different oxygen electrode SDC-SSC or SDC-Co-SSC symmetrical cells measured at 750, 800 and 850 °C SOEC operation temperatures.

In order to confirm the mesoporosity after this high temperature thermal treatments,  $N_2$ -physisorption analyses were performed in SDC and SDC-Co after seeing temperatures up to 900 and 1000 °C (**Table 3.3**). A progressive decrease of the BET surface area was observed when the thermal treatment temperature was increased up to 1000 °C due to a reduction of the pore size and shrinkage of the whole structure [11]. SDC and SDC-Co sintered at 900 °C presented higher surface area than the equivalent ones sintered at 1000 °C. Moreover, these values show that the addition of cobalt resulted in a decrease of the high surface area and porosity characteristic of mesoporous synthesised materials.

	Temperature (°C)	BET ( $m^2/g$ )
SDC	900	$39.6 \pm 0.3$
SDC-Co	900	$32.9 \pm 0.3$
SDC	1000	$25.7 \pm 0.2$
SDC-Co	1000	$13.5 \pm 0.1$

**Table 3.3:** Structural parameters obtained from  $N_2$ -physisorption analysis for SDC and SDC-Co treated up to 900 and 1000 °C.

Summarizing, since the serial and polarization resistances reveal that the addition of cobalt does not show a significant electrochemical improvement in the studied temperature range, the addition of Co was discarded for this work. Opposite, SDC

attached at 900 °C represents the optimized configuration for the fabrication of oxygen electrodes according to the presented BET values (**Table 3.3**), and resistance contributions (**Figure 3.19 to 2.21**), being our choice for the rest of this thesis.

### 3.5. Conclusion

Based on the application of the hard-template method, this chapter presents the synthesis and characterization of mesoporous materials for SOC electrodes. As basis for performing the replication of the powder structure, the mesoporosity of synthesised and commercial KIT-6 have been confirmed by N<sub>2</sub>-physisorption and LA-XRD characterization techniques. BET surfaces areas higher than 700 m<sup>2</sup>/g and defined pore sizes ranging from 5 to 8 nm have been obtained changing the applied hydrothermal temperature from 36 to 90 °C.

The mesoporosity of SDC, CGO and NiO synthesised materials with a thermal treatment at 600 °C have been demonstrated. Characteristic isotherms and hysteresis loops of mesoporous materials, classified as Type IV and H1, respectively, have been showed. BET surface areas of 110 ± 15, 97 ± 2 and 72 ± 9 m<sup>2</sup>/g have been obtained for synthesised SDC, CGO and NiO mesoporous materials, respectively. Besides, different distribution of pores have been characterized according with the employed KIT-6, mainly centred in 5 and 13 nm for the SDC, in 3 nm for the CGO and in 3.5 nm for the NiO. The contribution of a main diffraction peak indexed as (211) has been characterized by LA-XRD for the three replicated structures and the templates, confirming the successful replication of the mesostructure.

Besides, according to the XRD analysis, the formation of the correct phase has been confirmed for the three synthesised material. Microscopy techniques (SEM and TEM) have been used to characterize the obtained periodically repeated mesoporous structures and have validated the employed synthesis method.

Mesoporous SDC and CGO ionic conductors have been functionalized as oxygen electrodes by its infiltration with SSC and LSCF catalytic solutions. Both SDC-SSC and CGO-LSCF phases have been characterized by XRD and the obtained diffractogram fits with what is reported in the literature, confirming the formation of a MIEC nanocomposite and approving the adopted infiltration procedure. The SDC-SSC phase

has been studied in a XRD temperature chamber, focusing on the formation of secondary phases at the SOEC fabrication and operation temperatures. Besides, XRD measurements have confirmed the successful synthesis of the NiO-SDC composite based on mesoporous materials. It has been demonstrated from these results the stability and compatibility of both phases in the range of temperatures of interest for this application.

For optimizing the fabrication of the oxygen electrode, the electrochemical characterization of symmetrical cells and N<sub>2</sub>-physisorption measurements have been studied. Electrolyte-supported symmetrical cells based on SDC and SDC-Co mesoporous scaffolds have been thermally sintered at 800, 900 and 1000 °C. From the combination of both techniques, it has been presented SDC sintered up to 900 °C and infiltrated with SSC as the optimized oxygen electrode configuration.

### 3.6. References

- [1] L. Almar, A. Morata, M. Torrell, M. Gong, T. Andreu, M. Liu, and A. Tarancón, "A Durable Electrode for Solid Oxide Cells: Mesoporous Ce<sub>0.8</sub>Sm<sub>0.2</sub>O<sub>1.9</sub> Scaffolds Infiltrated with a Sm<sub>0.5</sub>Sr<sub>0.5</sub>CoO<sub>3-δ</sub> Catalyst," *Electrochim. Acta*, vol. 235, pp. 646–653, 2017.
- [2] "KIT-6 commercial." [Online]. Available: <https://www.acsmaterial.com/kit-291.html>.
- [3] IUPAC, "Reporting physisorption data for gas / solid systems with special reference to the determination of surface area and porosity area International Union of Pure and Applied Chemistry," *Pure Appl. Chem.*, vol. 57, pp. 603–619, 1985.
- [4] F. Kleitz, S. Hei Choi, and R. Ryoo, "Cubic Ia3d large mesoporous silica: synthesis and replication to platinum nanowires, carbon nanorods and carbon nanotubes," *Chem. Commun.*, pp. 2136–2137, 2003.
- [5] K. Sing, "The use of nitrogen adsorption for the characterisation of porous materials," in *Colloids and Surfaces A: Physicochemical and Engineering Aspects*, 2001, vol. 187–188, pp. 3–9.
- [6] F. Kleitz, S. Hei Choi, and R. Ryoo, "Cubic Ia3d large mesoporous silica: synthesis and replication to platinum nanowires, carbon nanorods and carbon nanotubes," *Chem. Commun.*, pp. 2136–2137, 2003.
- [7] A. Ruplecker, F. Kleitz, E.-L. Salabas, and F. Schüth, "Hard Templating Pathways for the Synthesis of Nanostructured Porous Co<sub>3</sub>O<sub>4</sub>," *Chem. Mater.*, vol. 19, pp. 485–496, 2007.
- [8] J. Wang, Y. Li, Z. Zhang, and Z. Hao, "Mesoporous KIT-6 silica–polydimethylsiloxane (PDMS) mixed matrix membranes for gas separation," *J. Mater. Chem. A*, vol. 3, no. 16, pp. 8650–8658, 2015.
- [9] Y. Ren, Z. Ma, and P. G. Bruce, "Ordered mesoporous metal oxides: synthesis and applications," *Chem. Soc. Rev.*, vol. 41, pp. 4909–4027, 2012.
- [10] F. Jiao, A. H. Hill, A. Harrison, A. Berko, A. V Chadwick, and P. G. Bruce, "Synthesis of Ordered Mesoporous NiO with Crystalline Walls and a Bimodal Pore Size Distribution," *J. AM. CHEM. SOC.* 2008, vol. 130, pp. 5262–5266, 2008.
- [11] L. Almar, T. Andreu, A. Morata, M. Torrell, L. Yedra, S. Estradé, F. Peiró, and A. Tarancón, "High-surface-area ordered mesoporous oxides for continuous operation in high temperature energy applications," *J. Mater. Chem. A*, vol. 2, pp. 3134–3141, 2014.
- [12] L. Almar, B. Colldeforns, L. Yedra, S. Estradé, F. Peiró, A. Morata, T. Andreu, and A. Tarancón, "High-temperature long-term stable ordered mesoporous Ni–CGO as an anode for solid oxide fuel cells," *J. Mater. Chem. A*, vol. 1, pp. 4531–4538, 2013.
- [13] D. Ding, X. Li, S. Y. Lai, K. Gerdes, and M. Liu, "Enhancing SOFC cathode performance by surface modification through infiltration," *Energy Environ. Sci.*,

vol. 7, pp. 552–575, 2014.

- [14] W. H. Kan, A. J. Samson, and V. Thangadurai, “Trends in electrode development for next generation solid oxide fuel cells,” *J. Mater. Chem. A*, vol. 4, pp. 17913–17932, 2016.
- [15] Y. Wang, Z. Yang, M. Han, and J. Chang, “Optimization of Sm<sub>0.5</sub>Sr<sub>0.5</sub>CoO<sub>3-δ</sub> - infiltrated YSZ for solid oxide fuel cells/electrolysis cells,” *RSC Adv*, vol. 182, pp. 112253–112259, 2016.
- [16] M. Torrell, L. Almar, A. Morata, and A. Tarancón, “Synthesis of mesoporous nanocomposites for their application in solid oxide electrolysis cells: microstructural and electrochemical characterization,” *Faraday Discuss.*, vol. 182, pp. 423–435, 2015.
- [17] J. M. Vohs and R. J. Gorte, “High-performance SOFC cathodes prepared by infiltration,” *Adv. Mater.*, vol. 21, no. 9, pp. 943–956, 2009.
- [18] S. Ping Jiang, “Nanoscale and nano-structured electrodes of solid oxide fuel cells by infiltration: Advances and challenges,” *Int. J. Hydrogen Energy*, vol. 37, pp. 449–470, 2012.
- [19] J. T. S. Irvine, D. Neagu, M. C. Verbraeken, C. Chatzichristodoulou, C. Graves, and M. B. Mogensen, “Evolution of the electrochemical interface in high-temperature fuel cells and electrolysis,” *Nat. Energy*, vol. 1, pp. 1–13, 2016.
- [20] L. Almar, A. Morata, M. Torrell, M. Gong, M. Liu, T. Andreu, and A. Tarancón, “Synthesis and characterization of robust, mesoporous electrodes for solid oxide fuel cells,” *J. Mater. Chem. A*, vol. 4, pp. 7650–7657, 2016.
- [21] H. Fan, M. Keane, N. Li, D. Tang, P. Singh, and M. Han, “Electrochemical stability of La<sub>0.6</sub>Sr<sub>0.4</sub>Co<sub>0.2</sub>Fe<sub>0.8</sub>O<sub>3-δ</sub>-infiltrated YSZ oxygen electrode for reversible solid oxide fuel cells,” *Int. J. Hydrogen Energy*, vol. 39, pp. 14071–14078, 2014.
- [22] “FAE S.A.U.” [Online]. Available: <http://www.fae.es/es/>.
- [23] C. Kleinlogel and L. J. Gauckler, “Sintering and properties of nanosized ceria solid solutions,” *Solid State Ionics*, vol. 135, no. 1–4, pp. 567–573, 2000.
- [24] D. P. Fagg, J. C. C. Abrantes, D. Pérez-Coll, P. Núñez, V. V. Kharton, and J. R. Frade, “The effect of cobalt oxide sintering aid on electronic transport in Ce<sub>0.8</sub>Gd<sub>0.2</sub>O<sub>2-d</sub> electrolyte,” *Electrochim. Acta*, vol. 48, pp. 1023–1029, 2003.
- [25] O. Yamamoto, Y. Arati, Y. Takeda, N. Imanishi, Y. Mizutani, M. Kawai, and Y. Nakamura, “Electrical conductivity of stabilized zirconia with ytterbia and scandia,” *Solid State Ionics*, vol. 79, pp. 137–142, 1995.
- [26] V. Vijaya Lakshmi, R. Bauri, A. S. Gandhi, and S. Paul, “Synthesis and characterization of nanocrystalline ScSZ electrolyte for SOFCs,” *Int. J. Hydrogen Energy*, vol. 36, no. 22, pp. 14936–14942, 2011.

# ***Chapter 4***

*Electrolyte- and fuel electrode-  
supported SOEC cells*



<b>4. Electrolyte- and fuel electrode-supported SOEC cells.....</b>	<b>131</b>
<b>4.1. Chapter overview .....</b>	<b>131</b>
<b>4.2. Characterization and performance of electrolyte-supported SDC-SSC SOECs..</b> <b>.....</b>	<b>132</b>
<b>4.3. Characterization and performance of fuel electrode-supported SDC-SSC</b> <b>SOECs .....</b>	<b>137</b>
<b>4.4. Conclusions .....</b>	<b>146</b>
<b>4.5. References .....</b>	<b>149</b>



## 4. Electrolyte- and fuel electrode-supported SOEC cells

### 4.1. Chapter overview

This chapter is focused on studying the influence of the cell configuration for the Solid Oxide Electrolysis Cells (SOECs) performance. Specifically, electrolyte- and fuel electrode-supported cells were fabricated employing the same  $\text{Sm}_{0.2}\text{Ce}_{0.8}\text{O}_{1.9}$ – $\text{Sm}_{0.5}\text{Sr}_{0.5}\text{CoO}_3$  (SDC-SSC) oxygen electrode. The performance and the microstructure of both cell configurations were studied in detail.

Since the chemical and crystallographic analysis was carried out in **Chapter 3**, the microstructural characterization is focused on a morphological analysis based on Scanning Electron Microscopy (SEM). With the aim of evaluating the performance of each configuration, the electrochemical characterization is focused on analysing the obtained I-V polarization curves and Electrochemical Impedance Spectroscopy (EIS) measurements under electrolysis and co-electrolysis fuel electrode gas compositions.

Firstly, the characterization of 6Yb4ScSZ Electrolyte-Supported Cells (ESCs) with fuel (Ni-SDC) and oxygen (SDC-SSC) electrodes based on mesoporous materials is presented in **section 4.2**. In this section, the fabrication of mesoporous electrodes and its preliminary electrochemical characterization on electrolysis and co-electrolysis operation modes are presented and discussed, confirming the potential of the proposed materials to be applied in SOECs.

Secondly, **section 4.3** is dedicated to the characterization of Ni-YSZ Fuel Electrode-Supported Cells (FESCs), which SDC-SSC oxygen electrode fabricated using the same mesoporous materials as in **section 4.2**. This section shows the suitability of applying this configuration for improving the SOEC performance, while suggesting the need to optimize the cell microstructure (to be carried out in the next chapters).

## 4.2. Characterization and performance of electrolyte-supported SDC-SSC SOECs

6Yb4ScSZ electrolyte-supported cells of 200  $\mu\text{m}$  in thickness (fabricated by FAE S.A.U. [1]) similar to the ones employed for the fabrication of the oxygen electrode symmetrical cells (**section 3.4**), were used for the fabrication of full electrolysis cells to be measured as SOEC devices. As explained in **Chapter 2**, these are circular disks of 2 cm in diameter and approximated active area of  $\approx 1.3 \text{ cm}^2$  of active area fabricated by tape casting.

A  $\text{Ce}_{0.8}\text{Gd}_{0.2}\text{O}_{1.9}$  (CGO) barrier layer ( $\approx 2 \mu\text{m}$ ) was deposited by Pulsed Laser Deposition (PLD) on one side of the electrolyte with the aim of avoiding the formation of lanthanum zirconate ( $\text{La}_2\text{Zr}_2\text{O}_7$ ) and strontium zirconate ( $\text{SrZrO}_3$ ) insulating phases by reaction between the oxygen electrode and the electrolyte phases, as well as avoid the loss of gadolinium by migration that could lead to a decrease of the ionic conductivity of the CGO barrier layer [2-4] (see **Chapter 5**). Firstly, NiO-SDC ( $\approx 50 \mu\text{m}$ ) mesoporous powder was deposited as fuel electrode. Secondly, in concordance with the lowest serial and polarization resistances obtained on the optimization of symmetrical cells (**section Error! Reference source not found.4**), SDC mesoporous scaffold ( $\approx 10\text{-}12 \mu\text{m}$ ) was sintered to the CGO barrier layer at 900  $^\circ\text{C}$ , and functionalized as oxygen electrode through its infiltration with SSC. Lastly, a SSC top layer ( $\approx 50 \mu\text{m}$ ) was deposited by air brushing. The composition of the fabricated cell is described as Ni-SDC/YbScSZ/SDC-SSC. More details about the fabrication procedure can be found in **section 2.5.2**.

A cross-section SEM image of the fabricated Ni-SDC/YbScSZ/SDC-SSC SOEC cells is presented in **Figure 4.1**. The fuel and oxygen electrodes interfaces with the electrolyte can be observed. **Figure 4.1a** shows a good attachment of the fuel electrode while **Figure 4.1b** shows a homogeneous oxygen electrode but a defective barrier layer. This not fully dense layer could favour local reactivity between the Zr and the Sr, which could eventually reduce the performance of the layer.

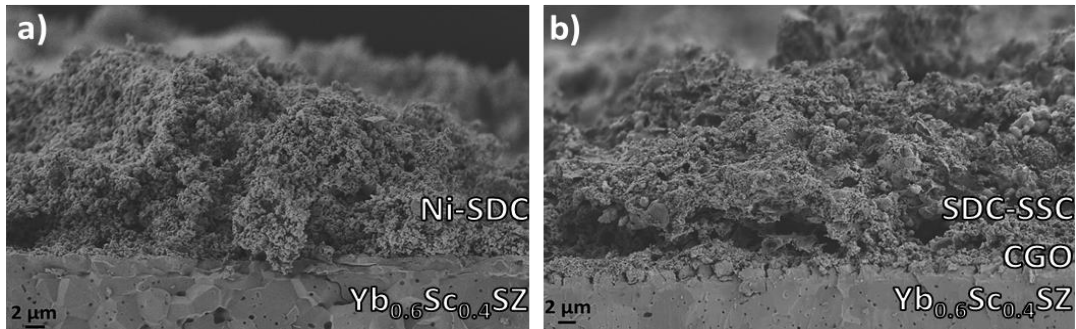


**Figure 4.1:** SEM cross section of the (a) fuel electrode- and (b) oxygen electrode-electrolyte interfaces.

Obtained cells were electrochemically characterized by measuring I-V polarization curves and EIS in electrolysis and co-electrolysis modes at 750 °C. Different fuel compositions were used on the fuel electrode chamber to evaluate the possible different behaviour of the fabricated cell: an electrolysis fuel composition (i) 17% H<sub>2</sub> + 17% H<sub>2</sub>O + Ar (Bal.) and a co-electrolysis fuel composition (ii) 17% H<sub>2</sub> + 17% CO<sub>2</sub> + 17% H<sub>2</sub>O + Ar (Bal.). Synthetic air was supplied to the oxygen electrode chamber in both cases.

The polarization curves of the fabricated cells operating at 750 °C are presented in the **Figure 4.2** showing an almost linear and very similar behaviour although working under different fuel compositions.

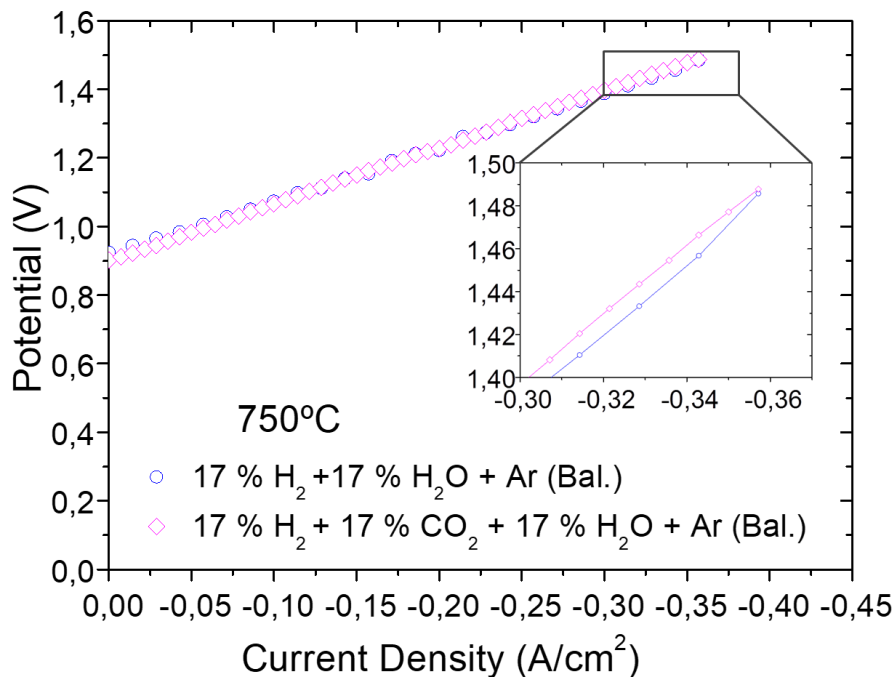


**Figure 4.2:** I-V curves recorded under electrolysis and co-electrolysis atmospheres at 750 °C for an ESC fabricated using SDC-SSC and NiO-SDC mesoporous electrodes.

The Open Circuit Voltage (OCV) values (**Figure 4.2**) slightly change between the electrolysis (0.93 V) and co-electrolysis (0.90 V) gas compositions. This was expected ~~due to~~ because the addition of CO<sub>2</sub> promotes the activity of the thermodynamically ruled Reverse Water Gas Shift (RWGS) reaction, although the relative amount of hydrogen is kept constant in the used fuel inlet compositions. The RWGS reaction generates certain amount of CO and H<sub>2</sub>O, when CO<sub>2</sub> and H<sub>2</sub> are mixed in the same chamber, promoting two different effects: i) first the OCV of the CO/CO<sub>2</sub> is slightly lower than the H<sub>2</sub>/H<sub>2</sub>O OCV, which decreases the final OCV value; ii) secondly, the generation of more H<sub>2</sub>O decreases the p<sub>H<sub>2</sub></sub> also affecting the final OCV value. Considering these effects, the measured OCV values are comparable with the theoretical ones, 0.96 and 0.92 V for electrolysis and co-electrolysis, respectively. These values were calculated from a model based on the chemical (RWGS reaction) and electrochemical considerations for both electrolysis and co-electrolysis gas mixtures. [5]. Approaching the theoretical values indicates a good gas tightness of the oxygen and fuel chambers.

Current densities as high as -0.25 A/cm<sup>2</sup> were injected at voltages of 1.30 V, as showed in **Figure 4.2**. Note that according to the I-V results, not important differences of the electrolyser performance under electrolysis and co-electrolysis atmospheres were found. More specifically, the inset of **Figure 4.2** shows that the overall Area Specific Resistance (ASR) and the injected current at 1.4 V are virtually the same for the two different fuel compositions, even when CO<sub>2</sub> is considered. The revealed fuel flexibility of the fabricated cells was more important at high voltages, where the measured fuel compositions fitted at the same values. On the other hand, this experiment confirms the suitability of the developed electrodes to operate under electrolysis.

The studied cell was also characterized by EIS in galvanostatic mode. The aim was to identify the different contributions to the total resistance of the processes involved. These measurements were performed at OCV and under BIAS voltage of 1.3 V. Nyquist plots measured and fitted for each gas composition at OCV and at BIAS= 1.3 V in electrolysis and co-electrolysis operation modes are presented in **Figure 4.3a** and **4.3b**, respectively, and their corresponding Bode plots are showed in **Figure 4.3c** and **4.3d**.

The same  $LR_s(R_{p1}Q_1)(R_{p2}Q_2)$  equivalent circuit was used for fitting the experimental EIS results measured on electrolysis and co-electrolysis modes. The equivalent circuit is composed by an inductance (L), a serial or ohmic resistance ( $R_s$ ) and (RQ) elements in series [6]. Q or Constant Phase Elements (CPE) have been introduced by substituting ideal capacitances C for a distribution of capacitances more suitable to fit depressed arcs observed in experimental data. The inductance contribution is a typical artefact introduced by the set-up, while the main serial resistance comes from the electrolyte, contact resistances and current collection. Finally, RQ elements are directly related to the different contributions of the electrodes processes. The  $n$  parameter used to define Q is related to the angle of the depressed arc ranging from  $n=0-1$ . When  $n = 1$ , the Q element becomes a pure capacitor [7].

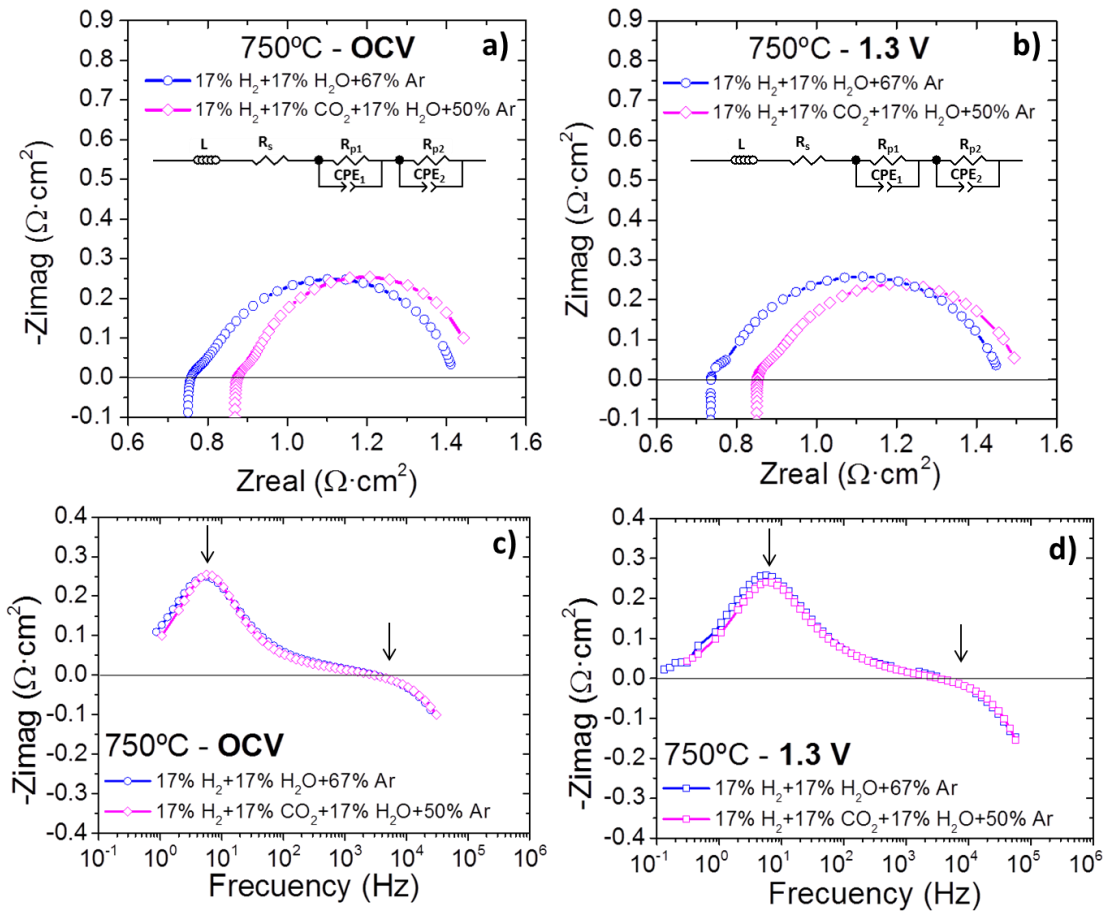


**Figure 4.3:** Nyquist plots and Bode plots obtained at OCV (a, c) and 1.3 V (b, d) under electrolysis and co-electrolysis atmospheres at 750 °C for an ESC based on mesoporous materials.

The values of each resistance, capacitance and frequencies obtained from the fitting of the experimental EIS data are presented in **Table 4.1**.  $R_s$  values presented in **Table 4.1** represent the contribution of the serial resistance to the ASR, and have been

calculated taking into account the ohmic contribution and the active area of the electrolyte (1.3 cm<sup>2</sup>). The C values represent the true capacitance calculated from the CPE element as  $C_p=(Q)^{(1/n)}R_{p1}^{(1-n/n)}$ . The ASR represents the overall resistance, including the contributions of the ohmic ( $R_s$ ) and polarization resistances ( $R_{p1}$  and  $R_{p2}$ ). It is important to highlight the high values of the serial resistance in both modes (0.6 and 0.7  $\Omega$ ), which represents more than 50% of the obtained overall ASR values ( $\approx$ 1.4 and 1.5  $\Omega\cdot\text{cm}^2$ ). This high serial resistance is directly related to the use of a thick 6Yb4ScSZ electrolyte, optimized to operate at  $T>800$  °C. The values are in good agreement with the ones measured by M. Torrell *et al.* [8] for a similar electrolyte. The difference in the serial resistance value between the first measurements under electrolysis and the second measures of the same cell under co-electrolysis mode (**Figure 4.3a** and **4.3b**) could be explained due to the fast degradation of the cell, especially of the interfaces of the electrolyte and the electrodes. The origin of this evolution is probably associated to the non-fully dense barrier layer and the corresponding formation of insulating phases.

	17% $\text{H}_2$ -17% $\text{H}_2\text{O}$ -67%Ar		17% $\text{H}_2$ -17% $\text{CO}_2$ -17% $\text{H}_2\text{O}$ -50%Ar	
	OCV	1,3 V	OCV	1,3 V
$R_s$ ( $\Omega\cdot\text{cm}^2$ )	$7.5\cdot 10^{-1}$	$7.5\cdot 10^{-1}$	$8.5\cdot 10^{-1}$	$8.5\cdot 10^{-1}$
$R_{p1}$ ( $\Omega\cdot\text{cm}^2$ )	$4.8\cdot 10^{-2}$	$4.7\cdot 10^{-2}$	$8.2\cdot 10^{-2}$	$1.0\cdot 10^{-1}$
$C_1$ (F/cm <sup>2</sup> )	$9.7\cdot 10^{-3}$	$4.5\cdot 10^{-3}$	$1.4\cdot 10^{-2}$	$2.1\cdot 10^{-2}$
$n_1$	0.77	0.89	0.56	0.65
f max (Hz)	$3.3\cdot 10^2$	$7.5\cdot 10^2$	$1.3\cdot 10^2$	$7.2\text{E}\cdot 10^1$
$R_{p2}$ ( $\Omega\cdot\text{cm}^2$ )	$6.1\cdot 10^{-1}$	$7.0\cdot 10^{-1}$	$5.2\cdot 10^{-1}$	$5.6\cdot 10^{-1}$
$C_2$ (F/cm <sup>2</sup> )	$4.7\cdot 10^{-2}$	$3.9\cdot 10^{-2}$	$5.1\cdot 10^{-2}$	$4.8\cdot 10^{-2}$
$n_2$	0.86	0.80	0.96	0.87
f max (Hz)	5.4	5.7	5.8	5.8
ASR ( $\Omega\cdot\text{cm}^2$ )	1.4	1.5	1.4	1.5

**Table 4.1:** Results from fitting EIS data recorded for the ESC based on mesoporous materials under electrolysis (17%  $\text{H}_2$  + 17%  $\text{H}_2\text{O}$  + Ar (Bal.)) and co-electrolysis gas (17%  $\text{H}_2$  + 17%  $\text{CO}_2$  + 17%  $\text{H}_2\text{O}$  + Ar (Bal.)) composition measured at OCV and 1.3 V. Here  $R_s$  values are suitable with Nyquist plots, and C represents the true capacitance calculated as  $C_p=(Q)^{(1/n)}R_{p1}^{(1-n/n)}$ .

Different behaviours of the cell are observed as a function of the applied BIAS during the EIS measurements (**Figure 4.3**). As it is explained in **section 2.7.3**, when the

measurements are performed at OCV, the information obtained on the Nyquist arc is mainly related with an operation region dominated by the serial resistance and the activation overpotential, while when a BIAS is applied (1.3 V), the regime of the cell is closer to the standard operation point where the dominant overpotentials are the ohmic and activation overpotentials, that are added to the overpotential generated by the serial resistance [9]. According to the Bode plots in **Figure 4.3c** and **4.3d**, the high and low frequency processes are equally contributing in the four representative EIS shown data, and the main polarization contribution comes from the lower frequency arc ( $R_{p2} \approx 1$  Hz), although a minor arc is observed at higher frequencies ( $R_{p1} \approx 10$ - $10^2$  Hz). It can be observed that the obtained Nyquist arcs follow the typical tear-like shape of the Mixed Ionic and Electronic Conductor (MIEC) materials. This is expected since the limiting electrode is likely the oxygen one, which is a composite of an ionic conductor functionalized with a MIEC material. This behaviour indicates that the non-charge transfer processes, generally produced by gas conversion and gas diffusion phenomena, are the major contributions to the polarization overpotentials, i.e.  $R_{p2}$  ( $\approx 10^{-1} \Omega \cdot \text{cm}^2$ ), in all the measured impedance spectra at different voltages and gas compositions. The other contribution to the polarization overpotential,  $R_{p1}$  ( $\approx 10^{-2} \Omega \cdot \text{cm}^2$ ), is most likely associated to charge-transfer processes. The negligible variation of the arc shape with the gas composition in both Nyquist plots made difficult assigning a dominant contribution to each electrode

Finally, it is important to mention that the electrodes performance seems to be eventually better in co-electrolysis conditions, which leads to a similar I-V curve even having an increase of the serial resistance.

### **4.3. Characterization and performance of fuel electrode-supported SDC-SSC SOECs**

Opposite to the previous section, here we will present fuel electrode-supported cells with a thin electrolyte. The electrolysis cells of this section were fabricated on the supports (fuel electrode and electrolyte) supplied by HTceramix/SOLIDpower (Switzerland) [10] in the frame of the H2020 European ECo project (n° 699892) [11]. These cells have a circular shape with an approximated active area of  $\approx 1.5 \text{ cm}^2$  (**Chapter 2**). The half-cells are composed by a porous Ni-YSZ fuel electrode support ( $\approx 300 \mu\text{m}$ ) and a dense YSZ electrolyte ( $\approx 8 \mu\text{m}$ ), both fabricated by tape casting. With

the same purpose than on ESCs, a CGO barrier layer ( $\approx 2 \mu\text{m}$ ) was deposited by PLD between the electrolyte and the oxygen electrode. The SDC-SSC oxygen electrode was fabricated following the same procedure than described in the previous section. Specifically, this electrode is composed by a SDC-SSC functional layer based on infiltrated mesoporous materials ( $\approx 10\text{-}12 \mu\text{m}$ ) and a SSC top layer fabricated by airbrushing a commercial ink ( $\approx 50 \mu\text{m}$ ).

A cross-section micrograph of the Ni-YSZ/YSZ/CGO<sub>bl</sub>/SDC-SSC/SSC cell is showed in **Figure 4.4**. It is possible to see that both the fuel electrode and the oxygen electrode are well attached to the electrolyte. Besides, the CGO barrier layer located on top of the electrolyte is slightly cracked along the cross-section.

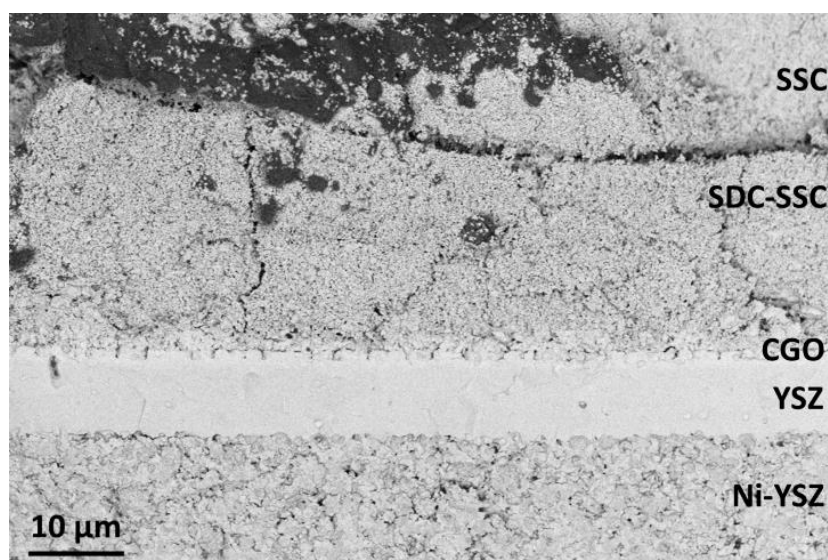


**Figure 4.4:** SEM cross-section micrograph of the SOEC cell after the electrochemical characterization. It is possible to distinguish the Ni-YSZ fuel electrode support, the YSZ electrolyte, the CGO barrier layer, and the oxygen electrode.

Fixing the operating temperature at  $750 \text{ }^\circ\text{C}$ , I-V polarization curves and EIS measurements were carried out in electrolysis (44%  $\text{H}_2\text{O}$ -11%  $\text{H}_2$ - Ar (Bal.)) and co-electrolysis (24%  $\text{H}_2\text{O}$ -24%  $\text{CO}_2$ -5%  $\text{H}_2$ -Ar (Bal.)) using synthetic air in the oxygen electrode. **Figure 4.5** shows the polarization curves obtained in galvanostatic mode.

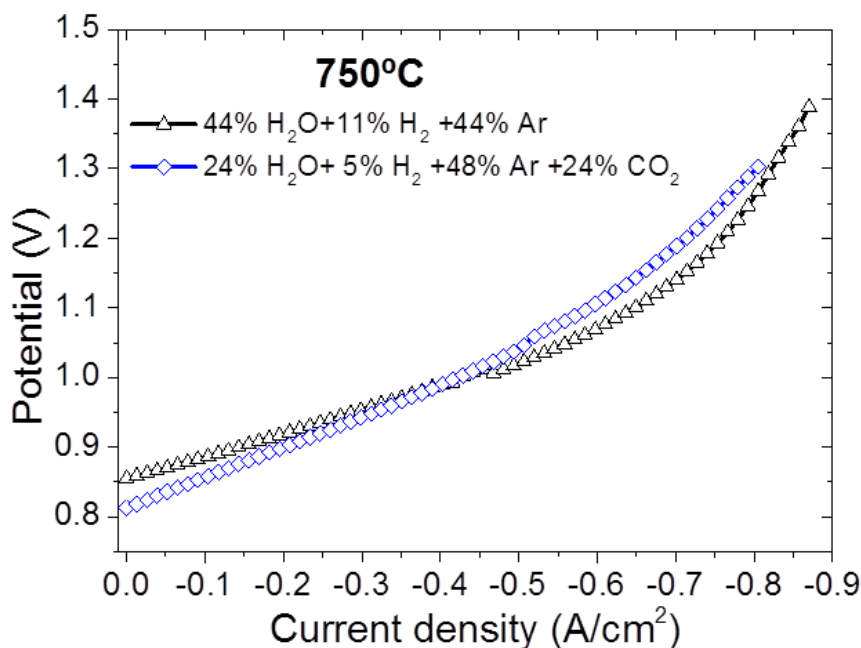


**Figure 4.5:** I-V curves recorded at electrolysis and co-electrolysis atmospheres at 750 °C for a SDC-SSC-oxygen electrode Ni-YSZ fuel electrode-supported cell.

The OCV obtained for the electrolysis composition was 0.86 V while the one for the co-electrolysis composition was 0.81 V. The expected difference in the measured OCVs is directly explained by the different fuel electrode gas composition. Following the Nernst equation (**equation 2.5**), the addition of CO<sub>2</sub> in the co-electrolysis gas composition results on a decrease of the OCV value, while it increases when higher amount of H<sub>2</sub> is added. Theoretical OCV was calculated for each employed gas compositions, resulting in 0.90 and 0.86 V for electrolysis and co-electrolysis fuel electrode gas compositions, respectively. The theoretical model applied takes into consideration chemical and electrochemical factors of each component of the gas mixture in function of its proportion on the final gas composition [5]. According to this estimation, the measured OCV values are slightly lower than theoretical ones although still acceptable. The small discrepancy reveals that a good sealing between fuel and oxygen electrodes atmospheres was obtained. A good seal provides a proper operation of the cell avoiding highly exothermic reactions between H<sub>2</sub> and O<sub>2</sub> (hot spots) that could, eventually, increase the real temperature or even bring the cell to a dramatic failure.

As it is presented in the I-V curve of the **Figure 4.5**, up to a maximum current density of -0.83 A/cm<sup>2</sup> at a potential of 1.30 V was injected in electrolysis mode, while for co-electrolysis this value was -0.81 A/cm<sup>2</sup> at the same potential. This comparable

behaviour reveals that there were not important differences in performance for electrolysis and co-electrolysis gas compositions. As a consequence, the obtained performance of the SOEC becomes independent of the fuel gas composition.

Besides, it is observed that both electrolysis and co-electrolysis I-V curves present different overall resistances (slopes) at low and high current densities, indicating that the limiting mechanisms or dominating overpotentials have changed with the injected current density. While a linear behaviour is observed for low injected current densities ( $< 0.5 \text{ A/cm}^2$ ), a continuous increase of resistance is present at high current densities revealing diffusion problems. Since the maximum steam conversion along the whole range of scanned current densities is 10 %, the diffusion issue should be mainly attributed to the microstructure of the electrodes. These would be likely related to the difficult flow of inlet gases through the mesoporous electrodes, increasing the contribution of diffusion overpotential. It is important to highlight that, in spite of the reported diffusion problems at high current densities, the maximum current densities injected in this FESCs are remarkably high compared to the previously presented electrolyte-supported one.

EIS measurements were also performed under electrolysis and co-electrolysis atmospheres in potentiostatic mode at OCV and under applied BIAS voltage of 0.90 V. As it has been previously explained, measuring EIS at different applied voltage conditions, close to the OCV or 0.9 V, allows obtaining different information about the main contributions to the overall resistance of the cell and the related overpotentials in different operating points [9].

The Nyquist plots of the EIS measurements (**Figure 4.6a** and **4.6b**) and its corresponding Bode plots (**Figure 4.6c** and **4.6d**) in electrolysis and co-electrolysis fuel electrode gas atmospheres measured at OCV and 0.90 V, respectively, are presented in **Figure 4.6**. Bode plots (**Figure 4.6c** and **4.6d**) obtained from the measurements of Ni-YSZ/YSZ/CGO<sub>bl</sub>/SDC-SSC/SSC cells operating under co-electrolysis atmosphere show three differentiated arcs, while under electrolysis mode only two arcs can be clearly observed (see arrows in the **Figure 4.6**).

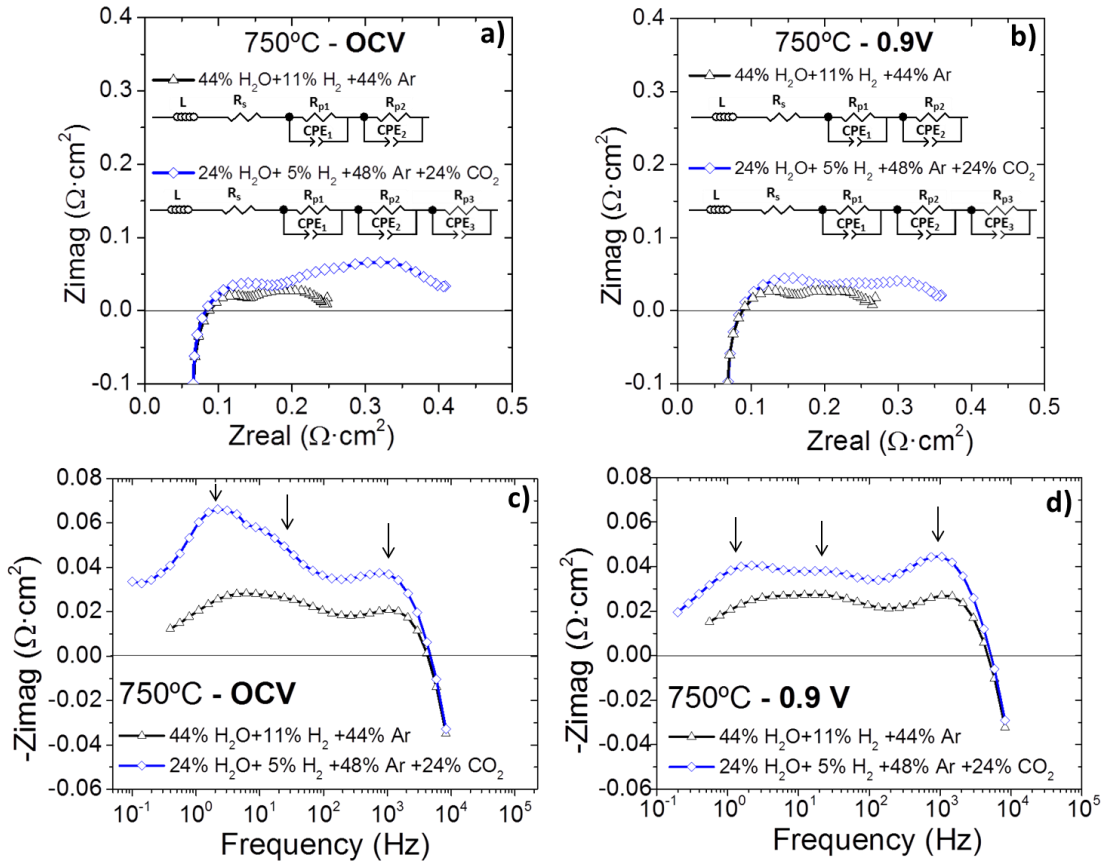


**Figure 4.6:** Nyquist plots and Bode plot obtained at OCV (a, c) and 0.9 V (b, d) at electrolysis and co-electrolysis atmosphere at 750 °C for a SDC-SSC-oxygen electrode FESC.

Since the number of detected contributions are different in the electrolysis and co-electrolysis modes, two different equivalent circuits have been used to fit the impedance spectroscopy measurements. Applying equivalent circuits composed by the same elements than the one presented in the previous section dedicated to ESCs, under electrolysis atmosphere the circuit was  $LR_s(R_{p1}Q_1)(R_{p2}Q_2)$ , while the one used for fitting the Nyquist plot obtained under co-electrolysis atmosphere was  $LR_s(R_{p1}Q_1)(R_{p2}Q_2)(R_{p3}Q_3)$ . All the parameters obtained from the fitting with the equivalent circuit model are listed in **Table 4.2**.

	44%H <sub>2</sub> O-11%H <sub>2</sub> -44%Ar		24%H <sub>2</sub> O-24%CO <sub>2</sub> -5%H <sub>2</sub> -48%Ar	
	OCV (V)	0.9 V	OCV (V)	0.9 V
<b>R<sub>s</sub> (Ω·cm<sup>2</sup>)</b>	5.7·10 <sup>-2</sup>	5.8·10 <sup>-2</sup>	5.0·10 <sup>-2</sup>	5.5·10 <sup>-2</sup>
<b>R<sub>p1</sub> (Ω·cm<sup>2</sup>)</b>	7.3·10 <sup>-2</sup>	8.4·10 <sup>-2</sup>	1.2·10 <sup>-1</sup>	1.4·10 <sup>-1</sup>
<b>C<sub>1</sub> (F/cm<sup>2</sup>)</b>	1.6·10 <sup>-1</sup>	1.8·10 <sup>-1</sup>	8.7·10 <sup>-2</sup>	1.0·10 <sup>-1</sup>
<b>n<sub>1</sub></b>	0.84	0.85	0.74	0.75
<b>f max (Hz)</b>	3.0·10 <sup>3</sup>	2.3·10 <sup>3</sup>	1.6·10 <sup>3</sup>	1.5·10 <sup>3</sup>
<b>R<sub>p2</sub> (Ω·cm<sup>2</sup>)</b>	1.2·10 <sup>-1</sup>	1.3·10 <sup>-1</sup>	1.4·10 <sup>-1</sup>	1.1·10 <sup>-1</sup>
<b>C<sub>2</sub> (F/cm<sup>2</sup>)</b>	9.7·10 <sup>-2</sup>	1.7·10 <sup>-1</sup>	3.9·10 <sup>-1</sup>	3.1·10 <sup>-1</sup>
<b>n<sub>2</sub></b>	0.55	0.51	0.79	0.72
<b>f max (Hz)</b>	7.9	8.94	1.6	1.5
<b>R<sub>p3</sub> (Ω·cm<sup>2</sup>)</b>			9.8·10 <sup>-2</sup>	5.2·10 <sup>-2</sup>
<b>C<sub>3</sub> (F/cm<sup>2</sup>)</b>			1.7·10 <sup>-1</sup>	3.0·10 <sup>-1</sup>
<b>n<sub>3</sub></b>			7.12·10 <sup>-1</sup>	8.51·10 <sup>-1</sup>
<b>f max (Hz)</b>			1.77·10 <sup>1</sup>	3.06·10 <sup>1</sup>
<b>ASR (Ω·cm<sup>2</sup>)</b>	2.5·10 <sup>-1</sup>	2.74·10 <sup>-1</sup>	4.14·10 <sup>-1</sup>	3.67·10 <sup>-1</sup>

**Table 4.1.** Results from fitting EIS data recorded at OCV and 0.9 V under electrolysis (44%H<sub>2</sub>O-11%H<sub>2</sub>O-44%Ar) and co-electrolysis gas (24%H<sub>2</sub>O-24%CO<sub>2</sub>-5%H<sub>2</sub>-48%Ar) compositions characterizing a SDC-SSC-oxygen electrode fuel-supported cell. Here R<sub>s</sub> values are suitable with Nyquist plots, and C represents the true capacitance calculated as  $C_p = (Q)^{(1/n)} R_{p1}^{(1-n/n)}$ .

A comparable serial resistance was obtained under all the measured conditions with values of approximately  $\approx 0.04 \Omega$ . These values are close to the resistance expected for the electrolyte for the transference of oxygen ions therefore suggesting that the main contribution to the serial resistance come from the electrolyte [12-14]. In lesser degree, some contributions of the electrolyte/electrode contact interfaces and current collectors, are observed [15]. In general, the ohmic contribution to the overall ASR is kept around  $\approx 0.05 \Omega \cdot \text{cm}^2$ . The similitude found between all fitted values related to the polarization resistance contributions is explained by the low conversion rates employed for the measurements.

Bode plots (**Figure 4.6c** and **4.6d**) allows comparing the change of the trend under electrolysis and co-electrolysis fuel composition. Since high frequency arcs ( $R_{p1} \approx 10^3$  Hz) do not show relevant changes as a function of fuel electrode composition, are

initially assigned to the oxygen electrode. Opposite, it is deduced that the arcs appearing at lower frequencies ( $R_{p2} \approx 1$  Hz and  $R_{p3} \approx 10$  Hz) are mainly related to the activity of the fuel electrode, presenting the major contribution to the polarization resistance. Specifically,  $R_{p2}$  is assigned with steam reduction, and since the third arc is only observed on co-electrolysis mode,  $R_{p3}$  is identified as an extra resistance associated with the reduction of  $\text{CO}_2$ , which becomes limiting only when SOEC works under co-electrolysis atmospheres.

According to the characteristic frequencies ( $\nu=1/RC$ ),  $R_{p1}$  is identified as a charge transfer process taking place at high frequencies, and in which the oxygen electrode is mainly involved; while  $R_{p2}$  and  $R_{p3}$  are attributed to mass transport processes occurring at low frequencies and dominated by the fuel electrode contribution.

The overall ASR values calculated from fitting Nyquist plots measured on electrolysis and co-electrolysis modes are also listed in **Table 4.2**. Therefore, fabricated and tested SDC-SSC FESCs present lower total resistance and hence better performance working under electrolysis than co-electrolysis gas compositions, as it has also been shown in previous publications like [16,17].

Different SEM micrographs focused on studying the oxygen electrode cross-section are presented in **Figure 4.7**. A general overview of the oxygen electrode/electrolyte interface is showed in **Figure 4.7a**, and micrographs presented as **Figure 4.7b**, **Figure 4.7c** and **Figure 4.7d** were acquired at different magnifications in order to observe the functional layer microstructure. **Figure 4.7b** presents a higher magnification micrograph of the microstructure close to the electrolyte, where it is possible to see a cave-like morphology embedded in the infiltrated mesoporous scaffold zone. Moreover, the micrograph on **Figure 4.7c** presents a zoom of the interface of the electrolyte, the CGO barrier layer and the infiltrated mesoporous SDC-SSC microstructure. Although the formed CGO barrier layer is not dense enough for avoiding the formation of insulating secondary phases, it is observed that the SDC mesoporous scaffold is perfectly attached to the CGO barrier layer, and any delamination occurred after the electrochemical characterization on electrolysis and co-electrolysis modes. **Figure 4.7d** presents a higher magnification micrograph of the cave-like morphology microstructure grown in the oxygen electrode functional layer.

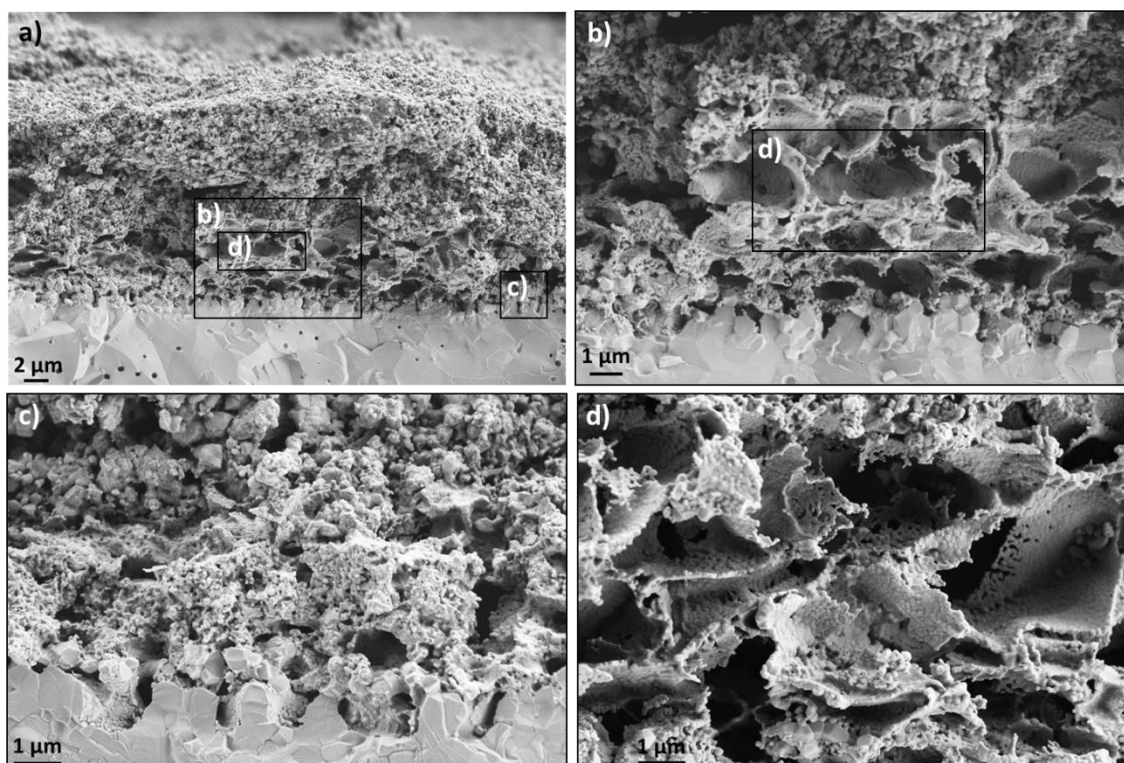


**Figure 4.7:** SEM cross-sections micrographs recorded after the electrochemical characterization of the cell (up-left). The micrographs labelled as (a), (b), (c) and (d) are zooms recorded at different zones of the cross-section.

The formed caves in the top of the oxygen electrode functional layer (**Figure 4.8**) were analysed by Energy-Dispersive X-Ray (EDX) for determining the elements present in this microstructure. It is important to know the composition of that microstructure in order to optimize the fabrication process and improve the electrochemical performance of the cell. The specific areas where the analysis was performed are marked with pink rectangles in the cross-section micrographs presented in **Figure 4.8a** and **4.8b**. Specifically, **Figure 4.8a** points the analysis to the cave-like microstructure, while **Figure 4.8b** marks the infiltrated mesoporous SDC-SSC material as the studied area. The resulting spectrums obtained from analysing each of these regions are showed in **Figure 4.8c**. They have been overlapped for facilitating the ratio comparison of the different elements involved in SDC and SSC compounds.

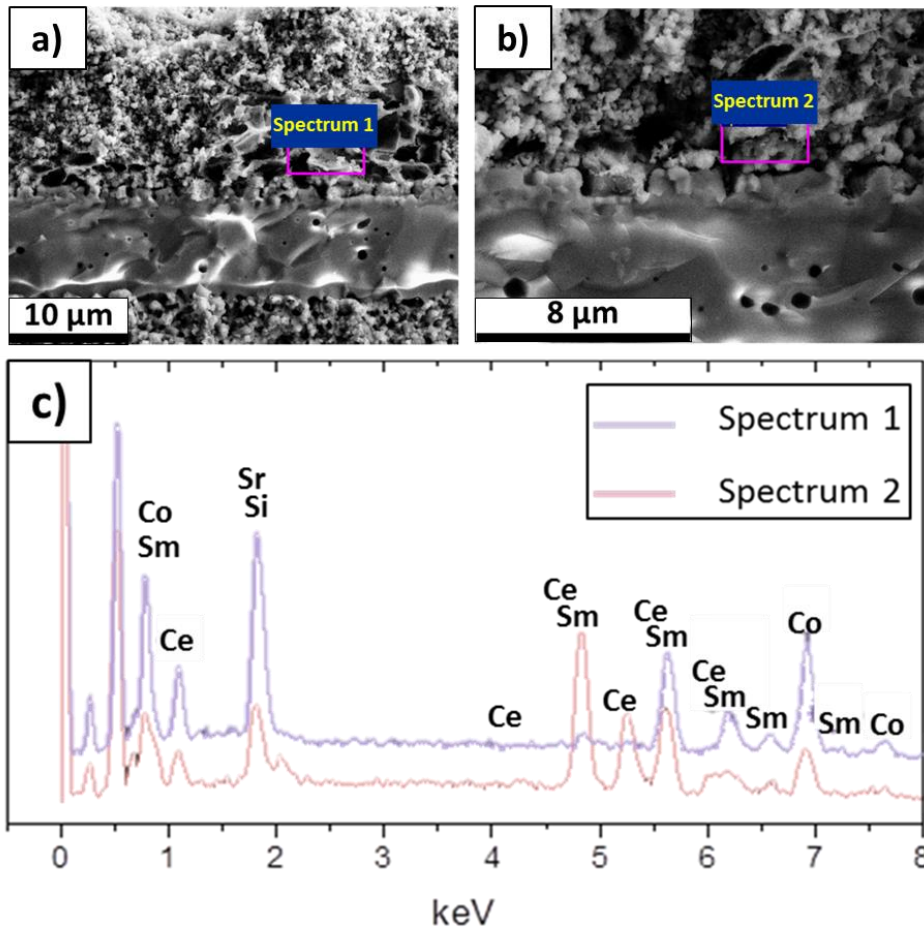


**Figure 4.8:** EDX analysis of two different points at the interface electrolyte-oxygen electrode. a) The analysis is focused on the new microstructure appeared, while in (b) the SDC-SSC infiltrated mesoporous material was analysed. Spectrums of the elements involved in each analysed area are presented in (c).

	Atomic %				
	Co	Sr	Ce	Sm	Others
Spectrum 1	49.2	22.8	3.00	24.4	0.6
Spectrum 2	27.0	11.7	43.1	16.2	2.0

**Table 4.3:** Atomic % of representative elements of SDC and SSC compounds for a qualitative analysis.

On one hand, the analysis performed to the cave-like microstructure (**Figure 4.8a**) shows a lower proportion of Ce (3.0%), which is a representative element of the SDC compound; and a dominant existence of Co (49.2%) and Sr (22.8%), which are representative elements of  $\text{Sm}_{0.5}\text{Sr}_{0.5}\text{CoO}_{3-\delta}$ . Ratios between the atomic percentage of the representative elements of each compound are reported for a quantitative analysis in **Table 4.3**. Specifically, Sm and Sr are appearing in the same proportion (24.4% Sm/22.8% Sr  $\approx$  1), while the double of Co was quantified ((24.4% Sm+ 22.8% Sr)/49.2% Co  $\approx$  1). The ratios obtained between those elements obey the stoichiometry of SSC compounds. According with this information, it is possible to conclude that the major

proportion of Co and Sr in the region analysed and presented in **Figure 4.8a**, and the proportional concordance between the elements involved, points SSC as the compound responsible of the observed microstructure in form of cave embedded in the oxygen electrode functional layer.

On the other hand, the analysis focused on the SDC-SSC infiltrated mesoporous (**Figure 4.8b**), shows the higher proportion of Ce (43.1%) respect the amounts of Co (27.0%) and Sr (11.7%). Although an overlapping of Sm and Ce is showed in the spectrum labelled as 2 due to their similar energy transitions (**Figure 4.8c**), the proportion of Co and Sr is observed to decrease but the presence of these elements remains until the electrolyte interface. This result confirms the correct SSC infiltration of the SDC mesoporous scaffold.

From SEM and EDX results, it is concluded that more SSC solution than the needed for infiltrating the thickness and density of the mesoporous scaffold was added. Once the mesoporous scaffold was infiltrated and exposed to high temperatures during the sintering and operation periods, the remaining SSC solution formed this porous microstructure constituted by thin layers and caves on top of the mesoporous scaffold. Although this phase could probably present high catalytic activity, it likely leads to high resistances associated to the injection of high current densities due to the formed SSC microstructure. This variation of the oxygen electrode microstructure probably explains the limited performance of the measured high temperature electrolysis cell. Hence, the optimization of the infiltration procedure is needed for improving the electrolyser performance.

#### **4.4. Conclusions**

This chapter aimed to compare the electrolyte-supported and fuel electrode-supported configurations for the fabrication of SOEC cells. SDC-SSC oxygen electrodes and Ni-SDC fuel electrodes have been successfully fabricated on the electrolyte-supported configuration. Alternatively, the focus has pointed on the prosperous fabrication of SDC-SSC mesoporous oxygen electrode on Ni-YSZ FESCs. Different electrochemical and microstructural characterization techniques have been applied for that propose.

The electrochemical characterization of the ESCs based on fuel and oxygen mesoporous electrodes has demonstrated the feasibility of this type of materials for being used in the fabrication of SOEC cells electrodes operated on electrolysis and co-electrolysis modes. Based on the oxygen electrode fabrication optimization, a maximum current density of  $-0.25 \text{ A/cm}^2$  was injected at 1.3 V. The obtained results by I-V polarization curves and EIS measurements demonstrate that recorded high resistances results on a low performing SOEC cell. Representing more than 50% of the ASR value, the high ohmic resistance registered is mainly explained by the employment of a thick electrolyte ( $\approx 200 \text{ }\mu\text{m}$ ). Besides, the need of optimizing the Ni-SDC fuel electrode and the possible low electronic conductivity of the infiltrated mesoporous scaffold could also be considered for explaining the measured ohmic resistance values.

On the other hand, the electrochemical characterization of fuel electrode-supported SOECs cells reveal higher performance than ESCs allowing the injection of current densities up to  $-0.83$  and  $-0.81 \text{ A/cm}^2$  at 1.3 V in electrolysis and co-electrolysis modes. The obtained electrochemical results demonstrate the feasibility of applying this configuration for the fabrication of SOEC cells based on mesoporous oxygen electrodes, enhancing the performance. The I-V polarization curves measured under electrolysis and co-electrolysis fuel electrode gas compositions have presented two slopes, revealing the existence of diffusion problems when high current densities are injected, likely related to the mesoporous structure of the electrodes.

The closeness between the measured serial resistance values and the theoretical resistance contribution calculated for the employed electrolyte, have revealed that the electrolyte constitutes the main contribution to the ohmic resistance, being this remarkably smaller than in the case of ESC. Alternatively, three electrochemical processes have contributed to the measured polarization resistance. Studying the capacitances, characteristic frequencies and the arcs presented on the Nyquist and Bode plots, it has been deduced that mass transport processes taking place in the fuel electrode have constituted the main limiting contribution. Apart from the  $\text{H}_2\text{O}$  electrochemical reduction, an additional resistance has appeared operating con co-electrolysis mode, that has been deduced to be related to the  $\text{CO}_2$  reduction. Besides,

it has been concluded that charge transfer processes have also limited the performance of the oxygen electrode.

In concordance with the stability of the obtained electrochemical results, the microstructural characterization of the fuel and oxygen electrodes interfaces have revealed a good attachment to the electrolyte. However, focusing the analysis on the oxygen electrode interface have revealed the existence of cave-like morphologies. SEM coupled to EDX analysis performed at different points have allowed concluding that this microstructure is constituted by layers of sintered SSC from the infiltration. This microstructure has been directly related to the mass transport electrochemical processes limiting the SOEC cells performances when high current densities were injected.

Taking into account all the results recorded from the electrochemical and microstructural analysis of electrolyte- and fuel electrode-supported SOEC cells based on SDC-SSC mesoporous oxygen electrodes, it is possible to conclude that an enhancement of the electrochemical performance has been achieved implementing the fuel electrode-supported configuration. Despite that, the microstructural characterization has demonstrated that an optimization of the infiltration procedure is needed for improving the performance of the oxygen electrode when high current densities are injected and for long operation times. Additionally, the barrier layer microstructure needs to be densified for improving the SOEC performance and avoiding the formation of insulating phases.

#### 4.5. References

- [1] "FAE S.A.U." [Online]. Available: <http://www.fae.es/es/>.
- [2] J. Laurencin *et al.*, "Degradation mechanism of  $\text{La}_{0.6}\text{Sr}_{0.4}\text{Co}_{0.2}\text{Fe}_{0.8}\text{O}_{3-\delta}/\text{Gd}_{0.1}\text{Ce}_{0.9}\text{O}_{2-\delta}$  composite electrode operated under solid oxide electrolysis and fuel cell conditions," *Electrochim. Acta*, vol. 241, pp. 459–476, 2017.
- [3] D. The *et al.*, "Microstructural comparison of solid oxide electrolyser cells operated for 6100 h and 9000 h," *J. Power Sources*, vol. 275, pp. 901–911, 2015.
- [4] M. Morales *et al.*, "Multi-scale analysis of the diffusion barrier layer of gadolinia-doped ceria in a solid oxide fuel cell operated in a stack for 3000 h," *J. Power Sources*, vol. 344, pp. 141–151, 2017.
- [5] L. Bernadet, J. Laurencin, G. Roux, D. Montinaro, F. Mauvy, and M. Reytier, "Effects of Pressure on High Temperature Steam and Carbon Dioxide Co-electrolysis," *Electrochim. Acta*, vol. 253, pp. 114–127, 2017.
- [6] A. Nechache, M. Cassir, and A. Ringuedé, "Solid oxide electrolysis cell analysis by means of electrochemical impedance spectroscopy: A review," *J. Power Sources*, vol. 258, pp. 164–181, 2014.
- [7] J. C. Ruiz-Morales *et al.*, *Pilas de combustible de óxidos sólidos (SOFC)*, 2 nd. 2008.
- [8] M. Torrell, S. García-Rodríguez, A. Morata, G. Penelas, and A. Tarancón, "Co-electrolysis of steam and CO<sub>2</sub> in full-ceramic symmetrical SOECs: a strategy for avoiding the use of hydrogen as a safe gas," *Faraday Discuss.*, vol. 182, pp. 241–255, 2015.
- [9] U.S. Department of Energy, *Fuel Cell Handbook*, vol. 7 Edition. 2004.
- [10] "HTceramix S.A." [Online]. Available: <http://www.solidpower.com/en/about-us/locations/>.
- [11] "ECo project." [Online]. Available: <http://www.eco-soec-project.eu/>.
- [12] A. Nechache, M. Cassir, and A. Ringuedé, "Solid oxide electrolysis cell analysis by means of electrochemical impedance spectroscopy: A review," *Journal of Power*

*Sources*, vol. 258. pp. 164–181, 2014.

- [13] F. Qiang, K. Sun, N. Zhang, X. Zhu, S. Le, and D. Zhou, "Characterization of electrical properties of GDC doped A-site deficient LSCF based composite cathode using impedance spectroscopy," *J. Power Sources*, vol. 168, pp. 338–345, 2007.
- [14] H. Fan, Y. Zhang, and M. Han, "Infiltration of La<sub>0.6</sub>Sr<sub>0.4</sub>FeO<sub>3</sub>-nanoparticles into YSZ scaffold for solid oxide fuel cell and solid oxide electrolysis cell," *J. Alloys Compd.*, vol. 723, pp. 620–626, 2017.
- [15] H. Fan, M. Keane, N. Li, D. Tang, P. Singh, and M. Han, "Electrochemical stability of La<sub>0.6</sub>Sr<sub>0.4</sub>Co<sub>0.2</sub>Fe<sub>0.8</sub>O<sub>3-δ</sub>-infiltrated YSZ oxygen electrode for reversible solid oxide fuel cells," *Int. J. Hydrogen Energy*, vol. 39, pp. 14071–14078, 2014.
- [16] S. D. Ebbesen, R. Knibbe, and M. Mogensen, "Co-Electrolysis of Steam and Carbon Dioxide in Solid Oxide Cells," *J. Electrochem. Soc.*, vol. 159, no. 8, pp. F482–F489, 2012.
- [17] C. Graves, S. D. Ebbesen, and M. Mogensen, "Co-electrolysis of CO<sub>2</sub> and H<sub>2</sub>O in solid oxide cells: Performance and durability," *Solid State Ionics*, vol. 192, pp. 398–403, 2011.

# ***Chapter 5***

*Optimization of the oxygen electrode for enhancing the performance of SOEC cells*



<b>5. Optimization of the oxygen electrode for enhancing the performance of SOEC cells.....</b>	<b>155</b>
<b>5.1. Chapter overview.....</b>	<b>155</b>
<b>5.2. Characterization of the state-of-the-art SOEC cells.....</b>	<b>156</b>
<b>5.3. Optimization strategy of SOEC oxygen electrodes.....</b>	<b>157</b>
<b>5.4. Comparison of SOEC cells .....</b>	<b>160</b>
<b>5.4.1. Performance comparison of SOEC cells .....</b>	<b>160</b>
<b>5.4.2. Microstructural analysis of SOEC cells .....</b>	<b>169</b>
<b>5.5. Conclusions.....</b>	<b>174</b>
<b>5.6. References .....</b>	<b>175</b>



## 5. Optimization of the oxygen electrode for enhancing the performance of SOEC cells

### 5.1. Chapter overview

The general aim of this work is to present the feasibility of using infiltrated mesoporous materials for fabricating electrodes to be applied on highly performing Solid Oxide Electrolysis Cells (SOECs). The results presented in **Chapter 4** demonstrate the possibility of applying the proposed approach. However, results showed that there is room for further optimization in terms of the cell architecture and microstructure. This chapter presents a deeper study focused on analysing the influence of the barrier layer and the oxygen electrode microstructure to the SOEC final performances. State-of-the-art (SoA) materials were selected for this study, i.e.  $\text{Ce}_{0.8}\text{Gd}_{0.2}\text{O}_{1.9}$  (CGO) for the barrier layer and  $\text{Ce}_{0.8}\text{Gd}_{0.2}\text{O}_{1.9}\text{-La}_{0.6}\text{Sr}_{0.4}\text{Co}_{0.2}\text{Fe}_{0.8}\text{O}_3$  (CGO-LSCF) for the oxygen electrode. Fuel electrode-supported cells of approximately  $\approx 1.5 \text{ cm}^2$  of active area were fabricated using the SoA materials. These cells are described as Ni-YSZ/YSZ/CGO<sub>bl</sub>/CGO-LSCF/LSCF and have been characterized in **section 5.2**.

The influence of the applied methods for the fabrication of the barrier layer and the use of mesoporous oxygen electrodes on the SOEC performance is the focus of the **section 5.3**. Specifically, PLD CGO barrier layers and mesoporous CGO-LSCF oxygen electrodes are discussed.

Finally, **section 5.4** compares the results arising from the three types of cells fabricated in this chapter, namely, SoA SOEC cells (called Cells<sub>HT</sub>), SOEC cells with mesoporous oxygen electrode (Cells<sub>meso</sub>) and SOEC cells with PLD barrier layers and mesoporous oxygen electrode (Cells<sub>PLD\_meso</sub>). Microstructural and electrochemical characterizations are carried out to compare the performance of these cells under similar operating conditions on co-electrolysis mode. I-V polarization curves and Electrochemical Impedance Spectroscopy (EIS) measurements are used for the performance evaluation while the microstructural characterization of the three types of cells is based on Scanning Electron Microscopy (SEM) and Energy-Dispersive X-Ray (EDX) analysis.

## 5.2. Characterization of the state-of-the-art SOEC cells

HTceramix/SOLIDpower (Switzerland) [1] fuel electrode-supported cells were taken as reference for characterizing the performance of the SoA SOEC cells. These electrolysis cells present circular shape with an active electrode area of around 1.5 cm<sup>2</sup>. These supports are composed by a thick and porous Ni-YSZ fuel electrode of around 300 μm in thickness, and a thin and dense Y<sub>2</sub>O<sub>3</sub>-ZrO<sub>2</sub> (YSZ) electrolyte of around 8 μm in thickness, both of them fabricated by tape casting. Both the CGO10% barrier layer (≈2 μm) and the oxygen electrode were fabricated by screen printing on top of the electrolyte. Specifically, porous functional active layers of CGO-LSCF composites (≈15 μm) and LSCF (≈18 μm) electrode layers were deposited as oxygen electrodes. These cells are from now on presented as Cells<sub>HT</sub>. The main information of this type of cell is recorded in **Table 5.1**.

	Fuel electrode	Electrolyte	Barrier layer	Oxygen electrode
Cells <sub>HT</sub>	Ni-YSZ (≈300 μm)	YSZ (≈8μm)	CGO10% (≈2 μm) <i>Screen printing</i>	CGO10%-LSCF (≈15μm) LSCF (≈18μm) <i>Screen printing</i>

**Table 5.1:** Compositional specifications of Cells<sub>HT</sub> taken as reference.

The microstructural and electrochemical characterization of Cells<sub>HT</sub> are presented in **Figure 5.1**. A general overview of the microstructure constituting the cross-section of Cells<sub>HT</sub> is presented in **Figure 5.1a** while a higher magnification micrograph is presented in **Figure 5.1b**, allowing a detailed observation of the microstructures constituting the electrolyte, the barrier layer and the oxygen electrode functional layer. Both micrographs reveal that commercial Cells<sub>HT</sub> present a dense electrolyte, a porous CGO barrier layer and a homogeneous and porous oxygen electrode.

The electrochemical characterization of Cells<sub>HT</sub> consisted on performing I-V polarization curves and EIS measurements under co-electrolysis fuel electrode gas composition (45% H<sub>2</sub>O +45% CO<sub>2</sub> + 10% H<sub>2</sub>) and synthetic air atmosphere on the oxygen electrode at 750 °C on galvanostatic mode. A maximum current density of -0.55 A/cm<sup>2</sup> was injected for this type of cell, as it is shown in **Figure 5.1c**. EIS measurements reveal a serial resistance of 0.21 Ω and an overall polarization

resistance of 0.33 and 0.34  $\Omega\cdot\text{cm}^2$  at OCV and  $-0.5 \text{ A/cm}^2$  respective operation points (Figure 5.1d).

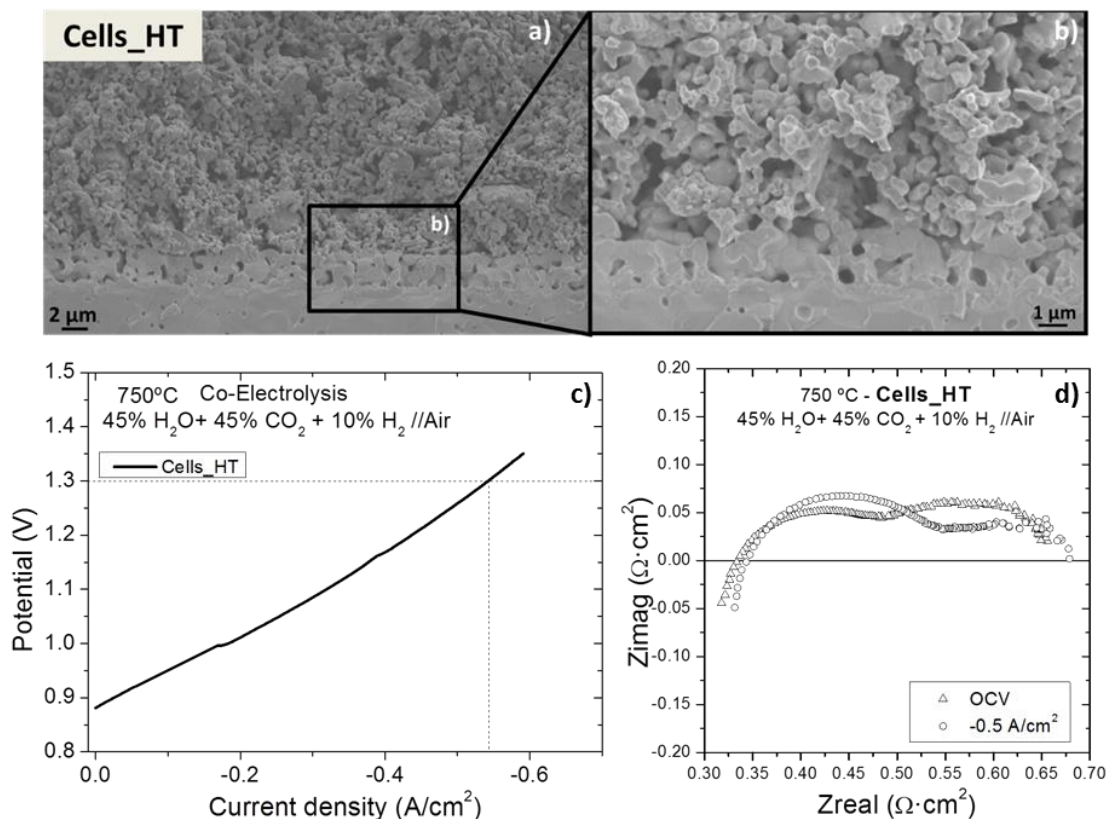


**Figure 5.1:** Characterization of Cells\_HT. a) Cross-section micrograph of the electrolyte, the barrier layer and the oxygen electrode, and b) as zoom of the oxygen electrode interface. Electrochemical characterization at 750 °C on co-electrolysis mode: c) I-V polarization curve and d) EIS measurements recorded at OCV and  $-0.5 \text{ A/cm}^2$  operation points.

### 5.3. Optimization strategy of SOEC oxygen electrodes

To allow a proper comparison, all the electrolysis cells presented in this chapter were fabricated using equivalent half cells (fuel electrode and electrolyte) from HTCeramics.

The state-of-the-art oxygen electrodes are based on composites of Mixed Ionic and Electronic Conductors (MIECs) and the corresponding electrolyte or a similar pure Ionic Conductor (IC). The aim is to improve the mechanical compatibility of the oxygen electrode with the electrolyte, enhance the catalytic activity, relax the mechanical and chemical stresses at the interface, and increase the number of points electrochemically active [2-5]. According to this, the oxygen electrode of the cells characterized in this chapter presents a bi-layer structure composed by a porous CGO-LSCF composite and a LSCF layer.

Moreover, the need of enhancing SOEC durability is currently one of the main problems for the market penetration of this technology [6,7]. As it is well known, diffusion of Sr, La and Zr elements from LSCF and YSZ compounds promotes the formation of lanthanum zirconate ( $\text{La}_2\text{Zr}_2\text{O}_7$ ) and strontium zirconate ( $\text{SrZrO}_3$ ) insulating phases in the interface of the oxygen electrode and the electrolyte, what increases the ohmic resistance by reducing the ionic conductivity [6-9]. A CGO barrier layer is usually incorporated at the electrolyte-electrode interface to avoid the described diffusion process [6-9]. As it is studied in this chapter, the microstructure and thickness of this CGO barrier layer is also affecting the performance of the cells.

In this line, new approaches for generating optimised diffusion barriers and oxygen electrode microstructures are proposed and analysed in this chapter in order to enhance the performance of high temperature electrolysis cells (SOECs). According to this purpose, Cells\_meso and Cells\_PLD\_meso were designed, fabricated and tested, and are also presented in this chapter. The three types of characterized cells are described as Ni-YSZ/YSZ/CGO<sub>bl</sub>/CGO-LSCF/LSCF.

Cells\_meso were fabricated introducing an infiltrated mesoporous-based oxygen electrode. This set of cells (**Figure 5.2**) have the same thin screen-printed CGO10% barrier layers ( $\approx 2 \mu\text{m}$ ) than Cells\_HT, but their oxygen electrodes have a bi-layer structure, including a mesoporous based functional layer, which substitutes the single screen-printed commercial oxygen electrode of the SoA Cells\_HT.

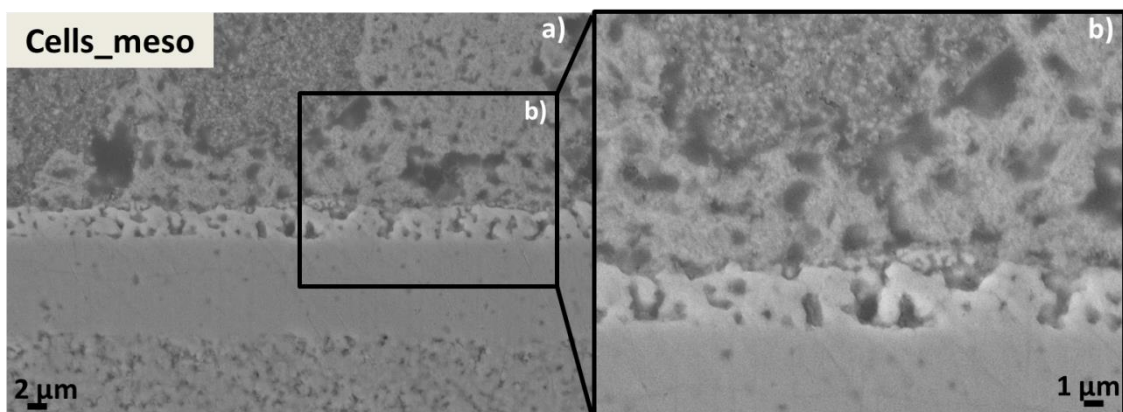


**Figure 5.2:** a) SEM cross-section micrograph of Cells\_meso oxygen electrodes, including a zoom of the interface.

Lastly, the Cells\_PLD\_meso are distinguished by substituting the screen-printed CGO barrier layer by one fabricated applying the PLD technique. In this set of SOEC

cells, CGO barrier layers ( $\approx 2 \mu\text{m}$ ) were deposited by PLD and densified by an annealing thermal treatment. When Cells\_PLD\_meso are studied by SEM, the **Figure 5.3a** and **5.3b** micrographs show a denser barrier layer than the previously presented for Cells\_HT and Cells\_meso. The fabrication of oxygen electrodes composed by infiltrated CGO-LSCF functional layers and LSCF layers were performed applying the same method than for Cells\_meso.

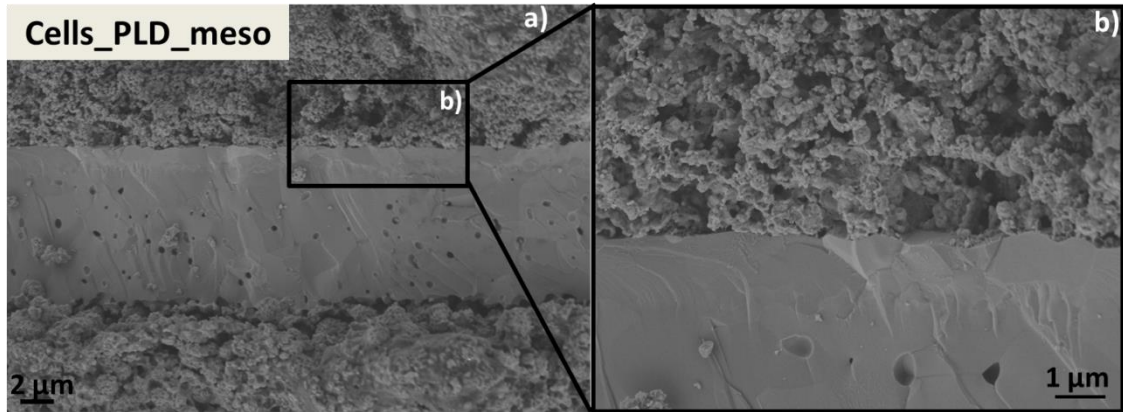


**Figure 5.3** a) SEM cross-section micrograph of Cells\_PLD\_meso oxygen electrodes, including a zoom of the interface.

The main information of the fabricated Cells\_meso and Cells\_PLD\_meso is recorded in **Table 5.2**:

	Fuel electrode	Electrolyte	Barrier layer	Oxygen electrode
Cells_meso	Ni-YSZ ( $\approx 300 \mu\text{m}$ ).	YSZ ( $\approx 8 \mu\text{m}$ )	CGO10% ( $\approx 2 \mu\text{m}$ ) Screen printing	CGO-LSCF ( $\approx 15 \mu\text{m}$ ) <i>infiltrated mesoporous</i> LSCF ( $\approx 30 \mu\text{m}$ ) <i>air brushing</i>
Cells_PLD_meso	Ni-YSZ ( $\approx 300 \mu\text{m}$ )	YSZ ( $\approx 8 \mu\text{m}$ )	CGO20% ( $\approx 2 \mu\text{m}$ ) PLD	CGO-LSCF ( $\approx 12 \mu\text{m}$ ) <i>infiltrated mesoporous</i> LSCF ( $\approx 30 \mu\text{m}$ ) <i>air brushing</i>

**Table 5.2:** Compositional specifications of fabricated Cells\_meso and Cells\_PLD\_meso.

## 5.4. Comparison of SOEC cells

### 5.4.1. Performance comparison of SOEC cells

Cells\_HT, Cells\_meso and Cells\_PLD\_meso fuel electrode-supported cells were electrochemically characterized under the same operation conditions in order to compare their performances. Specifically, I-V polarization curves and EIS measurements were performed on galvanostatic co-electrolysis mode at 750 °C.

All the measurements were recorded at the same gas composition: 45% H<sub>2</sub>O +45% CO<sub>2</sub>+10% H<sub>2</sub> as fuel electrode atmosphere, and synthetic air on the oxygen electrode chamber. 10% of H<sub>2</sub> was added in the fuel electrode gas composition in order to avoid the oxidation of Ni in presence of H<sub>2</sub>O when the hydrogen partial pressure (p<sub>H<sub>2</sub></sub>) is reduced to less than 0.1, ensuring the existence of a reducing atmosphere that stabilizes Ni as metal phase. I-V polarization curves of the three fuel electrode-supported cells were measured in galvanostatic mode and are presented in **Figure 5.4**:

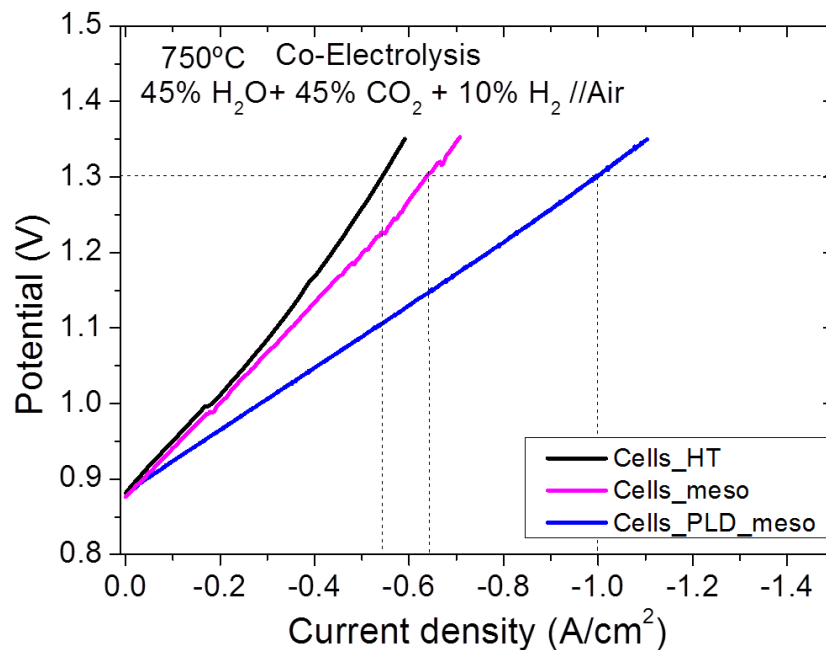


**Figure 5.4:** I-V polarization curves of Cells\_HT, Cells\_meso and Cells\_PLD\_meso fuel electrode-supported cells measured on co-electrolysis mode under the same operating conditions.

An Open Circuit Voltage (OCV) value of 0.88 V is obtained for all the cells. This voltage is in great agreement with the calculated OCV of 0.89 expected for our experimental conditions [10]. Obtaining the very same experimental OCV values for the three cells (and matching the theoretical one) confirms a great gas-tightness of the

chambers and the total absence of leakages between the fuel and the oxygen gas atmospheres. This fact allows a proper comparison of the obtained performances.

The maximum injected current densities for the different cells at 1.30 V is of  $-0.55 \text{ A/cm}^2$  for Cells\_HT,  $-0.64 \text{ A/cm}^2$  for Cells\_meso and  $-1.00 \text{ A/cm}^2$  for Cells\_PLD\_meso. A clear trend can be observed in **Figure 5.4**, which shows a progressive enhancement of the performance with the implementation of the proposed barrier layer and mesoporous oxygen electrodes. According to these results, first, the Cells\_meso show better performance than Cells\_HT, increasing the injected current density in ca.  $-0.1 \text{ A/cm}^2$  at 1.30 V. Second, comparing the Cell\_meso and Cell\_PLD\_meso, it is concluded that the introduction of a CGO barrier layer deposited by PLD and the progressive improvement of the oxygen electrode fabrication results in a significant enhancement of the performance, increasing the maximum injected current density in  $-0.36 \text{ A/cm}^2$  at the same voltage.

In concordance with the obtained results, the already presented advantages of the mesoporous materials has an impact in the final performance as well as the novel applied barrier layer. This last improvement is likely due to a minimization of the diffusion during the fabrication process (being at reduced temperatures by PLD), and the avoidance of gadolinium migration to the grain boundaries of the CGO barrier layer [7,8]. This barrier layer, which have been fabricated by PLD and has been sintered up to high temperatures, have demonstrated to be dense enough for avoiding degradation issues related to the destabilization of the involved phases. The increase on the performance showed by the obtained results of Cell\_PLD\_meso is a combination of both the barrier layer and the oxygen electrode improved microstructure.

The performances presented in **Figure 5.4** can be considered relevant when compared with the ones expected and reported in the bibliography. Before starting the comparison, it is important to mention that the referred works are at notably higher temperatures that the presented here and sometimes from milder electrolysis conditions (vs. co-electrolysis atmospheres). For example, Laurencin *et al.* [7] reported the characterization of a  $9 \text{ cm}^2$  cell fabricated following the same procedure than the here presented Cell\_HT obtaining a maximum injected current density of  $-0.70 \text{ A/cm}^2$

at 1.32 V under 50% H<sub>2</sub>O + 50% H<sub>2</sub> atmosphere on electrolysis mode at 850 °C. Other works dedicated to SOEC cells based on Ni-YSZ fuel electrode supports with a LSM-YSZ oxygen electrode under 45% H<sub>2</sub>O +10% H<sub>2</sub> + 45 %CO<sub>2</sub> /O<sub>2</sub> at 850 °C, presented -1.50 A/cm<sup>2</sup> of injected current density at 1.25 V [11]. Moreover, J. Hong *et al.* [12] presents a Ni-YSZ/YSZ/CGO/LSCF-CGO cell tested under 20% H<sub>2</sub>O + 5% H<sub>2</sub> + 40% CO<sub>2</sub> + 35% N<sub>2</sub> as fuel electrode gas composition and air as oxygen electrode atmosphere on co-electrolysis mode at 800 °C of operation temperature. A maximum current density of -0.80 A/cm<sup>2</sup> was injected at 1.35 V.

The three I-V curves presented on **Figure 5.4** show very linear trends with the increase of the injected current density. This behaviour can be explained by the ratio between the total flow and the employed inlet fuel electrode gas composition. In this case, where the total flow is of 144 NmL/min·cm<sup>-2</sup>, the fuel utilization of the inlet composition is lower than 10 %. In concordance with that, especially in Cells\_meso and Cells\_PLD\_meso, the linearity indicates that any diffusion resistance is being introduced, not by the lack of gas, which is in excess, neither by the mesoporous structure itself, overcoming one of the possible limitations of the proposed microstructures.

Same SOEC cells were characterized by EIS under 45% H<sub>2</sub>O +45% CO<sub>2</sub> +10% H<sub>2</sub> atmospheres for co-electrolysis operation. All the measurements were performed at a temperature of T=750 °C. Impedance spectroscopy data were measured at OCV and at -0.5 A/cm<sup>2</sup> in galvanostatic mode. The Nyquist plots measured at OCV for the three types of fabricated cells are presented in **Figure 5.5**. All impedance spectroscopy data were fitted with the same equivalent circuit, LR<sub>s</sub>(R<sub>p1</sub>Q<sub>1</sub>)(R<sub>p2</sub>Q<sub>2</sub>), where L represents the inductance from the set-up, R<sub>s</sub> the serial resistance, and RQ the polarization resistance contributions [13]. As it has been already explained in previous chapters, the main contribution to the serial resistance is generally attributed to the ionic mobility through the electrolyte, but also includes the resistance associated to the electrolyte-electrodes interfaces, and to the current collectors and contacts. Standard RQ elements, representing a parallel circuit of a resistance (R) and a “Q” or Constant Phase Element (CPE) have been used as a model fitting the experimental Nyquist arcs. The values obtained from the fitting for each parameter are presented in **Table 5.3**. Among

them, the C value associated to each resistance, represents the true capacitance calculated from the CPE element as  $C_p=(Q)^{(1/n)}R_{p1}^{(1-n/n)}$ , where  $n$  value ranges between 0 and 1, and indicates the angle of the depressed arc. Besides, the ohmic resistance values presented in **Table 5.3** are suitable with the values of **Figure 5.5**.

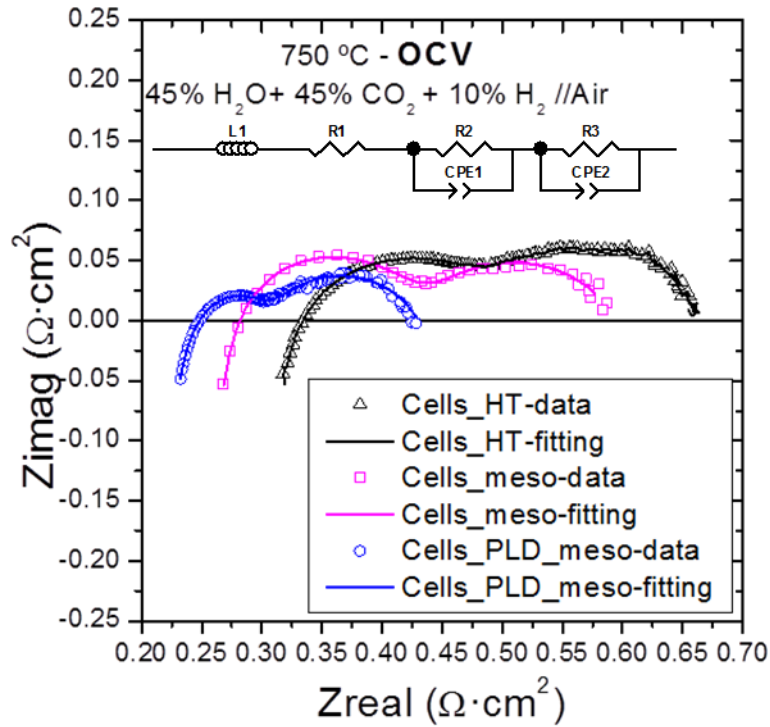


**Figure 5.5:** Nyquist plots of Cells\_HT, Cells\_meso and Cells\_PLD\_meso obtained from EIS measurements on co-electrolysis operation mode at OCV and 750 °C.

	Cells_HT	Cells_meso	Cells_PLD_meso
L (H)	$2.9 \cdot 10^{-7}$	$5.3 \cdot 10^{-7}$	$5.9 \cdot 10^{-7}$
$R_s$ ( $\Omega \cdot \text{cm}^2$ )	$3.3 \cdot 10^{-1}$	$2.8 \cdot 10^{-1}$	$2.4 \cdot 10^{-1}$
$R_{p1}$ ( $\Omega \cdot \text{cm}^2$ )	$2.4 \cdot 10^{-1}$	$2.3 \cdot 10^{-1}$	$7.6 \cdot 10^{-2}$
$C_1$ (F/cm <sup>2</sup> )	$2.6 \cdot 10^{-4}$	$4.8 \cdot 10^{-4}$	$7.8 \cdot 10^{-4}$
n	0.53	0.70	0.78
f max	$2.5 \cdot 10^3$	$1.3 \cdot 10^3$	$2.6 \cdot 10^3$
$R_{p2}$ ( $\Omega \cdot \text{cm}^2$ )	$1.6 \cdot 10^{-1}$	$1.6 \cdot 10^{-1}$	$1.6 \cdot 10^{-1}$
$C_2$ (F/cm <sup>2</sup> )	$1.3 \cdot 10^{-1}$	$2.4 \cdot 10^{-1}$	$4.0 \cdot 10^{-1}$
n	0.76	0.65	0.55
f max	7.5	3.9	2.4
$R_p$ total ( $\Omega \cdot \text{cm}^2$ )	$4.0 \cdot 10^{-1}$	$3.9 \cdot 10^{-1}$	$2.3 \cdot 10^{-1}$
ASR ( $\Omega \cdot \text{cm}^2$ )	$7.4 \cdot 10^{-1}$	$6.7 \cdot 10^{-1}$	$4.8 \cdot 10^{-1}$

**Table 5.3:** Electrochemical parameters values obtained from fitting each EIS data measured at OCV for Cells\_HT, Cells\_meso and Cells\_PLD\_meso (Figure 5.2) with the  $LR_s(R_{p1}Q_1)(R_{p2}Q_2)$  equivalent circuit. Here  $R_s$  values are suitable with Nyquist plots, and C represents the true capacitance calculated as  $C_p=(Q)^{(1/n)}R_{p1}^{(1-n/n)}$ .

The contribution of the electrolyte to the serial resistance was calculated to be on the order of  $\approx 0.04 \Omega$ , considering the YSZ conductivity at  $750 \text{ }^\circ\text{C}$  [14], the thickness of the electrolyte and the active area of the samples measured. The remarkable difference between the theoretical contribution of the electrolyte and the measured serial resistance ( $0.22$ ,  $0.18$  and  $0.16 \Omega$  for Cells\_HT, Cells\_meso and Cells\_PLD\_meso, respectively), evidences the already commented contribution of the additional resistances from current collectors and electrolyte-electrodes interfaces. As is clearly showed in **Figure 5.5**, an important difference on the serial resistance values measured for the different fabricated cells is also noticed. Since the same set-up was used for the electrochemical tests, the same contribution from the current collectors should be expected. This suggests that the difference between the serial resistance values are mainly due to the resistance associated to the different CGO barrier layers and the electrolyte-oxygen electrode interfaces.

Following the trend observed in the I-V curve measurements, Cells\_HT present higher serial resistance than Cells\_meso in the EIS measurements. This improvement on the serial resistance value can be explained by the improvement of the electronic pathway through a better infiltrated microstructure, which reduce the current collection resistance contribution. As a consequence of the favoured conduction of electrons, the ohmic and polarization resistance was reduced on characterized Cells\_meso. From the comparison of Cells\_meso and Cells\_PLD\_meso, it is deduced that the introduction of barrier layers deposited by PLD and sintered up to high temperatures, joint to the mesoporous microstructure of the oxygen electrode functional layer, results on an important improvement of the electrolyser performance.

As it can be seen in **Figure 5.5**, the three presented Nyquist plots are composed by two arcs contributing to the polarization resistance starting by the electrodes electrochemical processes [13]. The measurements were performed at OCV, where mainly the activation overpotential is contributing to the overall resistance [15]. The performed fittings determined the resistance associated to each of these arcs, as well as the capacitance and frequency that allow identifying the electrochemical process involved (**Table 5.3**). The concordance between the capacitances and characteristic

frequency values determined for the analysed Nyquist plot reveals that the same electrochemical processes are associated to  $R_{p1}$  at high frequencies ( $\approx 10^3$  Hz), and to  $R_{p2}$  at low frequency processes ( $\approx 1$  Hz) in the three types of cells.  $R_{p1}$ , caused by charge transfer processes, present characteristic capacitances around  $\approx 10^{-4}$  F/cm<sup>2</sup>; and  $R_{p2}$ , identified as non-charge transfer electrochemical processes, which are generally dominated by gas diffusion and gas conversion electrochemical processes, show capacitances around  $\approx 10^{-1}$  F/cm<sup>2</sup> [16-20]. The similarity of the three  $R_{p2}$  contributions leads to ascribe it to processes more controlled by the fuel electrode, which is common for the three cells. However, similar  $R_{p1}$  values were obtained for Cells\_HT and Cells\_meso as it is clearly shown in **Figure 5.6**, while it is considerable smaller for Cells\_PLD\_meso. Therefore, an enhancement of the electrodes performance is indicated by the lower  $R_{p1}$  resistance associated to Cells\_PLD\_meso if that resistance contribution is compared with the ones of Cells\_HT and Cells\_meso reported in **Table 5.3**. Comparing the fabrication procedures of the different cells (**Table 5.1** and **5.2**), it is deduced that the introduction of a dense CGO barrier layer and a functional layer based on infiltrated mesoporous materials are the main causes of the enhancement of the performance showed by Cell\_PLD\_meso. According to this, Cell\_PLD\_meso presents a considerable lower total polarization resistance contribution to the overall resistance if compared with Cells\_HT and Cells\_meso,  $\approx 2 \cdot 10^{-1}$  vs  $\approx 4 \cdot 10^{-1}$   $\Omega \cdot \text{cm}^2$ , indicating that the performance of the electrodes was improved by the implementation of the proposed approaches.

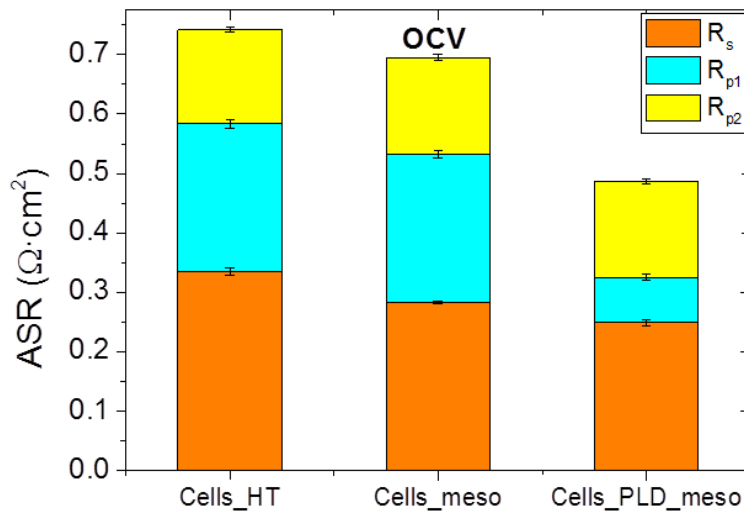


**Figure 5.6:** Bars plot of  $R_s$ ,  $R_{p1}$  and  $R_{p2}$  values (Table 5.2) and its corresponding errors obtained from fitting impedance data measured at OCV of the three Cells\_HT, Cells\_meso and Cells\_PLD\_meso types of cells. The total value of the column is the overall ASR of the three cells.

The overall Area Specific Resistance (ASR) (**Table 5.3**) associated to each type of cells was calculated as the sum of the contributions from the serial ( $R_s$ ) and polarization resistances ( $R_{p1}$  and  $R_{p2}$ ), which were obtained from fitting the Nyquist plots measured at OCV and presented in **Figure 5.5**, resulting in 0.74, 0.69 and 0.49  $\Omega\cdot\text{cm}^2$  for Cells\_HT, Cells\_meso and Cells\_PLD\_meso, respectively. ASR calculated from the slope of the I-V curve [21] (**Figure 5.4**) are 0.67, 0.66 and 0.43  $\Omega\cdot\text{cm}^2$ . The tendency of these values perfectly matches with the trend shown by the overall total resistance contribution (ASR) obtained from the fitting of the EIS data (**Table 5.3**), what validate the fittings. The difference between the values obtained from both the I-V polarization curves slopes and the ones obtained from the Nyquist fitting is explained by the nature of both measurements. While EIS measurements are developed at OCV; the value obtained from the slope of the I-V curve considers all the current density-voltage range of measurements, averaging different parts, probably with different limiting processes.

EIS measurements were also performed in galvanostatic mode at  $-0.5 \text{ A/cm}^2$  and  $750 \text{ }^\circ\text{C}$  for the three types of cells under study. The obtained Nyquist plots are presented in **Figure 5.7**. As it has been already explained in previous sections, impedance measurements performed at different operation conditions could provide different information about the electrochemical processes involved. At this low operation voltage, it is expected the contribution from the activation overpotential and an additional contribution from the ohmic overpotential [15]. This overpotential is related to the resistance of ions and electrons for passing through the electrolyte and the electrodes, but also to other phenomena in the electrodes that shows ohmic behaviours. In line with the OCV measurements, impedance data recorded at  $-0.5 \text{ A/cm}^2$  were fitted with the same  $LR_s(R_{p1}Q_1)(R_{p2}Q_2)$  equivalent circuit in order to identify the different electrochemical processes contributing to the polarization resistance, and analysing them [13]. The values obtained for the fitted parameters are summarised in **Table 5.4**.

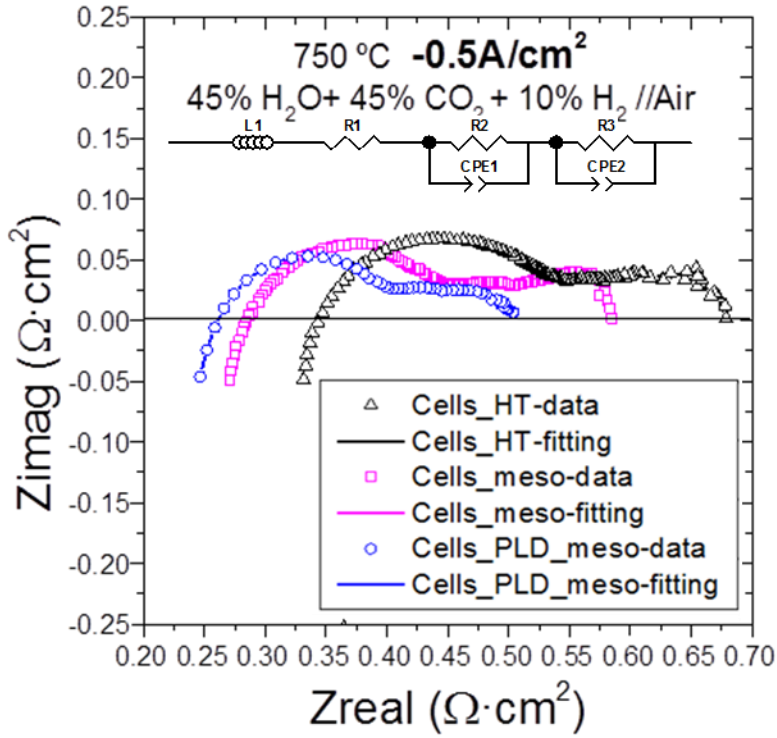


**Figure 5.7:** Nyquist plots of cells Cells<sub>HT</sub>, Cells<sub>meso</sub> and Cells<sub>PLD\_meso</sub> obtained from EIS measurements on co-electrolysis operation mode at  $-0.5 \text{ A/cm}^2$  and  $750 \text{ °C}$ .

	Cells <sub>HT</sub>	Cells <sub>meso</sub>	Cells <sub>PLD_meso</sub>
L (H)	$5.3 \cdot 10^{-7}$	$4.3 \cdot 10^{-7}$	$5.8 \cdot 10^{-7}$
$R_s$ ( $\Omega \cdot \text{cm}^2$ )	$3.3 \cdot 10^{-1}$	$2.9 \cdot 10^{-1}$	$2.6 \cdot 10^{-1}$
$R_{p1}$ ( $\Omega \cdot \text{cm}^2$ )	$2.6 \cdot 10^{-1}$	$1.9 \cdot 10^{-1}$	$1.6 \cdot 10^{-1}$
$C_1$ ( $\text{F/cm}^2$ )	$1.7 \cdot 10^{-4}$	$4.0 \cdot 10^{-4}$	$4.6 \cdot 10^{-4}$
n	$6.9 \cdot 10^{-1}$	$7.3 \cdot 10^{-1}$	$7.9 \cdot 10^{-1}$
f max (Hz)	$3.5 \cdot 10^3$	$2.1 \cdot 10^3$	$2.1 \cdot 10^3$
$R_{p2}$ ( $\Omega \cdot \text{cm}^2$ )	$1.5 \cdot 10^{-1}$	$1.8 \cdot 10^{-1}$	$1.2 \cdot 10^{-1}$
$C_2$ ( $\text{F/cm}^2$ )	$3.1 \cdot 10^{-1}$	$3.7 \cdot 10^{-1}$	$2.0 \cdot 10^{-1}$
n	$5.8 \cdot 10^{-1}$	$5.0 \cdot 10^{-1}$	$5.5 \cdot 10^{-1}$
f max (Hz)	3.3	2.4	7.0
$R_p$ total ( $\Omega \cdot \text{cm}^2$ )	$4.2 \cdot 10^{-1}$	$3.6 \cdot 10^{-1}$	$2.8 \cdot 10^{-1}$
ASR ( $\Omega \cdot \text{cm}^2$ )	$7.5 \cdot 10^{-1}$	$6.5 \cdot 10^{-1}$	$5.4 \cdot 10^{-1}$

**Table 5.4:** Electrochemical parameters values obtained from fitting each EIS data measured at  $-0.5 \text{ A/cm}^2$  for cells Cells<sub>HT</sub>, Cells<sub>meso</sub> and Cells<sub>PLD\_meso</sub> (Figure 5.3) with the  $LR_s(R_{p1}Q_1)(R_{p2}Q_2)$  equivalent circuit. Here  $R_s$  values are suitable with Nyquist plots, and C represents the true capacitance calculated as  $C_p = (Q)^{(1/n)} R_{p1}^{(1-n)}$ .

Ohmic resistance values presented in **Table 5.4** are in concordance with the ones presented in **Table 5.3**, validating the employed equivalent circuit applied for fitting.

As it has been indicated for the measurements recorded at OCV, the significant difference between the resistance associated to the YSZ electrolyte in these operating conditions and the measured serial resistances indicates that the main contribution to this resistance comes from the electrolyte-electrodes interfaces. Furthermore, the important difference between the measured values for the Cells\_HT, Cells\_meso and Cells\_PLD\_meso, what is clearly observable in **Figure 5.8**, indicates the influence of different microstructure of the proposed oxygen electrodes and its interfaces to the overall resistance. As previously discussed, these values are in concordance with the implementation of an oxygen electrode functional layer based on infiltrated mesoporous materials and a PLD barrier layer.

Related with the ohmic resistance difference found for the three types of cells, Nurk *et al.* have reported the existence of a serial resistance dependence with the deposition method of the CGO barrier layer and its later sintering temperature [6]. Specifically, those authors found the highest serial resistance for a CGO barrier layer sintered at 950 °C with the cathode sintered at 1100 °C; while the lowest serial resistance value was measured for a CGO layer deposited by PLD and sintered at 1300 °C with an  $\text{La}_{0.6}\text{Sr}_{0.4}\text{Co}_{0.2}\text{O}_3$  (LSC) electrode treated at 950 °C [6]. It is important to notice that the best fabrication conditions reported by Nurk *et al.* for the fabrication of the barrier layer and the oxygen electrode are very close to the ones applied for the fabrication of Cell\_PLD\_meso.

Also in concordance with the analysis of the measurements recorded at OCV, two main polarization resistance contributions are detected on the Nyquist plots measured at  $-0.5 \text{ A/cm}^2$  (**Figure 5.7**). The fitting of impedance spectroscopy data reveals the contribution of two resistances,  $R_{p1}$  and  $R_{p2}$ . The contribution of  $R_s$ ,  $R_{p1}$  and  $R_{p2}$  for the overall ASR can be easily observed in **Figure 5.8**. According to the capacitance and frequency values presented in **Table 5.4**, the capacitance ( $\approx 10^{-4} \text{ F/cm}^2$ ) and summit frequency ( $\approx 10^3 \text{ Hz}$ ) values indicated that the  $R_{p1}$  resistance contribution was produced by charge transfer processes probably related to the electrode-electrolyte interface [16-20]; while the low frequency electrochemical process ( $\approx 1 \text{ Hz}$ ) was identified as non-charge transfer processes, presenting characteristic capacitances of  $10^{-1} \text{ F/cm}^2$  [16-20]. This second arc could be related with the fuel conversion process.

As it is observed in **Figure 5.8**, different  $R_{p1}$  and  $R_{p2}$  values were measured for the three types of cells. A progressive decrease of these values is observed comparing them from Cells\_HT to Cells\_PLD\_meso, showing the influence of the two introduced microstructural modifications.

Besides, Cells\_PLD\_meso present similar total polarization resistance value than the calculated from impedances data measured at OCV,  $0.28 \Omega \cdot \text{cm}^2$ . That indicates constant contribution of the electrochemical processes involved in Cells\_PLD\_meso when higher current densities are injected. This evidences that Cells\_PLD\_meso present a microstructure able to electrolyse  $\text{H}_2\text{O}$  and  $\text{CO}_2$  molecules independently of the injected current density, what constitutes a limitation for Cells\_HT and Cells\_meso.

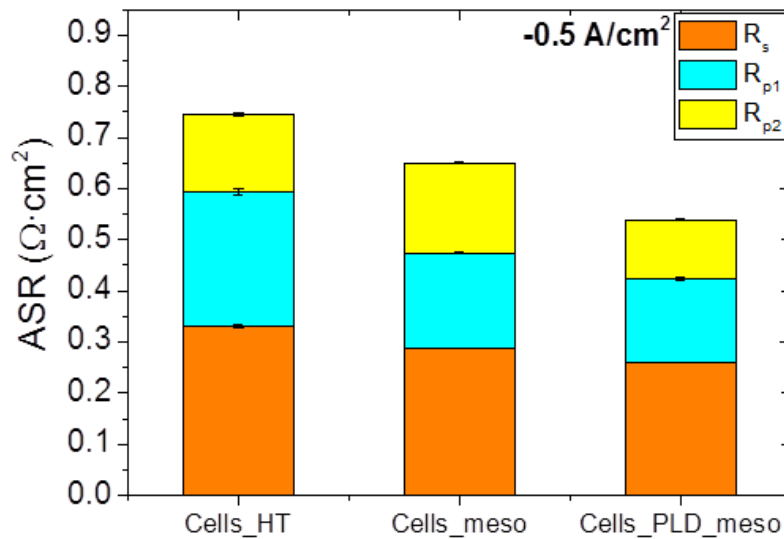


**Figure 5.8:** Bars plot of  $R_s$ ,  $R_{p1}$  and  $R_{p2}$  values (Table 5.3) and its corresponding errors obtained from fitting impedance data at  $-0.5 \text{ A/cm}^2$  of the three Cells\_HT, Cells\_meso and Cells\_PLD\_meso types of cells. The total value of the column is the overall ASR of the three cells.

#### 5.4.2. Microstructural analysis of SOEC cells

The oxygen electrode microstructural composition of the three compared types of cells was also characterized by SEM coupled to EDX. The main objective of the SEM characterization is to find a correlation between the microstructure of the different parts of the cell, and the obtained electrochemical results. A cross-section micrograph of the three types of electrolysis cells, showing the electrolyte, the barrier layer and the oxygen electrode was recorded using Secondary Electron Detector (SE2) detector to be used as reference for performing the EDX analysis. This technique allows the observation of the distribution of each element along the cross-section. The cross-

section micrographs and mappings of La, Ce and Zr as representative elements of LSCF, CGO and YSZ are presented as **Figure 5.9**, **5.10** and **5.11** for Cells\_HT, Cells\_meso and Cells\_PLD\_meso, respectively.

As explained in the cell descriptions, LSCF is used for the fabrication of the oxygen electrode in both the nanocomposite and the bulk layer. The corresponding La mapping obtained for Cells\_HT is showed in **Figure 5.9b**. Although a high density of this material is observed in the area corresponding to bulk LSCF, La mapping also shows a lack of this element (representing the LSCF) in the nanocomposite layer close to the electrolyte, where the Ce mapping (**Figure 5.9c**) evidences the presence of the CGO compound. That results in low percolation and a lack of active sites between the infiltrated LSCF and the electrode. Furthermore, **Figure 5.1a** and **5.1b** show a porous CGO barrier layer. Both issues negatively affect the oxygen electrode functionalization, and consequently, explains the low electrochemical performance obtained as electrolyzers. Besides, a higher density of Ce and Zr (**Figure 5.9d**) elements is observed above, which corresponds to the CGO barrier layer and the electrolyte.

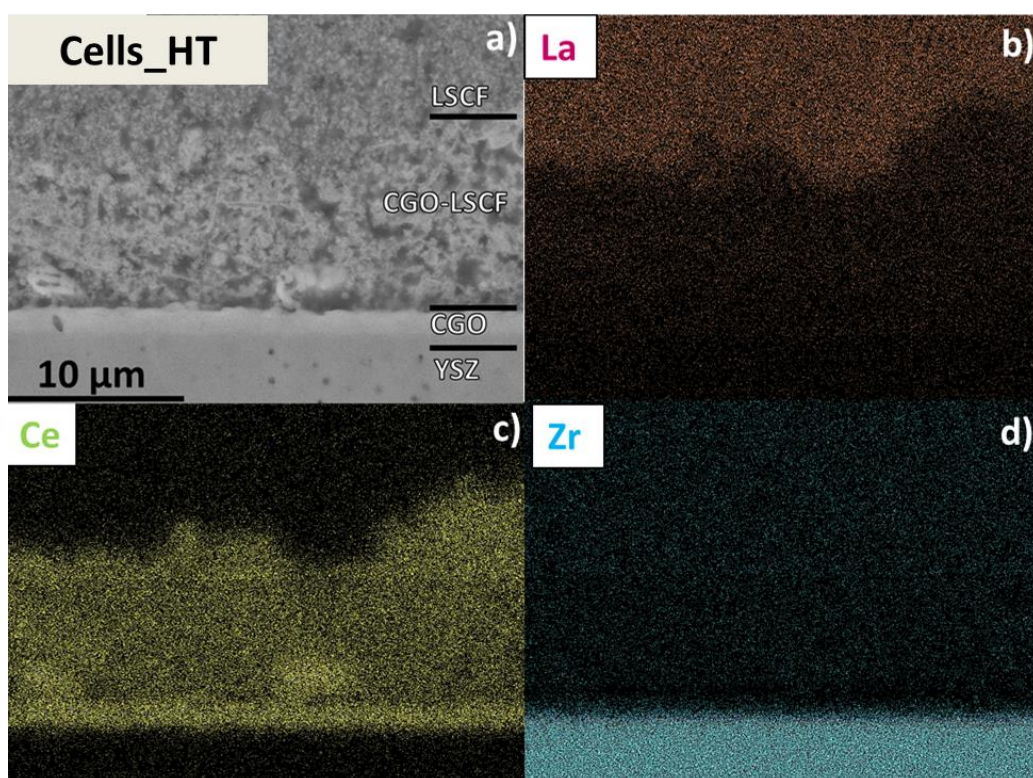


**Figure 5.9:** (a) Cross-section micrograph of Cells\_HT where it is possible to distinguish the compounds constituting the electrolyte-oxygen electrode interface. EDX mappings of La (b), Ce (c) and Zr (d) are representing LSCF, CGO and YSZ compounds.

Contrary, EDX mapping of La (**Figure 5.10b**), recorded analysing Cells\_meso, shows a more homogeneous distribution of this element along the electrode and slightly lower on the mesoporous scaffold, which area is marked by the Ce mapping presented as **Figure 5.10c**. These mappings confirm that CGO and LSCF form the desired interconnected nanocomposite well infiltrated. In concordance with this microstructural characterization, the electrochemical results reveal that the implementation of the bi-layer oxygen electrode, in which the microstructure closest to the electrolyte is constituted by an infiltrated composite based on mesoporous materials, has enhanced the performance of this type of cells. Note the presence of the Zr in the Ni-YSZ composite from the mapping of Zr (**Figure 5.10d**), with a lower presence than the above area corresponding to the electrolyte.

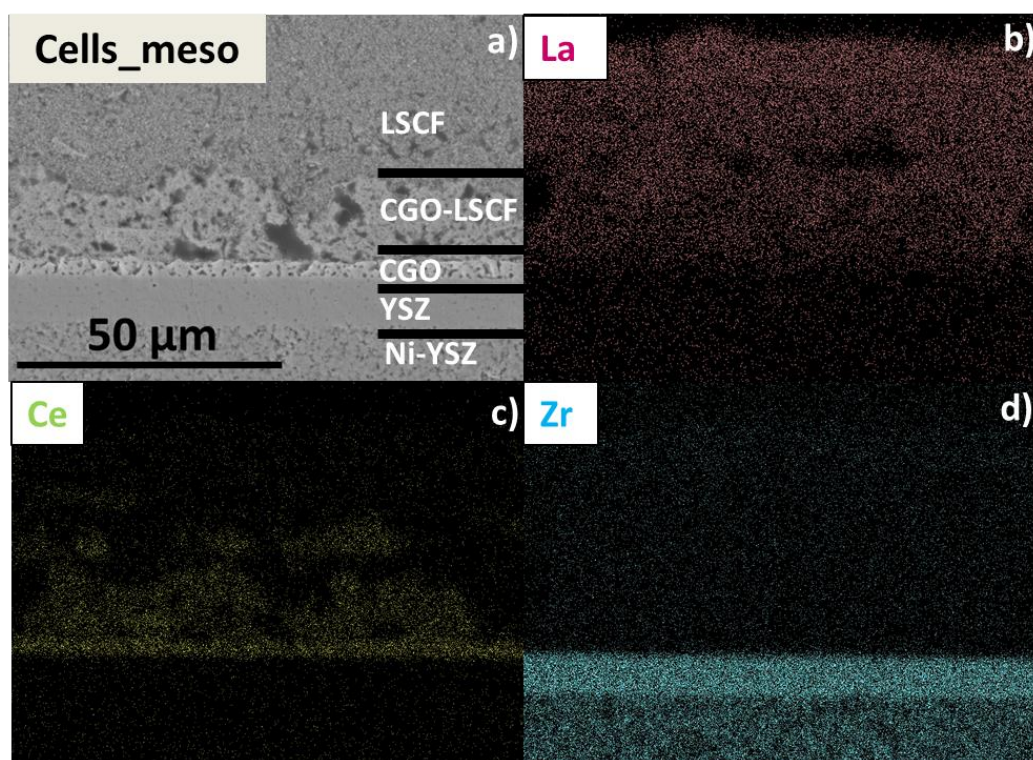


**Figure 5.10:** (a) Cross-section micrograph of Cells\_meso where it is possible to distinguish the compounds constituting the electrolyte-oxygen electrode interface. EDX mappings of La (b), Ce (c) and Zr (d) are representing LSCF, CGO and YSZ compounds.

Finally, the mappings recorded from Cells\_PLD\_meso show also a higher percentage of La (**Figure 5.11b**) in the area corresponding to the electrode, but it is also observable its presence in the area corresponding to the infiltrated CGO mesoporous scaffold functional layer (**Figure 5.11c**), as it was expected. These results confirm the reliability of the employed method for the fabrication of a CGO-LSCF percolated nanocomposite

by infiltration of mesoporous materials. Besides, a higher density of Ce is observed below the mesoporous scaffold, which indicates the existence of a dense CGO barrier layer (**Figure 5.11c**). The results obtained from the electrochemical characterization, highlighting that the highest current density of  $-1.00 \text{ A/cm}^2$  was injected by this type of cells at 1.30 V, reveal that the enhancement of both the barrier layer and the oxygen electrode microstructures could be the key for improving the SOEC performance.

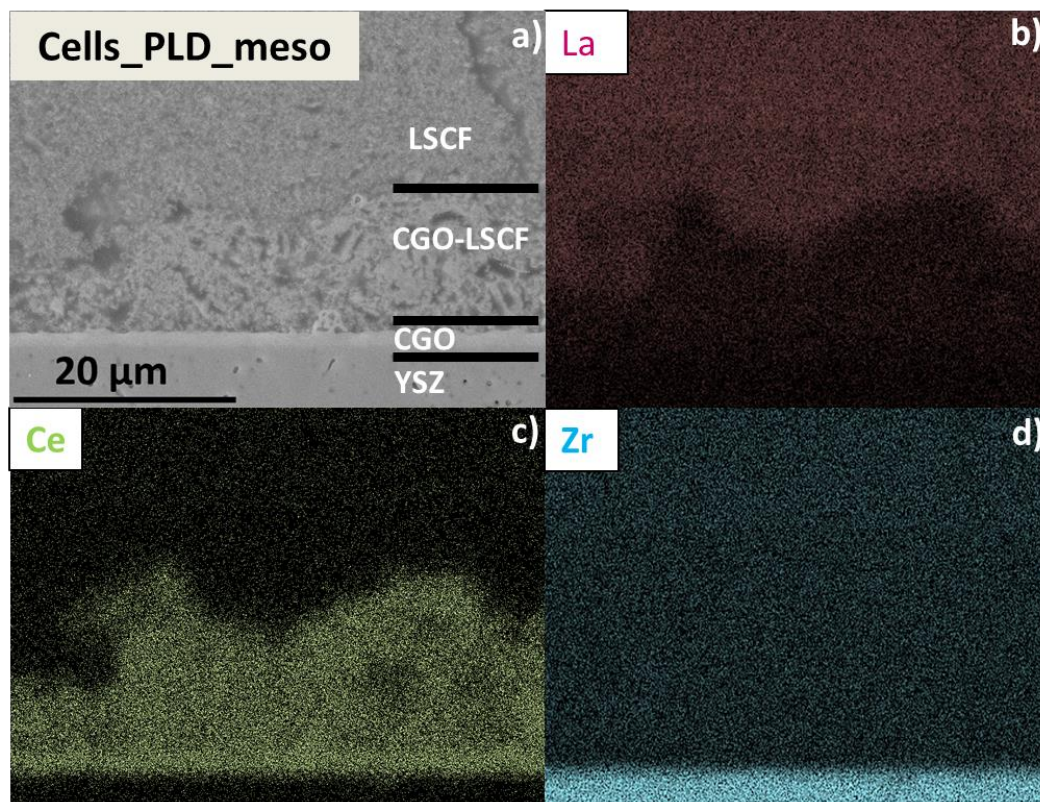


**Figure 5.11:** (a) Cross-section micrograph of Cells\_PLD\_meso where it is possible to distinguish the compounds constituting the electrolyte-oxygen electrode interface. EDX mappings of La (b), Ce (c) and Zr (d) are representing LSCF, CGO and YSZ compounds.

Moreover, it is important validating the percolation of the electronic and ionic conductive paths previously detected by EDX-mappings and confirm the functionalization of the ceramic backbone. **Figure 5.12** shows a SEM micrograph of the percolated ionic (CGO) and electronic (LSCF) conductive oxygen electrode functional layer recorded employing an InLens detector at low voltage ( $V = 0.9 \text{ keV}$ ). This detector, combined with low voltages set-ups of the microscopy, enhances the contrast between the percolated electronic conductive phases and the isolated or insulating phases of the studied materials, allowing the differentiation of the electron percolated paths [22] within the fabricated nanocomposite, and confirming the correct and

homogeneous infiltration of the CGO backbone by the LSCF. A scheme of the enhanced TPB distribution presented by these new nanostructured composite electrodes is shown in **Figure 5.13**.

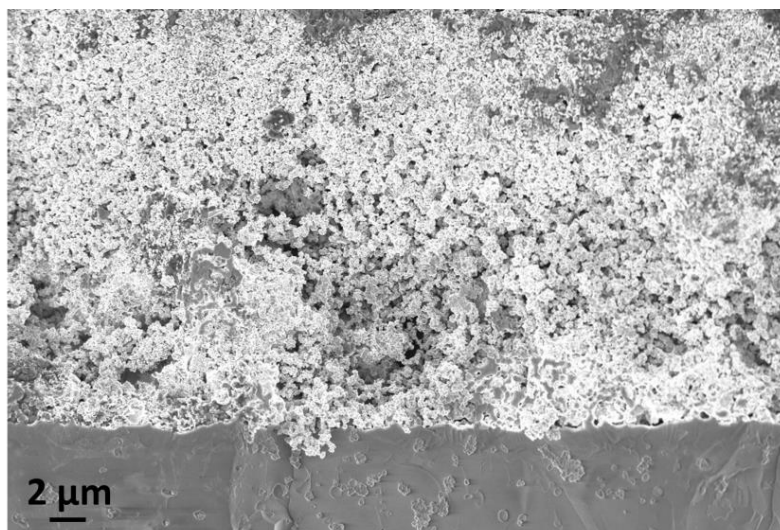


**Figure 5.12:** SEM cross section micrograph of the electrolyte-oxygen electrode interface using an InLens detector at low voltage for showing the successful percolation of the LSCF phase through the CGO mesoporous material.

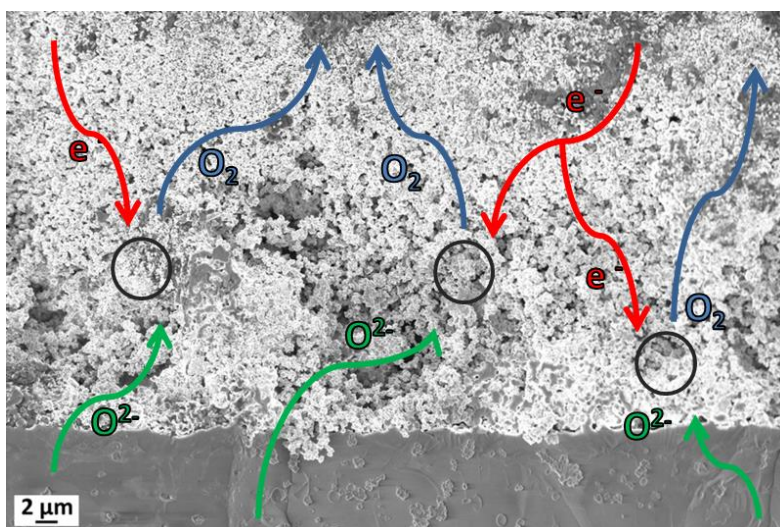


**Figure 5.13:** Scheme of the increase of the TPB active points for the electrochemical reactions due to the implementation of a nanocomposite based on mesoporous materials.

The findings from this structural and microstructural characterization are in concordance and explain the electrochemical results presented in the previous section, where the quality of the infiltration of the CGO scaffold and the density of the barrier layer leads the obtained performance. All the layers constituting each cell (**Figure 5.1a**, **5.1b**, **5.2** and **5.3**) are perfectly attached between them, showing homogeneous and stable microstructures. The thickness of the YSZ electrolyte, the CGO barrier layer, and

the CGO-LSCF nanocomposite of the three characterized cells are comparable between them (**Table 5.1** and **5.2**). According to all this, the reason of the observed improvement in the electrochemical performance of the cells produced in this work is likely ascribed to the reduction of the porosity of the barrier layer produced by PLD, and the nanostructure and good interpenetration of the two phases composing the nanocomposite; both influencing the overall SOEC performance, as it has been already demonstrated.

## 5.5. Conclusions

Three different electrolyte-oxygen electrode interfaces, all of them described as Ni-YSZ/YSZ/CGO<sub>bl</sub>/CGO-LSCF/LSCF, have been successfully designed, fabricated and tested on fuel electrode-supported cells. More specifically, SoA cells (Cells<sub>HT</sub>) provided by HTCeramics were compared with modified cells fabricated at IREC with novel mesoporous oxygen electrodes alone (Cells<sub>meso</sub>) or together with PLD CGO barrier layers (Cells<sub>PLD\_meso</sub>). For ensuring a proper comparison analysis, these variations were based on half cells (fuel electrode and electrolyte) also provided by HTCeramics.

The performance of the SoA cells, Cells<sub>HT</sub>, have been of a maximum injected current of  $-0.55 \text{ A/cm}^2$  at 1.30 V and 750 °C in co-electrolysis mode. An increase of the performance of the cell by employing a mesoporous oxygen electrode in Cells<sub>meso</sub> was observed achieving up to  $-0.64 \text{ A/cm}^2$  at the same conditions. Moreover, the implementation of the PLD barrier layer together with the mesoporous functional layer, Cells<sub>PLD\_meso</sub> results in the best performing SOEC cell with an injected current of  $-1 \text{ A/cm}^2$  at 1.30 V. The microstructural analysis of the different cells have revealed that the highest density of the diffusion barrier layer deposited by PLD could play a major role avoiding reactivity between the electrolyte and the oxygen electrode. Moreover, low voltage SEM analysis and EDX-mappings of the mesoporous based composites of CGO-LSCF showed their good interconnection of materials and the presence of active percolation pathways. By connecting the microstructural and electrochemical characterization, it has been concluded that the implementation of the new approaches based on mesoporous functional layers and PLD deposited barrier layers has resulted in an enhancement of the electrochemical performance of the SoA SOEC cells.

## 5.6. References

- [1] "HTceramix S.A." [Online]. Available: <http://www.solidpower.com/en/about-us/locations/>.
- [2] J. T. S. Irvine, D. Neagu, M. C. Verbraeken, C. Chatzichristodoulou, C. Graves, and M. B. Mogensen, "Evolution of the electrochemical interface in high-temperature fuel cells and electrolyzers," *Nat. Energy*, vol. 1, pp. 1–13, 2016.
- [3] J. Laurencin *et al.*, "Reactive Mechanisms of LSCF Single-Phase and LSCF-CGO Composite Electrodes Operated in Anodic and Cathodic Polarizations," *Electrochim. Acta*, vol. 174, pp. 1299–1316, 2015.
- [4] H. Fan, M. Keane, N. Li, D. Tang, P. Singh, and M. Han, "Electrochemical stability of La<sub>0.6</sub>Sr<sub>0.4</sub>Co<sub>0.2</sub>Fe<sub>0.8</sub>O<sub>3-δ</sub>-infiltrated YSZ oxygen electrode for reversible solid oxide fuel cells," *Int. J. Hydrogen Energy*, vol. 39, pp. 14071–14078, 2014.
- [5] A. V. Virkar, "Mechanism of oxygen electrode delamination in solid oxide electrolyzer cells," *Int J Hydrog. Energ*, vol. 35, pp. 9527–9543, 2010.
- [6] G. Nurk *et al.*, "Mobility of Sr in Gadolinia Doped Ceria Barrier Layers Prepared Using Spray Pyrolysis, Pulsed Laser Deposition and Magnetron Sputtering Methods," *J. Electrochem. Soc.*, vol. 163, no. 2, pp. F88–F96, 2016.
- [7] J. Laurencin *et al.*, "Degradation mechanism of La<sub>0.6</sub>Sr<sub>0.4</sub>Co<sub>0.2</sub>Fe<sub>0.8</sub>O<sub>3-δ</sub>/Gd<sub>0.1</sub>Ce<sub>0.9</sub>O<sub>2-δ</sub> composite electrode operated under solid oxide electrolysis and fuel cell conditions," *Electrochim. Acta*, vol. 241, pp. 459–476, 2017.
- [8] M. Morales *et al.*, "Multi-scale analysis of the diffusion barrier layer of gadolinia-doped ceria in a solid oxide fuel cell operated in a stack for 3000 h," *J. Power Sources*, vol. 344, pp. 141–151, 2017.
- [9] D. The *et al.*, "Microstructural comparison of solid oxide electrolyser cells operated for 6100 h and 9000 h," *J. Power Sources*, vol. 275, pp. 901–911, 2015.
- [10] L. Bernadet, J. Laurencin, G. Roux, D. Montinaro, F. Mauvy, and M. Reytier, "Effects of Pressure on High Temperature Steam and Carbon Dioxide Co-electrolysis," *Electrochim. Acta*, vol. 253, pp. 114–127, 2017.
- [11] C. Graves, S. D. Ebbesen, and M. Mogensen, "Co-electrolysis of CO<sub>2</sub> and H<sub>2</sub>O in solid oxide cells: Performance and durability," *Solid State Ionics*, vol. 192, pp. 398–403, 2011.
- [12] J. Hong, C. Balamurugan, H.-N. Im, S.-Y. Jeon, Y.-S. Yoo, and S.-J. Song, "The Electrochemical Properties of Nanocrystalline Gd<sub>0.1</sub>Ce<sub>0.9</sub>O<sub>1.95</sub> Infiltrated Solid Oxide Co-Electrolysis Cells," *J. Electrochem. Soc.*, vol. 165, no. 3, pp. F132–F141, 2018.
- [13] A. Nechache, M. Cassir, and A. Ringuedé, "Solid oxide electrolysis cell analysis by means of electrochemical impedance spectroscopy: A review," *J. Power Sources*, vol. 258, pp. 164–181, 2014.

- [14] A. Lakki, R. Herzog, C. R. M. Weller H. Schubert, and M. K. G. B. O. GoÈrke, "Mechanical loss, creep, diffusion and ionic conductivity of ZrO<sub>2</sub>-8 mol%Y<sub>2</sub>O<sub>3</sub> polycrystals," *J. Eur. Ceram. Soc.*, vol. 20, pp. 285–296, 2000.
- [15] U.S. Department of Energy, *Fuel Cell Handbook*, vol. 7 Edition. 2004.
- [16] H. Fan, M. Keane, N. Li, D. Tang, P. Singh, and M. Han, "Electrochemical stability of La<sub>0.6</sub>Sr<sub>0.4</sub>Co<sub>0.2</sub>Fe<sub>0.8</sub>O<sub>3-δ</sub>-infiltrated YSZ oxygen electrode for reversible solid oxide fuel cells," *Int. J. Hydrogen Energy*, vol. 39, pp. 14071–14078, 2014.
- [17] M. Shah and S. A. Barnett, "Solid oxide fuel cell cathodes by infiltration of La<sub>0.6</sub>Sr<sub>0.4</sub>Co<sub>0.2</sub>Fe<sub>0.8</sub>O<sub>3-δ</sub> into Gd-Doped Ceria," *Solid State Ionics*, vol. 179, pp. 2059–2064, 2008.
- [18] Y. Tan *et al.*, "High-performance oxygen electrode for reversible solid oxide cells with power generation and hydrogen production at intermediate temperature," *Int. J. Hydrogen Energy*, vol. 42, pp. 4456–4464, 2017.
- [19] L. dos Santos.Gómez, J. M. Porras-Vázquez, E. . Losilla, F. Martín, J. R. Ramos-Barrado, and D. Marrero-López, "Stability and performance of La<sub>0.6</sub>Sr<sub>0.4</sub>Co<sub>0.2</sub>Fe<sub>0.8</sub>O<sub>3-d</sub> nanostructured cathodes with Ce<sub>0.8</sub>Gd<sub>0.2</sub>O<sub>1.9</sub> surface coating," *J. Power Sources*, vol. 347, pp. 178–185, 2017.
- [20] H. Fan, Y. Zhang, and M. Han, "Infiltration of La<sub>0.6</sub> Sr<sub>0.4</sub> FeO<sub>3</sub>- nanoparticles into YSZ scaffold for solid oxide fuel cell and solid oxide electrolysis cell," *J. Alloys Compd.*, vol. 723, pp. 620–626, 2017.
- [21] A. Nechache *et al.*, "Diagnosis of a cathode-supported solid oxide electrolysis cell by electrochemical impedance spectroscopy," *Electrochim. Acta*, vol. 210, pp. 596–605, 2016.
- [22] A. Hauch, P. S. Jørgensen, K. Brodersen, and M. Mogensen, "Ni/YSZ anode - Effect of pre-treatments on cell degradation and microstructures," *J. Power Sources*, vol. 196, pp. 8931–8941, 2011.

# ***Chapter 6***

*Performance and long-term stability of optimized SOEC cells in co-electrolysis mode*



<b>6. Performance and long-term stability of optimized SOEC cells in co-electrolysis mode .....</b>	<b>181</b>
<b>6.1. Chapter overview .....</b>	<b>181</b>
<b>6.2. Electrochemical characterization and performance of the CGO-LSCF SOEC cells in co-electrolysis mode .....</b>	<b>183</b>
<b>6.3. Microstructural characterization of the CGO-LSCF SOEC cells.....</b>	<b>187</b>
<b>6.4. Results of the long-term operation tests of the CGO-LSCF SOEC cell in co-electrolysis mode.....</b>	<b>190</b>
<b>6.4.1. Long-term electrochemical characterization and performance.....</b>	<b>190</b>
<b>6.4.2. Post-test cell microstructural characterization.....</b>	<b>194</b>
<b>6.5. Conclusions .....</b>	<b>199</b>
<b>6.6. References.....</b>	<b>201</b>



## 6. Performance and long-term stability of optimized SOEC cells in co-electrolysis mode

### 6.1. Chapter overview

This chapter<sup>1</sup> presents a detailed analysis of the performance and long-term stability of the enhanced Solid Oxide Electrolysis Cells (SOECs) (with Pulsed Laser Deposition-PLD barrier layers and mesoporous oxygen electrodes) presented in **Chapter 4**.

Ni-YSZ fuel electrode-supported cells (fabricated by HTceramix/SOLIDpower) were employed as substrates for testing the developed oxygen electrodes based on infiltrated mesoporous materials. An optimized dense  $\text{Ce}_{0.8}\text{Gd}_{0.2}\text{O}_{1.9}$  (CGO) barrier layer was deposited by PLD (as discussed in **section 2.5.3**) to avoid interdiffusion between the oxygen electrode and the electrolyte. A composite based in the infiltration of a CGO mesoporous ionic conductor scaffold with a  $\text{La}_{0.6}\text{Sr}_{0.4}\text{Co}_{0.2}\text{Fe}_{0.8}\text{O}_3$  (LSCF) Mixed Ionic and Electronic Conductor (MIEC) phase has been proposed.

In order to evaluate the potential of the proposed oxygen electrode interface, it was electrochemically characterised at a fixed temperature ( $T=750\text{ }^\circ\text{C}$ ) in co-electrolysis mode. This characterization was based on the study of obtained I-V polarization curves and Electrochemical Impedance Spectroscopy (EIS) measurements. EIS measurements were performed with the aim of analysing the origin of each resistive process contributing to the total cell resistance. Identifying the electrochemical processes involved allowed us understanding the microstructural factors limiting the performance.

Firstly, **section 6.2** is devoted to the electrochemical characterization of these fuel electrode-supported cells. The microstructural characterization of these cells is reported in **section 6.3**. The feasibility of the oxygen electrode fabrication method is discussed and confirmed by the microstructural characterisation. Finally, **section 6.4.1** presents a long-term operation study performed on CGO-LSCF cells on co-electrolysis mode. Both, EIS measurements at different times and post-mortem microstructural

---

<sup>1</sup> Part of the results presented in this chapter are published as “*Infiltrated mesoporous oxygen electrodes for high temperature co-electrolysis of  $\text{H}_2\text{O}$  and  $\text{CO}_2$  in solid oxide electrolysis cells*” in Journal of Materials Chemistry A (DOI: 10.1039/c8ta01045e) [22].

characterization (**section 6.4.2**), allowed determining the responsible electrochemical process for the cell degradation.

## 6.2. Electrochemical characterization and performance of the CGO-LSCF SOEC cells in co-electrolysis mode

This section presents the electrochemical characterization of Ni-YSZ fuel electrode-supported ( $\approx 300 \mu\text{m}$ ) SOECs, fabricated using CGO-LSCF ( $\approx 10\text{-}12 \mu\text{m}$ ) nanostructured oxygen electrodes separated from the electrolyte ( $\approx 7 \mu\text{m}$ ) by a PLD-deposited CGO barrier layer, and a LSCF thicker layer ( $\approx 30\text{-}50 \mu\text{m}$ ).

The same half-cells supplied by HTceramix/SOLIDpower presented in **Chapter 5** were used for testing the fabricated CGO-LSCF oxygen electrode. Fabricated cells resulted in the following configuration: Ni-YSZ/YSZ/CGO<sub>bl</sub>/CGO-LSCF/LSCF [1-5]. Note that the produced cells include a functional layer based on LSCF infiltration of CGO mesoporous materials. As it has been previously explained, the sintering temperature of the mesoporous material was optimized from testing a set of oxygen electrode symmetrical cells based on Sm<sub>0.2</sub>Ce<sub>0.8</sub>O<sub>1.9</sub> (SDC) mesoporous scaffolds (**section 3.4**).

The electrochemical characterization of the CGO-LSCF oxygen electrode was based on I-V curves and EIS measurements. Those measurements were performed employing 45% H<sub>2</sub>O + 45% CO<sub>2</sub> + 10% H<sub>2</sub> and synthetic air gas compositions at the operation temperature of 750 °C.

I-V curves were measured with the aim of characterising the electrochemical performance of fuel electrode-supported SOECs with the developed CGO-LSCF oxygen electrode. **Figure 6.1** shows the injected current density as a function of the measured voltage.

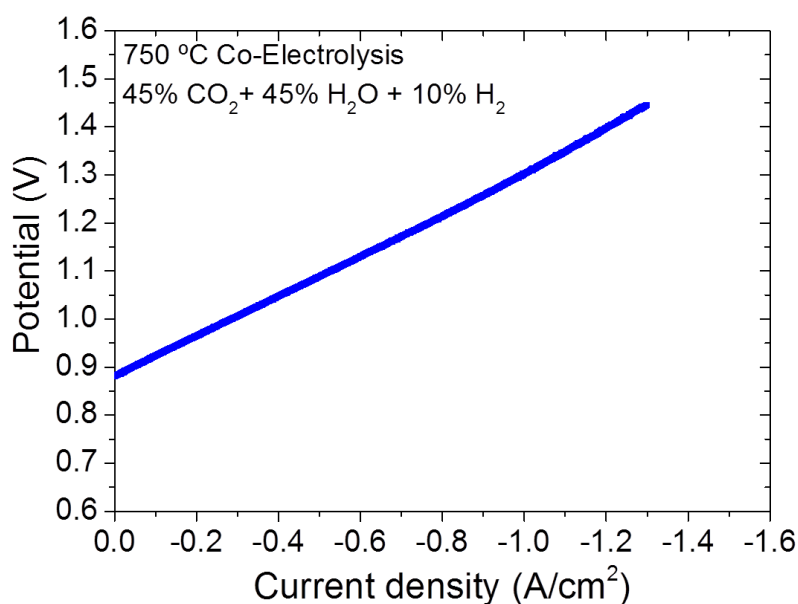


**Figure 6.1:** I-V polarization curve of a Ni-YSZ/YSZ/CGO<sub>bl</sub>/CGO-LSCF/LSCF SOEC initially tested under co-electrolysis and synthetic air atmospheres at 750 °C.

An Open Circuit Voltage (OCV) of 0.88 V was measured at equilibrium during the first tests and was kept constant during the long-term operation (see next section). The same model for the calculation of the OCV described in previous chapters was employed in this case. A theoretical OCV value of 0.89 V was calculated taking into account the gas compositions and temperature of the experimental setup conditions. As it was explained, this model considers chemical and electrochemical factors of the fuel electrode gas mixture species in the same proportion that these species are involved [6]. Although differences between measured and theoretical OCV values are expected from the experimental factors associated to the measurement, the good agreement between them indicates a good sealing of the tested cell.

A current density of  $-1.0 \text{ A/cm}^2$  was injected at a potential of 1.3 V (**Figure 6.1**) in this electrolysis cell electrochemically characterized in galvanostatic operation mode. This result is remarkably better than the obtained for the previously presented SDC-Sm<sub>0.5</sub>Sr<sub>0.5</sub>CoO<sub>3</sub> (SSC) oxygen electrode (**section 4.3**) and indicates an important improvement on the fabrication of the functional layer based on infiltrated mesoporous materials. Specifically, the infiltrated volume has been adapted to the deposited mesoporous thickness ( $8 \pm 1 \text{ } \mu\text{L}/\mu\text{m}$  of total infiltration volume/scaffold thickness), and the infiltration has been progressively performed, allowing the evaporation of the solvent without blocking the mesopores. Besides, these results are

remarkable and comparable to publications focused on the fabrication of oxygen electrodes by infiltration. Current densities of  $-0.56 \text{ A/cm}^2$  [7] and  $-0.98 \text{ A/cm}^2$  [4] were injected on SOECs which oxygen electrodes were based on  $\text{La}_{0.8}\text{Sr}_{0.2}\text{FeO}_3$  (LSF) and LSCF infiltrating YSZ scaffolds, both measured at 1.3 V.

Fabricated SOEC cells with the same 45%  $\text{H}_2\text{O}$  + 45%  $\text{CO}_2$  + 10%  $\text{H}_2$  and synthetic air co-electrolysis gas composition were also characterized by EIS. The operation temperature was kept at 750 °C along all the measurements. The initially measured Nyquist plot at OCV under these operation conditions on galvanostatic mode and its corresponding fitting are presented in **Figure 6.2**.

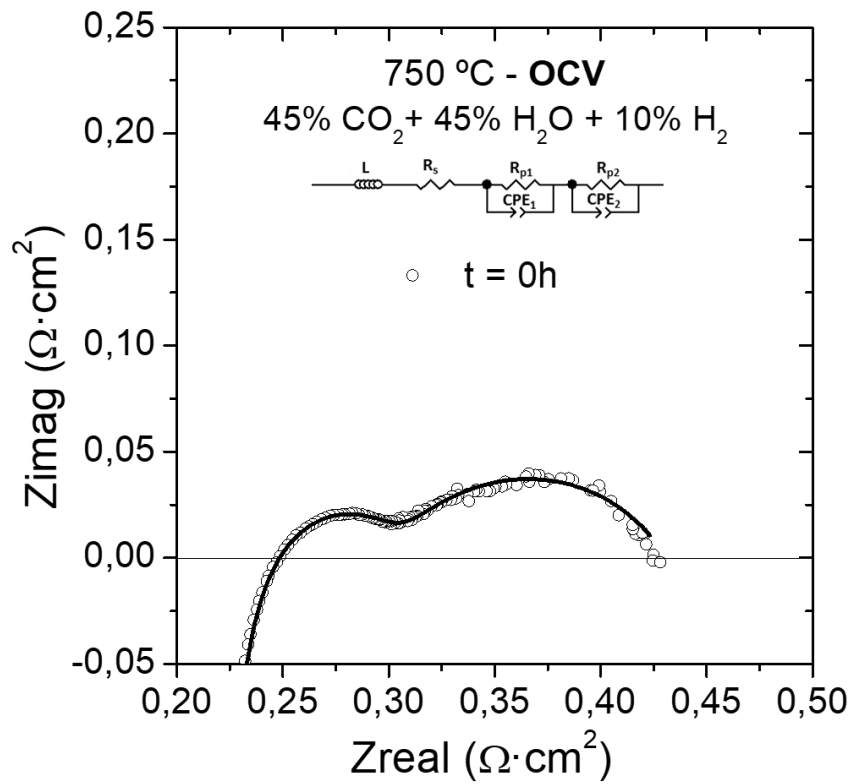


**Figure 6.2:** Initial Nyquist plot from EIS measurements obtained at co-electrolysis and synthetic air gas composition atmospheres for a cell operating at 750 °C at OCV.

Also in this case, an electrical equivalent circuit is proposed for fitting the measured EIS data, deconvolute and discuss the electrochemical processes occurring on SOEC and contributing to the overall Area Specific Resistance (ASR). The electrical equivalent circuit proposed for fitting the Nyquist plot presented in **Figure 6.2** is  $LR_s(R_{p1}Q_1)(R_{p2}Q_2)$ , and it is composed by an inductance L representing the contributions from the set-up wiring [8], a serial resistance ( $R_s$ ) in series which value mainly depend from the electrolyte and other serial contributions [4]; and  $R_pQ$  that are related to two

electrochemical processes taking place in the electrodes and contributing to the polarization resistance. The element  $R_pQ$  is composed by a resistance and a constant phase element in parallel [9]. The values obtained from the fitting for each parameter are presented in **Table 6.1**.

Time (h)	$R_s$ ( $\Omega \cdot \text{cm}^2$ )	$R_{p1}$ ( $\Omega \cdot \text{cm}^2$ )	$C_{p1}$ ( $\text{F}/\text{cm}^2$ )	$n_1$	$f_{\text{max}}$ (Hz)	$R_{p2}$ ( $\Omega \cdot \text{cm}^2$ )	$C_{p2}$ ( $\text{F}/\text{cm}^2$ )	$n_2$	$f_{\text{max}}$ (Hz)
0	$2.20 \cdot 10^{-1}$	$7.62 \cdot 10^{-2}$	$7.81 \cdot 10^{-4}$	0.79	$2.68 \cdot 10^3$	$1.61 \cdot 10^{-1}$	$4.07 \cdot 10^{-1}$	0.55	2.43

**Table 6.1:** Electrochemical parameters obtained from fitting the Nyquist plot showed in Figure 4.4 measured at OCV at 750 °C under co-electrolysis (45%  $\text{H}_2\text{O}$ + 45%  $\text{CO}_2$ + 10%  $\text{H}_2$ /Air). Here,  $C_p$  represents the true capacitance calculated from the CPE element as  $C_p = (Q)^{(1/n)} \cdot R_{p1}^{(1-n/n)}$ .

The serial resistance obtained fitting the experimental impedance data is 0.14  $\Omega$ . The theoretical YSZ conductivity [10] of a 7  $\mu\text{m}$ -thick electrolyte operating at 750 °C is calculated to be 0.04  $\Omega$ . Comparing both values it is deduced that apart from the electrolyte, the serial resistance has additional ohmic contributions from the interfaces and the current collection. Note that the serial resistance values presented in **Table 4.3** are expressed in  $\Omega \cdot \text{cm}^2$ , in concordance to the values represented in the Nyquist plot.

Two arcs are clearly differentiated from the obtained Nyquist plots, which are directly related to the two electrochemical processes on the electrodes contributing to the polarization resistance at OCV. At this operation conditions, the main contribution to the total resistance is presented by the electrodes activation overpotentials [11]. The values obtained for the resistance and capacitances of each arc (**Table 4.3**) are from 1 to 3 orders of magnitude different, what makes possible the differentiation of the involved electrochemical processes. Their characteristic frequency allows separating the process as a high frequency process and the other one as a low frequencies process. The high frequency ( $\approx 10^3$  Hz) arc can be described as a charge transfer process at the electrode-electrolyte interface, since the  $R_{p1}$  characteristic capacitance obtained from the fitting is in the order of magnitude of  $10^{-4}$   $\text{F}/\text{cm}^2$  [12,13]. The charge transfer electrochemical process is controlled by the electrocatalytic activity and ionic conductivity of the composite electrode material. This process also depends on the Triple Phase Boundary (TPB) length where the electrochemical reactions takes place and are dependant of the adsorption processes of the electrochemical species [4,8,14]. Since optimal operation of both fuel and oxygen electrodes is required for a good performing SOEC, both electrodes have been

considered contributing to charge transfer processes in this work. Non-charge transfer processes, generally dominated by gas diffusion and gas conversion processes, are characteristic of frequencies lower than 0.1 Hz [4,8,14] also influencing the performance of both electrodes. In this measurement, capacitances in the order of magnitude of  $10^{-1}$  F/cm<sup>2</sup> and characteristic frequency values of  $\approx 1$  Hz were recorded for  $R_{p2}$  (**Table 4.3**), pointing mass transportation as the electrochemical process dominating this resistance contribution [12,13]. The overall ASR calculated by taking into account all the contributions of the fitted Nyquist (ohmic and polarization resistances) results in  $0.45 \text{ } \Omega\cdot\text{cm}^2$ , which is in line with the value of  $0.43 \text{ } \Omega\cdot\text{cm}^2$  retrieved by considering the slope of the measured IV polarization curve [15].

### 6.3. Microstructural characterization of the CGO-LSCF SOEC cells

Ni-YSZ fuel electrode-supported cells with YSZ electrolyte and CGO-LSCF infiltrated mesoporous oxygen electrodes were structurally characterized by Scanning Electron Microscopy (SEM) with the aim of studying the microstructure. Cross-section micrographs of the YSZ electrolyte and CGO-LSCF oxygen electrode interfaces are presented in **Figure 6.3**. Both micrographs were acquired using different detectors of SEM in order to get different microstructural information. The micrograph of **Figure 6.3a** presents the SOEC oxygen electrode configuration acquired using a Secondary Electron Detector (SE2). Two different layers with different microstructure are distinguished: a layer of 10-12  $\mu\text{m}$  of CGO backbone infiltrated by LSCF and a thicker layer of bulk LSCF. The micrograph presented in **Figure 4.8b** was acquired using an InLens detector at low voltage ( $V= 0.9 \text{ keV}$ ). When operating at low voltages (i.e. 0.9 KeV-1.1 keV), the InLens mode of SEM allows detecting electron conductive paths [16]. In this case, in which the CGO scaffold was infiltrated with LSCF as active phase, InLens-SEM permits following the infiltration of the LSCF showed as brightness areas through the electron percolated path. Micrograph presented in **Figure 6.3b** validates the formation of active and percolating electronic paths, confirming the correct infiltration of the CGO backbone by LSCF.

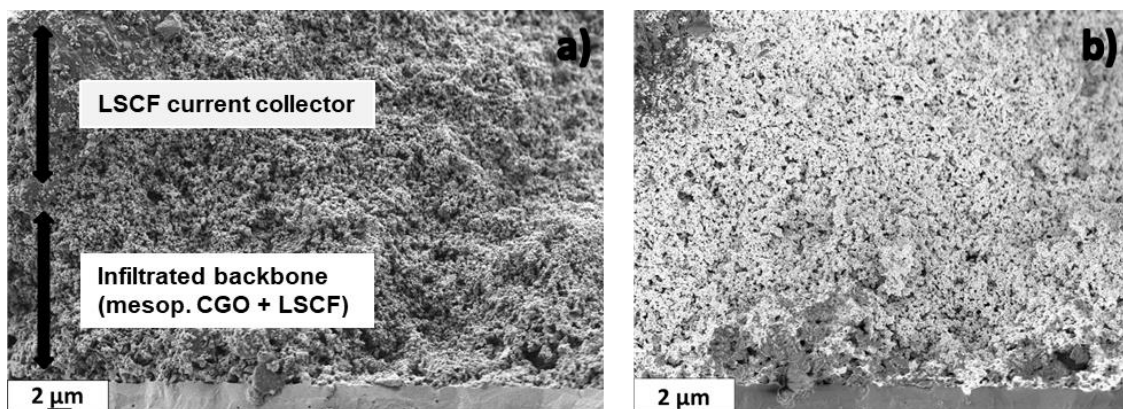


**Figure 6.3:** SEM micrographs of a SOEC cross-section showing the YSZ electrolyte, the CGO barrier layer and the CGO-LSCF oxygen electrode: a) the electrode configuration of the cell was recorded using a SE2, b) percolating paths are showed using low voltage InLens detector.

Energy Dispersive X-Ray (EDX) compositional mappings (**Figure 6.4**) were also recorded in the fabricated electrolyte-oxygen electrode interface of the fuel electrode-supported cells. This analysis was performed in order to confirm the functionalization of deposited CGO as oxygen electrode, and to evaluate the adopted infiltration procedure, testing the composition of the generated nanocomposite. The interface cross-section micrograph taken as a reference for analysing different elements is presented in **Figure 6.3a**. Maps showed correspond to the most representative elements of the compounds present in the cross-section.

These different elements; La (**Figure 6.3b**), Sr (**Figure 6.3c**), Co (**Figure 6.3d**) and Fe (**Figure 6.3e**) are the elements constituting LSCF, which were used for fabricating the electrode and infiltrating the scaffold. Ce (**Figure 6.3f**) and Gd (**Figure 6.3g**) are the main elements of the CGO barrier layer and the mesoporous scaffold deposited on top. Zr (**Figure 6.3h**) is the most representative element of the YSZ electrolyte, and O (**Figure 6.3i**) is present in all the compounds that have been detailed. It is clearly observed that La is mainly present in the current collector but also whitening the functional layer of CGO (recognized from Ce and Gd obtained EDX-Mappings). Although the effect is less intense, Sr and Co EDX-mappings are also located in the area corresponding to the ionic conductor scaffold. This result confirms the interpenetration between CGO and LSCF compounds in the infiltrated mesoporous layer, and the successful formation of the desired CGO-LSCF nanocomposite by a homogeneous and reproducible infiltration process. Comparing coloured layers with the cross-section reference micrograph (**Figure 6.3a**), it is observed that Ce and Gd

mainly occupy the mesoporous scaffold. Besides, a thin dense layer appeared below the scaffold in the resulting Ce EDX-mapping. This layer corresponds to the dense CGO barrier layer and its presence is confirmed between the electrolyte and the scaffold. **Figure 6.3h** presents the EDX-Mapping of Zr. The area occupied by the electrolyte is clearly defined in this mapping micrograph. Finally, the O EDX-Mapping shows the presence of this element in all the compounds involved in the studied cross-section.

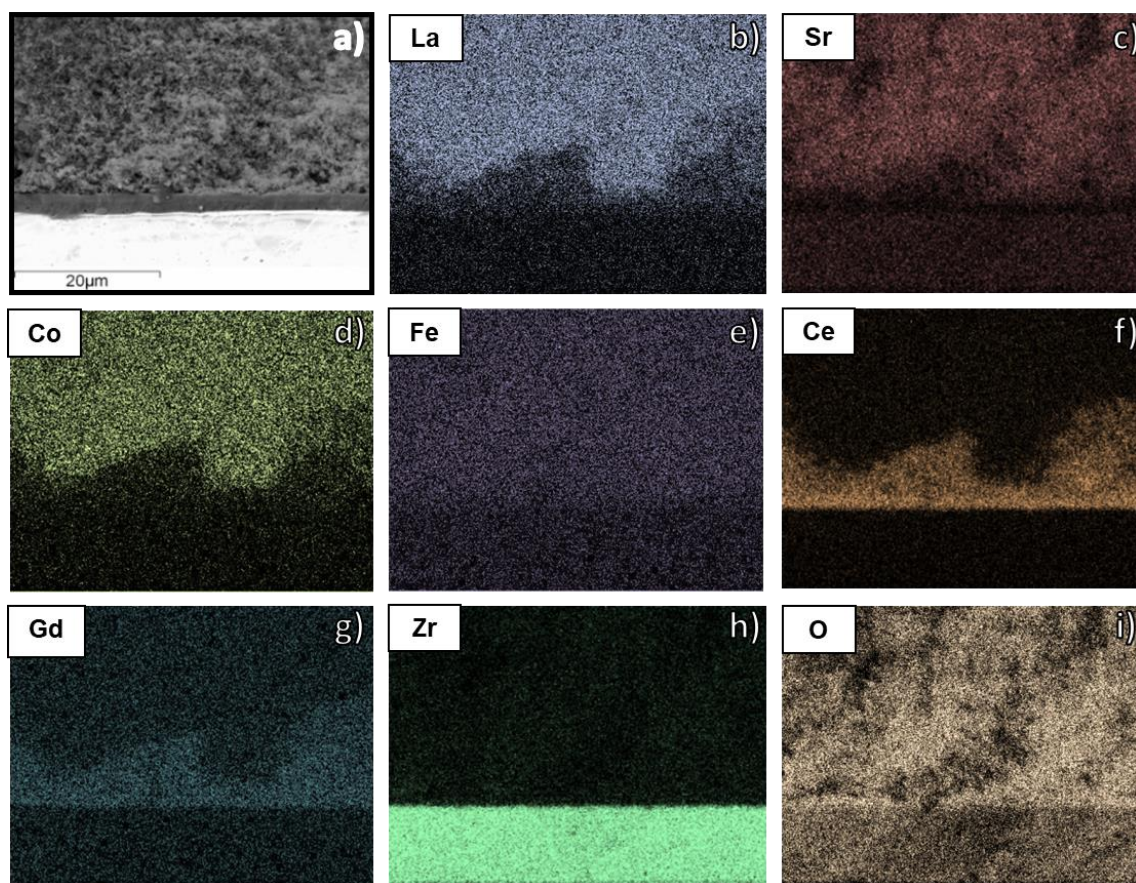


**Figure 6.3:** EDX mapping of the different elements involved in the fabricated CGO-LSCF oxygen electrode functional layer. The cross-section taken as reference for performing the analysis is presented in micrograph (a). EDX-Mapping of La (b), Sr (c), Co (d), Fe (e), Ce (f), Gd (g), Zr (h) and O (i) are representative elements of LSCF, CGO and YSZ compounds.

In conclusion, the feasibility of the applied infiltration procedure was tested by two characterization techniques. SEM microscopy using different detectors and EDX compositional mappings of the elements involved in CGO and LSCF compounds, confirm the successful fabrication and stability of the percolated CGO-LSCF nanocomposite on fuel electrode-supported cells.

## 6.4. Results of the long-term operation tests of the CGO-LSCF SOEC cell in co-electrolysis mode

### 6.4.1. Long-term electrochemical characterization and performance

Cells with the same configuration (Ni-YSZ/YSZ/CGO<sub>bil</sub>/CGO-LSCF/LSCF) were tested on long-term operation in order to evaluate the stability of the CGO-LSCF oxygen electrode functional layer, operating for more than 1400 h.

The SOEC was working during 1400 h of operation on co-electrolysis mode under 45% H<sub>2</sub>O + 45% CO<sub>2</sub> + 10% H<sub>2</sub> and synthetic air gas at 750 °C, as it is presented in **Figure 6.4**. The evolution of the cell performance under continuous co-electrolysis operation was evaluated measuring the voltage evolution at different injected current densities. EIS measurements were recorded in galvanostatic mode keeping the same fuel and oxygen electrode gas atmospheres.

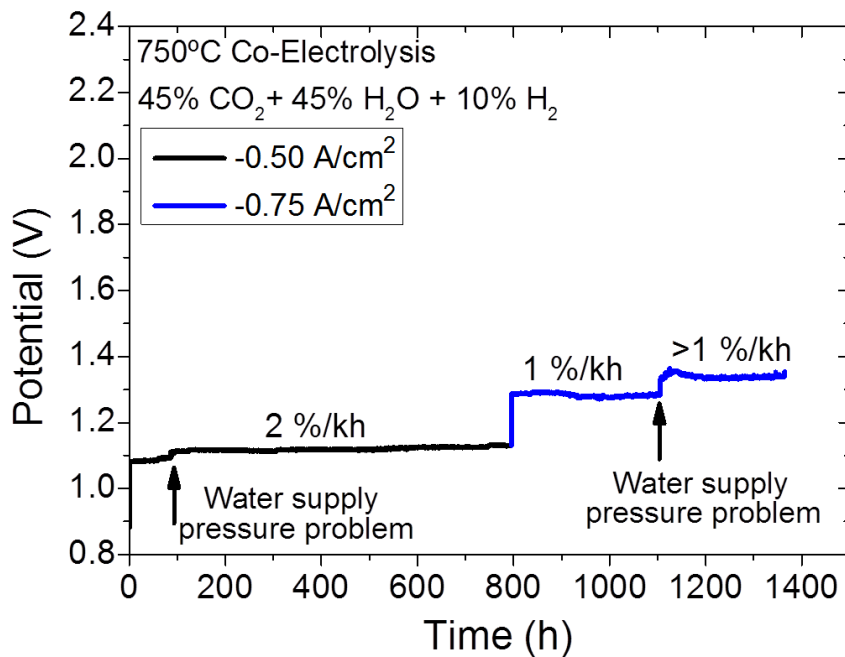


**Figure 6.4:** Long-term evolution of a Ni-YSZ/YSZ/CGO<sub>bil</sub>/CGO-LSCF/LSCF SOEC cell operated at 750 °C in galvanostatic mode at injected current densities of -0.5 and -0.75 A/cm<sup>2</sup> under 45% H<sub>2</sub>O+ 45% CO<sub>2</sub>+ 10% H<sub>2</sub>/Air atmospheres.

Two different current densities were injected to the high temperature electrolysis cell along the long-term operation test. During the first 800 h, the cell was operating under -0.5 A/cm<sup>2</sup> injected current densities. The cell degraded around 2 %/Kh (25 μV/h), without taking into account the step promoted by a water supply issue occurred at 90 h. The low degradation rate obtained during the first 800 h of test under -

0.5 A/cm<sup>2</sup> shows the stability and good performance of the fabricated cells, confirming the potential of the mesoporous scaffold based functional layer for SOEC. During the second part of the measurement, the injected current density was increased to -0.75 A/cm<sup>2</sup> and maintained until the final 1400 h of test (600h at -0.75 A/cm<sup>2</sup>). The obtained cell degradation rate was 1 %/kh (10 μV/h) from 800 to 1100 h of operation, achieving a voltage of 1.3 V (thermoneutral). Although the degradation rate was performing at very low rate, at 1150 h another issue related to the water fuel inlet increased the operation voltage at 1.34 V. The degradation rate registered from this point to the end of the experiment continued keeping as low as around 0.85 %/kh (12 μV/h). Summarising, three degradation rates were registered during 1400 h of operation under two different high current densities. Among them, an expected stepped increase of the potential was reasonably registered when the injected current density was increased from -0.5 to -0.75 A/cm<sup>2</sup>. The other two steps of the voltages were caused by external issues related to the set-up. It needs to be noted that successful operation of electrolysis technology is very sensitive to steam condensation. In spite of these issues related to the set-up, the remarkable obtained results confirm the potential of the proposed technology, which is based on infiltrated mesoporous materials, for improving the performance of the oxygen electrode owing to solid oxide electrolysis cells.

It is important to highlight that unexpected higher degradation rates were recorded at injected current density of -0.5 A/cm<sup>2</sup> than at -0.75 A/cm<sup>2</sup>. This can be explained by comparing the initial microstructure with the one resulting from the long-term experiment, performed under continuous injected current densities and co-electrolysis atmosphere. It is concluded from these results that once the microstructure stabilizes, the degradation rate decreases with time and is not directly related with the change of the injected current. This hypothesis also supports the fact that the generated microstructure, with a better distribution of TPB, is able to accept higher current densities with any affection on the cell degradation. The current paths and their current density are not limiting the degradation of studied cells.

The evolution of the electrochemical processes involved on the degradation rates was periodically studied recording I-V polarization curves and electrochemical

impedance spectrums. EIS measurements were performed at OCV and 1.3 V in order to study the different effects at equilibrium voltage and under operation, and respectively see the contribution of the activation and diffusion overpotentials.

Nyquist plots of the impedance spectroscopy at OCV were periodically recorded at the beginning of the experiment ( $t=0$  h), and at 800, 900, 1100 and 1300 h of operation (**Figure 6.5**) with the aim of studying the evolution of the limiting electrochemical processes. The experimental impedance spectroscopy data were fitted using the same electrical equivalent circuit,  $LR_s(R_{p1}Q_1)(R_{p2}Q_2)$ , previously used for the presented characterisation in **section 6.2**. Each electrochemical parameter value obtained from the fitting, including resistances, capacitances,  $n$  values and characteristic frequencies [17] are presented in **Table 6.2**. Note that the ohmic resistance values presented in **Table 6.2** are suitable with the Nyquist plot presented in **Figure 6.5**.

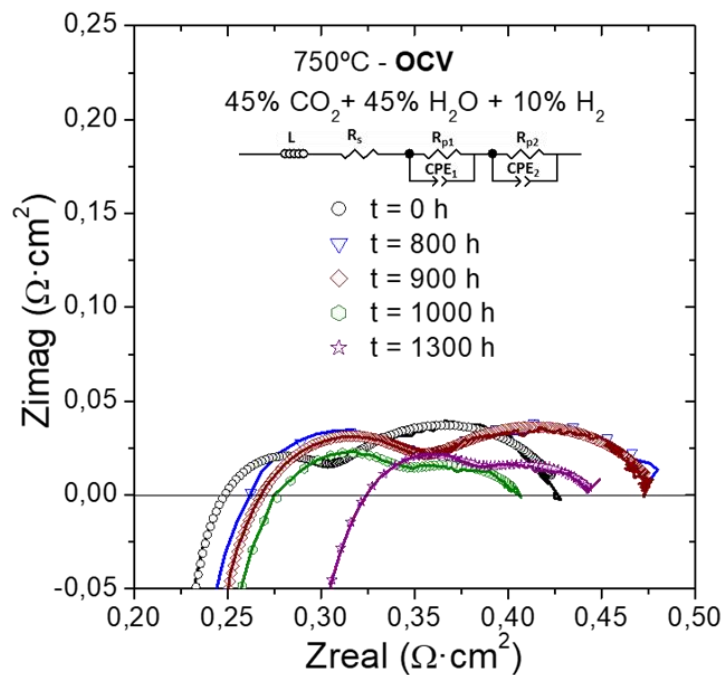


**Figure 6.5:** Nyquist plot of the impedance spectroscopy recorded at different times ( $t=0$ , 800, 900, 1100 and 1300 h) during a long-term operation test of a Ni-YSZ/YSZ/CGO<sub>bl</sub>/CGO-LSCF/LSCF high temperature electrolysis cell.

The tendency observed in **Figure 6.5** reveals that the serial resistance increases, being the 40 % of the total resistance with an initial value of 0.1  $\Omega$ , to more than 50% with a final measured serial resistance of 0.2  $\Omega$  after 1300 h of co-electrolysis operation at 750  $^{\circ}\text{C}$ . Concerning the polarization resistance, two arcs are observed in all the studied Nyquist plots measured at different times. As a consequence, two

different contributions to the total resistance were deconvoluted. In agreement with the analysis reported in **section 6.2**, a charge transfer process is identified as the limiting electrochemical process related to  $R_{p1}$  increasing in the first 800 h and slightly decreasing until the end of the experiment despite the increase of the injected current density from  $-0.5$  to  $-0.75$   $A/cm^2$ .  $R_{p2}$  contribution is dominated by non-charge transport processes, more related with the gas conversion than the diffusion, since is not increasing with the increase of the injected current. The highest contribution of the non-charge transfer electrochemical process to the total polarization resistance occurred at the beginning of the experiment, with a resistance ( $R_{p2}$ ) value of  $0.16$   $\Omega/cm^2$ . Due to a possible rearrangement of the microstructure, the  $R_{p2}$  value progressively decreased until achieving a value of  $0.067$   $\Omega/cm^2$  at the end of the experiment. According to this, the contribution of  $R_{p2}$  to the total polarization resistance decreased from around 40% to a final 20 %. Overall, the contribution of the polarization resistance to the total resistance, as sum of  $R_{p1}$  and  $R_{p2}$ , decreased from an initial 60% to a final 47 %. These results reveal that at low injected current densities, the degradation is dominated by the ohmic resistance, which is related to the electrolyte resistance to the transference of ions, the contact at the electrode/electrolyte interface and current collectors.

Time (h)	$R_s$ ( $\Omega \cdot cm^2$ )	$R_{p1}$ ( $\Omega \cdot cm^2$ )	$C_{p1}$ ( $F/cm^2$ )	$n_1$	$f_{max}$ (Hz)	$R_{p2}$ ( $\Omega \cdot cm^2$ )	$C_{p2}$ ( $F/cm^2$ )	$n_2$	$f_{max}$ (Hz)
0	$2.20 \cdot 10^{-1}$	$7.62 \cdot 10^{-2}$	$7.81 \cdot 10^{-4}$	0.79	$2.68 \cdot 10^3$	$1.61 \cdot 10^{-1}$	$4.07 \cdot 10^{-1}$	0.55	2.43
800	$2.26 \cdot 10^{-1}$	$1.22 \cdot 10^{-1}$	$4.38 \cdot 10^{-4}$	0.80	$2.98 \cdot 10^3$	$1.34 \cdot 10^{-1}$	$1.77 \cdot 10^{-1}$	0.62	6.70
900	$2.30 \cdot 10^{-1}$	$1.18 \cdot 10^{-1}$	$3.95 \cdot 10^{-4}$	0.80	$3.42 \cdot 10^3$	$1.39 \cdot 10^{-1}$	$1.76 \cdot 10^{-1}$	0.59	6.50
1100	$2.36 \cdot 10^{-1}$	$9.15 \cdot 10^{-2}$	$3.93 \cdot 10^{-4}$	0.83	$2.98 \cdot 10^3$	$8.36 \cdot 10^{-2}$	$1.37 \cdot 10^{-1}$	0.43	9.86
1300	$2.83 \cdot 10^{-1}$	$9.52 \cdot 10^{-2}$	$4.16 \cdot 10^{-4}$	0.74	$4.02 \cdot 10^3$	$6.76 \cdot 10^{-2}$	$1.80 \cdot 10^{-1}$	0.53	13.08

**Table 6.2:** Values of electrochemical parameters obtained from fitting Nyquist plots measured at OCV and at different times along the long-term operation employing an electrical equivalent circuit. Here,  $C_p$  represents the true capacitance calculated from the CPE element as  $C_p = (Q)^{(1/n)} \cdot R_{p1}^{(1-n/n)}$ .

Nyquist plots obtained at different operation times from the impedance spectroscopy measurements at 1.3 V were also fitted with the  $LR_s(R_{p1}Q_1)(R_{p2}Q_2)$  electrical equivalent circuit. The values obtained from fitting the serial resistance  $R_s$ , and the polarization resistances,  $R_{p1}$  and  $R_{p2}$ , were plotted with the aim of analysing its evolution along the operation time as it is presented in **Figure 6.6**. In this plot, serial resistance is observed to decrease from the beginning to 800 h. Although a slight

increase is noticed from 800 to 1100 h, then an abrupt increase is observed from 1100 to 1300 h of operation, probably related with the H<sub>2</sub>O supply accident. Contrary, both  $R_{p1}$  and  $R_{p2}$  polarization resistances values increased from the beginning to 800 h but decreased from this point to the end of the experiment, although the injected current was increased to  $-0.75 \text{ A/cm}^2$ . These results are in agreement with the conclusions extracted from analysing the impedance spectroscopy data recorded at OCV. Besides, the results presented confirm that the degradation observed in **Figure 6.4** was mainly caused by a progressive increase of the serial resistance, while both the fuel and oxygen electrode improved its performance along the operation time, which could be related with a problem in the fuel electrode/electrolyte contact interface

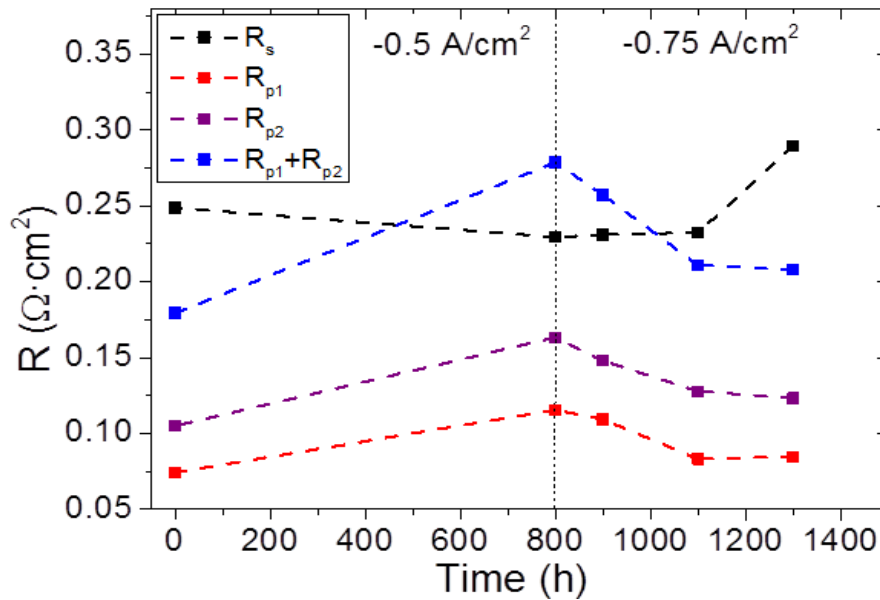


**Figure 6.6:** Evolution of the serial ( $R_s$ ) and both polarization ( $R_{p1}$  and  $R_{p2}$ ) resistances obtained from impedance spectroscopy measurements at 1.3 V at different points of the SOEC operation period.

#### 6.4.2. Post-test cell microstructural characterization

The cell operated during 1400 h of operation was structurally characterized by SEM coupled to EDX with the objective of finding correlation between the microstructure and the obtained electrochemical results. The main goal was finding microstructural evidences able to explain the decrease of the overall cell performance along 1400 h of operation time, caused by the electrochemically determined increase of the serial resistance contribution.

A cross-section SEM micrograph of the electrolyte-oxygen electrode interface is presented in **Figure 6.7**. It is clearly visible that the microstructure of the oxygen

electrode was perfectly attached to the electrolyte after being exposed to injected current densities higher than  $-1.2 \text{ A/cm}^2$ , and 1400 h of continuous co-electrolysis operation under current densities of  $-0.5 \text{ A/cm}^2$  and  $-0.75 \text{ A/cm}^2$ . **Figure 6.7a** shows the continuous and homogeneous microstructure of the CGO mesoporous scaffold infiltrated with LSCF and attached to the dense CGO barrier layer deposited on top of the electrolyte. This cross-section micrograph, which was taken by SEM at low energy, confirms the applied fabrication method and thermal treatment for the deposition of the mesoporous CGO as scaffold of the oxygen electrode functional layer. The micrograph presented in **Figure 6.7b** presents a cross-section of the entire electrolyte-oxygen electrode interface recorded by SEM using an electron beam of 20 kV and a SE2. In this micrograph it is possible to distinguish different microstructures. Starting from the bottom, the dense dark layer is assigned to the electrolyte, while the thin and brightness layer deposited on top corresponds to the dense CGO barrier layer deposited by PLD. The SEM micrograph shows the oxygen electrode constituted by two different microstructures. A porous layer is observed on top of the CGO barrier layer. This CGO scaffold, object of the present work, was infiltrated with LSCF as catalytic and electronic conductor in order to form a nanocomposite with the target of improving the oxygen electrode performance. Besides, a dense layer formed by the bulk LSCF is observed on top of the nanocomposite. Although this micrograph shows different microstructure on the oxygen electrode, a good continuity is observed between both the CGO-LSCF nanocomposite and bulk LSCF, ensuring the electrode performance.

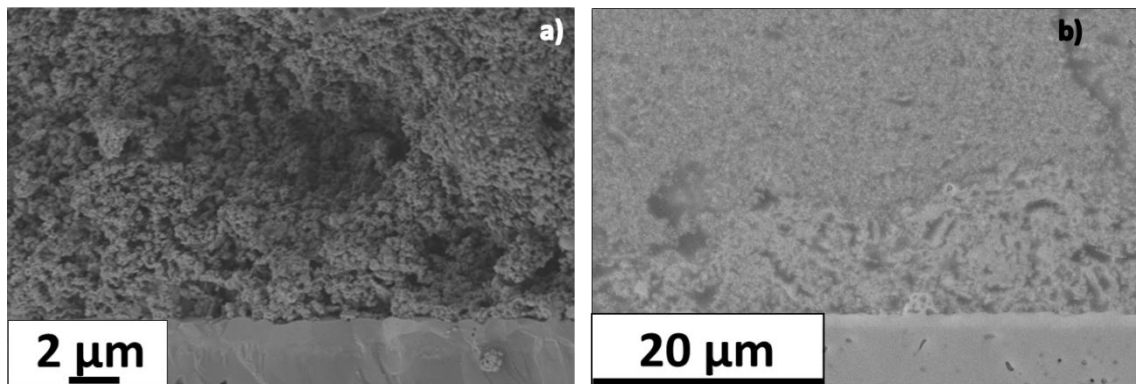


**Figure 6.7:** SEM cross-section micrographs of the electrolyte-oxygen electrode interface after 1400 h of operation under co-electrolysis (45%  $\text{H}_2\text{O}$ - 45%  $\text{CO}_2$ - 10%  $\text{H}_2$ )/synthetic air atmospheres. A barrier layer is distinguished between both. Micrograph a) was taken at 3 kV and b) at 20 kV.

Mappings of the main elements involved in the oxygen electrode-electrolyte interface were performed and are presented in **Figure 6.8**. In particular, the stability of the fabricated functional layer was studied after long-term co-electrolysis operation injecting high current densities. **Figure 6.8a** shows the cross-section micrograph taken as reference. Mappings of the different elements chosen for studying the oxygen electrode compounds are presented as **Figure 6.8b**, **6.8c**, **6.8d**, **6.8e** and **6.8f**. These elements are: La (**Figure 6.8b**) and Co (**Figure 6.8c**) as representative elements of the LSCF, Ce (**Figure 6.8d**) and Gd (**Figure 6.8e**) CGO elements; and Zr (**Figure 6.8f**) as representative element of the YSZ electrolyte. According to the distinguished areas in the reference micrograph (**Figure 6.8a**), EDX mappings show a main concentration of La and Co on the area assigned to the LSCF bulk layer, and of Ce and Gd elements in the area of the CGO scaffold. However, La and Co mappings also show its presence on the CGO scaffold area. These results confirm the good stability of the infiltrated CGO-LSCF nanocomposite as oxygen electrode functional layer after its co-electrolysis operation for 1400 h under continuous injection of  $-0.5 \text{ A/cm}^2$  and  $-0.75 \text{ A/cm}^2$  currents. The Zr mapping (**Figure 6.8f**) shows the electrolyte corresponding area.

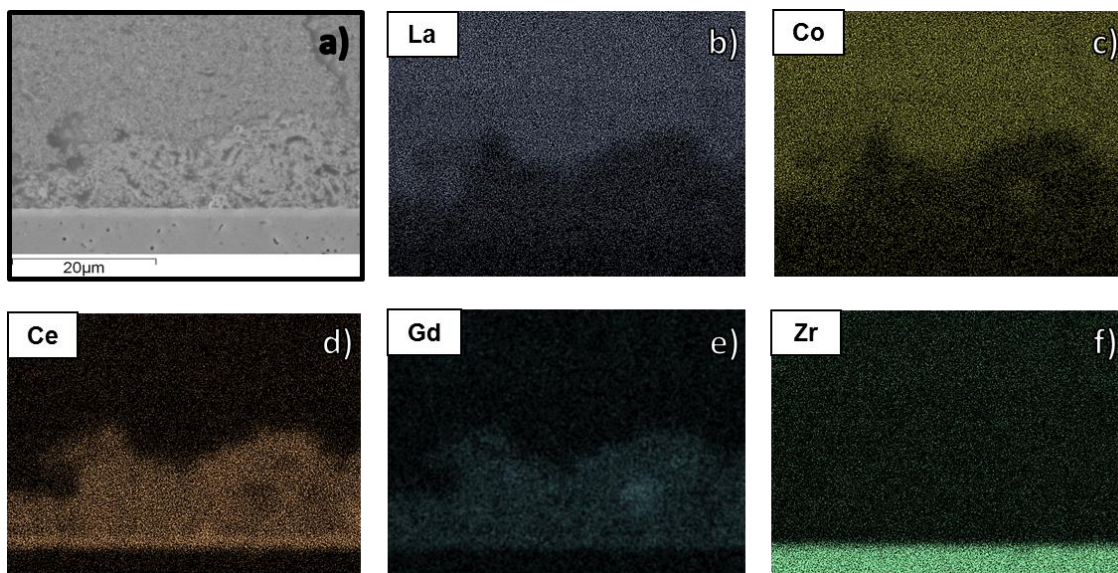


**Figure 6.8:** EDX mapping of the electrolyte-oxygen electrode interface (including the barrier layer) of the cell operated for 1400 h. a) Cross-section micrograph taken as reference. Mappings of La (b), Co (c), Ce (d), Gd (e), Zr (f) representative elements of LSCF, CGO and YSZ compounds.

A comparison of these mappings with the ones recorded for the as-fabricated sample (**Figure 6.3**) allows evaluating the effect of the long-term operation under continuous injection of current. It is seen from their comparison that after this

operation tests, the oxygen electrode functional layer keeps its porous structure and the LSCF is still homogeneously infiltrating the CGO scaffold. Besides, this CGO mesoporous material remains well attached to the CGO barrier layer, which also seems unaltered. Those results confirm that the LSCF infiltrated CGO mesoporous scaffold constitutes a recommended and stable architecture for the long-term operation of SOEC oxygen electrodes.

The study of the microstructure of the electrolyte-oxygen electrode did not explain the serial resistance increase reported by impedance spectroscopy measurements at OCV and 1.3 V, which was attributed as the main responsible of the reported degradation registered along 1400 h of operation. In this case, further microstructural studies were needed for finding evidences of the degradation rates. The fuel electrode-electrolyte interface was studied by SEM. **Figure 6.9** shows two cross-section micrographs of this interface recorded using different detectors for its comparison. **Figure 6.9a** was acquired using a SE2, which allows a better observation of the microstructure and morphology of the electrode cross-section. These micrographs show a fuel electrode well attached to the electrolyte and any delamination of this interface after long time operating. The micrographs presented in **Figure 6.9b** were also acquired by SEM, but in this case, using an InLens detector at low voltage. This detector highlight the electronic percolation path of the electrode as brightness contrast phase [16]. In this particular case, the Ni phase is the one appearing in bright colour, and it allows observing that most of the percolation was lost in the area next to the electrolyte. Furthermore, agglomerated Ni appearing in **Figure 6.9b** decreases the number of TPB points performing H<sub>2</sub> oxidation. The inset micrograph is a zoom of the fuel electrode-electrolyte interface. It shows a poor percolation of the Ni phase, what results on a loose of contact between both the electronic and ionic conductive paths in some points of the interface, justifying the observed increase in the serial resistance. The Ni migration produces a lack of electronic conductive path close to the electrolyte and generated an area dominated by the YSZ ionic conductive phase, which results, in fact, as an increase on the effective electrolyte thickness, leading to an increase of the serial contribution of the resistance. Results showed in **Figure 6.5** and **Figure 6.6** allow establishing a correlation between the microstructural migration of Ni located in the

region close the electrolyte, and the increase of the serial resistance ( $R_s$ ) value measured by impedance spectroscopy at both OCV and 1.3 V. In spite of the decrease of the fuel electrode thickness, the measured polarization resistance ( $R_{p1}$ ) evidences that this electrode continued working properly in the reduction of  $H_2O$  and  $CO_2$  probably due the activity of deeper TPB sites along the electrode

Different models were proposed for explaining what causes the degradation of the Ni-YSZ electrode [18-21] since this electrode has an important influence on the final SOC performance. It was reported the loss of Ni percolation in the interface of the Ni-YSZ fuel electrode and the YSZ electrolyte when high current densities were injected during SOEC operation [18]. Besides, Ni particles were agglomerated in this Ni-YSZ active area, which were far from the fuel electrode-electrolyte interface. As a consequence of the loss of activity and percolation of the electronic conductive phase (Ni) observed in the Ni-YSZ electrode close to the electrolyte, a progressive increase of the serial resistance was measured by impedance spectroscopy along the operation time.

The microstructural characterization presented in **Figure 6.9** and the degradation mechanism of Ni-YSZ electrodes reported in the literature explains the degradation rate showed in **Figure 6.4**. Operation under high injected current densities leads to the loss of electronic percolation in the Ni-YSZ composite next to the electrolyte, and to Ni agglomeration in the fuel electrode electrochemically active area. Both consequences were probably emphasized by reported steam supply problems. As result, a progressive increase of the serial resistance was noted by impedance spectroscopy measurements (**Figure 6.5**), which was exhibited on the evolution of the degradation rate (**Figure 6.4**). It is important highlighting that in spite of that, the Ni-YSZ electrochemically active continued working properly.

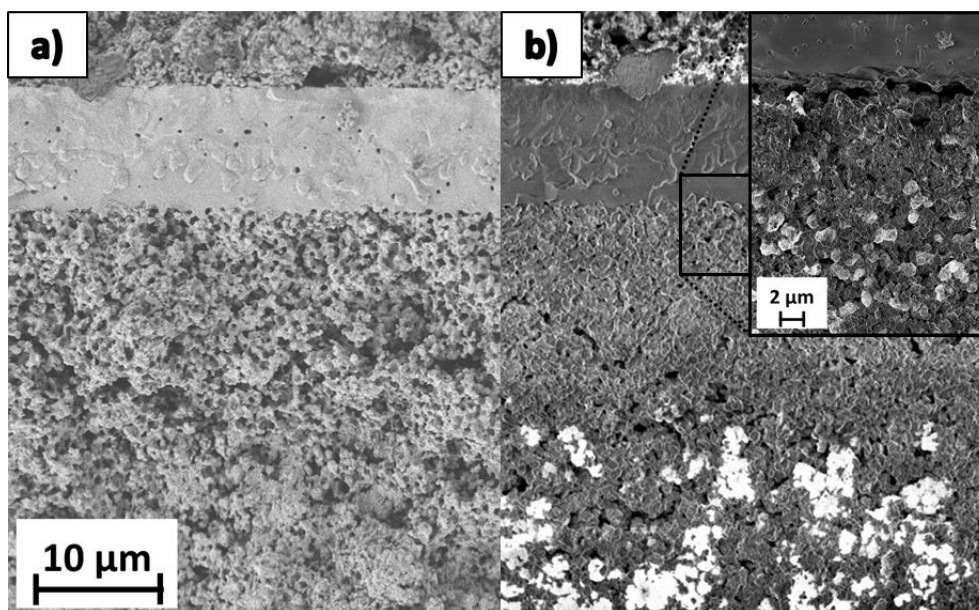


**Figure 6.9:** SEM cross-section micrographs of the electrolyte-fuel electrode interface after 1400 h of operation under co-electrolysis (45% H<sub>2</sub>O+45% CO<sub>2</sub>+10% H<sub>2</sub>)/synthetic air atmospheres using (a) secondary detector and (b) low voltage InLens SEM detectors. Inset of (b) presents a zoom of the fuel electrode percolation at the electrolyte interface.

## 6.5. Conclusions

CGO-LSCF infiltrated mesoporous oxygen electrodes have been fabricated on fuel electrode-supported SOEC, electrochemically characterized in co-electrolysis mode at 750 °C. Studying the fabricated CGO-LSCF oxygen electrode by different SEM detectors, it has been observed a good attachment between the electrolyte and the oxygen electrode microstructure and have been confirmed the successful fabrication of a homogeneous microstructure. Besides, EDX-Mappings have validated the employed infiltration method for obtaining intimately percolated CGO-LSCF oxygen electrode functional layers.

Current densities as high as  $-1.2 \text{ A/cm}^2$  have been injected for this cell configuration under a 45% H<sub>2</sub>O+ 45% CO<sub>2</sub>+ 10% H<sub>2</sub>/Air gas composition, improving the performance previously obtained. Operation at current densities of  $-0.5 \text{ A/cm}^2$  and  $-0.75 \text{ A/cm}^2$  for more than 1400 h were carried out, showing low degradation rates of 2%/kh and <1%/kh, respectively.

EIS measurements revealed an increase in the total resistance with the time. The increase of the ohmic resistance has been attributed as the main source of degradation, which is associated with the current collection at the fuel electrode. The post-mortem microstructural analysis showed the stability of the infiltrated oxygen

electrode functional layer, while a loss of percolation was detected in the electrolyte-fuel electrode interface due to a deactivation of the Ni particles from the Ni-YSZ functional layer. According to this, Ni migration and accumulation have caused the increase of the serial resistance along 1400 h of operation time. The decrease of the degradation rates with the operation time when high current densities are injected ( $-0.75 \text{ A/cm}^2$ ) shows a continuous rearrangement of the CGO-LSCF oxygen electrode, which brings a certain improvement of their electrochemical performance.

## 6.6. References

- [1] J. T. S. Irvine, D. Neagu, M. C. Verbraeken, C. Chatzichristodoulou, C. Graves, and M. B. Mogensen, "Evolution of the electrochemical interface in high-temperature fuel cells and electrolyzers," *Nat. Energy*, vol. 1, pp. 1–13, 2016.
- [2] J. Laurencin *et al.*, "Reactive Mechanisms of LSCF Single-Phase and LSCF-CGO Composite Electrodes Operated in Anodic and Cathodic Polarizations," *Electrochim. Acta*, vol. 174, pp. 1299–1316, 2015.
- [3] J.-C. Chang *et al.*, "Fabrication and characterization of Sm<sub>0.2</sub>Ce<sub>0.8</sub>O<sub>2</sub>-i-Sm<sub>0.5</sub>Sr<sub>0.5</sub>CoO<sub>3</sub>-i composite cathode for anode supported solid oxide fuel cell," *J. Power Sources*, vol. 196, pp. 3129–3133, 2010.
- [4] H. Fan, M. Keane, N. Li, D. Tang, P. Singh, and M. Han, "Electrochemical stability of La<sub>0.6</sub>Sr<sub>0.4</sub>Co<sub>0.2</sub>Fe<sub>0.8</sub>O<sub>3-δ</sub>-infiltrated YSZ oxygen electrode for reversible solid oxide fuel cells," *Int. J. Hydrogen Energy*, vol. 39, pp. 14071–14078, 2014.
- [5] Y. Wang, Z. Yang, M. Han, and J. Chang, "Optimization of Sm<sub>0.5</sub>Sr<sub>0.5</sub>CoO<sub>3-δ</sub>-infiltrated YSZ electrodes for solid oxide fuel cell/electrolysis cell," *RSC Adv.*, vol. 6, pp. 112253–112259, 2016.
- [6] L. Bernadet, J. Laurencin, G. Roux, D. Montinaro, F. Mauvy, and M. Reyrier, "Effects of Pressure on High Temperature Steam and Carbon Dioxide Co-electrolysis," *Electrochim. Acta*, vol. 253, pp. 114–127, 2017.
- [7] H. Fan, Y. Zhang, and M. Han, "Infiltration of La<sub>0.6</sub>Sr<sub>0.4</sub>FeO<sub>3</sub>-nanoparticles into YSZ scaffold for solid oxide fuel cell and solid oxide electrolysis cell," *J. Alloys Compd.*, vol. 723, pp. 620–626, 2017.
- [8] L. dos Santos.Gómez, J. M. Porrás-Vázquez, E. . Losilla, F. Martín, J. R. Ramos-Barrado, and D. Marrero-López, "Stability and performance of La<sub>0.6</sub>Sr<sub>0.4</sub>Co<sub>0.2</sub>Fe<sub>0.8</sub>O<sub>3-d</sub> nanostructured cathodes with Ce<sub>0.8</sub>Gd<sub>0.2</sub>O<sub>1.9</sub> surface coating," *J. Power Sources*, vol. 347, pp. 178–185, 2017.
- [9] A. Nechache, M. Cassir, and A. Ringuedé, "Solid oxide electrolysis cell analysis by means of electrochemical impedance spectroscopy: A review," *J. Power Sources*, vol. 258, pp. 164–181, 2014.
- [10] A. Lakki, R. Herzog, C. R. M. Weller H. Schubert, and M. K. G. B. O. GoÈrke, "Mechanical loss, creep, diffusion and ionic conductivity of ZrO<sub>2</sub>-8 mol%Y<sub>2</sub>O<sub>3</sub> polycrystals," *J. Eur. Ceram. Soc.*, vol. 20, pp. 285–296, 2000.
- [11] U.S. Department of Energy, *Fuel Cell Handbook*, vol. 7 Edition. 2004.
- [12] S. H. Jensen, A. Hauch, P. V. Hendriksen, M. Mogensen, N. Bonanos, and T. Jacobsen, "A Method to Separate Process Contributions in Impedance Spectra by Variation of Test Conditions," *J. Electrochem. Soc.*, vol. 154, no. 12, pp. B1325–B1330, 2007.
- [13] R. Barfod, M. Mogensen, T. Klemensø, A. Hagen, Y.-L. Liu, and P. Vang Hendriksen, "Detailed Characterization of Anode-Supported SOFCs by Impedance Spectroscopy," *J. Electrochem. Soc.*, vol. 154, no. 4, pp. B371–B378, 2007.

- [14] A. Hauch, K. Brodersen, M. Chen, and M. B. Mogensen, "Ni / YSZ electrodes structures optimized for increased electrolysis performance and durability," *Solid State Ionics*, vol. 293, pp. 27–36, 2016.
- [15] A. Mahmood, S. Bano, J. H. Yu, and K. H. Lee, "High-performance solid oxide electrolysis cell based on ScSZ/GDC (scandia-stabilized zirconia/gadolinium-doped ceria) bi-layered electrolyte and LSCF (lanthanum strontium cobalt ferrite) oxygen electrode," *Energy*, vol. 90, pp. 344–350, 2015.
- [16] A. Hauch, P. S. Jørgensen, K. Brodersen, and M. Mogensen, "Ni/YSZ anode - Effect of pre-treatments on cell degradation and microstructures," *J. Power Sources*, vol. 196, pp. 8931–8941, 2011.
- [17] A. Nechache *et al.*, "Diagnosis of a cathode-supported solid oxide electrolysis cell by electrochemical impedance spectroscopy," *Electrochim. Acta*, vol. 210, pp. 596–605, 2016.
- [18] M. B. Mogensen *et al.*, "Relation Between Ni Particle Shape Change and Ni Migration in Ni–YSZ Electrodes – a Hypothesis," *Fuel Cells*, vol. 17, pp. 434–441, 2017.
- [19] M. Torrell, A. Morata, P. Kayser, M. Kendall, K. Kendall, and A. Tarancón, "Performance and long term degradation of 7 W micro-tubular solid oxide fuel cells for portable applications," *J. Power Sources*, vol. 285, pp. 439–448, 2015.
- [20] M. Pihlatie, A. Kaiser, P. H. Larsen, and M. Mogensen, "Dimensional Behavior of Ni–YSZ Composites during Redox Cycling," *J. Electrochem. Soc.*, vol. 156, no. 3, pp. B322–B329, 2009.
- [21] V. Papaefthimiou *et al.*, "Operando observation of nickel/ceria electrode surfaces during intermediate temperature steam electrolysis," *J. Catal.*, vol. 352, pp. 305–313, 2017.
- [22] E. Hernández, F. Baiutti, A. Morata, M. Torrell, and A. Tarancón, "Infiltrated mesoporous oxygen electrodes for high temperature co-electrolysis of H<sub>2</sub> O and CO<sub>2</sub> in solid oxide electrolysis cells," *J. Mater. Chem. A*, vol. 6, no. 20, pp. 9699–9707, 2018.

# ***Chapter 7***

*Scale up of developed fuel  
electrode supported SOEC:  
Large Area Cells*



<b>7.</b>	<b>Scale up of developed fuel electrode supported SOEC: Large Area Cells. ....</b>	<b>207</b>
7.1.	Chapter overview .....	207
7.2.	Microstructural characterization of the oxygen electrode functional layers applied in large area cells.....	208
7.3.	Electrochemical characterization of large area SOECs.....	212
7.3.1.	Electrochemical characterization of large cells under electrolysis mode	212
7.3.2.	Electrochemical characterization under co-electrolysis mode .....	219
7.4.	Results of the long-term operation test on large area SOECs .....	224
7.4.1.	Electrochemical characterization and performance .....	224
7.4.2.	Post-test microstructural characterization.....	227
7.5.	Comparison of the performance of fuel electrode-supported cells (button- and large area cells).....	231
7.6.	Conclusions .....	232
7.7.	References .....	235



## 7. Scale up of developed fuel electrode supported SOEC: Large Area Cells.

### 7.1. Chapter overview

As a natural extension of the proved success in the use of mesoporous oxygen electrodes in the previous chapters, this chapter is devoted to scale up the fabrication of large area Solid Oxide Electrolysis Cells (SOECs) containing the optimized electrodes. Large area cells are prepared for being employed in real stack manufacturing (out of the scope of the present work). Half-cells composed by a Ni-YSZ fuel electrode support, a  $\text{Y}_2\text{O}_3\text{-ZrO}_2$  (YSZ) electrolyte and a  $\text{Ce}_{0.8}\text{Gd}_{0.2}\text{O}_{1.9}$  (CGO) barrier layer of  $25\text{ cm}^2$  were supplied by HTceramix/SOLIDpower for scaling-up the oxygen electrode fabrication procedure, based on a  $\text{Ce}_{0.8}\text{Gd}_{0.2}\text{O}_{1.9}\text{-La}_{0.6}\text{Sr}_{0.4}\text{Co}_{0.2}\text{Fe}_{0.8}\text{O}_3$  (CGO-LSCF) functional layer and a LSCF layer. The resulting configuration is described as Ni-YSZ/YSZ/CGO<sub>bl</sub>/CGO-LSCF/LSCF and its microstructural characterisation is presented in **Section 7.2**

Results on electrolysis and co-electrolysis mode under different fuel and oxygen electrodes gas compositions are presented in **section 7.3**. A detailed analysis of impedance spectroscopy data for identifying the main electrochemical processes related to the obtained resistance contributions are also presented in this section. Moreover, the influence on the cell performance of different oxygen electrodes is evaluated in terms of its initial performance and after being operated under co-electrolysis mode for 600 h (**section 7.4**). Finally, the comparison of the electrochemical performance of button and large area fuel electrode-supported cells is presented in **section 7.5**.

The work presented in this chapter corresponds to the results obtained during an international stage at the Denmark Technical University (DTU) [1] research facilities under the frame of the Efficient Co-Electrolyser for Efficient Renewable Energy Storage (ECo) project (nº 699892) [2].

## 7.2. Microstructural characterization of the oxygen electrode functional layers applied in large area cells

Half-cells of  $5 \times 5 \text{ cm}^2$  total area ( $16 \text{ cm}^2$  of active area) were employed as a substrate for scaling up the fabrication of the mesoporous oxygen electrodes, previously developed and optimized for button cells ( $1.54 \text{ cm}^2$ ). These half-cells were fabricated by the company HTceramix/SOLIDpower (Switzerland) and are considered the SoA in the field [3]. They are composed by a Ni-YSZ fuel electrode support of  $\approx 300 \mu\text{m}$  in thickness and a  $7 \mu\text{m}$ -thick 8YSZ electrolyte fabricated by tape casting, and a CGO barrier layer of  $3 \mu\text{m}$  in thickness deposited by screen printing on top of the 8YSZ electrolyte.

As in previous chapters, the oxygen electrode deposited for the present study was a CGO-LSCF composite based on a first functional CGO-LSCF layer ( $\approx 10\text{-}12 \mu\text{m}$ ) fabricated on top of the CGO barrier layer, which was obtained through the infiltration of the LSCF active phase into the CGO mesoporous scaffold. On top of this, a thicker layer of standard LSCF was deposited ( $\approx 50 \mu\text{m}$ ). With this, the attained cells presented the same configuration previously defined for the button cells (**Chapter 6**) and designed as Ni-YSZ/YSZ/CGO<sub>bl</sub>/CGO-LSCF/LSCF. As previously described, the CGO mesoporous material was airbrushed using a 3D printing frame with automatic 3-axis (x, y and z) (Print3D Solutions) [4] (more details about the fabrication procedure can be found in **section 2.5.3**).

Two cells, named A and B, were infiltrated with different volumes of the LSCF catalytic active solution with the aim of optimizing the volume needed for fabricating large area cells, ensuring homogeneous infiltration of the total mesoporous material and avoiding the excess of infiltrating solution (see **Table 7.1**). Different oxygen electrode functional layers were fabricated maintaining the total amount of CGO deposited and varying the LSCF volume on the range of  $240 \mu\text{L}$  to  $690 \mu\text{L}$ . As a rule of thumb, it was defined that button cells had to be infiltrated with  $7\text{-}9 \mu\text{L}$  of LSCF solution/ $\mu\text{m}$  of scaffold thickness. This ratio was maintained also for the fabrication of large area oxygen electrodes. Following this rule, the oxygen electrode of cell A was infiltrated with a total volume of  $240 \mu\text{L}$ . In order to ensure the electronic phase percolation in the mesoporous scaffold leading to a good oxygen electrode functional

layer, cell B was infiltrated with almost the triple volume. As it was previously described (**section 2.4.4**), oxygen electrodes were fabricated by three infiltration steps and its separated thermal treatments up to 500 °C, and a final single treatment at 800 °C for the formation of the desired LSCF phase [5,6]. A summary of the main parameters used during the fabrication procedures of tested cells is presented in **Table 7.1**:

Cell	wt mesoporous (mg)	V infiltration (μL)/step	V infiltrated (μL)	wt infiltrated (mg)
A	25.8	80	240	6.3
B	26.1	230	690	13.7

**Table 7.1:** Parameters of the fabricated oxygen electrodes.

As it has been already stated in previous chapters, the microstructure of the oxygen electrode functional layer is one of the parameters with higher influence on the final performance of fuel electrode-supported cells. According to this, it has to be noted that the task of transferring the fabrication procedure ensuring the reproducibility and homogeneity of the microstructure from button to large area cells is crucial, and represents an important challenge due to the nature of the fabrication process and the complexity of the developed electrodes architecture.

Studying the micrographs of the fabricated oxygen electrode by using Scanning Electron Microscopy (SEM), it is possible to observe different microstructures associated to each part of the electrode. **Figure 7.1** and **Figure 7.2** present cross-section micrographs of cells A and B respectively. All presented micrographs were obtained using a Secondary Electron Detector (SE2) at different magnifications.

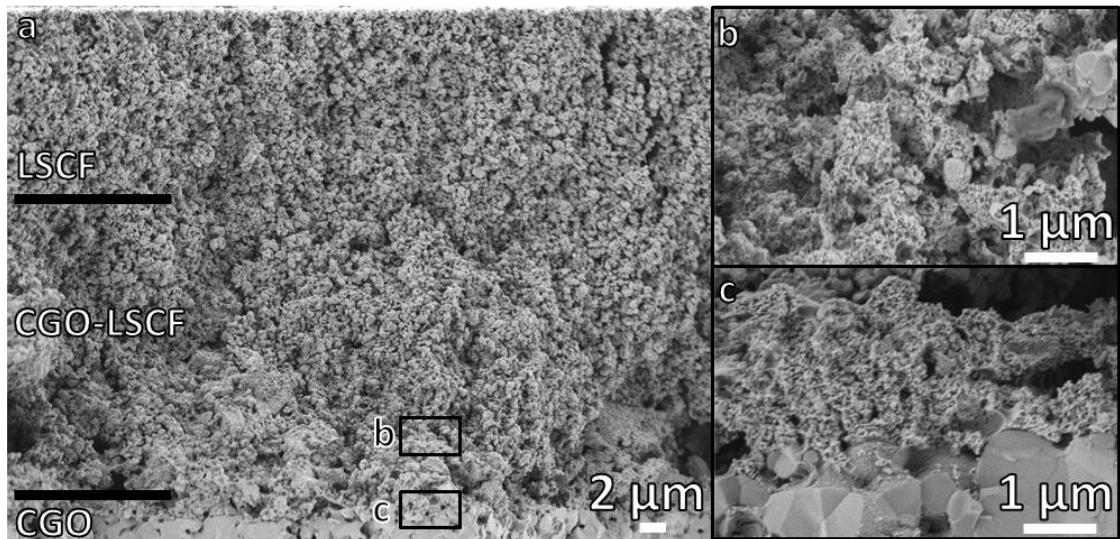


**Figure 7.1:** a) SEM cross-section micrograph of the CGO-LSCF oxygen electrode fabricated for cell A. Zoom b) shows the oxygen electrode microstructure and c) presents a higher magnification micrograph of the barrier layer/functional layer interface.

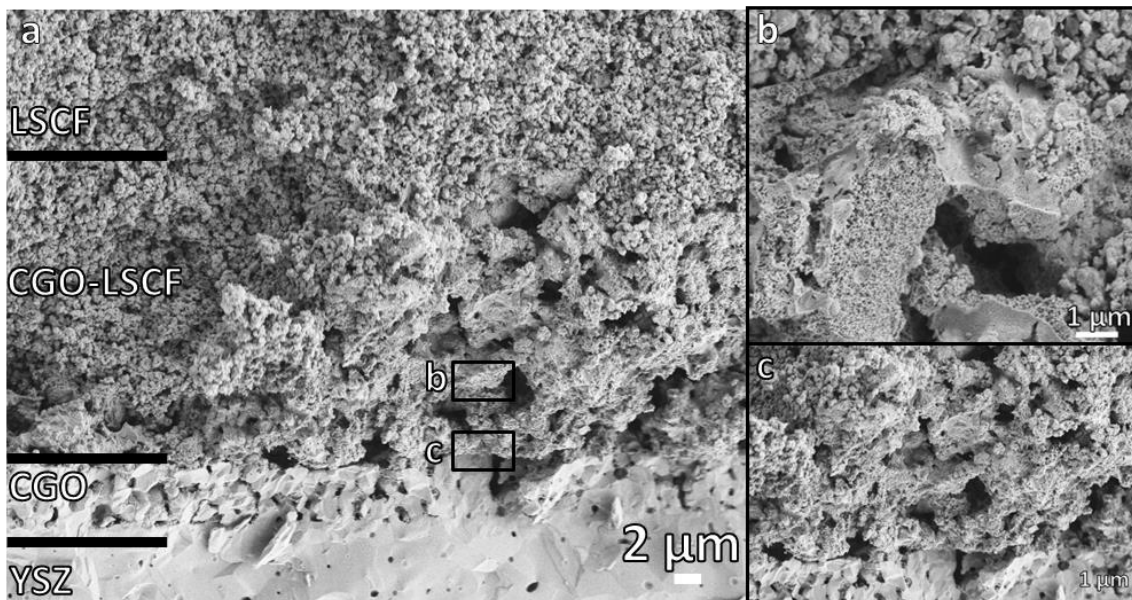


**Figure 7.2:** a) SEM cross-section micrograph of the CGO-LSCF oxygen electrode fabricated for cell B. Zoom b) shows the oxygen electrode microstructure and c) presents a higher magnification micrograph of the barrier layer/functional layer interface.

Both **Figure 7.1a** and **Figure 7.2b** show cross-sections micrographs of the oxygen electrode interface of cell A and B, respectively, where, according to the differentiated microstructure, it is possible to distinguish a porous and thin CGO barrier layer, the CGO-LSCF infiltrated mesoporous functional layer, and a denser and thicker LSCF layer.

Two high magnification insets (labelled as “b” and “c” micrographs) are also presented in order to make easier the comparison between the microstructures in both specific areas. The microstructure of the functional layer, formed by infiltrated

mesoporous material (**Figure 7.1b** and **7.2b**), show significant microstructural differences if both cell A and B are compared. In **Figure 7.1c** and **7.2c**, the microstructure of the barrier layer-mesoporous scaffold interface is studied. A good attachment of the mesoporous scaffold to the barrier layer is observed in cell A and cell B.

Considering the three presented micrographs corresponding to cell A (**Figure 7.1**), an ideal case of infiltrated scaffold microstructures is observed when 240  $\mu\text{L}$  of LSCF (the lowest range of the study) were infiltrated into the CGO mesoporous scaffold sintered to the CGO barrier layer.

Contrary, it is observed the formation of a characteristic morphology in form of cave in the oxygen electrode functional layer when  $\approx 700 \mu\text{L}$  of volume were infiltrated to the B large area cell, as it is shown in the micrographs presented as **Figure 7.2**. Besides, the morphology found in the oxygen electrode of this cell B is similar to the  $\text{Sm}_{0.2}\text{Ce}_{0.8}\text{O}_{1.9}$ -  $\text{Sm}_{0.5}\text{Sr}_{0.5}\text{CoO}_3$  (SDC-SSC) oxygen electrode microstructure of the Ni-YSZ/YSZ/CGO<sub>b</sub>/SDC-SSC/SSC button cell, also infiltrated with excess volume of the SSC solution, which was previously presented in **Figure 4.7 (section 4.3)**.

The conclusions took from this SEM study of the oxygen electrode functional layers microstructures, fabricated on fuel electrode-supported large area cells, are in concordance with the conclusions determined by the microstructural characterization of the button cells on **Chapter 4**. It is deduced that the addition of an excess of infiltration solution might result on the formation of the cave-like microstructure observed in **Figure 7.2**, which could result on bad performing cells when measured on electrolysis mode, as it has also been demonstrated from the electrochemical characterization in previous chapters. The hypothesis behind the drop on the performance when an excess of infiltration solution is added is that, the excess of LSCF solution forms very thin and porous layers on top of the mesoporous scaffold, giving place to the caves-like microstructure. This phase could present a high catalytic activity but limited performance due to the probably much higher resistance to the current injection and a lack of percolation of the ionic path for the generation of the active Triple Phase Boundary (TPB) points.

On the contrary, infiltrating the CGO scaffold with less than 240  $\mu\text{L}$  seems to result on an uncomplete percolation of electron conducting phase constituting the oxygen electrode functional layer. As it has been previously reported and demonstrated in this thesis, the percolation of both phases is critical for the oxygen electrode performance. As consequence, lack of LSCF infiltrating the CGO scaffold would result on a low performing SOEC.

### 7.3. Electrochemical characterization of large area SOECs

The performance of fabricated large area fuel electrode-supported cells was evaluated by means of electrochemical techniques. The electrochemical characterization is based on analysing I-V polarization curves and Electrochemical Impedance Spectroscopy (EIS) measurements[7] under different electrolysis and co-electrolysis modes. As it has been previously explained, impedance measurements show the electrochemical processes contributing and limiting the performance of each of the electrodes. These processes are identified changing the fuel and oxygen electrode atmospheres during the electrochemical characterization. The gas compositions used for the different tests performed at the DTU facilities are summarized in the following **Table 7.2**:

Test mode	Temperature (°C)	Fuel electrode gas composition	Air electrode gas composition	Dedicated section
Electrolysis	750	20% H <sub>2</sub> O + 80% H <sub>2</sub>	O <sub>2</sub>	section 6.3.1
Electrolysis	750	50% H <sub>2</sub> O + 50% H <sub>2</sub>	O <sub>2</sub>	section 6.3.1
Electrolysis	750	50% H <sub>2</sub> O + 50% H <sub>2</sub>	Synthetic air	section 6.3.1
Co-Electrolysis	750	45% H <sub>2</sub> O + 10% H <sub>2</sub> + 45% CO <sub>2</sub>	O <sub>2</sub>	section 6.3.2
Co-Electrolysis	750	65% H <sub>2</sub> O + 10% H <sub>2</sub> + 25% CO <sub>2</sub>	O <sub>2</sub>	section 6.3.2

**Table 7.2:** Test conditions for the electrochemical characterization of large area Ni-YSZ/YSZ/CGO<sub>b</sub>/CGO-LSCF/LSCF electrolyser cells.

#### 7.3.1. Electrochemical characterization of large cells under electrolysis mode

Fabricated large area SOECs were tested in galvanostatic electrolysis mode under different gas compositions at 750 °C in order to study the performance and identify the electrochemical limiting processes related to the obtained overall Area Specific Resistance (ASR), constituted by the contribution of the ohmic ( $R_s$ ) and polarization

( $R_p$ ) resistances. Two different electrolysis fuel electrode gas compositions were used: 20 %  $H_2O$  + 80 %  $H_2$  and 50 %  $H_2O$  + 50 %  $H_2$ , while the oxygen electrode gas composition was varied between pure  $O_2$  and synthetic air (21 %  $O_2$  + 79 %  $N_2$ ). The performed I-V polarization curves are presented in **Figure 7.3**.

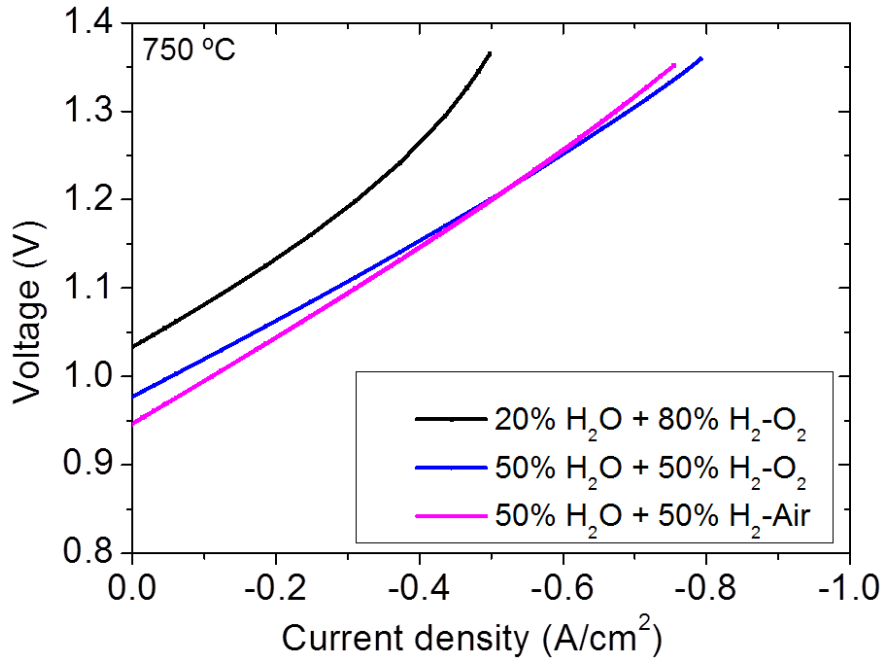


**Figure 7.3:** I-V polarization curves measured on large area cells under different fuel and oxygen electrode gas compositions at 750 °C on electrolysis mode.

First of all, Open Circuit Voltages (OCVs) measured with fuel compositions with major proportion of  $H_2$  (20%  $H_2O$  + 80 %  $H_2$ ) results in the highest value (1.04 V). Moreover, it has to be noted that the OCV of the I-V curves measured under the same fuel electrode gas composition (50%  $H_2O$  + 50 %  $H_2$ ) present different values. This is due to change of the anodic chamber composition. Operating under  $O_2$ , the OCV shows higher values (0.98 V) than operating under synthetic air (0.95 V). In any case, the three obtained different OCV values approach the ones predicted by the Nernst equation, namely, 1.05 V for the electrochemical characterization under 20%  $H_2O$  + 80 %  $H_2$  and  $O_2$  fuel and oxygen electrode atmospheres while [8] 0.99 V and 0.96 V for  $O_2$  and synthetic air measured under 50%  $H_2O$  + 50 %  $H_2$  fuel electrode gas composition, respectively.

To determine and compare the maximum injected current densities, the value at 1.30 V (thermoneutral voltage operation) has been adopted as a reference. If the complete set of I-V polarization curves is compared (**Figure 7.3**), better performance

and higher current densities are achieved when higher is the percentage of steam on the inlet fuel composition [9] According to this, it can be seen that the cell measured under a fuel electrode gas composition which contains lower percentage of water, 20 % H<sub>2</sub>O + 80 % H<sub>2</sub>, shows lower performance, injecting a current of 7.04 A that results in a -0.44 A/cm<sup>2</sup> of maximum injected current density at 1.30 V. The oxygen electrode gas composition, which was varied between pure O<sub>2</sub> (100 %, blue line) and synthetic air (21 % of O<sub>2</sub>, pink line) maintaining constant the fuel electrode gas composition, shows a slight influence in the maximum injected current density that could be related to the variation of the total resistance and the initial OCV. In any case, a minor influence of the oxygen electrode gas composition over the fuel composition is evidenced from these results. Comparing the obtained results at 1.30 V, a maximum total current injection of 11.04 A, results in a current density of -0.69 A/cm<sup>2</sup> on large area cells injected when O<sub>2</sub> is used as oxygen electrode gas flow, while 10.72 A resulting in -0.67 A/cm<sup>2</sup> was the maximum current density injected for a synthetic air oxygen electrode atmosphere, both keeping the same fuel electrode 50% H<sub>2</sub>O + 50 % H<sub>2</sub> gas composition.

It has to be highlighted that, on electrolysis mode, differently than in fuel cell mode, the oxygen feed (oxygen electrode atmosphere) on the oxygen electrode chamber is not participating on the electrolysis and co-electrolysis involved reactions and does not seem to be the main limiting factor of the cell performance. However, the oxygen electrode, focus of the present work, is described as the main key factor on the performance and stability of SOEC, being its interface with the electrolyte a critical point, as it is explained in the literature for standard electrodes [10-14]. It is also important to note here that the activity of both electrodes is clearly dependant, so the limitations that are seen changing the fuel electrode composition are affecting the performance and main processes of both electrodes.

Besides, when the slopes of the I-V polarisation curves obtained at higher current densities are analysed, it is possible to observe a clear contribution of gas diffusion issues, evidenced by a deviation of the slope from the linearity. So, the exponential increase on the slope of the I-V curves is directly related with the overall ASR at that operation conditions [9]. Described gas diffusion issues, observed at the 20 % H<sub>2</sub>O + 80

% H<sub>2</sub> specific fuel electrode gas composition, reveal a limitation of the electrode microstructure arrangement when current densities higher than -0.25 A/cm<sup>2</sup> are injected.

A detailed analysis of the measured impedances (EIS) under common fuel and oxygen electrode gas compositions is presented here. As it has been previously explained, the electrochemical processes contributing and limiting the oxygen and fuel electrodes performance are visible changing both electrodes gas compositions [15]. According to this, in this section it is reported that comparing data recorded for the same cell changing the operation parameters allows identifying and distinguishing the fuel and oxygen electrode contributions [16]. In order to deconvolute the different limiting processes on the cell performance, EIS measurements were performed alternating current in galvanostatic mode at OCV and the obtained Nyquist plots (**Figure 7.4**) were analysed.

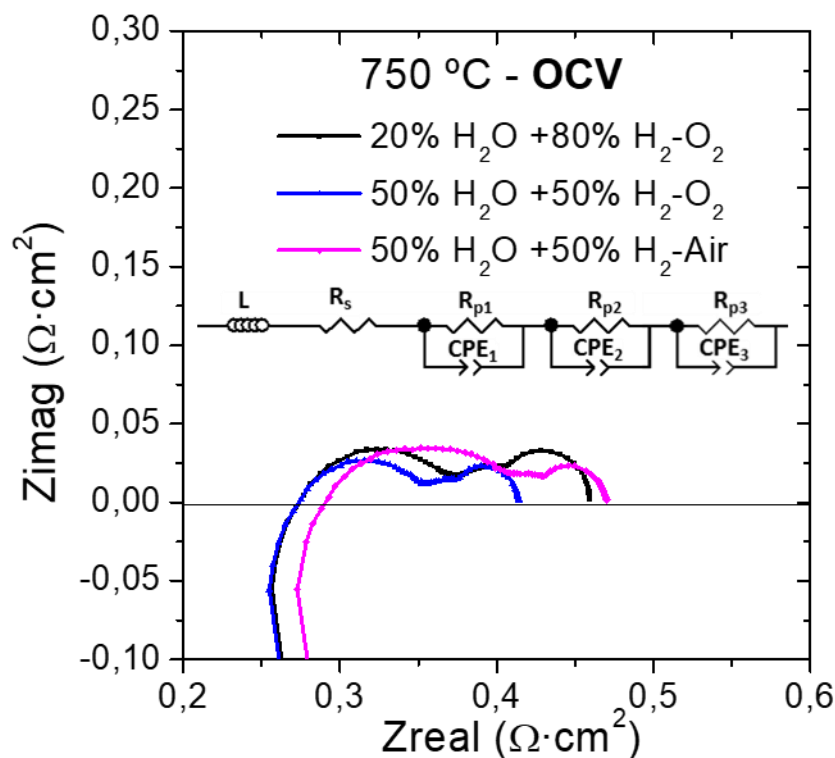


**Figure 7.4:** Nyquist plots measured at OCV on electrolysis mode on large area cells under different fuel and oxygen electrodes gas compositions at 750 °C.

The three Nyquist plots presented in **Figure 7.4** are analysed and fitted employing an equivalent circuit presented as LR<sub>s</sub>(R<sub>p1</sub>Q<sub>1</sub>)(R<sub>p2</sub>Q<sub>2</sub>)(R<sub>p3</sub>Q<sub>3</sub>). As it has been explained in previous chapters, L is the inductance and R<sub>s</sub> is the serial resistance. RQ represents a

parallel circuit composed by R as a resistance and Q as a Constant Phase Element (CPE) substituting ideal C capacitances. The RQ elements of the equivalent circuit represent contributions of the electrodes to the polarization resistance and correspond to real arcs presented on the Nyquist plots. Each arc represents the existence of an electrochemical processes dominating the reactions taking place in the electrodes at the given frequency. The introduction of Q takes into consideration a distribution of relaxation times represented by  $n$  ( $0 \leq n \leq 1$ ) observed as a depression angle on experimental arcs, instead of a perfect semicircle ( $n=1$ ) typical from pure capacitances (C) [17]. **Table 7.3** records the resistances, frequencies and capacitances values obtained from fitting Nyquist plots with the proposed equivalent circuit.

Usually, the main ohmic contribution comes from the resistance of the electrolyte to the ionic conductivity [7,18]. According to this, a theoretical serial resistance of  $0.0015 \Omega$  was calculated from the electrolyte contribution taking into account the theoretical YSZ conductivity [19], the operation temperature, and the thickness and active area of the electrolyte ( $\approx 7 \mu\text{m}$  and  $16\text{cm}^2$ ). Therefore, the expected ASR of the electrolyte is  $0.024 \Omega\cdot\text{cm}^2$ . Analysing the obtained arcs, different serial resistances ( $R_s$ ) were measured when the oxygen electrode gas composition was changed. As it is shown in **Figure 7.4**, the arcs measured under  $\text{O}_2$  shows a serial area specific resistance of  $0.27 \Omega\cdot\text{cm}^2$  (corresponding to a total resistance of  $0.017 \Omega$ ), while this value was of  $0.29 \Omega\cdot\text{cm}^2$  ( $0.019 \Omega$ ) when the atmosphere was changed to synthetic air ( $21\% \text{O}_2$ ). The difference between the theoretical and measured serial resistances can be attributed to additional contributions, which are mainly the resistance generated by the contact of the electrolyte-electrode at the interface, and the resistance related to current collectors.

These values explain the difference on the overall ASR reported in **Figure 7.3** maintaining the same fuel gas composition ( $50\% \text{H}_2\text{O} + 50\% \text{H}_2$ ), which resulted on slightly different injected current densities. The increase of the serial resistance could be explained by the progressive evolution of the cell (especially the electrode-electrolyte or -current collector interfaces). Regarding the contributions to the polarization resistance, the oxygen electrode fabricated on large area fuel electrode-supported cells was studied changing the gas composition in this electrode.

Specifically, the percentage of O<sub>2</sub> was changed from 100 % O<sub>2</sub> to 21 % O<sub>2</sub>-N<sub>2</sub> (Bal.) (synthetic air) at the oxygen electrode atmosphere, while the fuel electrode gas composition was maintained constant at 50% H<sub>2</sub>O + 50 % H<sub>2</sub>. Nyquist and Bode plots recorded from impedance measurements at OCV under these gas compositions are presented in **Figure 7.5**. The analysis of the characteristic capacitances and frequencies determined from Nyquist plots and Bode plots respectively, allow identifying the specific electrochemical process causing each resistance [16,20].

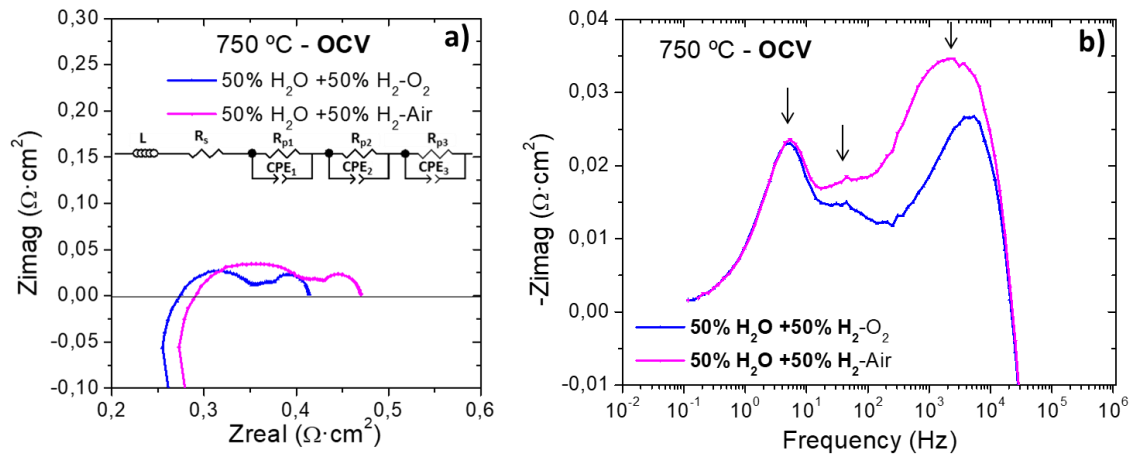


**Figure 7.5:** Nyquist and Bode plots recorded at OCV for large area cells under electrolysis fuel electrode gas composition (50% H<sub>2</sub>O + 50% H<sub>2</sub>) changing the gas composition of the oxygen electrode between O<sub>2</sub> (100% of O<sub>2</sub>) and synthetic air (21% of O<sub>2</sub>) at 750 °C.

Concerning the polarization contributions, both Nyquist plots (**Figure 7.5a**) are composed by three similar arcs contributing to it. The values recorded in **Table 7.3** for the fitted Nyquist plots allowed identifying the electrochemical processes related to each resistance. According to the high frequency ( $\approx 10^3$  Hz) contribution observed on the Bode plot and the order of magnitude of the capacitance ( $10^{-4}$  F/cm<sup>2</sup>), R<sub>p1</sub> is assigned to charge transfer processes dominated by the oxygen electrode [18,21-23].

Moreover, R<sub>p2</sub> and R<sub>p3</sub> ( $10^{-4}$  Ω and  $10^{-3}$  Ω) are assigned as fuel electrode contributions since both resistances present characteristic frequencies at 1 and 10 Hz, and all recorded capacitances present values on the order of magnitude of  $10^{-1}$  F/cm<sup>2</sup>. According to these values it is concluded that R<sub>p2</sub> and R<sub>p3</sub> are caused by non-charge transfer processes taking place on the fuel electrode [18,21-23]. These results are in concordance with Bode plots (**Figure 7.5b**), which show the similar electrochemical process contributions at low frequencies because of the same fuel electrode gas composition.

Following the same strategy than on the oxygen electrode study, Ni-YSZ fuel electrode was also studied recording EIS measurements at different fuel electrode gas compositions. The composition at the fuel electrode chamber was varied from 20 % H<sub>2</sub> + 80 % H<sub>2</sub> to 50 % H<sub>2</sub>O + 50 % H<sub>2</sub>, maintaining pure O<sub>2</sub> at the oxygen electrode chamber. The Nyquist and Bode plots obtained by the EIS characterization recorded at OCV and 750 °C are presented in **Figure 7.6**.

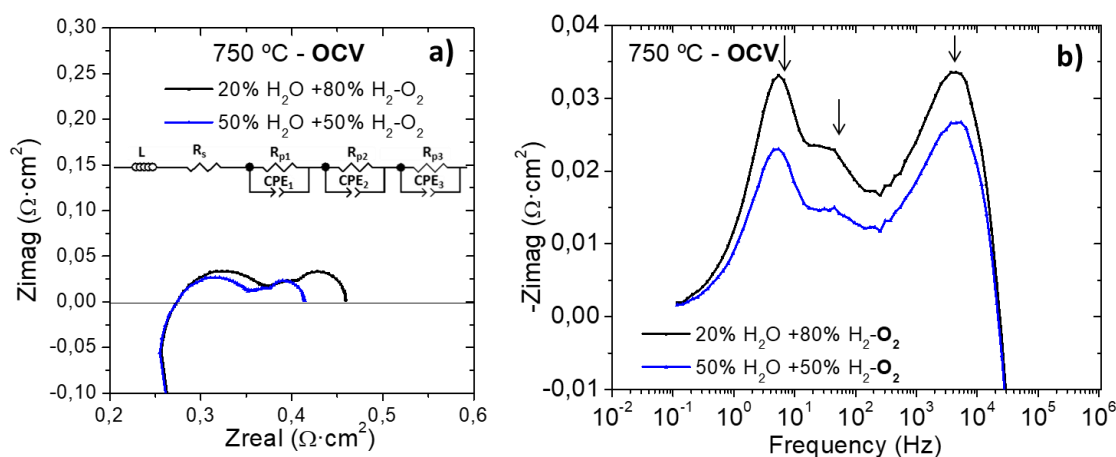


**Figure 7.6:** Nyquist and Bode plots recorded at OCV for large area cells under two different electrolysis fuel electrode gas composition (20 % H<sub>2</sub> + 80 % H<sub>2</sub> and 50 % H<sub>2</sub>O + 50 % H<sub>2</sub>) maintaining O<sub>2</sub> as oxygen electrode atmosphere at 750 °C of operation temperature.

Nyquist plots presented in **Figure 7.6a** show three characteristic arcs related to the polarization resistance, as the ones observed in **Figure 7.5a**. The resistances, capacitances and frequency values recorded in **Table 7.3** are obtained from fitting the impedances presented in **Figure 7.6a** with the equivalent previously explained,  $LR_s(R_{p1}Q_1)(R_{p2}Q_2)(R_{p3}Q_3)$ .  $R_{p1}$  is identified again as a charge transfer process related to the oxygen electrode according to the orders of magnitude of the obtained frequency ( $10^3$ ) and capacitance ( $10^{-4}$ ) [18,21-23]. The results obtained and recorded in **Table 7.3** show that  $R_{p1}$  is influenced by the amount of O<sub>2</sub> present in the oxygen electrode. Specifically, the  $R_{p1}$  values measured at 20 % H<sub>2</sub> + 80 % H<sub>2</sub> and 50 % H<sub>2</sub>O + 50 % H<sub>2</sub> fuel electrode gas compositions under O<sub>2</sub> are closer between them than the resistance measured under 50 % H<sub>2</sub>O + 50 % H<sub>2</sub>-Air. In addition, the capacitance ( $10^{-1}$  F/cm<sup>2</sup>) and frequencies ( $10^0 - 10^1$  Hz) values obtained for  $R_{p2}$  and  $R_{p3}$  from the fitting allow associating these resistances to non-charge transfer electrochemical processes [18,21-23]. The contributions observed in the Bode plot (**Figure 7.6b**) confirm the association of these resistances to the fuel electrode processes.

	50%H <sub>2</sub> O+50%H <sub>2</sub> /O <sub>2</sub>	50%H <sub>2</sub> O+50%H <sub>2</sub> /Air	20%H <sub>2</sub> O+80%H <sub>2</sub> /O <sub>2</sub>
R <sub>s</sub> (Ω·cm <sup>2</sup> )	2.7·10 <sup>-1</sup>	2.9·10 <sup>-1</sup>	2.7·10 <sup>-1</sup>
R <sub>p1</sub> (Ω·cm <sup>2</sup> )	1.3·10 <sup>-1</sup>	2.0·10 <sup>-1</sup>	1.4·10 <sup>-1</sup>
C <sub>p1</sub> (F/cm <sup>2</sup> )	1.3·10 <sup>-4</sup>	1.5·10 <sup>-4</sup>	1.4·10 <sup>-4</sup>
n <sub>1</sub>	0.66	0.50	0.66
f max (Hz)	9.6·10 <sup>3</sup>	5.5·10 <sup>3</sup>	7.8·10 <sup>3</sup>
R <sub>p2</sub> (Ω·cm <sup>2</sup> )	1.6·10 <sup>-2</sup>	6.4·10 <sup>-3</sup>	2.6·10 <sup>-2</sup>
C <sub>p2</sub> (F/cm <sup>2</sup> )	1.7·10 <sup>-1</sup>	5.2·10 <sup>-1</sup>	1.2·10 <sup>-1</sup>
n <sub>2</sub>	1.00	1.00	1.00
f max (Hz)	6.1·10 <sup>1</sup>	4.7·10 <sup>1</sup>	5.2·10 <sup>1</sup>
R <sub>p3</sub> (Ω·cm <sup>2</sup> )	4.0·10 <sup>-2</sup>	3.5·10 <sup>-2</sup>	5.6·10 <sup>-2</sup>
C <sub>p3</sub> (F/cm <sup>2</sup> )	8.7·10 <sup>-1</sup>	9.7·10 <sup>-1</sup>	5.7·10 <sup>-1</sup>
n <sub>3</sub>	1.00	1.00	1.00
f max (Hz)	4.6	4.7	4.9
ASR (Ω·cm <sup>2</sup> )	4.56·10 <sup>-1</sup>	5.3·10 <sup>-1</sup>	5.0·10 <sup>-1</sup>

**Table 7.3:** Results from fitting EIS data measured at OCV at 750 °C and recorded at different gas compositions for large area Ni-YSZ/YSZ/CGO<sub>bil</sub>/CGO-LSCF/LSCF electrolysis cells. Here, C<sub>p</sub> represents the true capacitance calculated as  $C_p = (Q)^{(1/n)} R_{p1}^{(1-n/n)}$ .

The total resistance values obtained from the slope of the I-V curves and the EIS are in good agreement (**Table 7.4**). These total resistance values reveal major resistance measured under 20 % H<sub>2</sub>O + 80 % H<sub>2</sub> compared to 50 % H<sub>2</sub>O + 50 % H<sub>2</sub>, both under pure O<sub>2</sub>. Besides, measurements under synthetic air atmosphere are more resistive than the ones under O<sub>2</sub> when the same 50% H<sub>2</sub>O+ 50% H<sub>2</sub> fuel electrode gas compositions was maintained constant. These conclusions are in concordance with the tendencies observed from I-V curves and EIS measurements plots (**Figure 7.3** and **7.4**).

	50%H <sub>2</sub> O+50%H <sub>2</sub> /O <sub>2</sub>	50%H <sub>2</sub> O+50%H <sub>2</sub> /Air	20%H <sub>2</sub> O+80%H <sub>2</sub> /O <sub>2</sub>
ASR (Ω·cm <sup>2</sup> ) (I-V slope)	4.7·10 <sup>-1</sup>	5.3·10 <sup>-1</sup>	5.4·10 <sup>-1</sup>
ASR (Ω·cm <sup>2</sup> ) (EIS fitting)	4.6·10 <sup>-1</sup>	5.3·10 <sup>-1</sup>	5.0·10 <sup>-1</sup>

**Table 7.4:** Comparison of total polarization resistance values obtained from the slope of I-V curves (**Figure 7.3**) and fitting of EIS measurements (**Figure 7.5a** and **Figure 7.6a**) recorded detailed atmospheres.

### 7.3.2. Electrochemical characterization under co-electrolysis mode

Large area cells with the same Ni-YSZ/YSZ/CGO<sub>bil</sub>/CGO-LSCF/LSCF configuration, were electrochemically characterized under co-electrolysis mode. The electrochemical

characterization was based on performing I-V polarization curves and EIS measurements at 750 °C on galvanostatic mode. The electrochemical measurements were performed under two co-electrolysis atmospheres: 45 % H<sub>2</sub>O + 10 % H<sub>2</sub> + 45 % CO<sub>2</sub> and 65 % H<sub>2</sub>O + 10 % H<sub>2</sub> + 25 % CO<sub>2</sub>. The cells were also tested changing the oxygen electrode atmosphere from O<sub>2</sub> (100 % of O<sub>2</sub>) to synthetic air (21 % of O<sub>2</sub>). I-V polarization curves measured under co-electrolysis for two different fuel and oxygen gas compositions are presented in **Figure 7.7**.

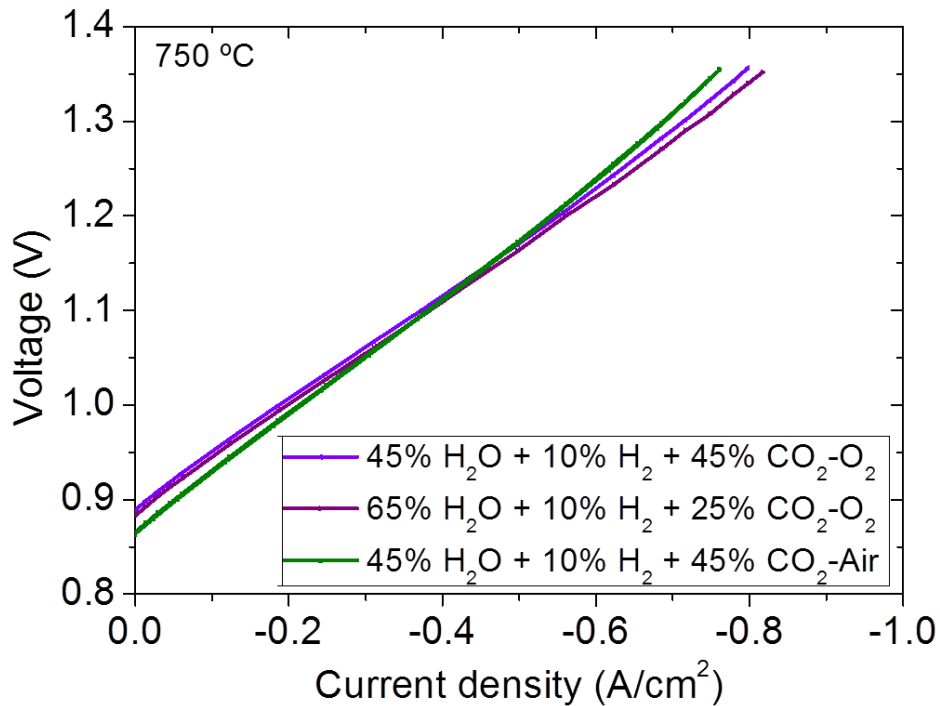


**Figure 7.7:** I-V polarization curves measured on large area cells under different co-electrolysis fuel electrode and oxygen electrodes gas compositions at 750 °C.

In spite of a small difference on the maximum injected current density, I-V polarization curves measured under different co-electrolysis fuel electrode gas compositions and O<sub>2</sub> present the same OCV value, which is 0.88 V. These OCVs values are in concordance with the theoretically calculated ones according to the H<sub>2</sub>O, H<sub>2</sub> and CO<sub>2</sub>; as well as O<sub>2</sub> and N<sub>2</sub> proportions in each gas composition [8]. OCVs were calculated as 0.89 V for the two co-electrolysis gas compositions and O<sub>2</sub> atmosphere. However, the theoretical OCV value decreases to 0.86 V for the third measurement under 45 % H<sub>2</sub>O + 10 % H<sub>2</sub> + 45 % CO<sub>2</sub> and synthetic air, which is in concordance with the experimentally measured value of 0.87 V.

Current densities around 11 A were injected in these large area cells, achieving maximum current densities of  $-0.72 \text{ A/cm}^2$  for the first (45 %  $\text{H}_2\text{O}$  + 10 %  $\text{H}_2$  + 45 %  $\text{CO}_2$ ) and  $-0.74 \text{ A/cm}^2$  for the second (65 %  $\text{H}_2\text{O}$  + 10 %  $\text{H}_2$  + 25 %  $\text{CO}_2$ ) co-electrolysis atmospheres measured under  $\text{O}_2$  at 1.30 V. The I-V measured under 45 %  $\text{H}_2\text{O}$  + 10 %  $\text{H}_2$  + 45 %  $\text{CO}_2$  and synthetic air presents lower performance than the measured with the same co-electrolysis fuel electrode atmosphere since  $-0.69 \text{ A/cm}^2$  was the maximum injected current density. As it can be seen, the maximum injected current density did not change significantly when both electrodes atmospheres were varied, showing a high fuel flexibility of the developed electrolyser.

However, obtained values reveal slightly different behaviours at high injected current densities, resulting on higher performance when electrochemical measurements were performed under 65 %  $\text{H}_2\text{O}$  + 10 %  $\text{H}_2$  + 25 %  $\text{CO}_2$  and  $\text{O}_2$  gas compositions. Besides, these results denote that higher performances are achieved when more proportion of  $\text{H}_2\text{O}$  is present on the inlet fuel electrode gas composition and  $\text{O}_2$  instead of synthetic air on the oxygen electrode chamber, confirming the trend observed testing different cells under electrolysis mode (**section 7.4.1**), and aligned with results already reported in the literature [24]. It is important to highlight that any diffusion issue was detected on these measurements when current densities as high as 11 A were injected to this large area cell. This demonstrates the feasibility of the proposed microstructure to fabricate SOEC electrodes, and operate on co-electrolysis mode even at fuel conversion values higher than 30%.

EIS measurements were performed on co-electrolysis mode following the same gas composition than the I-V measured in **Figure 7.7** (45 %  $\text{H}_2\text{O}$  + 10 %  $\text{H}_2$  + 45 %  $\text{CO}_2$  and 65 %  $\text{H}_2\text{O}$  + 10 %  $\text{H}_2$  + 25 %  $\text{CO}_2$  co-electrolysis compositions and,  $\text{O}_2$  and synthetic air atmospheres) to identify the electrochemical processes contributing to the final resistance of each electrode when the gas compositions are changed. Presented Nyquist arcs were recorded at OCV in galvanostatic mode at the operation temperature of 750 C, and the obtained results are presented in **Figure 7.8a**. The three measured Nyquist plots have similar shape. Unexpected variations on the serial resistances are observed when the oxygen electrode gas composition was changed between  $\text{O}_2$  and synthetic air, as it was also detected in the results discussed on the

previous **section 7.3.1** for the measurements performed under electrolysis atmosphere. According with the Bode plot (**Figure 7.8b**), the polarization resistance contribution of each Nyquist plot is given by three arcs: one arc at high frequencies ( $\approx 10^3$  Hz), followed by a smaller one at frequencies of  $\approx 10^2$  Hz, and a larger one at lower frequencies ( $\approx 1$  Hz).

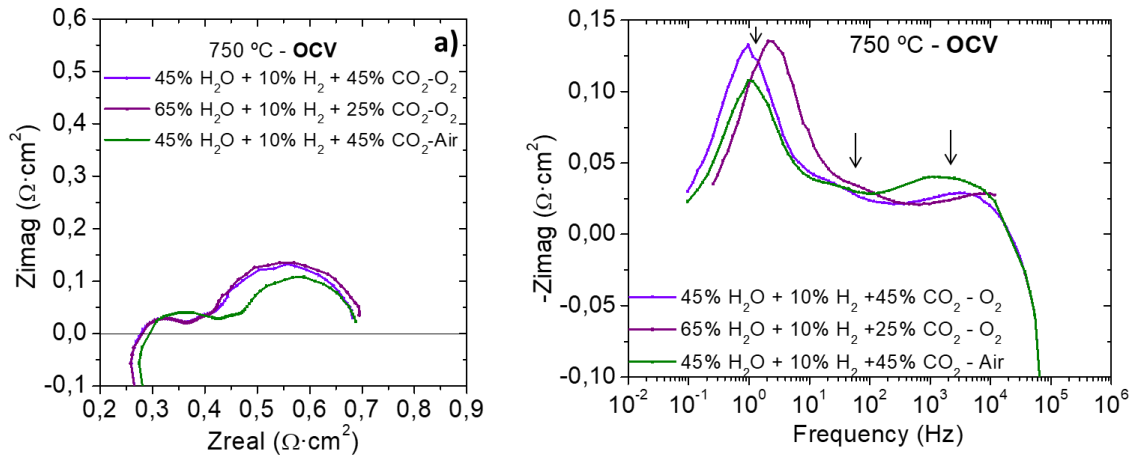


**Figure 7.8:** Nyquist (a) and Bode (b) plot measured at OCV for large area cells under two different co-electrolysis fuel electrode gas compositions and two oxygen electrode ones.

Nyquist plots recorded under both co-electrolysis atmospheres were fitted by the same equivalent circuit,  $LR_s(R_{p1}Q_1)(R_{p2}Q_2)(R_{p3}Q_3)$ . As, in previous reported fittings, L is the inductance affected by the test station set-up,  $R_s$  is mainly controlled by the electrolyte ionic and contact resistances; and RQ, composed by a resistance R and a constant phase element Q in parallel, represent the electrodes polarization resistances contribution presented in form of arcs or semicircles in the Nyquist plots [7]. The fitted values are presented in **Table 7.5** for different gas compositions, which allows determining the different electrochemical processes in charge of the measured resistances, and also identifying the responsible mechanism for each contribution.

	45% $H_2O$ +10% $H_2$ +45% $CO_2/O_2$	65% $H_2O$ +10% $H_2$ +25% $CO_2/O_2$	45% $H_2O$ +10% $H_2$ +45% $CO_2/Air$
$R_s$ ( $\Omega \cdot cm^2$ )	$2.4 \cdot 10^{-1}$	$2.4 \cdot 10^{-1}$	$2.4 \cdot 10^{-1}$
$R_{p1}$ ( $\Omega \cdot cm^2$ )	$1.0 \cdot 10^{-1}$	$1.0 \cdot 10^{-1}$	$1.9 \cdot 10^{-1}$
$C_{p1}$ (F/ $cm^2$ )	$1.7 \cdot 10^{-4}$	$1.6 \cdot 10^{-4}$	$2.2 \cdot 10^{-4}$
$n_1$	0.71	0.67	0.49
f max (Hz)	$9.0 \cdot 10^3$	$9.3 \cdot 10^3$	$3.7 \cdot 10^3$
$R_{p2}$ ( $\Omega \cdot cm^2$ )	$1.8 \cdot 10^{-1}$	$2.1 \cdot 10^{-1}$	$1.1 \cdot 10^{-1}$
$C_{p2}$ (F/ $cm^2$ )	$1.6 \cdot 10^{-1}$	$4.0 \cdot 10^{-1}$	$3.8 \cdot 10^{-1}$
$n_2$	0.40	0.36	0.48
$R_{p3}$ ( $\Omega \cdot cm^2$ )	$1.9 \cdot 10^{-1}$	$1.9 \cdot 10^{-1}$	$1.5 \cdot 10^{-1}$
$C_{p3}$ (F/ $cm^2$ )	$8.4 \cdot 10^{-1}$	$8.6 \cdot 10^{-1}$	$9.0 \cdot 10^{-1}$
$n_3$	1.00	1.00	1.00
f max (Hz)	$9.9 \cdot 10^{-1}$	$9.6 \cdot 10^{-1}$	1.2
ASR ( $\Omega \cdot cm^2$ )	0.71	0.74	0.69

**Table 7.5:** Results from fitting with  $LR_s(R_{p1}Q_1)(R_{p2}Q_2)(R_{p3}Q_3)$  equivalent circuit EIS data recorded at OCV for large area cells measured on co-electrolysis mode at 750 °C. Here,  $C_p$  represents the true capacitance calculated as  $C_p=(Q)^{(1/n)}R_{p1}^{(1-n/n)}$ .

As it is indicated in **Figure 7.9**, in concordance with the values presented in **Table 7.5**,  $R_{p1}$  is identified as a charge transfer processes occurring on the CGO-LSCF oxygen electrode at high frequencies, while  $R_{p2}$  and  $R_{p3}$  are caused by non-charge transfer processes taking place in the Ni-YSZ fuel electrode at lower frequencies [18,21-23]. Specifically,  $R_{p2}$  present a mass diffusion-like shape (corresponding to a CPE with  $n=0.45$ ), and  $R_{p3}$  is attributable to gas diffusion process (typically represented with a pure capacitance,  $n=1$ ). This analysis fits with the conclusions obtained from the electrolysis study on the same SOEC cells.

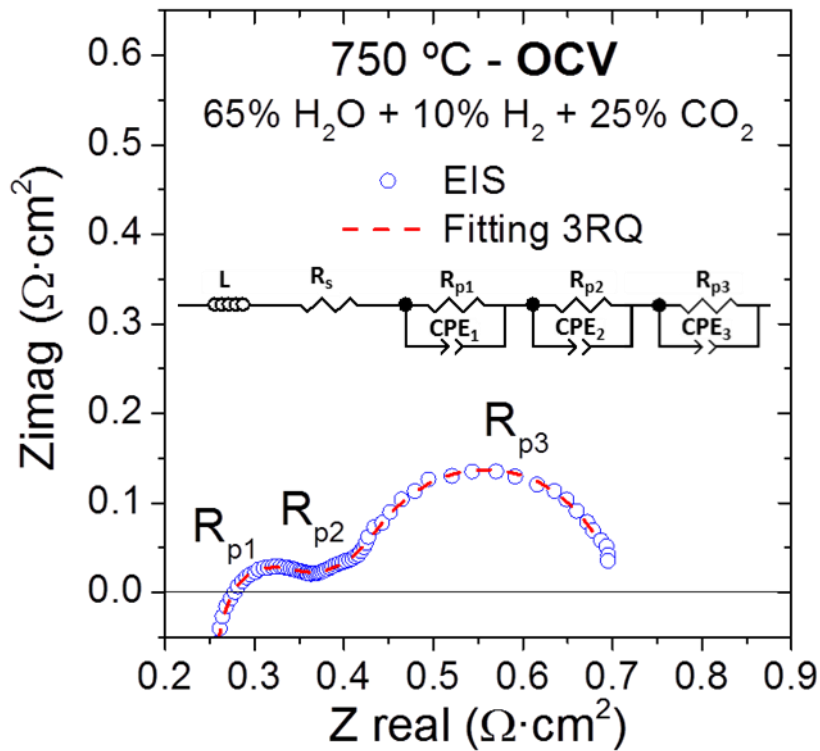


**Figure 7.9:** Nyquist plot measured at OCV for large area cells and fitted with the  $LR_s(R_{p1}Q_1)(R_{p2}Q_2)(R_{p3}Q_3)$  equivalent circuit. The resistances associated to each arc of the Nyquist plot have been identified.

Overall ASR values of 0.57 and 0.63  $\Omega\cdot\text{cm}^2$  are determined under  $\text{O}_2$  and synthetic air oxygen electrode atmospheres, respectively, for the co-electrolysis 45 %  $\text{H}_2\text{O}$  + 10 %  $\text{H}_2$  + 45 %  $\text{CO}_2$  measurements. In concordance with the trend observed in **Figure 7.7**, the I-V polarization curve measured under 65 %  $\text{H}_2\text{O}$  + 10 %  $\text{H}_2$  + 25 %  $\text{CO}_2/\text{O}_2$  presents the lowest overall ASR value, calculated as 0.56  $\Omega\cdot\text{cm}^2$ .

#### 7.4. Results of the long-term operation test on large area SOECs

##### 7.4.1. Electrochemical characterization and performance

The Ni-YSZ fuel electrode-supported cells with mesoporous CGO-LSCF based oxygen electrode were evaluated under co-electrolysis mode with 65 %  $\text{H}_2\text{O}$  + 10 %  $\text{H}_2$  + 25 %  $\text{CO}_2$  fuel composition and  $\text{O}_2$  on the oxygen electrode side. The operation temperature was maintained at 750 °C, and a galvanostatically controlled current density of -0.5  $\text{A}/\text{cm}^2$  (8 A) was injected. The evolution of the voltage during the long-term test recorded on galvanostatic operation mode is presented in **Figure 7.12**. A degradation rate of 12.18 %/kh was recorded along 600 h of continuous operation, exceeding 1.4 V during the last 100 h of operation. It is important to mention that the cell employed for this long-term test was prior operated during 300 h for carrying out the

electrochemical characterization, i.e. was operated under extreme conditions (especially those imposed by the complete I-V curves recorded).

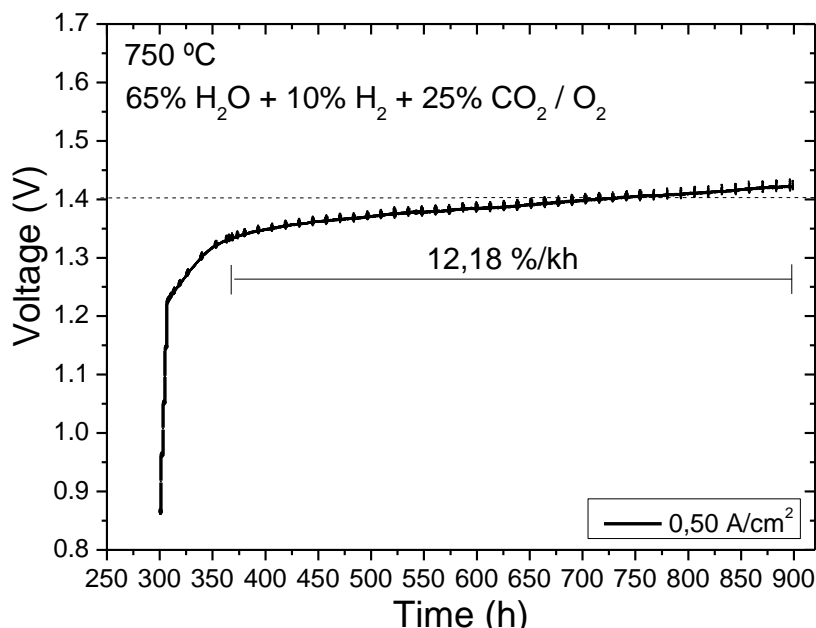


**Figure 7.12:** Long-term voltage evolution measured for a long area cell on co-electrolysis mode (65% H<sub>2</sub>O + 10% H<sub>2</sub> + 45% CO<sub>2</sub>/O<sub>2</sub> gas compositions) under -0.5 A/cm<sup>2</sup> injected current densities for 600 h of continuous operation.

EIS measurements on continuous operation at -0.5 A/cm<sup>2</sup> were recorded every hour for analysing the electrochemical processes contributing to the increase of the degradation rate. Nyquist and Bode plots of the EIS measurements recorded at 300, 600 and 900 h along the operation time are presented in **Figure 7.13** for analysing its evolution. An evolution of the serial and polarization resistances are observed along the continuous operation on co-electrolysis mode (**Figure 7.13a**). From the different Bode plots presented in **Figure 7.13b**, it is observed that the arcs appearing at lower ( $\approx 1$  Hz) and higher ( $\approx 10^4 - 10^5$  Hz) frequencies maintain similar resistance contribution while the one measured at intermediate frequencies ( $\approx 10^1 - 10^3$  Hz) increase its contribution with the operation time.

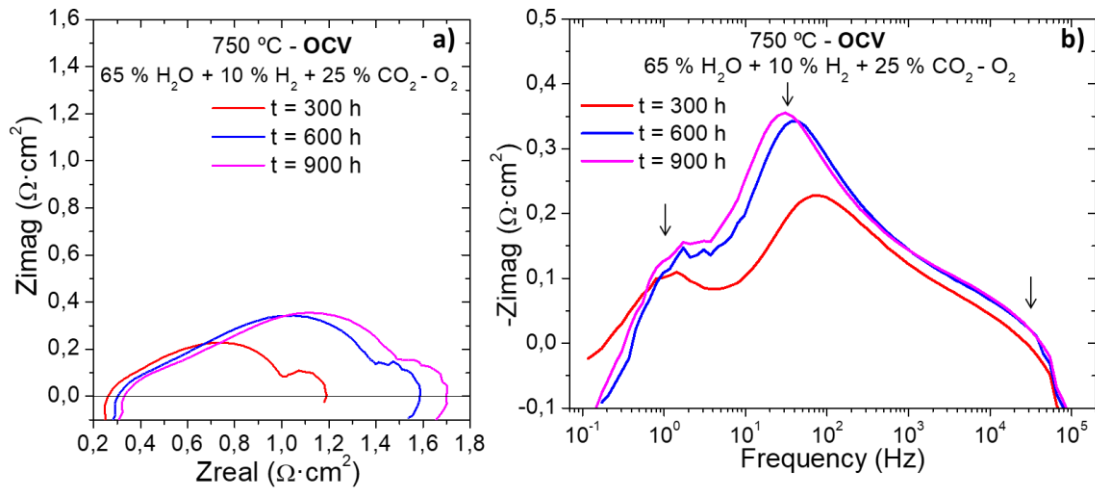


**Figure 7.13:** Nyquist (a) and Bode (b) plots of EIS measurements recorded at 300 (beginning of the experiment), 600 and 900 h under co-electrolysis mode injecting current densities of  $-0.5 \text{ A/cm}^2$  at  $750 \text{ }^\circ\text{C}$  on continuous operation.

The contribution of each electrochemical process to the overall resistance was analysed employing an equivalent circuit. The impedance spectroscopies (EIS) measured on galvanostatic mode under  $-0.5 \text{ A/cm}^2$  of injected current density along the long-term operation were fitted applying the same  $LR_s(R_{p1}Q_1)(R_{p2}Q_2)(R_{p3}Q_3)$  equivalent circuit than before. The values of different parameters obtained from fitting each EIS measurement with the detailed equivalent circuit are presented in **Table 7.7**.

	t = 300 h	t = 600 h	t = 900 h
$R_s (\Omega \cdot \text{cm}^2)$	2.0E-01	2.3E-01	2.5E-01
$R_{p1} (\Omega \cdot \text{cm}^2)$	3.8E-01	6.6E-01	7.5E-01
$C_{p1} (\text{F/cm}^2)$	5.4E-03	6.8E-03	6.7E-03
$n_1$	0.88	0.87	0.84
f max (Hz)	7.62E+01	3.56E+01	3.17E+01
$R_{p2} (\Omega \cdot \text{cm}^2)$	4.6E-01	5.6E-01	5.6E-01
$C_{p2} (\text{F/cm}^2)$	5.6E-04	3.7E-04	2.1E-04
$n_2$	0.45	0.45	0.45
$R_{p3} (\Omega \cdot \text{cm}^2)$	1.5E-01	1.4E-01	1.4E-01
$C_{p3} (\text{F/cm}^2)$	1.1	8.6E-01	8.8E-01
$n_3$	1.00	1.00	1.00
f max (Hz)	1.0	1.3	1.3
ASR ( $\Omega \cdot \text{cm}^2$ )	1.2	1.6	1.7

**Table 7.7:** Results from fitting with an equivalent circuit including a transmission line element EIS data recorded at 300, 600 and 900 h under  $-0.5 \text{ A/cm}^2$  for large area cells measured on co-electrolysis mode

at 750 °C. Here  $R_s$  values are suitable with Nyquist plots, and  $C_p$  represents the true capacitance calculated as  $C_p = (Q)^{(1/n)} R_{p1}^{(1-n/n)}$ .

First, a slight increase of the serial resistance ( $R_s$ ) is noticed during the accumulated operation time. This can be attributed to the evolution of the barrier layer-mesoporous scaffold interface and current collectors during the long operation time (as it has been previously noticed on electrolysis and co-electrolysis measurements presented in **sections 7.3.1** and **7.3.2**). However, the polarization resistance is the main contribution to the overall total resistance (ASR) of the cell. The characteristic capacitance and frequency values obtained from the fitting confirm that the charge transfer processes are the main contributions to the  $R_{p1}$ , mainly caused by the oxygen electrode, as previously discussed [7,24,27-29]. Moreover, a continuous increase of the initial small resistance observed at intermediate frequencies ( $\approx 10^1 - 10^3$  Hz) is clearly observed from the Nyquist and Bode plots (**Figure 7.13**). Taking into account the characteristic frequency and the previous analysis, the contribution of  $R_{p2}$  is attributed to the fuel electrode. More specifically, this arc presents a mass diffusion-like shape ( $n=0.45$ ), typically caused by a mass transport controlled process such as an oxide ion diffusion. On the other hand,  $R_{p3}$  presents a more stable evolution. The characteristic frequencies and capacitances of  $R_{p3}$  suggests that the associated process has an origin in the gas diffusion limitations occurring at the fuel electrode level [18,21-24]. This process is typically represented as a pure capacitance ( $n=1$ ).

All in all, the major degradation of these cells could be attributed to the appearance of mass and gas transport limitations in the fuel electrode. This clearly indicates an evolution of the microstructure to a more closed structure with major issues in the oxygen diffusion pathway in the Ni-YSZ composite (likely caused by Ni migration).

#### **7.4.2. Post-test microstructural characterization**

The large area cell ( $16 \text{ cm}^2$ ), characterized on co-electrolysis modes for almost 1000 h, was structurally characterized by SEM coupled to Energy Dispersive X-Ray (EDX) analysis after injecting a maximum current density of 11 A ( $-0.74 \text{ A/cm}^2$ ), and continuous operation under  $-0.5 \text{ A/cm}^2$  for 600 h. The post-test characterization aims studying the state of the microstructure for establishing an explanation of the obtained electrochemical results after its long-term test operation.

Cross-section micrographs involving the electrolyte-oxygen electrode interface were recorded employing a SE2 at different magnifications and are showed in **Figure 7.14**. The cross-section microstructures presented in **Figure 7.14a** allows distinguishing the dense YSZ electrolyte, a porous and thin CGO barrier layer, a CGO-LSCF infiltrated mesoporous scaffold as functional layer and on the top a thicker commercial LSCF electrode layer. It can be clearly observed different microstructures forming the oxygen electrode and the consolidated architecture of the electrode, which validates the applied fabrication approach. A higher magnification micrograph of the CGO barrier layer and the CGO-LSCF infiltrated mesoporous functional layer interface is presented in **Figure 7.14b**. That micrograph presents a CGO-LSCF functional layer mainly attached to the CGO barrier layer and properly connected to the LSCF microstructure. However, a lack of homogeneity of the mesoporous scaffold (CGO-LSCF functional layer) deposited on top of the barrier layer is observed. The densification of the CGO barrier layer is also needed for improving the SOEC performance.

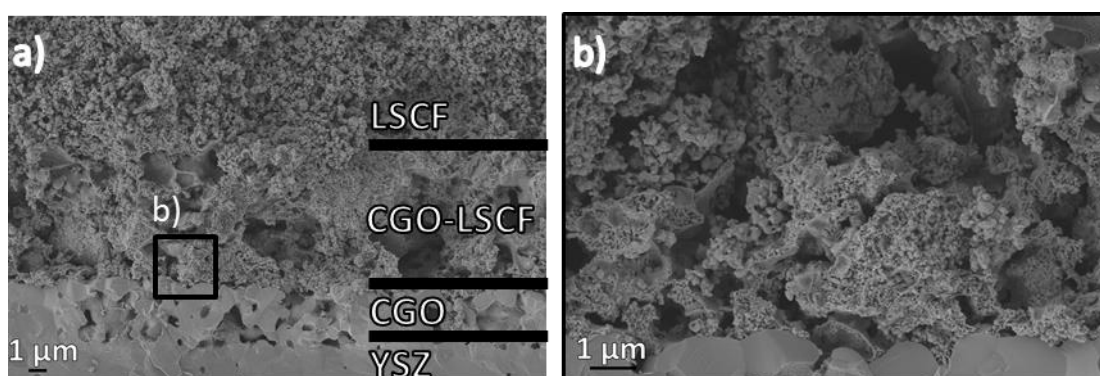


**Figure 7.14:** (a) SEM cross-section micrograph of the electrolyte-oxygen electrode interface microstructure after almost 1000 h of electrochemical characterization under different electrolysis and co-electrolysis gas compositions and  $O_2$ . Micrograph (b) is presented as a zoom of (a) focused on the electrolyte-CGO-LSCF functional layer interface.

The characterization of the CGO-LSCF nanocomposite was performed by SEM coupled to EDX. Coupling the analysis of both techniques allowed validating the infiltration of the mesoporous scaffold and its stability after the long operation time under co-electrolysis mode. The aim of this analysis is to identify the oxygen electrode region occupied by each element. **Figure 7.15a** show the cross-section oxygen electrode micrograph taken as reference for analysing the elements distribution; and **7.15b**, **7.15c** and **7.15d** the mappings obtained for lanthanum (La), cerium (Ce) and

zirconium (Zr), respectively. La is studied as representative element of the LSCF compound, which was employed for infiltrating the deposited CGO mesoporous material and as an electrode; Ce represents the CGO compound used as barrier layer and as mesoporous scaffold, and Zr is the main element of the YSZ electrolyte. Those micrographs show a main lanthanum distribution in the upper area as well as a minor density in the cerium area corresponding to the CGO mesoporous scaffold (**Figure 7.15**). A higher density of cerium (**Figure 7.15c**) is presented in a band corresponding to CGO barrier layer, which is located on top of the area corresponding to the YSZ electrolyte according to **Figure 7.15d**. This analysis confirms the prevalent infiltration of the mesoporous scaffold after an exhaustive electrochemical characterization under different fuel and oxygen electrodes gas compositions on electrolysis and co-electrolysis modes for 300 h and its continuous operation under  $-0.5 \text{ A/cm}^2$  injected current density for 600 h.

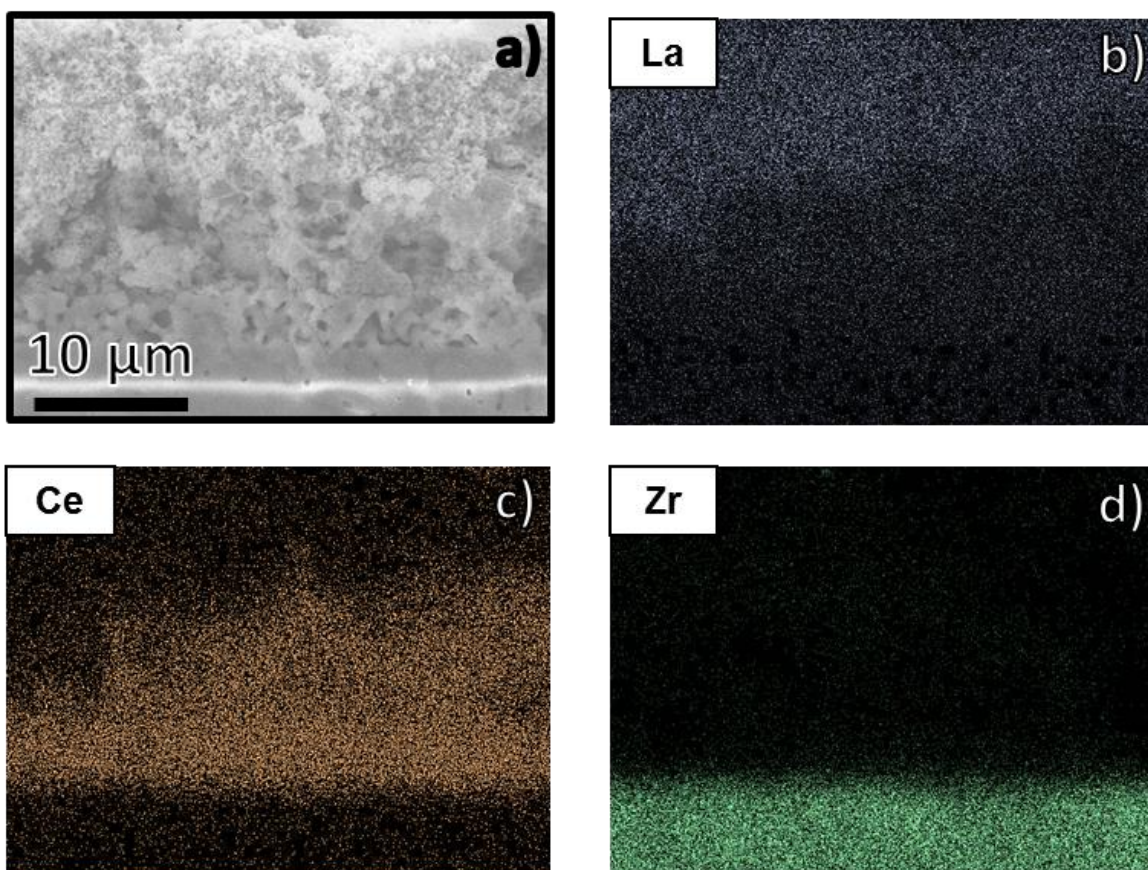


**Figure 7.15:** (a) Reference micrograph of the oxygen electrolyte/oxygen electrode interface after almost 1000 h of electrochemical characterization under different condition at 750 °C, and EDX mappings of La (b), Ce (c) and Zr (d) as representative elements of LSCF, CGO and YSZ compounds.

The results presented in **Figure 7.14** and **7.15** demonstrate the feasibility of infiltrating mesoporous materials for fabricating oxygen electrodes. Despite the inhomogeneity of the mesoporous scaffold observed by post-mortem SEM characterization (**Figure 7.14**), **Figure 7.15** confirms the successful infiltration of the mesoporous scaffold and its stability for long operation times.

The Ni-YSZ fuel electrode and its interface with the YSZ electrolyte was also studied by SEM. **Figure 7.16** shows two different micrographs recorded employing different SEM detectors. **Figure 7.16a** was recorded employing a SE2, which allows observing the microstructure and topography of the fuel electrode and its interface. Although it shows a homogeneous porous microstructure properly attached to the electrolyte, it is remarkable the small size of the porosity, which could be in the origin of the presence of a gas diffusion arc in the impedance spectra. The micrograph presented in **Figure 7.16b** presents a micrograph taken by an InLens detector at low voltage ( $\approx 2$  kV). This detector highlights in bright colour the electronic pathway corresponding to the Ni component of the Ni-YSZ electrode [25]. Accordingly, a substantial part of the Ni can be considered non-percolating. This observation could be in the origin of the increasing electrochemical resistances associated to the fuel electrode in the degradation experiments.

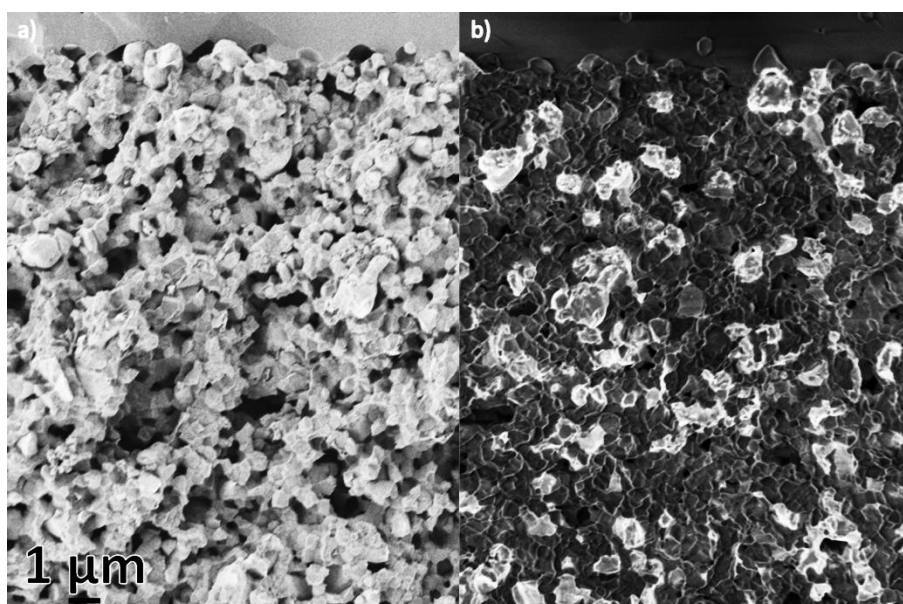


**Figure 7.16:** SEM cross-section micrographs of the YSZ electrolyte/Ni-YSZ fuel electrode interface recorded employing (a) SE2 and (b) Low voltage and InLens detectors after a long electrochemical characterization of the SOEC cell.

### 7.5. Comparison of the performance of fuel electrode-supported cells (button- and large area cells)

As a summary of the obtained results, the performance of button and large area cells on co-electrolysis mode are compared in this section. For this comparison, the total polarization resistance ( $R_{pTOT}$ ) associated to the electrodes performance in button cells are calculated as the sum of  $R_{p1}$ ,  $R_{p2}$  and  $R_{p3}$ , and as the sum of  $R_{p1}$ ,  $R_1$  and  $R_3$  for large area cells. Specifically, the total contribution of the polarization resistance recorded for different oxygen electrodes, cells sizes and gas compositions measured on co-electrolysis mode are presented in the **Table 7.8**. The button cells values compared in this section have been previously presented in this thesis.

The resistance values presented in **Table 7.8** are in good agreement with the evolution of the performance reported along this thesis, even when different equivalent circuits were used for fitting each impedance. As it is expected, a drop on the cell performance is detected on larger area cells.

Co-Electrolysis		
Oxygen electrode	CGO-LSCF	CGO-LSCF
Fuel gas composition	45% H <sub>2</sub> O + 45% CO <sub>2</sub> +10% H <sub>2</sub> / Air	45% H <sub>2</sub> O + 45% CO <sub>2</sub> +10% H <sub>2</sub> / Air
Cell size	Button	Large area
$R_{p1}$ ( $\Omega \cdot \text{cm}^2$ )	$7.6 \cdot 10^{-2}$	$1.9 \cdot 10^{-1}$
$R_{p2}$ ( $\Omega \cdot \text{cm}^2$ )	$1.6 \cdot 10^{-1}$	$1.1 \cdot 10^{-1}$
$R_{p3}$ ( $\Omega \cdot \text{cm}^2$ )	---	$1.5 \cdot 10^{-1}$
$R_{pTOT}$ ( $\Omega \cdot \text{cm}^2$ )	$2.4 \cdot 10^{-1}$	$4.5 \cdot 10^{-1}$

**Table 7.8:** Polarization resistance contributions measured for different oxygen electrodes under co-electrolysis atmospheres on different cell sizes. Results from button cells have been presented on previous chapters.

Focusing the comparison on CGO-LSCF fabricated cells characterized under the same co-electrolysis gas composition (45% H<sub>2</sub>O + 45% CO<sub>2</sub> +10% H<sub>2</sub>/Air), it is stated a major contribution of the polarization resistance ( $R_{pTOT}$ ) on large area than on button Ni-YSZ fuel electrode-supported cells. Results obtained from the electrochemical characterization of both cells are presented in **Figure 7.12**. That difference on the polarization resistance is evidenced in **Figure 7.12b**, which can be explained by the scaling up issues during the fabrication of large area cells. An important difference in the serial resistance is also shown between button and large area cells. Besides from the

attachment of the mesoporous scaffold to the barrier layer during the fabrication process, it is important to take in account that CGO barrier layers of both sizes cells were fabricated applying different methods (PLD in the case of the button cell and screen printing on large area cells), what could have had influence on the overall cell performance, as showed in **Figure 7.12a**, and specifically, on the ohmic resistance contribution. The current collection is also more difficult for large areas, which could suppose an increase of the  $R_s$ .

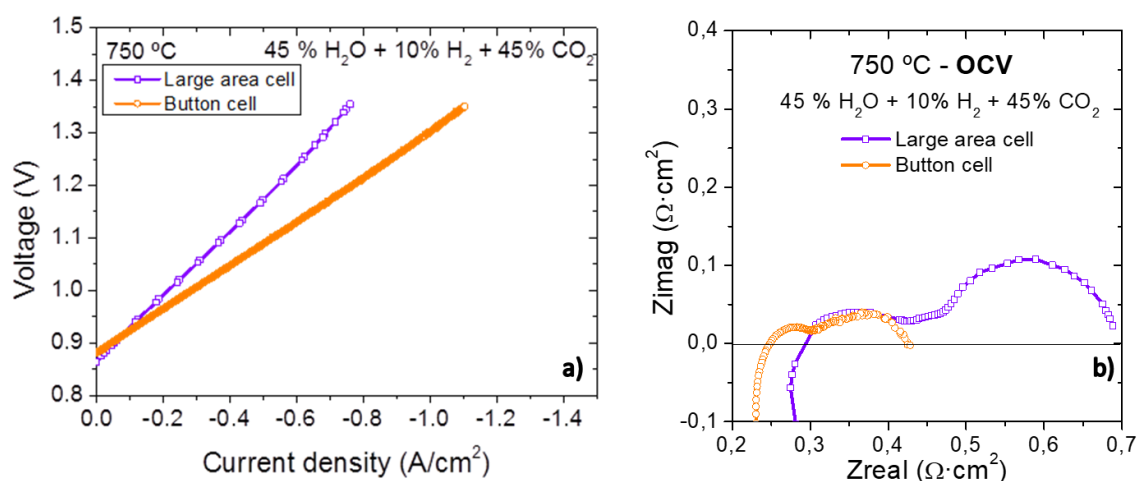


**Figure 7.17:** I-V polarization curves (a) and Nyquist plots at OCV (b) comparing button and large area cells measured under the same co-electrolysis (45% H<sub>2</sub>O + 10% H<sub>2</sub> + 45% CO<sub>2</sub>) gas composition at 750 °C.

At the light of the obtained results, it is possible to conclude the success in employing mesoporous oxygen electrodes and their suitability for scaling in large areas. However, it is also clear that further improvements are required to optimize the scaling process in order to reproduce the excellent results obtained for button cells.

## 7.6. Conclusions

This chapter presents the successful fabrication and characterization of square SOEC cells of 25 cm<sup>2</sup> of area (16 cm<sup>2</sup> of active area) made of CGO-LSCF oxygen electrodes based on infiltrated mesoporous materials. The relation between the LSCF infiltrated volume employed during the oxygen electrode fabrication procedure and the resulting microstructure was analysed by SEM showing that higher LSCF volumes induce the formation of undesirable cave-like microstructures. It is concluded that the infiltrating volume plays an important role on the fabrication of a good functional layer microstructure.

Large area cells were electrochemically characterized at 750 °C under different fuel and oxygen electrode gas compositions on electrolysis and co-electrolysis mode. I-V polarization curves evaluated the performance of the measured cell, while EIS measurements recorded at OCV were analysed for identifying the electrochemical processes contributing to the polarization cell resistance.

I-V polarization curves were measured on electrolysis mode under 20% H<sub>2</sub>O + 80% H<sub>2</sub>O and 50 % H<sub>2</sub>O + 50% H<sub>2</sub>O fuel electrode gas compositions and O<sub>2</sub> and synthetic air oxygen electrodes gas compositions, showing high fuel flexibility. The highest performance, injecting a maximum current density of -0.80 A/cm<sup>2</sup> was measured under the 50% H<sub>2</sub>O + 50% H<sub>2</sub>O-O<sub>2</sub> atmosphere. This result allows concluding that higher performances are obtained under high steam proportion on the fuel electrode atmosphere, and pure O<sub>2</sub> on the oxygen electrode atmosphere. The analysis of the Nyquist plots recorded at OCV under the same gas compositions identifies a charge transfer process related to the oxygen electrode at higher frequencies, and non-charge transfer processes located at low frequencies as main contribution of the fuel electrode resistance.

The electrochemical characterization on co-electrolysis mode was performed under 45% H<sub>2</sub>O + 10% H<sub>2</sub> + 45% CO<sub>2</sub> and 65% H<sub>2</sub>O + 10% H<sub>2</sub> + 25% CO<sub>2</sub> fuel electrode gas compositions; and O<sub>2</sub> and synthetic air atmospheres on the oxygen electrode. Although high fuel flexibility and stability are deduced from the I-V curve measured on co-electrolysis mode, a maximum current density of -0.82 A/cm<sup>2</sup> was injected on large area cells characterized under 65% H<sub>2</sub>O + 10% H<sub>2</sub> + 25% CO<sub>2</sub>-O<sub>2</sub> fuel and oxygen atmospheres. The analysis of impedance spectroscopy measurements shows the existence of a charge transfer process contributing to the oxygen electrode resistance. Besides, it was concluded that resistances associated to non-charge transfer processes at the fuel electrode dominate the overall resistance.

The feasibility of applying the proposed procedure for the fabrication of oxygen electrodes on large area cells was confirmed by a long operation test performed on co-electrolysis mode under -0.5 A/cm<sup>2</sup> for 600 h. EIS analysis concluded that the major contribution to the degradation of the cells was associated to mass- and gas diffusion-limiting processes occurring in the fuel electrode. The origin of this degradation seems

to be related with a loss of percolation of the Ni in the Ni-YSZ electrode (by Ni migration processes taking place in the operating conditions).

The large area cell operated for 600 h under co-electrolysis composition were microstructurally characterized by SEM coupled to EDX. SEM micrographs show a post-mortem oxygen electrode microstructure where is possible identifying each of its constituting layers. Besides, SEM coupled to EDX validates the prevalent infiltration of the mesoporous scaffold together with a certain inhomogeneity of the mesoporous scaffold. The microstructural characterization of the Ni-YSZ electrode shows the presence of non-percolating Ni caused by the co-electrolysis operation (or the initial electrochemical characterization of the cells).

Finally, a qualitative comparison of fuel electrode-supported button and large area cells, with CGO-LSCF fabricated oxygen electrodes, and characterized under the same co-electrolysis gas compositions have been presented, proving the reproducibility of the method for fabricating oxygen electrodes on different size cells. However, different resistance values have been obtained from the electrochemical characterization. It is concluded that these differences are related to the challenge and difficulties associated to the fabrication of the CGO-LSCF oxygen electrode on large area cells; and evidences the need of optimizing this fabrication process on large area cells for obtaining higher performing cells.

## 7.7. References

- [1] "DTU Energy." [Online]. Available: <http://www.energy.dtu.dk/english>.
- [2] "ECo project." [Online]. Available: <http://www.eco-soec-project.eu/>.
- [3] "HTceramix S.A." [Online]. Available: <http://www.solidpower.com/en/about-us/locations/>.
- [4] "Print3D Solutions." [Online]. Available: <http://print3dsolutions.net/la-empresa/equipos/>.
- [5] L. Almar *et al.*, "A Durable Electrode for Solid Oxide Cells: Mesoporous Ce<sub>0.8</sub>Sm<sub>0.2</sub>O<sub>1.9</sub> Scaffolds Infiltrated with a Sm<sub>0.5</sub>Sr<sub>0.5</sub>CoO<sub>3-δ</sub> Catalyst," *Electrochim. Acta*, vol. 235, pp. 646–653, 2017.
- [6] M. Torrell, L. Almar, A. Morata, and A. Tarancón, "Synthesis of mesoporous nanocomposites for their application in solid oxide electrolyser cells: microstructural and electrochemical characterization," *Faraday Discuss.*, vol. 182, pp. 423–435, 2015.
- [7] A. Nechache, M. Cassir, and A. Ringuedé, "Solid oxide electrolysis cell analysis by means of electrochemical impedance spectroscopy: A review," *J. Power Sources*, vol. 258, pp. 164–181, 2014.
- [8] L. Bernadet, J. Laurencin, G. Roux, D. Montinaro, F. Mauvy, and M. Reytier, "Effects of Pressure on High Temperature Steam and Carbon Dioxide Co-electrolysis," *Electrochim. Acta*, vol. 253, pp. 114–127, 2017.
- [9] A. Brisse, J. Schefold, and M. Zahid, "High temperature water electrolysis in solid oxide cells," *Int. J. Hydrogen Energy*, vol. 33, pp. 5375–5382, 2008.
- [10] A. V. Virkar, "Mechanism of oxygen electrode delamination in solid oxide electrolyzer cells," *Int J Hydrog. Energ*, vol. 35, pp. 9527–9543, 2010.
- [11] J. T. S. Irvine, D. Neagu, M. C. Verbraeken, C. Chatzichristodoulou, C. Graves, and M. B. Mogensen, "Evolution of the electrochemical interface in high-temperature fuel cells and electrolyzers," *Nat. Energy*, vol. 1, pp. 1–13, 2016.
- [12] P. Moçoteguy and A. Brisse, "A review and comprehensive analysis of degradation mechanisms of solid oxide electrolysis cells," *International Journal of Hydrogen Energy*, vol. 38, pp. 15887–15902, 2013.
- [13] T. Jacobsen and M. Mogensen, "The Course of Oxygen Partial Pressure and Electric Potentials across an Oxide Electrolyte Cell," *ECS Trans.*, vol. 13, no. 26, pp. 259–273, 2008.
- [14] R. Knibbe, M. L. Traulsen, A. Hauch, S. D. Ebbesen, and M. Mogensen, "Solid Oxide Electrolysis Cells: Degradation at High Current Densities," *J. Electrochem. Soc.*, vol. 157, no. 8, pp. B1209–B1217, 2010.
- [15] A. Nechache, M. Cassir, and A. Ringuedé, "Solid oxide electrolysis cell analysis by means of electrochemical impedance spectroscopy: A review," *Journal of Power Sources*, vol. 258, pp. 164–181, 2014.
- [16] S. H. Jensen, A. Hauch, P. V. Hendriksen, M. Mogensen, N. Bonanos, and T. Jacobsen, "A Method to Separate Process Contributions in Impedance Spectra

- by Variation of Test Conditions," *J. Electrochem. Soc.*, vol. 154, no. 12, pp. B1325–B1330, 2007.
- [17] J. C. Ruiz-Morales *et al.*, *Pilas de combustible de óxidos sólidos (SOFC)*, 2 nd. 2008.
- [18] H. Fan, M. Keane, N. Li, D. Tang, P. Singh, and M. Han, "Electrochemical stability of La<sub>0.6</sub>Sr<sub>0.4</sub>Co<sub>0.2</sub>Fe<sub>0.8</sub>O<sub>3-δ</sub>-infiltrated YSZ oxygen electrode for reversible solid oxide fuel cells," *Int. J. Hydrogen Energy*, vol. 39, pp. 14071–14078, 2014.
- [19] A. Lakki, R. Herzog, C. R. M. Weller H. Schubert, and M. K. G. B. O. Goërke, "Mechanical loss, creep, diffusion and ionic conductivity of ZrO<sub>2</sub>-8 mol%Y<sub>2</sub>O<sub>3</sub> polycrystals," *J. Eur. Ceram. Soc.*, vol. 20, pp. 285–296, 2000.
- [20] A. Hauch, S. D. Ebbesen, S. H. Jensen, and M. Mogensen, "Highly efficient high temperature electrolysis," *J. Mater. Chem.*, vol. 18, pp. 2331–2340, 2008.
- [21] R. Barfod, M. Mogensen, T. Klemensø, A. Hagen, Y.-L. Liu, and P. Vang Hendriksen, "Detailed Characterization of Anode-Supported SOFCs by Impedance Spectroscopy," *J. Electrochem. Soc.*, vol. 154, no. 4, pp. B371–B378, 2007.
- [22] L. dos Santos.Gómez, J. M. Porrás-Vázquez, E. . Losilla, F. Martín, J. R. Ramos-Barrado, and D. Marrero-López, "Stability and performance of La<sub>0.6</sub>Sr<sub>0.4</sub>Co<sub>0.2</sub>Fe<sub>0.8</sub>O<sub>3-d</sub> nanostructured cathodes with Ce<sub>0.8</sub>Gd<sub>0.2</sub>O<sub>1.9</sub> surface coating," *J. Power Sources*, vol. 347, pp. 178–185, 2017.
- [23] M. Shah and S. A. Barnett, "Solid oxide fuel cell cathodes by infiltration of La<sub>0.6</sub>Sr<sub>0.4</sub>Co<sub>0.2</sub>Fe<sub>0.8</sub>O<sub>3</sub> - δ into Gd-Doped Ceria," *Solid State Ionics*, vol. 179, pp. 2059–2064, 2008.
- [24] C. Graves, S. D. Ebbesen, and M. Mogensen, "Co-electrolysis of CO<sub>2</sub> and H<sub>2</sub>O in solid oxide cells: Performance and durability," *Solid State Ionics*, vol. 192, pp. 398–403, 2011.
- [25] A. Hauch, P. S. Jørgensen, K. Brodersen, and M. Mogensen, "Ni/YSZ anode - Effect of pre-treatments on cell degradation and microstructures," *J. Power Sources*, vol. 196, pp. 8931–8941, 2011.

# ***Chapter 8***

## *Conclusions*



## 8. Conclusions

This thesis was devoted to the implementation of mesoporous materials, characterized for their high surface area and stability at high temperatures, for the fabrication of highly performing Solid Oxide Electrolysis Cells (SOECs) electrodes on electrolysis and co-electrolysis modes. Experimental, technological and theoretical aspects were covered to attain this purpose. The most relevant achievements are listed below,

**Mesoporous electrodes materials** synthesis and characterization to validate the applied fabrication methods:

- **Mesoporous  $\text{Sm}_{0.2}\text{Ce}_{0.8}\text{O}_{1.9}$  (SDC),  $\text{Ce}_{0.8}\text{Gd}_{0.2}\text{O}_{1.9}$  (CGO) and NiO powders** were synthesised. The application of the Brunauer-Emmett-Teller (BET) method demonstrated the success of the hard-template method for obtaining surfaces areas as high as  $110 \pm 15$ ,  $97 \pm 2$  and  $72 \pm 9 \text{ m}^2/\text{g}$ , respectively. The Barrett-Joyner-Halenda (BJH) method demonstrated that it is possible to obtain the desired pore size by controlling the template hydrothermal temperature. Low-Angle X-Ray Diffraction (LA-XRD) and scanning and transmission microscopy (SEM and TEM) techniques confirmed the periodicity of the replicated mesoporous structure from the mesoporous silica template to named metal oxide replicas. The phase formation was confirmed by X-Ray Diffraction (XRD).
- **Mesoporous electrodes** were structurally characterized. The fabrication procedures applied for the functionalization of the mesoporous scaffolds forming SDC-SSC ( $\text{Sm}_{0.5}\text{Sr}_{0.5}\text{CoO}_{3-\delta}$ ), CGO-LSCF ( $\text{La}_{0.6}\text{Sr}_{0.4}\text{Co}_{0.2}\text{Fe}_{0.8}\text{O}_3$ ) and NiO-SDC electrodes based on mesoporous materials were approved by XRD measurements, demonstrating the compatibility and stability between the composite phases at the expected operating temperatures.
- Based on an optimization study of the attachment temperature of the mesoporous scaffold this was fixed at  $900 \text{ }^\circ\text{C}$ , establishing the basis for fabricating the SOEC cells.

The influence of the **cell configuration** on the SOEC performance was studied:

- **Electrolyte- and fuel electrode-supported** SOECs operating on electrolysis and co-electrolysis modes were also studied fabricating SDC-SSC infiltrated mesoporous oxygen electrodes. A maximum current density of  $-0.25 \text{ A/cm}^2$  was injected in electrolyte-supported cells at 1.3 V, while  $-0.83$  and  $-0.81 \text{ A/cm}^2$  were injected on electrolysis and co-electrolysis modes, respectively, on fuel electrode-supported cells at  $750 \text{ }^\circ\text{C}$ . Although the microstructural characterization revealed the need of optimizing the infiltration of the mesoporous scaffold during the oxygen electrode fabrication, it is clear that the limiting resistance comes from the thick electrolyte employed in ESCs, despite using an intermediate temperature alternative to YSZ, i.e. Scandia- Yterbia-doped zirconia. As a conclusion, the fuel electrode-supported configuration is considered more suitable in this range of temperatures.

The **oxygen electrode interface** was optimized comparing different Ni-YSZ/YSZ/CGO<sub>bl</sub>/CGO-LSCF/LSCF fuel electrode-supported cells based on screen printed and PLD deposited barrier layers. Moreover, the effect of employing mesoporous oxygen electrodes was also evaluated by comparing with SoA SOEC cells provided by HTCeramix/SolidPower (in the frame of the EU ECo project):

- Analysing the electrochemical performance on co-electrolysis mode at  $750 \text{ }^\circ\text{C}$ , a maximum current density of  $-0.55 \text{ A/cm}^2$  at 1.30 V was injected for the state-of-the-art (SoA) cells, while the injection of  $-0.64 \text{ A/cm}^2$  of oxygen electrodes based on mesoporous materials evidenced an increase of the performance. The introduction of the PLD barrier layers to the mesoporous oxygen electrode resulted on the injection of up to  $-1 \text{ A/cm}^2$ , which are the best performing SOECs in this thesis.
- The good interconnection of materials and the existence of active percolation pathways microstructurally characterized by low voltage SEM confirmed the enhancement of the electrochemical performance compared to SoA SOEC cells.

The **performance of optimized SOECs** was studied in co-electrolysis mode:

- The optimized SOEC cells accepted a current injection as high as  $-1.2 \text{ A/cm}^2$  at 1.4 V and  $750 \text{ }^\circ\text{C}$  under co-electrolysis mode conditions

(45% H<sub>2</sub>O + 45% CO<sub>2</sub> + 10% H<sub>2</sub> / Air). The stability of the infiltrated mesoporous functional layer has been validated during 1400 h of continuous operation. Degradation rates of 2%/kh and <1%/kh have been registered injecting current densities of 0.5 A/cm<sup>2</sup> and 0.75 A/cm<sup>2</sup>, respectively.

- The analysis of Electrochemical Impedance Spectroscopy (EIS) measurements allowed determining that the main source of degradation is the increase of the ohmic resistance. The post-mortem microstructural characterization has allowed attributing this electrochemical result to the loss of percolation detected in the electrolyte-fuel electrode interface. The continuous improvement of the CGO-LSCF oxygen electrode has been evidenced by the decrease of the degradation rates along the operation time.

Finally, optimized oxygen electrodes have been **scaled up to large area** cells:

- The electrochemical characterization on (co-)electrolysis mode at 750 °C has showed high fuel flexibility, recording a highest performance of -0.80 A/cm<sup>2</sup> under 50% H<sub>2</sub>O + 50% H<sub>2</sub>O-O<sub>2</sub> atmospheres and -0.82 A/cm<sup>2</sup> under 65% H<sub>2</sub>O + 10% H<sub>2</sub> + 25% CO<sub>2</sub>-O<sub>2</sub> atmospheres.
- The feasibility of applying mesoporous materials on large area fuel electrode-supported cells have been confirmed by a test performed for 600 h injecting a constant current density of -0.5 A/cm<sup>2</sup>.
- The post-mortem microstructural characterization showed the stability of the infiltration of the mesoporous scaffold, validating the proposed approach for fabricating mesoporous oxygen electrode functional layers on large area cells. However, the reported lower performance of these large area cells, compared to equivalent button cells, indicates that there is still room for further optimization, especially regarding the current collection.



# ***Appendix A***

*Resumen de la Tesis*



## A. Resumen de la Tesis

La necesidad de cambiar el modelo energético actual por un sistema basado en energías renovables ha tomado importancia en los últimos años debido a la existencia de problemas medioambientales directamente relacionados con el uso de combustibles fósiles. Las fuentes de energía renovables, al contrario que los sistemas energéticos tradicionales, se caracterizan por estar descentralizadas. Como consecuencia de ello, estas fuentes de energías hacen posible un sistema energético diversificado. Sin embargo, una de las principales desventajas de estos sistemas energéticos es que producen energía eléctrica de forma discontinua, lo cual genera un claro desajuste entre la generación y el consumo energético. Como consecuencia de ello, desarrollar tecnologías de almacenamiento de la energía eléctrica generada por fuentes de energía renovables es imprescindible. Entre las tecnologías que se están desarrollando para el almacenamiento de energía eléctrica, los electrolizadores de alta temperatura basados en óxidos sólidos (SOEC) se presentan como una tecnología prometedora (**Figura A.1**).

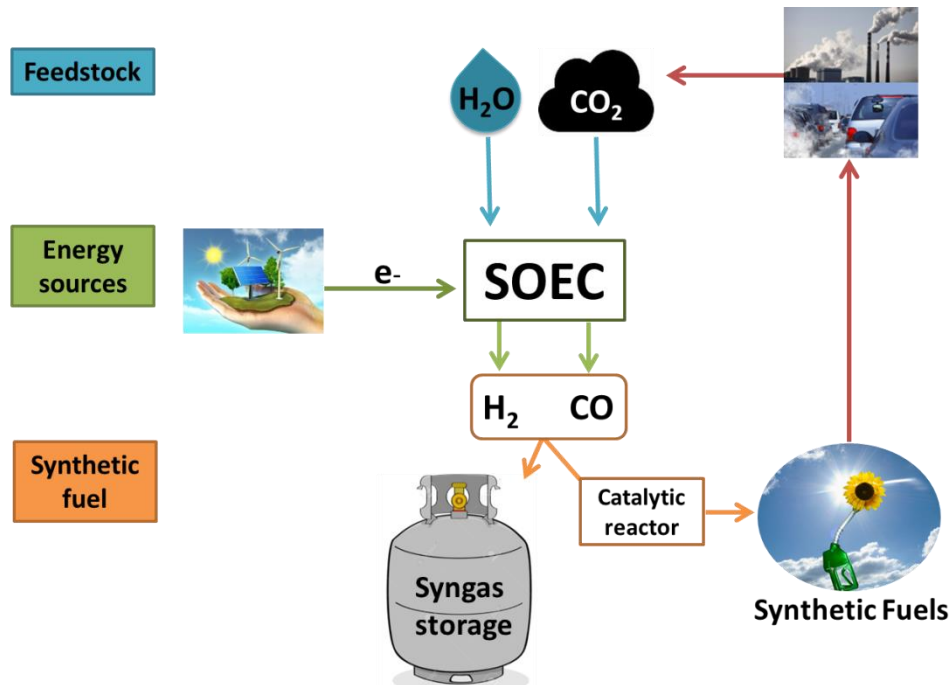


**Figura A.1:** Ciclo energético neutro en emisiones de CO<sub>2</sub> basado en el empleo de energías renovables y electrolizadores SOEC para la producción de combustibles químicos.

Alcanzando eficiencias mayores de un 85%, los electrolizadores SOEC permite convertir energía eléctrica en energía química mediante la reducción de las moléculas

de agua (H<sub>2</sub>O), dióxido de carbono (CO<sub>2</sub>), o la combinación de ambas; generándose hidrógeno (H<sub>2</sub>), monóxido de carbono (CO) o gas de síntesis (H<sub>2</sub> +CO) como producto (Figura A.2). El interés por desarrollar la tecnología SOEC está justificado si se consideran la posibilidad de usar el hidrógeno generado como combustible en pilas de combustible y la necesidad de transformar y reducir la cantidad de CO<sub>2</sub> que existe en la atmósfera.

### Solid Oxide Electrolysis Cell (SOEC)

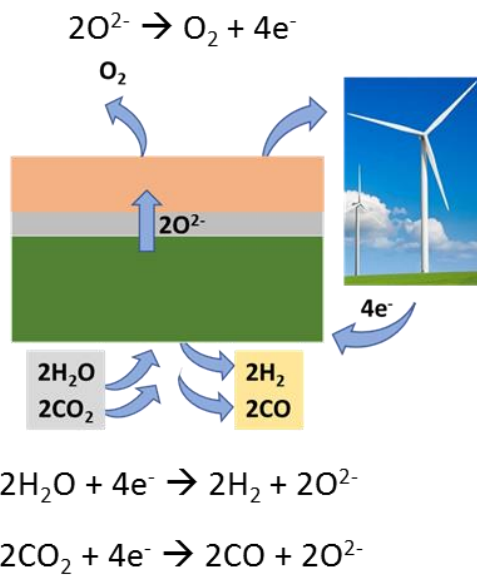


**Figura A.2:** Esquema del funcionamiento de los electrolizadores de alta temperatura basados en óxidos sólidos (SOEC)

Así, el aprovechamiento de la energía eléctrica proveniente de energías renovables por los electrolizadores de alta temperatura (SOEC), y la combinación de esta tecnología con las pilas de combustible, permitiría generar un ciclo cerrado de consumo y generación de energías con emisiones de carbono bajas o nulas.

De acuerdo con este escenario energético, el trabajo que se presenta en esta tesis tiene como objetivo mejorar el rendimiento de los electrolizadores SOEC. Para ello, la propuesta que se presenta está basada en utilizar óxidos metálicos mesoporosos, caracterizados por poseer alta área superficial y ser estables a altas temperaturas, en la fabricación de electrodos SOEC. Diferentes aspectos experimentales, tecnológicos y teóricos han sido tratados para conseguir el objetivo propuesto durante el desarrollo de esta tesis.

Esta tesis está organizada en ocho capítulos, los cuales son brevemente descritos a continuación:

El **capítulo 1** introduce el escenario energético actual, presentando los electrolizadores SOEC como una prometedora tecnología para almacenar energía eléctrica. De acuerdo con ello, los principios básicos del funcionamiento de la tecnología SOEC, así como el estado-del-arte de los materiales empleados para la fabricación de estos electrolizadores, son explicados. Por último se explica el marco en el que se sitúa esta tesis.

El **capítulo 2** describe los métodos experimentales y las técnicas empleadas a lo largo de esta tesis. Concretamente, se describen los procedimientos aplicados para la síntesis de materiales y para la fabricación de los electrodos. Esta sección también incluye las técnicas de caracterización aplicadas.

El **capítulo 3** de esta tesis presenta los resultados obtenidos a partir de la caracterización estructural de los materiales mesoporosos  $\text{Sm}_{0.2}\text{Ce}_{0.8}\text{O}_{1.9}$  (SDC),  $\text{Ce}_{0.8}\text{Gd}_{0.2}\text{O}_{1.9}$  (CGO) and NiO sintetizados aplicando el método del *hard-template*, y de los electrodos fabricados, que son SDC-SSC ( $\text{Sm}_{0.5}\text{Sr}_{0.5}\text{CoO}_{3-\delta}$ ), CGO-LSCF ( $\text{La}_{0.6}\text{Sr}_{0.4}\text{Co}_{0.2}\text{Fe}_{0.8}\text{O}_3$ ) and NiO-SDC. Diferentes técnicas de caracterización (fisorción de nitrógeno, difracción de rayos X a bajos ángulo-LA-XRD y microscopías) confirman que la estructura mesoporosa se ha transferido correctamente desde el molde (KIT-6) a las correspondientes réplicas, mostrando altas áreas superficiales y repetición periódica de la estructura mesoporosa (**Figura A.3**), así como la formación de la fase deseada.

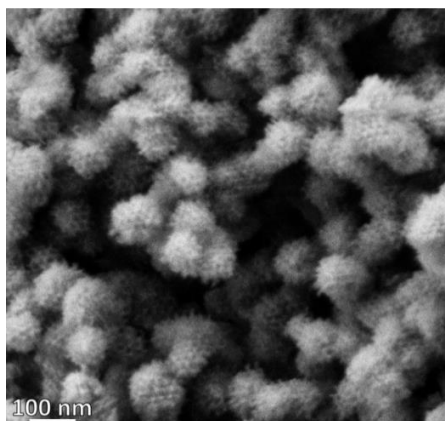


**Figura A.3:** Micrografía adquirida por microscopía electrónica de barrido (SEM) de NiO mesoporoso sintetizado empleando el método *hard-template*.

Los procedimientos aplicados para la funcionalización de los materiales mesoporosos también han sido validados mediante medidas de difracción de rayos X (XRD), demostrando la compatibilidad y estabilidad existente entre las fases a las típicas temperaturas de operación. Además, la temperatura de adhesión del material mesoporoso ha sido optimizada y se ha fijado a 900 °C.

El **capítulo 4** estudia dos configuraciones de electrolizadores operando en electrólisis y co-electrólisis. Con el objetivo de comparar ambas celdas, se ha fabricado el mismo SDC-SSC electrodo de oxígeno, basado en materiales mesoporosos. De acuerdo a la caracterización electroquímica llevada a cabo a 750 °C, densidades de corriente más altas fueron inyectadas en los electrolizadores soportados por el electrodo de combustible, alcanzando valores de  $-0.83$  y  $-0.81$  A/cm<sup>2</sup> operando en electrólisis y co-electrólisis, respectivamente; mientras que la máxima densidad de corriente inyectada por los electrolizadores cuyo soporte es el electrolito fue  $-0.25$  A/cm<sup>2</sup>. Los resultados presentados en este capítulo demuestran que el rendimiento de los electrolizadores soportados sobre el electrolito está limitado por la resistencia introducida por su grosor. En consecuencia, se considera que la configuración soportada en el electrodo de combustible es más apropiada para la fabricación de SOEC.

El **capítulo 5** presenta un estudio enfocado en analizar la influencia de la microestructura de la intercara del electrodo de oxígeno en el rendimiento de los electrolizadores SOEC. Para ello se comparan electrolizadores fabricados con los mismos materiales pero diferentes métodos de fabricación. Concretamente, se compara el rendimiento alcanzado cuando la barrera de difusión (CGO) ha sido depositada por *screen-printing* o mediante láser pulsado (PLD), así como la fabricación del electrodo de oxígeno (CGO-LSCF) por *screen printing* o por aerografía de materiales mesoporosos (**Figura A.4**). La caracterización electroquímica ha demostrado que la máxima densidad de corriente ( $-1$  A/cm<sup>2</sup>) ha sido inyectada por el electrolizador cuya barrera de difusión ha sido fabricada por PLD y la capa funcional del electrodo de oxígeno mediante aerografía de materiales mesoporosos, y su posterior infiltración con LSCF como material catalíticamente activo (*Cells\_PLD\_meso* en **Figura A.4**). Estos resultados son confirmados mediante la caracterización microestructural de dicha intercara.

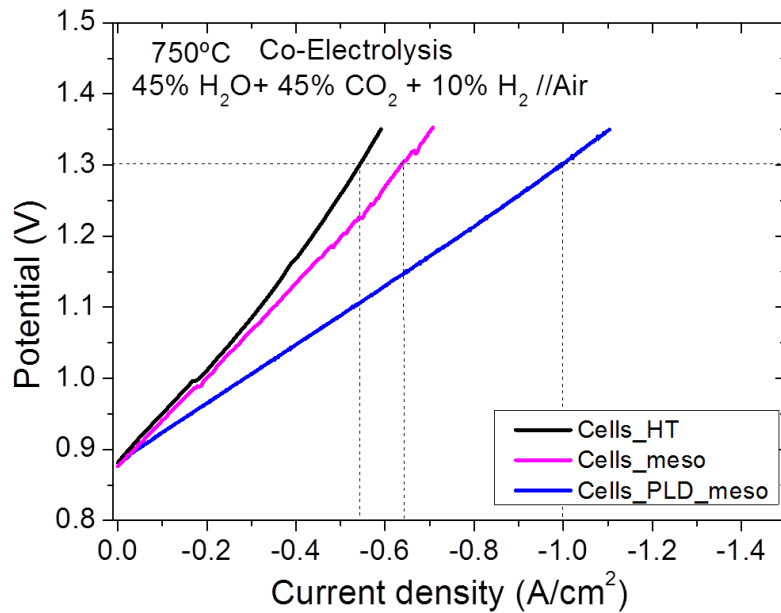


**Figura A.4:** Curvas I-V de celdas soportadas en electrodo de combustible medidas en co-electrolisis, en las que la capa barrera y el electrodo de oxígeno han sido respectivamente fabricados por: screen-printing (*Cells\_HT*), screen printing-aerografía (*Cells\_meso*) y PLD-aerografía (*Cells\_PLD\_meso*).

El **capítulo 6** muestra un estudio detallado del rendimiento de los electrolizadores fabricados con el electrodo de oxígeno optimizado, el cual está constituido por una capa funcional fabricada mediante infiltración (LSCF) del material mesoporoso (CGO), resultando en el CGO-LSCF composite; y una capa de LSCF (**Figura A.5**).

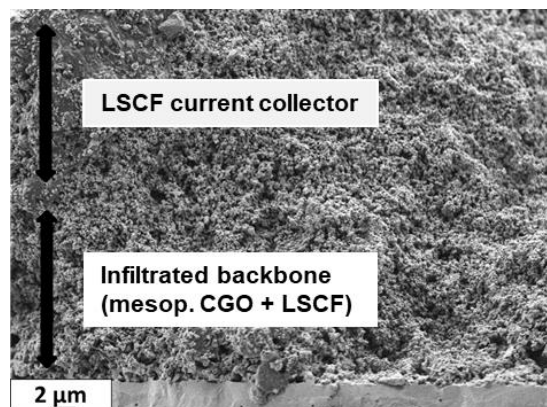


**Figura A.5:** Intercara de un electrolizador en el que es posible diferenciar la capa funcional mesoporosa (CGO-LSCF) del resto del electrodo de LSCF.

Altas densidades de corriente como  $-1.2 \text{ A/cm}^2$  han sido inyectada a  $750 \text{ }^\circ\text{C}$  operando en co-electrolisis. Además, la estabilidad de dicha capa funcional ha sido comprobada mediante operación continua durante 1400 h, registrando baja degradación ( $2\%/kh$  and  $<1\%/kh$ ) cuando diferentes densidades de corriente fueron inyectadas ( $-0.5 \text{ A/cm}^2$  and  $-0.75 \text{ A/cm}^2$ ). La combinación de técnicas electroquímicas y microestructurales han permitido concluir que dicha degradación ha sido debida a la pérdida de percolación

sufrida por el electrodo de combustible, lo cual ha resultado en un aumento de la resistencia óhmica. Estos resultados han demostrado que el electrodo de oxígeno compuesto por el CGO-LSCF composite mejora continuamente durante el tiempo de operación.

Por último, el **capítulo 7** muestra los resultados obtenidos del escalado de los electrodos mesoporosos en celdas de mayor área ( $25 \text{ cm}^2$ ) (**Figura A.6**). A partir de la caracterización electroquímica es posible concluir que los electrolizadores presentan alta flexibilidad ante las composiciones de gases utilizadas, obteniéndose rendimientos de  $-0.80 \text{ A/cm}^2$  in  $-0.82 \text{ A/cm}^2$  como máximas densidades de corriente inyectadas operando en electrólisis y en co-electrólisis. Además, la estabilidad de los electrodos mesoporosos propuestos ha sido validada inyectando  $-0.5 \text{ A/cm}^2$  durante 600 h, y confirmada a través de la caracterización microestructural.

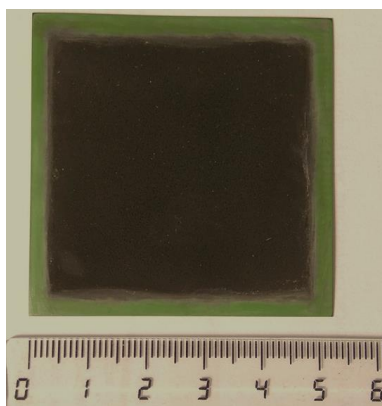


**Figura A.6:** Electrolizador de  $25 \text{ cm}^2$  soportado en el electrodo de combustible y cuyo electrodo de oxígeno se ha fabricado mediante infiltración de materiales mesoporosos.

# Scientific Contributions

## Publications

1. *Infiltrated mesoporous oxygen electrodes for high temperature co-electrolysis of H<sub>2</sub>O and CO<sub>2</sub> in solid oxide electrolysis cells.* E. Hernández, F. Baiutti, A. Morata, M. Torrell and A. Tarancón. *J. Mater. Chem. A*, 2018, 6, 9699-9707. (Published)

## Conferences

1. *Dynamic and exothermal operation of (co)electrolysis solid oxide electrolysis cells: stability of different electrodes.* L. Bernadet, E. Hernández, I. Guevara, C. Moncasi, A. Morata, M. Torrell, A. Tarancón. E-MRS 2018. Oral presentation.
2. *Electrochemical characterization of LSCF-CGO infiltrated mesoporous oxygen electrodes for SOEC under co-electrolysis in dynamic operation.* L. Bernadet, E. Hernández, I. Guevara M. Torrell, A. Tarancón. 13th European SOFC & SOEC Forum. Oral presentation.
3. *Infiltrated mesoporous materials as electrode for Solid Oxide Electrolyser Cells.* E. Hernández, M. Torrell, F. Baiutti, A. Morata, A. Tarancón. 21st International Conference on Solid State Ionics. Oral presentation.
4. *Solid Oxide Electrolyser Cells oxygen electrode based on infiltrated nanocomposite mesoporous materials.* M. Torrell, E. Hernández, F. Baiutti, A. Morata, A. Tarancón. 1st International Conference on Electrolysis. Oral presentation.
5. *3D printed electrolytes for Solid Oxide Electrolyser devices with complex hierarchical geometries.* M. Torrell, E. Hernández, F. Baiutti, A. Morata, A. Tarancón. 1st International Conference on Electrolysis. Poster presentation.
6. *Infiltrated mesoporous materials as oxygen electrode for Solid Oxide Electrolyser Cells.* E. Hernández, M. Torrell, F. Baiutti, I. Sánchez, A. Morata, A. Tarancón. Aportando valor al CO<sub>2</sub>. Poster presentation.

7. *Solid Oxide Electrolysis Cells (SOEC) based on infiltrated nanocomposite mesoporous materials.* E. Hernández, M. Torrell, F. Baiutti, A. Morata, A. Tarancón. Workshop on Degradation Mechanisms in Solid Oxide Cells and Systems. Poster presentation.
8. *Optimization of the adhesion of highly thermal stable nanocomposite mesoporous electrodes for Solid Oxide Cell.* E. Hernández, M. Torrell, A. Morata, A. Tarancón. 21<sup>st</sup> World Hydrogen Energy Conference 2016. Oral presentation.
9. *Characterization of Solid Oxide Electrolyzer Cells nanocomposite electrodes based on mesoporous ceramic scaffolds infiltration.* M. Torrell, E. Hernández, A. Morata, A. Tarancón. 12<sup>th</sup> European SOFC & SOE Forum. Oral presentation.